Non-Destructive Characterisation Of Structural Ceramics Using Impedance Spectroscopy

A Thesis Submitted For The Degree Of Doctor Of Philosophy

By

Xin Wang

Department Of Mechanical Engineering

Brunel University

September, 2001

Abstract

The aim of this project was to explore the potential applications of impedance spectroscopy (IS) in the non-destructive characterisation of structural ceramics.

A major advantage in the use of the IS technique is its capability in distinguishing the properties of different microstructural origins in materials, e.g., grains and grain boundaries, etc. In this thesis, a review of the theoretical aspects of IS is presented. An analytical approach and numerical analyses are conducted to illustrate how impedance spectra become resolved and why the spectral resolution is dependent on the representation formaiism as well as on the difference between the electrical properties of different microstructural features.

Three categories of structural ceramics, i.e. Al_2O_3/SiC nanocomposites, thermal barrier coatings and clay-based ceramics, were used as the model materials for this IS study. Both sintering and degradation phenomenon have been examined. Conventional analytical techniques, such as SEM, XRD, EDS, TGA and dilatometry, were used to aid in the understanding of IS and to prove the reliability of impedance measurements. The research results indicate:

- For Al_2O_3/SiC nanocomposites, IS can be used to examine the conducting mechanisms for the materials containing different quantities of SiC particles. The content of SiC can be correlated to the impedance spectral features and dielectric constant of the material. The oxidation scale formed at the surface gives a separate relaxation process. Based on the capacitive effect of this relaxation process, the thickness can be determined non-destructively using IS.
- For thermal barrier coatings, three relaxation processes can be found in the impedance spectra, which correspond to the top coating, oxidation layer and microstructural defects in the top coating, respectively. The thickness of the oxidation layer can be quantitatively related to the diameter of the corresponding semicircle in electrical modulus spectrum. In the meantime, the top coating degradation could also be monitored using IS.

- For clay-based ceramics, the impedance spectra consist of a high frequency semicircle and a low frequency tail, which correspond to bulk effect and electrode effect, respectively. The variation of the bulk conductivity with sintering time can be quantitatively correlated to the densification of the material during sintering. The electrode effect tail is directly related to the capacitive effect of the electrode/specimen interface, which could be an effective indicator of the electrode temperature.

Therefore IS is a useful technique for non-destructive characterisation of structural ceramics.

List Of Publications

This thesis describes research carried out by the author in the Department of Material Engineering initially and then Department of Mechanical Engineering at Brunel University, under the supervision of Dr. Ping Xiao. No part of this thesis has been accepted or is being currently submitted for any degree or other qualification in this university or elsewhere. The publications that have been generated during my PhD studies are listed as follows:

1) **X. Wang** and P. Xiao, "Nondestructive characterisation of alumina/silicon carbide nanocomposites using impedance spectroscopy", *J. Euro. Ceram. Soc.*, **20** (2000) 2591-2599.

2) **X. Wang**, J. Mei and P. Xiao, "Determining oxide growth in thermal barrier coatings(TBCs) non-destructively using impedance spectroscopy", *J. Mater. Sci. Lett.*, **20** (2001) 47-49.

3) **X. Wang**, J. Mei and P. Xiao, "Non-destructive evaluation of thermal barrier coatings using impedance spectroscopy", *J. Euro. Ceram. Soc.*, **21** (2001) 855-859

4) **X. Wang**, and P. Xiao, "Characterisation of the sintering process of clay-based materials using impedance spectroscopy", *J. Euro. Ceram. Soc.*, **in press.**

5) **X. Wang**, and P. Xiao, " In-situ monitoring of ceramic sintering using impedance spectroscopy", *British Ceramic Proceedings*, **accepted**

6) J. Mei **X. Wang**, and P. Xiao, " Characterisation of oxide layers and thermal barrier coatings using impedance spectroscopy", *Materials Research Society Symposium Proceedings*, **accepted.**

7) S.-H. Song, **X. Wang**, and P. Xiao, "Effect of microstructural defects on the electrical properties of TiO_2," *Mater. Sci. Eng. B*, **accepted.**

The majority of results presented in this thesis have been published as follows: chapter 5 was written with the results that have been published in **ref 1**; chapter 6 was based on the results published in the **refs. 2, 3 and 6**; chapter 7 was written with the results published in **refs. 4 and 5**.

Acknowledgements

I would like to express my deepest gratitude to my supervisor, Dr. Ping Xiao, for his encouragement, guidance throughout my PhD studies, and the painstaking effort of seeking financial support for this project.

I am grateful to all the technical staff and secretaries in the Department of Materials Engineering and Department of Mechanical Engineering, for their support and help in various ways. Thanks are due to Dr. Sue Woodise for her friendly attitude and professional instruction in setting up XRD, TGA and dilatometer etc.

I am deeply indebted to Dr Houzheng Wu, at Oxford University, for his kindness in providing Al_2O_3/SiC samples, stimulating discussions, and most importantly, friendship.

I would like to thank my colleagues, Junqin Li, Shenhua Song, Ammer Jadoon, Md Shawkat Ali and Ying Yuan, for the jokes, the funny anecdotes as well as the friendly arguments. Thanks to them, my PhD has never become a '**P**ermanent **hea**d**D**ache'

I want to thank my parents for their everlasting support and love. Special thanks to my wife, Yanxiang, and my daughter, Yuanyuan, for their patience, support and encouragement throughout all these difficult times.

Contents

1 Introduction

1.1 The Need for Non-Destructive Characterisation (NDC) of Ceramics

The need to characterise ceramic materials by non-destructive analytical methods is growing rapidly, especially for in-process and in-service examination of ceramic materials and components. This growth is mainly stimulated by the increased automation of ceramic manufacturing processes, the demand for greater reliability in components and more severe demands on the performance of ceramic materials. The exploration and development in this field will undoubtedly lead to the improvement of materials quality and competitiveness, as well as the reliability of components in service.

There are many conventional analytical methods available for the investigation of ceramic materials, e.g. electron probe microanalysis, differential thermal analysis (DTA), thermogravimetry (TGA), x-ray fluorescence and diffraction, and various types of spectroscopy (infrared spectroscopy, Raman spectroscopy etc.). Recently some highly sophisticated instrumentation such as nuclear magnetic resonance (NMR), scanning tunnel microscopy (STM), atomic force microscopy (AFM), etc. have begun to be applied to the characterisation of ceramic microstructures. Among these analytical methods, some are costly and time-consuming, but yield detailed information, others are relatively inexpensive and can be performed easily and rapidly, but yield limited information. However, most of them are destructive and typically off-line in nature, and it is difficult to adapt these measurements into the in-process and in-service examination of materials.

1.2 The State-Of -The-Art Of NDC Techniques For Ceramic Materials

The art and science of non-destructive testing (NDT) is very old. In ancient China, a pottery tradesman would perform a quality inspection on a ceramic article by patting and listening for the characteristic response from it. This is an effective technique that is still in practice nowadays in China. This may be regarded as a primitive version of sonic NDT.

Nowadays a wide range of NDT techniques have been developed for metallic materials and components. By contrast, the modern non-destructive evaluation (NDE) of ceramic materials is a relatively young field. So far the choices of techniques, for example, x-ray and sonic techniques, which have appeared to be effective and efficient for characterising ceramics in both green and sintered form, and for both in-process and in-service circumstance, are very limited. In many cases, such NDE instrumentation is too delicate and too expensive for routine use on the factory floor. Although advances in NDE equipment have been made in the past decade, which have resulted in major reductions in equipment costs, on line NDE sensors are still rarely encountered in high volume ceramic manufacturing applications at the present time (Schilling and Gray, 1998). Therefore further investigation and development of robust, inexpensive NDE methods are highly desirable.

1.3 Impedance Spectroscopy As A NDC Technique

Impedance spectroscopy (IS) has been used for several decades for investigating electrochemical kinetics. This technique has demonstrated its capability in many instances. It has been applied in fields ranging from metal or semiconductor electrode/electrolyte interfaces, electrode/layer/electrolyte systems, to porous electrodes (Gabrielli and Keddam, 1996). IS has been proven to be a powerful tool for the study of the electrical properties and microstructure of ionic, electronic, or mixed conductor ceramics (Lanfredi and Rodrigues, 1999). In the past decade, a number of works revealed that IS could be used as a non-destructive tool for the detection of structural defects in ceramics, especially in zirconia-based materials and cementitious materials (Kleitz *et al.* 1995, McCarter *et al.* 1988).

Besides being non-destructive, the technique of IS has the following advantages:

- IS can be adapted to on-line manufacturing or testing environments;
- IS does not require special sample preparation: theoretically the measurements can be performed on objects of any size and with any complex shape;
- IS equipment is relatively cheap, portable, and can provide quick and economical measurements without slowing production or testing progress;
- Unlike x-ray and γ-ray techniques, IS is non-hazardous.

1.4 About This Study

Brittleness appears to be an intrinsic weakness of ceramic materials. The principal limitations of applying ceramics for structural purpose are brittleness, low reliability and difficulty in predicting fracture. As a consequence, the main issue concerning the characterisation of structural ceramics is invariably the detection of various defects, such as cracks, pores and other forms of inhomogeneities in structure, either in the manufacturing process or in service.

Previous studies have revealed that IS is capable of detecting structural defects in some ionically-conducting ceramic materials. However, these studies on zirconia-based-materials are rather scattered, and far from being systematic and comprehensive. Very limited success has been actually achieved when structural defects were correlated to various IS parameters. Meanwhile, to our knowledge, no attempt seems to have been addressed in applying IS to characterising structural ceramics other than zirconia-based materials and cementitious materials.

The aim of this study is to investigate the feasibility of applying IS as an NDC method for a wide range of structural ceramics. For this purpose, a number of different ceramic materials have been covered, which fall into different electrically conductive categories, e.g. insulator, semiconductor and insulator/semiconductor composites as well as ionically-conducting materials. The circumstances of both in-service and in-process examination of ceramic materials have been considered. Attempts have also been made to establish quantitative as well as qualitative relations correlating microstructural inhomogeneities in the materials to their electrical properties.

This thesis is concerned with three representative material categories as following:

Al_2O_3/SiC nano-composites, a typical example of insulator/electronic conductor composites and representative of a series of SiC/carbon fibre reinforced ceramics, with the conductive phase being dispersed in an insulating ceramic matrix. The electrical conduction behaviour ranges from being insulating to semi-conducting, depending on the content of the conductive disperse phase.

Thermal barrier coatings (TBCs), consisting of yttria stabilised zirconia (YSZ) as the top coating and metal alloys as the bond coating and substrate. After oxidation, a semi-conducting oxide layer is formed. TBCs are a multi-layer solid-electrolyte/semiconductor/metal system

A clay compact during sintering, a typical glassy phase/insulator composite is representative of the category of clay-based ceramics, such as white ware and porcelains etc.. The glassy phase exhibits considerable alkali ion conductivity at high temperatures, while the porosity and other solid particles, such as undissolved silica, are insulating in nature.

The experimental results and theoretical analysis conducted in this work demonstrated that:

- For the insulator/electronic conductor composites, the content and orientation of the conductive phase are closely related to the IS parameters deduced from impedance spectra. The oxidation scale formed at the surface can be determined non-destructively by IS, a task that is very difficult for other techniques, such as SEM, weight gain measurement, optical microscopical observation etc. to fulfil.

- In TBCs, the electrical response from the oxide layer is well separated from those from other phases. The thickness of the oxide layer formed at the interface of the top coat / bond coat is reflected in the complex modulus plots. Not only bond coat oxidation, but also top coat degradation can be monitored using IS.

- During the sintering of clay-based ceramics, the formation of liquid phase and the shrinkage rate of the ceramic body can be monitored by *in-situ* impedance measurements. The electrode effect in the impedance spectra is representative of the local temperature, which can be an effective indicator of the firing of clay-based ceramics.

Therefore it is fair to say that IS is a powerful tool for the non-destructive characterisation of structural ceramics.

2 Literature Review

2.1 Introduction

Non-destructive testing (NDT) can be defined as "the application of physical principles for detecting inhomogeneities in materials without impairing the usefulness of the material" (McGonnagle, 1971). The primary purpose of NDT is to determine the existing state or quality of a material, with a view to acceptance or rejection (McGonnagle, 1971). Similarly, non-destructive evaluation (NDE) or non-destructive characterisation (NDC) refers to applying non-destructive techniques in the evaluation or characterisation of materials or components.

The ceramic industries have already recognised the need for increased monitoring of their manufacturing processes to measure microstructural evolution and detect the presence of defects (Wadley and Mehrabian, 1984). The interest in materials' property-determination by non-destructive techniques is increasing, especially for in-process and in-service inspection of structural and electronic materials and components (Ruud, 1984). Various non-destructive techniques have been employed in NDE for suspensions, composites and films as well as green bodies and sintered ceramics. These techniques include ultrasonic techniques (Komarenko *et al.* 1994; Challis and Tebbutt, 1998; Ahn, 1998; Kathrina and Rawlings, 1996; Boccaccini and Boccaccini, 1997), x-ray techniques (Huss *et al.* 1998), optical methods (Goller and Pye, 1998) and sonic detection (Pape, 1998), etc.

No matter what type of NDT technique it is, a certain form of energy, e.g. ultrasonic waves, optical light or x-radiation, etc. should invariably be utilised and some material properties provide the base for detecting the inhomogeneities. For example, the basic principle utilised in thermography is to apply heat to the test specimen and measure or observe the resulting temperature distribution, by using a video-thermographic camera (Curtis *et al.* 1993), or simply using surface-mounted thermal couples. Flaws alter the temperature distribution on or in the specimen. In the radiography method, x-ray or gamma radiation is used, and the radiated intensity from the sample is determined by the

thickness, density and defects of the materials, therefore it can generate shadows on photographic films (Nevadunsky and Lucas, 1975). In the ultrasonic technique, ultrasonic impulses generated by a piezoelectric transducer are used. The echo signal resulting from the reflection or scattering from the object is detected by the same piezoelectric device or another receiver. The phase delay between the reflection from different surfaces is correlated to the material properties (Dunyak *et al.* 1992).

In impedance spectroscopy, the energy applied is the electric field with varying frequency, and the electrical response during measurement is determined by the electrical properties of the materials under investigation. There are three variables, the real and imaginary components of the electrical response and the frequency in impedance measurement. A change in the ceramic microstructure and inhomogeneities leads to a change of electrical properties of materials and thereby may cause a change of the impedance spectrum. The electrical response from different phases, e.g., grain and grain boundary, and different physical processes, for example, the electrode/materials interfacial reaction, are normally reflected in different frequency domains. For instance, in YSZ (yttria stabilised zirconia) and $BaTiO_3$, the relaxation frequency for the grain interior is always in a high frequency range, and the electrode effect is in a low frequency range, with the response from the grain boundary phase being in an intermediate frequency range. Therefore the electrical response from different phases can be separated in the impedance spectra and the microstructure and properties of ceramic materials can be correlated to the IS parameters. This constitutes the fundamental attribute of using IS for characterising ceramics.

However, for our first impression, most ceramic materials, especially structural ceramics, appear to be insulators, or at least have very poor electrical conductance. As a matter of fact, most oxide ceramics are semiconductors, among which only a few examples are listed as following:

n-type (metal-excess) semiconductors: BeO, WO_3 CaO, ZnO, TiO_2, $MgAl_2O_4$ etc.;

p-type (metal-deficit) semiconductors: Cr_2O_3, $MgCr_2O_4$, MnO, NiO, CoO, PbO, etc.(Kubaschewski and Hopkins, 1962).

Partially or fully stabilised zirconia ceramics are not only good ionic conductors, but also typical phase-transformation-toughed structural materials that have many technical applications. All the alkali glasses are alkali ion conductors. It should also be noted that the conductivity enhancement of a semiconductor can be achieved by raising the temperature and/or doping with a small amount of impurities in the materials. Many ceramic materials that are insulators at room temperature may show ionic conduction at high temperature (Kingery *et al.* 1976c). In this sense, most ceramics can be made deliberately, at least partially, conductive to meet the requirement of impedance measurements. Meanwhile, it is important to note that many ceramic composites contain carbon and silicon carbide phases which exhibit significant electrical conductance at room temperature (Zhang *et al.* 1992). This is why electrical resistance measurements can be used to monitor the fracture (Wang *et al.* 1998) and detect the fatigue in ceramic composites (Ishida and Miyayama, 1994). Therefore IS appears to be applicable to the characterisation of most ceramics, particularly those belonging to either ionic conductor, semiconductor, or conductor/insulator composites.

2.2 Impedance And Impedance Spectroscopy

2.2.1 Impedance Measurement

IS measurement is usually made with cells having two identical electrodes applied to the faces of a sample. There are several different electrical stimuli which are used in IS, but the most common and standard one is to measure impedance directly in the frequency domain by applying a single-frequency voltage to the interface and measuring the phase shift and amplitude. The small amplitude of electrical stimuli ensures that there is a linear relationship between the current and potential, and that the response is in a steady state; that is, it does not change with time and many measurements can be averaged. A wide range of frequencies, usually over several orders of magnitude, is applied so that processes having different time constants can be detected within one experiment (Macdonald and Johnson, 1987).

2.2.2 Concept of Impedance

The concept of electrical impedance was first introduced by Oliver Heaviside in the 1880s and was soon after developed in terms of vector diagrams and complex representation by A. E. Kennelly and especially C. P. Steinmetz. Impedance is a more general concept than resistance because it takes phase differences into account (Macdonald and Johnson, 1987).

In order to understand the basis of IS, it is helpful to consider some simple electronic analogues which mimic closely the systems of interest (Christensen and Hamnett, 1994). If we consider first a simple resistor and apply a steady, small sinusoidal potential, $V\sin(\omega t)$, across a resistor that has a resistance R, then the current through the resistor is determined by:

$$I = \frac{V}{R} = \frac{V \sin(\omega t)}{R} \qquad (2\text{-}1)$$

When the same signal is applied across a capacitor that has a capacitance C, then the current through the capacitor is given by:

$$I = \frac{dQ}{dt} = C\frac{dV}{dt} = C\frac{d(V \sin(\omega t))}{dt} = C\omega V \sin(\omega t + \pi/2) \qquad (2\text{-}2)$$

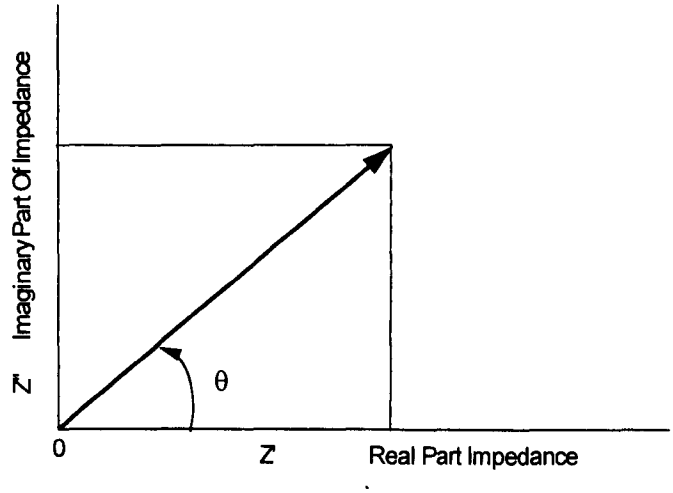

Figure 2-1 The impedance Z plotted as a planar vector using rectangular and polar coordinates

Now we can see the current response from a pure resistor is in the same phase as the applied potential signal, while the current response from a capacitor always leads the

potential signal by 90°. It is not difficult to conceive that the current response from any circuit that is composed of both a resistor and a capacitor would have a phase difference with the applied sinusoidal potential signal. The phase difference is in between 0~90°, and the impedance can be expressed in terms of in-phase component and out-of-phase component. For this reason, impedance is usually expressed by a vector quantity, $Z(\omega)=Z'+jZ''$, where Z' is the in-phase component or real part of the complex, Z'' is the out-of-phase component or imaginary part of the complex, and $j\equiv\sqrt{-1}\equiv\exp(j\pi/2)$. Impedance can be plotted with either rectangular or polar coordinates (Macdonald and Johnson, 1987), as shown in Fig.2-1. Here the two rectangular coordinate values are:

$$Z'=|Z|\cos(\theta) \quad \text{and} \quad Z''=|Z|\sin(\theta) \qquad (2\text{-}3)$$

With the phase angle

$$\theta=\tan^{-1}(Z''/Z') \qquad (2\text{-}4)$$

and the modulus

$$|Z|=[(Z')^2+(Z'')^2]^{1/2} \qquad (2\text{-}5)$$

2.2.3 Various Formalisms Of IS

From Eqs. 2-3~2-5, we can understand that the data from impedance measurements can be expressed in a number of different ways. Plotting impedance data in a complex plane with real and imaginary coordinates gives a complex plane plot. Although complex impedance plane plots are frequently called "Nyquist diagrams", this is thought to be a misnomer by J. R. Macdonald (Macdonald and Johnson, 1987) and this term should be avoided. We also can plot the total impedance $|Z|$ and phase angle θ as a function of frequency ω. The plots of $\log|Z|$ vs. $\log\omega$ and θ vs. $\log\omega$ are called Bode plots.

There are three other possible complex formalisms which can be derived from complex impedance, the electric modulus M*, the admittance Y* (or A*), and the permittivity ε^* and these quantities are interrelated (Hodge *et al.* 1976):

$$M^*=j\omega C_0 Z^*=M'+jM'' \qquad (2\text{-}6)$$

$$\varepsilon^* = (M^*)^{-1} \qquad (2\text{-}7)$$

$$Y^* = (Z^*)^{-1} \qquad (2\text{-}8)$$

$$Y^* = j\omega C_0 \varepsilon^* \qquad (2\text{-}9)$$

Where ω is the angular frequency $2\pi f$, C_0 is the vacuum capacitance of the empty measuring cell, $C_0 = e_0/k$, e_0 is the permittivity of free space (8.854×10^{-14} F/cm), and $k = l/A$, the cell constant where l is the thickness and A the area (Sinclair and West, 1989).

Among these four formalisms, the admittance Y*, the impedance Z* and the permittivity ε^* have normal meanings as defined in many textbooks, while the concept of electrical modulus M* is relatively new. It can be better understood by comparing it with the shear modulus in mechanical relaxation. The vanishing of M'' at low frequencies implies the lack of a restoring force for flow of charge in a conducting dielectric under the influence of a steady electric field (Provenzano *et al.* 1972). The electrical modulus (M) and the complex permittivity (ε^*) bear the same relationship to one another as do the modulus and the compliance in mechanical relaxation (Ambrus, *et al.* 1972).

If these different quantities are plotted in complex planes, then various complex plane diagrams (Z'' vs. Z', Y'' vs. Y', M'' vs. M' and ε''vs.ε') can be obtained. If they are plotted as a function of frequency in a way similar to a Bode plot, then so called 'spectroscopic displays' (Y'', Z'' and M'' etc. vs. $\log_{10}\omega$) are obtained (Hodge *et al.* 1976). These different representation diagrams are illustrated in **Appendix I**. They are sometimes called admittance spectrum (Y'' vs. Y'), modulus spectrum (M'' vs. M') and dielectric permittivity spectrum (ε''vs.ε') etc., but impedance spectroscopy is a general term that is used to include and denote all these spectra (Macdonald and Johnson, 1987).

2.3 General Characterisation Procedure Using IS

IS involves a relatively simple electrical measurement that can readily be automated and whose results may often be correlated with many complex materials variables: from mass transport in corrosion to defects and microstructure of solids (Macdonald and Johnson, 1987).

The essence of the impedance technique is that the cell is always mimicked by a suitable model system, in which the properties of the materials and the electrode/materials interface are represented by appropriate electrical analogues. The impedance of the cell is

then measured over a wide frequency range (Christensen and Hamnett, 1994). The model parameters are obtained by determining parametric values which give the best fit to the impedance data. Finally the model must be correlated with the physical system to establish the reliability of the model and to establish that the model values determined from the fit are physically reasonable. If not, the model may have to be modified and the entire analysis process repeated. Clearly the required analysis is not always straightforward and is usually quite involved (Johnson and Worrell, 1987).

A flow diagram of a general characterisation procedure using IS is proposed by Macdonald and Johnson (1987), as in Fig.2-2.

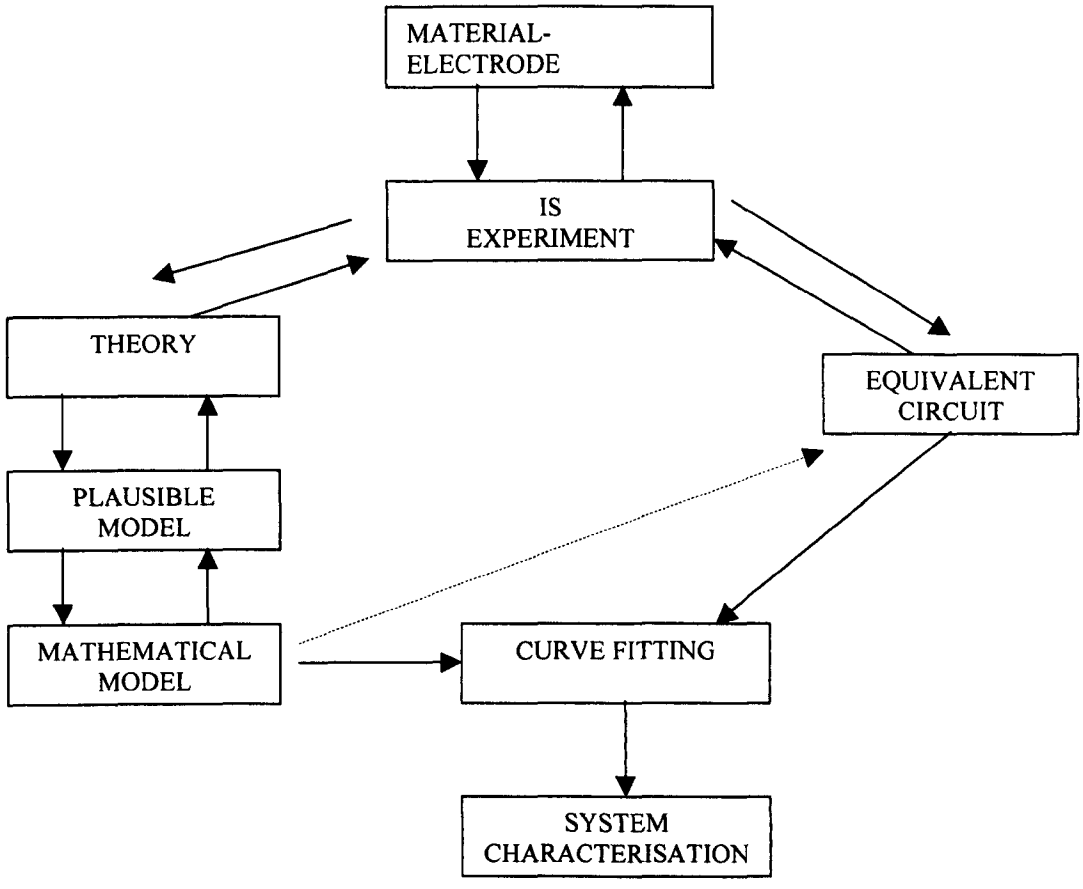

Figure 2-2 Flow diagram for the measurement and characterisation of a material-electrode system.

It has been realised that the simulation of impedance experiments on its own generally cannot provide a definite analysis of a system, since there is frequently more than one equivalent circuit that fits, numerically, a given experimental data set (Sinclair and West, 1989). Therefore a set of impedance data could not be properly understood and interpreted before we have a proper physical model for the particular system. An appropriate model is always built based on adequate knowledge of the particular system, among which are the type of charge carriers, the migration path of charge carriers, the charge transfer and mass transfer on the electrode/materials interface etc.

2.4 Electrical Conduction In Ceramics Materials

2.4.1 Introduction

The electrical conductivity associated with ceramics is, in most cases, semi-conductive or ionic. To understand correctly the electrical conductance mechanism, it is necessary to establish an equivalent circuit model for the ceramic and thereby interpret the IS properly.

2.4.2 Electrical Conduction In Semiconductors

The electrical conductance of a semiconductor can be understood in terms of the electron energy band structure. As shown in Fig.2-3, the electronic band structures of semiconductor and insulators are fundamentally different from those of metals because of the existence of the band gap which lies between a filled valence band and an empty conduction band (Jiles, 1994). For metals there is always a finite concentration of electrons in the conduction band, so metals always display high electronic conductivity. For insulators, the band gap is sufficiently high so that normally there are no electrons able to move through the crystal. For semiconductors, the concentration of electrons in the conduction band depends on both temperature and composition (Kingery *et al.* 1976c).

Electronic conductivity in semiconductors is due to the presence of donor- or acceptor-type point defects, which at room temperature are fully ionised, giving rise to delocalised electrons in the conduction band (n-type) and holes in the valence band (p-type)

respectively. A typical order of magnitude for the concentration of donors or acceptors, and hence of electronic free charge carriers, is between 10^{16} and 10^{18} cm^{-3}, i.e., about six orders of magnitude lower than in metals (Gomes and Vanmaekelbergh, 1996).

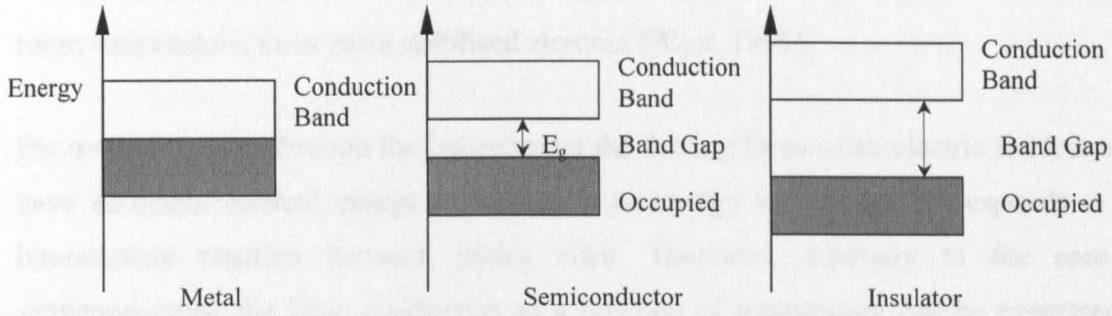

Figure 2-3 Simplified band structure diagrams of a metal, semiconductor and insulator. Typical values of the band gap: 0eV in metals, 0.5-5eV in semiconductors and 5.0eV or greater in insulators.

The conductivity of a semiconductor increases exponentially with temperature (Jiles, 1994):

$$\sigma_i \propto \exp(-\frac{E_g}{kT}) \qquad (2\text{-}10)$$

where E_g is the band gap and k is the Boltzmman constant.

For ceramics having low electrical conductivity (lower than 10^{-5} $S \bullet cm^{-1}$), even minor variations in composition, impurity content, heat treatment, stoichiometry and other variables can have a significant effect on electrical conductance. This is because the impurity atoms introduce new localised energy levels for electrons intermediate between the valence band and the conduction band. If the new energy levels are unoccupied and lie close to the energy of the top of the valence band, it is easy to excite electrons out of the filled band into these new acceptor levels (Kingery *et al.* 1976c).

2.4.3 Ionic Conduction In Crystalline Materials

One kind of charge carrier that is always present and can contribute to electrical conductivity is the ions present in crystalline materials. Electrical conductivity resulting from ion migration is important in many ceramic materials especially at high

temperatures (Kingery *et al.* 1976c). Among the oxide ionic conductors, the most well-studied and useful materials to date are those with the fluorite-related structure, especially ones based on ZrO_2, ThO_2, CeO_2 and Bi_2O_3. The most common of these is the ZrO_2 family, in which the mobile species is the oxide ion (Huggins, 1978). Pure ZrO_2 is cubic only above ~2400°C. 8 mol % of Y_2O_3 is needed to stabilise the cubic form to room temperature, as in yttria stabilised zirconia (West, 1995).

For an ion to move through the lattice under the driving force of an electric field, it must have sufficient thermal energy to pass over an energy barrier that corresponds to the intermediate position between lattice sites. Therefore, similarly to the case of semiconductors, the ionic conduction as a function of temperature can be expressed as (Kingery *et al.* 1976c):

$$\sigma_i \propto \exp(-\frac{\Delta G}{kT}) \qquad (2\text{-}11)$$

where ΔG is the potential barrier.

However it is important to note that some materials may exhibit mixed ionic-electronic conductivity. For example, undoped nano-CeO_2 electrolyte is an ionic conductor, but also exhibits enhanced electronic conductivity (Chiang *et al.* 1997); bismuth oxide-based materials are very good oxygen–ion conductors, but they develop electronic conductivity in low oxygen partial pressures (Shuk and Wiemhofer, 1996; Badwal *et al.* 1998). Meanwhile some semiconductors also exhibit ionic conductivity, for example, $SrTiO_3$ exhibits both electronic and ionic conduction (Choi and Tuller, 1988). Titanium dioxide exhibits either n or p type conductivity in addition to ionic conductivity, depending on oxygen partial pressure (Tuller, 2000). Both single crystalline (Nowotny *et al.* 1998) and nanocrystalline titania (Knauth and Tuller, 1999) have an ionic conductivity of about 2.5×10^{-5} S•cm^{-1} at 1000K, at high P_{O_2}, etc.

2.4.4 Ionic Conduction In Glass And Molten States

The two most important constituents present in all glasses are network formers and network modifiers. Network formers are compounds of a covalent nature such as SiO_2, P_2O_3, B_2O_3, GeS_2, P_2S, GeO_2 etc., in which all the oxygen atoms are covalently bound to

the network former cations in tetrahedral or triangular elementary units. The macromolecules are formed by an assembly of these units in which at least one atom of oxygen, called a bridging atom, is shared (Ravaine and Souquet, 1978). Network modifiers, such as Li_2O, Na_2O, K_2O and Ag_2O etc., can interact strongly with the structure of network formers, leading to the breaking of the oxygen bridging linking two network former cations. The addition of a modifier introduces ionic bonds, giving rise to cationic conduction. For instance, in a silicate glass containing K_2O, the reaction between silica and potassium oxide may be expressed schematically as in Fig. 2-4 (Souquet, 1995). In this way the charge carriers K^+ are created.

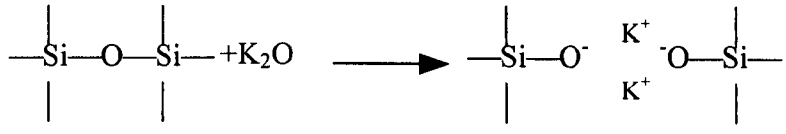

Figure 2-4 Schematic of reaction between silica and potassium oxide in silicate glass.

At the same time, some oxygen atoms that are not bridging can be negative charge carriers and remain in the vicinity of alkali cations or alkaline earth cations of the network modifier oxides (Ravaine and Souquet, 1978). According to the polarisation study of glasses (Doi, 1987, Carlson *et al.* 1972 & 1974), it is clear that some oxygen-ion conduction is possible by movement of non-bridging oxygen ions in the highly polarised field near the anode. Normally alkali ions are the major charge carriers, while the conductivity in the alkali-depleted-region is via non-bridging oxygen ions. The oxygen-ion conduction in some glasses has been thought to be six or seven orders of magnitude lower than that for alkali ion conduction (Badwal, 1995).

For a given silicate composition, little or no difference is seen between the structure of the glassy and molten states as deduced from the diffraction and spectroscopy measurements: i.e., the inter-ionic distances and oxygen co-ordination numbers for cations are essentially the same for the glassy and molten states (Turdogan, 1983). Therefore the electrical conduction mechanism of the molten states can be assumed to be similar to that of glass. However, it is important to note that charge carriers in the liquid are expected to be more mobile than in the solid state, for this reason the liquid is a much

better ionic conductor than the solid (Bockris *et al.* 1952). Above the glass transition temperature (T_g), the ions move partly in response to the viscous flow of the surrounding medium; below T_g the mode of transport may involve the discrete hopping of ions past effectively frozen barriers presented by the host glass matrix (Sidebottom *et al.* 1995). An Arrhenius temperature dependence of electrical conductivity normally shows a discontinuity at the transition range corresponding to the freezing of the glass structure at this temperature, and the activation energy below T_g is normally substantially smaller (Sidebottom *et al.* 1995).

The temperature dependence of glass conductivity over a considerable temperature range can be expressed as:

$$\sigma = \sigma_o \exp(-\frac{E}{RT}) \qquad (2\text{-}12)$$

where E is an experimental activation energy for conductivity.

In terms of Eqs. 2-10, 2-11, 2-12, we can see that whatever the conduction mechanism, electronic, ionic or mixed conduction, the electrical conductivity of ceramic materials (σ) is thermally activated and can be expressed by an Arrhenius law:

$$\sigma = \sigma_o \exp(-\frac{E_a}{RT}) \qquad (2\text{-}13)$$

The activation energy for conduction (E_a) can be calculated from the slope of the straight line given by $\log\sigma$ vs. 1/T.

2.4.5 Ionic Conduction on Particle Surfaces

A typical example of the ionic conduction along a particle surface is the 'surface proton hopping' in ionic-type humidity sensors. Quite a few oxide ceramics demonstrate a change in their electrical properties because of water-adsorption processes on their surface, which permit their use as humidity sensors (Traversa, 1995). As dry oxides are kept in contact with humid air, water molecules chemisorb to the available sites on the oxide surface, to form hydroxyl ions. When the first layer of water molecules is formed, subsequent layers of water molecules are physically adsorbed on to the first hydroxyl

layer (McCafferty and Zettlemoyer, 1971). When only hydroxyl ions are present on the oxide surface, the charge carriers are protons, which hop between adjacent hydroxyl groups. When the first layer of water is continuous, charge transfer is governed by proton hopping between neighbouring water molecules in the continuous film (Fleming, 1981).

Ionic conduction along particle surfaces is an important factor that needs to be considered, especially in understanding the impedance spectra of very porous ceramic materials. Frequently, because of surface conduction, the well-known phenomenon of two-bulk–semicircles, corresponding to grain and grain boundary respectively, is not present in the impedance spectrum.

2.5 Physical Model And Equivalent Circuit

2.5.1 Brick Layer Model

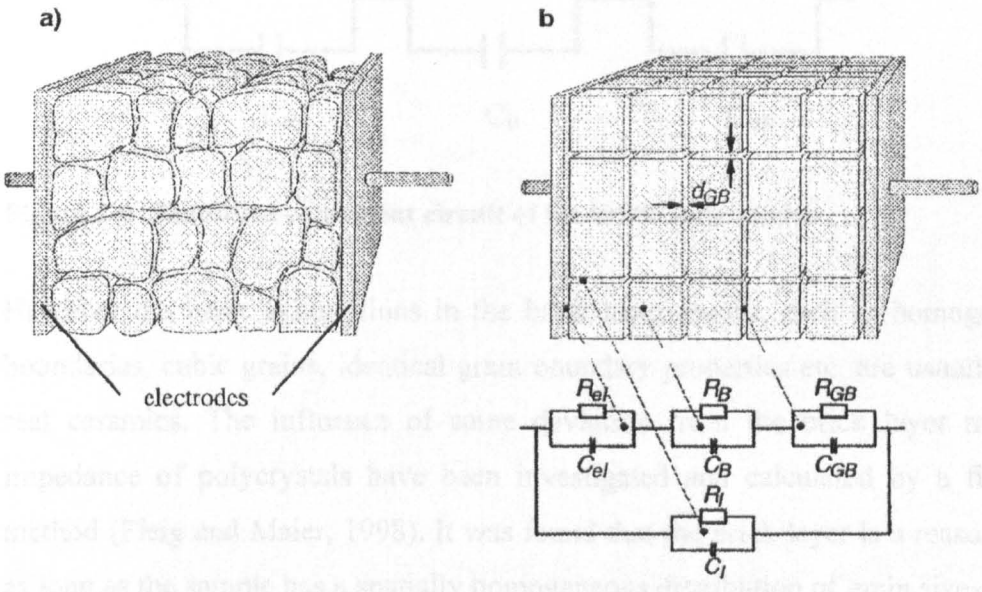

Figure 2-5 (a) schematic of a real ceramic microstructure. (b) Simplified brick-layer model and equivalent electrical network consisting of different RC elements. Indices: el=electrode/ceramic interface, B=bulk, GB=grain boundary channels perpendicular to the electrode interface (after Waser and Hagenbeck, 2000).

For a dense ceramic material, an ideally simplified microstructural model is the so-called brick layer model (or brick-wall model), as shown in Fig.2-5, where the ceramic is assumed to consist of identical cubic grains separated by a continuous grain boundary phase (Waser and Hagenbeck, 2000).

In a broad range of electroceramic materials which show ionic conduction, mixed ionic-electronic conduction or pure electronic conduction, grain boundaries often act as barriers to the transport of charge carriers (Waser and Hagenbeck, 2000), therefore resistive layers at the grain boundary interfaces are formed. For example, at 500°C the conductivity of grain boundaries in CaO-stabilised zirconia is at least two orders of magnitude lower than that of the grains (Aoki *et al.* 1996). In such cases, the electrical conduction along the grain boundary channels perpendicular to the electrode is very small and assumed to be negligible, and therefore the equivalent circuit for the brick layer model can be further simplified as shown in Fig. 2-6.

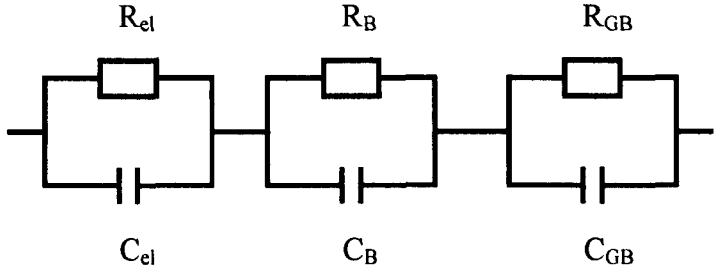

Figure 2-6 Simplified equivalent circuit of the brick layer model.

However the basic assumptions in the brick layer model, such as homogeneous grain boundaries, cubic grains, identical grain boundary properties etc. are usually violated in real ceramics. The influence of some deviation from the brick layer model on the impedance of polycrystals have been investigated and calculated by a finite element method (Fleig and Maier, 1998). It was found that the brick layer is a reasonable model, as long as the sample has a spatially homogeneous distribution of grain sizes, an isotropic distribution of grain orientations, isotropic conductivities, a relatively narrow grain size distribution and uniform grain boundary properties. The brick layer model fails when there exist imperfect contacts (lateral inhomogeneities) between grains, or grain

boundary properties demonstrate a very broad or bimodal distribution (Fleig and Maier 1999a and Fleig, 2000).

2.5.2 Constriction Model

The constriction model was first proposed by Bauerle (Bauerle, 1969) for characterising the grain and grain boundary effects in stabilised zirconia. According to this model oxygen-ions are partially blocked at the grain boundaries by the segregated phases which partially cover the grain boundaries. In their study of the conductivity of a Li superionic conductor, Bruce and West (1983) also pointed out that the transport of charge carriers takes place through a constriction mechanism as some sections of the diffusion paths are blocked by the poorly conducting phases, such as glassy phase, voids, and any other second insulating phases.

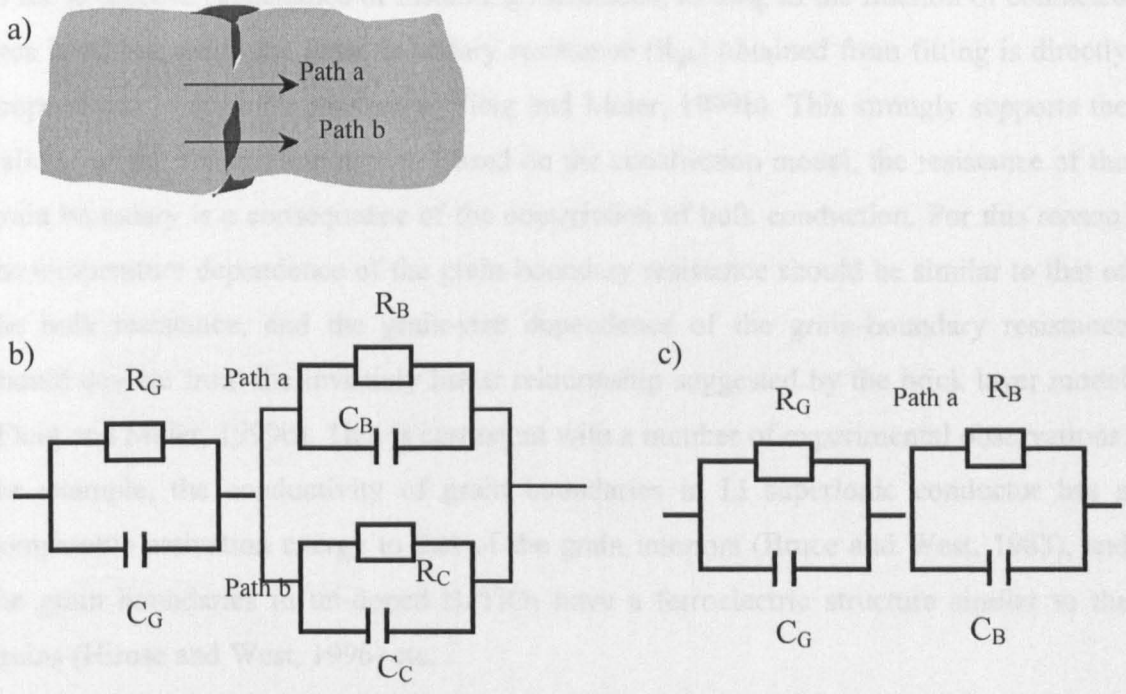

Figure 2-7 (a) Schematic of the constriction model, with the dark areas representing insulating phase. (b) Equivalent circuit of the constriction model. (c) Simplified equivalent circuit of the constriction. Indices: G= grain, B= grain boundary, C= insulating phase. (Note: the electrode effect is not included in this diagram).

Based on the constriction model, the grain boundary resistivity is actually the constriction resistance at grain contacts, rather than that due to the presence of a

continuous grain boundary phase as in the brick layer model. As shown in Fig.2-7a, b, in such a case, the electrical conduction across the grain boundary actually consists of two conduction paths, one crossing the insulating phase, another through the direct contact of two grains. The equivalent circuit can be simplified as in Fig. 2-7c, if the conduction path crossing the insulating phase is neglected*.

Therefore the equivalent circuit for the constriction model is actually the same as that for brick layer model. For this reason the constriction model sometimes is also called the brick layer model. However, because the constriction model is established on a different physical basis, the interpretation of the IS from it should be different from that for a brick layer model with a continuous grain boundary phase.

According to the finite element calculation conducted by Fleig and Maier (1999b), the grain boundary capacitance obtained from a fit using two RC elements in series is close to the geometric capacitance of insulating inclusions, as long as the fraction of contacted area is <25%, while the grain boundary resistance (R_{gb}) obtained from fitting is directly proportional to the bulk resistance (Fleig and Maier, 1999b). This strongly supports the validity of the constriction model. Based on the constriction model, the resistance of the grain boundary is a consequence of the constriction of bulk conduction. For this reason, the temperature dependence of the grain boundary resistance should be similar to that of the bulk resistance, and the grain-size dependence of the grain-boundary resistance should deviate from the inversely linear relationship suggested by the brick layer model (Fleig and Maier, 1999b). This is consistent with a number of experimental observations: for example, the conductivity of grain boundaries in Li superionic conductor has a comparable activation energy to that of the grain interiors (Bruce and West, 1983), and the grain boundaries in un-doped $BaTiO_3$ have a ferroelectric structure similar to the grains (Hirose and West, 1996) etc.

Badwal (1995) and Dessemond *et al.* (1993) suggested that the constriction model is more suitable for the study of the ZrO_2-based materials. It was found that the influence on the IS of voids and second phases is similar to that of grain boundaries (Badwal,

* **Please note that in order to avoid unnecessary repetitions, the electrode effect is not included here, just for the sake of simplicity of discussion. For the detailed discussion on electrode effect, see section 2.8.**

1995). The blocking effect of grain boundaries is invariably found to disappear at high temperature, which can only be explained by using the constriction model. According to the brick layer model, a continuous grain boundary layer is assumed to be present in the microstructure. Therefore the activation energy of the grain boundaries is expected to be different from that of grains and the blocking effect of the grain boundaries should always exist whatever the temperature. This has frequently been found not to be the case according to many reports (Badwal, 1995; Dessemond *et al.* 1993; Bruce and West, 1983).

2.5.3 Multi-layer Model

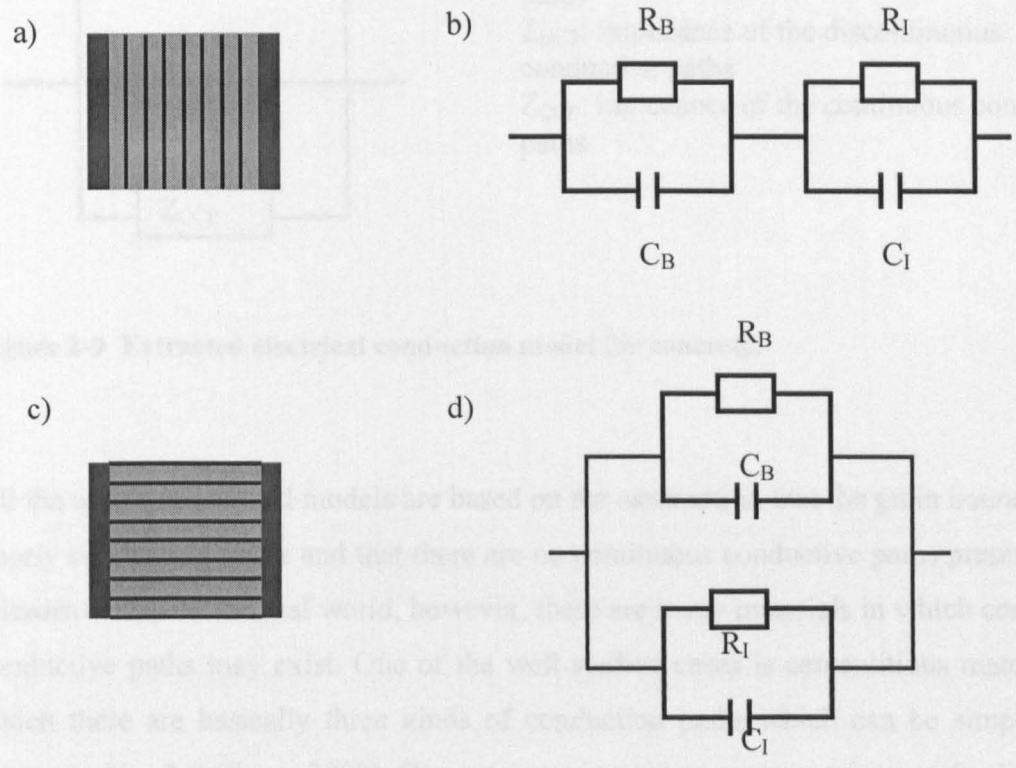

Figure 2-8 (a) Series layer model. (b) Equivalent circuit of the series layer model. (c) Parallel layer model. (d) Equivalent circuit for the parallel layer model. Indices: B= bulk phase, I= interface between two layers.

This model is suitable for representing multi-layer materials and materials with well aligned columnar grains. Typical cases are the series layer model in which layers are arranged parallel to the electrodes, and the parallel layer model in which layers are aligned perpendicular to the electrodes (Fig.2-8 a-d). Two semicircles should appear in

the complex impedance plot for the series layer model. By contrast there should be no separate semicircle for different phases in the parallel layer model.

Nitrogen-stabilized-zirconia has a microstructure consisting of well aligned columnar grains, for which the grain boundaries and bulk grains have been successfully characterised using a multi-layer model by taking impedance measurements along and perpendicular to the orientation of the columnar grains (Lee *et al.* 2000).

2.5.4 Continuous Conductive Path Model

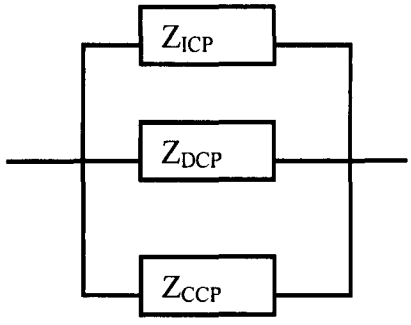

Z_{ICP}: impedance of the 'insulating' conductive paths
Z_{DCP}: impedance of the discontinuous conductive paths
Z_{CCP}: impedance of the continuous conductive paths

Figure 2-9 Extracted electrical conduction model for concrete.

All the above-mentioned models are based on the assumption that the grain boundary is a poorly conducting phase and that there are no continuous conductive paths present in the microstructure. In the real world, however, there are many materials in which continuous conductive paths may exist. One of the well-studied cases is cementitious materials, in which there are basically three kinds of conduction paths which can be simplified as shown in Fig. 2-9 (Song, 2000). Cement paste is a heterogeneous mixture of solid, liquid and gaseous components (Macphee *et al.* 1997). The continuous conductive paths are actually created by the continuous networks of pores filled with liquid that is not pure water but a solution of moderate ionic strength and therefore capable of conducting electricity (Christensen *et al.* 1994), while the un-reacted cement and entrapped air is insulating, and the blocked liquid-filled pores are discontinuous conductive paths (Macphee *et al.* 1997).

Some electroceramics, e.g., Ni-doped $SrTiO_3$, may exhibit high grain boundary conductivity under certain circumstances, and continuous conductive paths are thus formed. In this case, the equivalent circuit can be expressed schematically as in Fig. 2-10.

Another example is ionic-type humidity sensors. In this type of device, the conductance is created by proton hopping along particle surfaces (Fleming, 1981), and the porous nature and high surface area of these materials provide an easy access of humidity and the conductive paths are obviously continuous throughout the material.

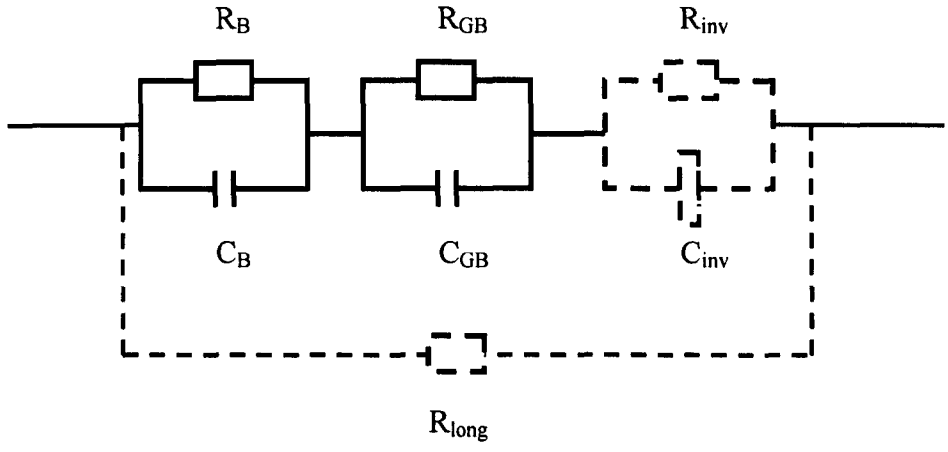

Figure 2-10 Schematic of the equivalent network describing the small-signal properties of a ceramic taking conduction along the grain boundaries into account. The index 'inv' hints at the RC-network elements of the inversion layer, the index 'long' describes the longitudinal GB resistance (after Waser and Hagenbeck, 2000).

Complications arise when there are short-circuit pathways present in materials. The typical feature of the continuous path model is that normally there is only one semicircle corresponding to the bulk effect, because in most cases the continuous conductive paths will dominate the electrical conduction and thus shield the effects from other elements in the circuit. For this reason, care needs to be taken when interpreting the impedance spectra, where electrical responses from grain and grain boundary are not resolved so that it is very difficult to distinguish the different effects from different phases.

2.6 Representations Of Impedance Spectroscopy

The complex impedance plane plot and the Bode plot appear to be the most commonly used representations of IS. A semicircular arc in a complex plane plot normally represents a particular physical /chemical process in the bulk or at the electrode/material interface, while the Bode plot explicitly shows the dependence of the total impedance and phase angle on the frequency. In the complex plane plot, detailed information, such as relaxation frequency, semicircular diameters and depressed angles etc., sometimes can be easily perceived.

However, as has been mentioned in section 2.2, there are four different immitance functions related with IS and hence there are many different ways of representing impedance spectra, with each one highlighting different features (Hodge *et al.* 1976). Therefore, in order to have a deep understanding of IS and extract more useful, more precise information from impedance measurement data and the proper representations of this data are important.

Bauerle (1969) demonstrated the usefulness of the complex admittance approach in solid electrolyte studies, while Armstrong *et al.* (1974) have favoured the complex impedance formalism for analysing data on β-alumina and $RbAg_4I_5$. Macedo *et al.* (Macedo *et al.* 1972, and Ambrus *et al.* 1972) were among the first to exploit the modulus and used it for analysing conductivity relaxation in glasses and in concentrated aqueous solutions.

Owing to its simplicity, the electrical modulus formalism has found wide acceptance among many researchers. This formalism suppresses the undesirable experimental artifacts associated with electrode polarisation, leaving a clean data presentation (Macedo *et al.* 1972). Hodge *et al.* (1975) extended the modulus treatment to the study of solid electrolyte systems. It had been shown that a combined analysis using both the complex impedance and the complex modulus formalisms have certain advantages (Hodge *et al.* 1976; Sinclair and West, 1989).

The Debye peak in spectroscopic plots of the imaginary components, Z'' and M'' versus log ω can be described by (Morrison *et al.* 2001):

$$Z'' = R\left(\frac{\omega RC}{1+(\omega RC)^2}\right) \qquad (2\text{-}14)$$

$$M'' = \frac{\varepsilon_o}{C}\left(\frac{\omega RC}{1+(\omega RC)^2}\right) \qquad (2\text{-}15)$$

where ω is the angular frequency and ε_o the permittivity of free space. The frequency at the Debye maxima for each RC element is given by

$$\omega_{max}=2\pi f_{max}=(RC)^{-1}=\tau^{-1} \qquad (2\text{-}16)$$

where τ is the time constant of the RC element, f_{max} is the relaxation frequency. Both are independent of the geometry of the sample and are intrinsic properties of the RC element. The electrical relaxation under consideration here is associated with the long-range conductivity processes. To distinguish it from dielectric relaxation involving dipole reorientation, an electrical relaxation of this sort is called conductivity relaxation (Provenzano *et al.* 1972).

The magnitudes of Debye peaks at the peak maxima are given by

$$Z''_{max}=R/2 \qquad (2\text{-}17)$$

$$M''_{max}=\varepsilon_o/2C \qquad (2\text{-}18)$$

Hence the magnitude of R and C can be estimated from either Z''_{max} or M''_{max} using Eqs. 2-17, 2-18.

From Eqs. 2-14, 2-15, we can understand that the power of combined usage of impedance and modulus spectroscopy is that the Z'' plot highlights phenomena with the largest resistance whereas M'' picks out those with smallest capacitances (Sinclair and West, 1994).

Badwal (1988) pointed out that the complex impedance plot is useful when the relaxation times of various processes differ as a consequence of different capacitive components, while the modulus or permittivity plane plots are more suitable for a system where the relaxation times differ due to different resistive components.

As has been already mentioned in the previous section, the most frequently used physical model is the ideal brick layer model (Fig. 2-5), for which, according to Abrantes *et al.* (2000b), the real and imaginary parts of the impedance ($Z^*=Z'-jZ''$) are described by

$$Z'=R_B/[1+(\omega/\omega_B)^2]+R_{gb}/[1+(\omega/\omega_{gb})^2]+R_{el}/[1+(\omega/\omega_{el})^2] \qquad (2\text{-}19)$$

$$Z''=R_B(\omega/\omega_B/[1+(\omega/\omega_B)^2]+R_{gb}(\omega/\omega_{gb})/[1+(\omega/\omega_{gb})^2]+$$
$$R_{el}(\omega/\omega_{el})/[1+(\omega/\omega_{el})^2] \qquad (2\text{-}20)$$

and the imaginary part (M'') of modulus (M*=M'+jM'')

$$M''=(Co/C_B)(\omega/\omega_B)/[1+(\omega/\omega_B)^2]+(Co/C_{gb})(\omega/\omega_{gb})/[1+(\omega/\omega_{gb})^2]+$$
$$(Co/C_{el})(\omega/\omega_{el})/[1+(\omega/\omega_{el})^2] \quad (2\text{-}21)$$

where C_o is the vacuum capacitance of the cell.

Tangent loss is related to the real and imaginary parts of impedance:

$$\tan(\delta)=\frac{Z'}{Z''} \quad (2\text{-}22)$$

By plotting tg (δ) vs. log f, we will have peaks at frequencies $f_{p1}\approx(f_{gb}f_b)^{1/2}(R_{gb}/R_b)^{1/2}$, indicating an approximate transition from the bulk to grain boundary contributions, and $f_{p2}\approx(f_{gb}f_{el})^{1/2}(R_{gb}/R_{el})^{-1/2}$ indicating a transition from grain boundary to the electrode contributions, respectively. Meanwhile we can also have minima at $f_{min1}=f_{gb}[(R_B+R_{gb})/R_B]^{1/2}$, $f_{min2}=f_{el}[(R_B+R_{gb}+R_{el})/(R_B+R_{gb})]^{1/2}$ respectively (Abrantes *et al.* 2000c). For this reason the alternative representation of log (tg(δ)) vs. log(f) is believed to be more useful for an overall analysis of impedance spectra and to obtain a wide range of relevant parameters, even if the bulk and grain boundary arcs overlap in the complex impedance plot. In the plot of log (tg(δ)) vs. log(f), the peaks indicate electrode to grain boundary transition, and/or the grain boundary to bulk transition. Local minima can be used to extract the grain boundary or the electrode relaxation frequencies (Abrantes *et al.* 2000c).

Abrantes *et al.* (2000a) also suggested that the plots of Z' vs. (Z''/ω), or Z' vs. (Z''/f) should be suitable to extract relaxation frequencies and resistance values relevant to the bulk, grain boundary, and electrode effects, even for cases when the difference between the bulk and grain boundary relaxation frequencies may not exceed one order of magnitude.

2.7 Non-Ideality Of Realistic Materials

The impedance spectra of realistic materials usually cannot be fitted simply employing an ideal RC circuit. For a wide range of materials, the complex plane plot of impedance (Z*), electric modulus (M*) and complex dielectric constant (ε*) for the bulk effect normally does not show a perfect semicircle as predicted by an ideal RC element circuit, instead it shows a depressed semicircle with its axis depressed below the real axis by an

angle $\alpha\pi/2$ (Cole and Cole, 1941, and Jonscher, 1978), as shown in Fig. 2-11. This kind of non-ideal (non-Debye) behaviour can also be observed in the broadening of the Debye peak in the modulus spectrum (M'' vs. log (f)) (Hodge *et al.* 1976).

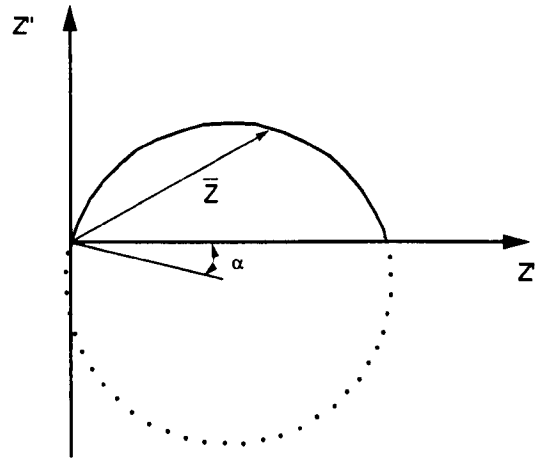

Figure 2-11 A depressed semicircle in the impedance plane, the full circle completed by dotted line can be expressed by Eq. 2-25.

The non-ideal response, i.e., the frequency dispersion from real materials, has not been fully understood, but many studies point to chemical, physical, and even geometrical inhomogeneities in material properties. According to Jonscher and Reau (1978), the conducting species in the bulk moving by discontinuous jumps interact with one another in a manner demanded by "screened hopping", which may lead to a frequency-dependence of electrical response and therefore a non-Debye behaviour results. Hodge *et al.* (1976) mentioned that the random orientation of anisotropically conducting crystals and the presence of phases of more than one composition or structure may contribute to the broadening of the Debye peak. By carrying out finite element calculations, Fleig and Maier (1998) demonstrated that the varying thickness of the grain boundaries could lead to the depression of the grain boundary semicircle. Fleig and Maier (1998) also proposed that an extreme grain size distribution and spatially inhomogeneous grain size distributions could cause detours for the electrical current, and therefore could lead to a change of the shape of the impedance spectra. Macdonald and Franceschetti (1987) proposed that the non-ideal response could be described in terms of a distribution of

relaxation times which might be associated with a distribution of hopping-barrier-height activation energies because of inhomogeneous material properties. Such a distribution of relaxation times will lead to frequency-dependent effects.

A depressed semicircle in the impedance spectrum is fitted using a constant phase element (CPE) connected in parallel with a resistor or a capacitor, or a CPE connected in series with a resistor (Raistrick, 1987). The impedance of the CPE is given by:

$$Y = A(j\omega)^n = A\omega^n[\cos(\frac{n\pi}{2}) + j\sin(\frac{n\pi}{2})] \qquad (2\text{-}23)$$

Where A is a constant that is independent of frequency, ω is the angular frequency and $j = \sqrt{-1}$. When n=1, the CPE describes an ideal capacitor; when n=0, the CPE acts as a pure resistor (Macdonald and Franceschetti, 1987). Thus a CPE can represent a wide variety of non-ideal elements.

For a CPE connected in parallel with a resistor R, the total impedance can be expressed by the Debye equation:

$$Z = \frac{R}{1+(j\omega\tau)^n} \qquad (2\text{-}24)$$

By combining Eqn. 2-23 and Eqn. 2-24, we can obtain an equation:

$$(Z'-\frac{R}{2})^2 + [Z''+\frac{R}{2}\tan(\alpha)]^2 = \frac{R^2}{4}[1+\tan^2(\alpha)] \qquad (2\text{-}25)$$

which depicts a full circle which is displaced from the real axis as shown in Fig.2-11 (in dotted line), with a diameter of $R\sqrt{1+\tan^2\alpha}$ and the centre at $(\frac{R}{2},-\frac{R}{2}\sqrt{(1+\tan^2\alpha)})$, and the depressed angle in the Fig. 2-11 is related to the exponent n:

$$\alpha=(1\text{-}n)\pi/2 \qquad (2\text{-}26)$$

Therefore both the exponent, n, in the Debye equation and the depressed angle, α, of the semicircle in the complex impedance plot describe the extent of the departure of real materials from the ideal Debye behaviour.

2.8 Electrode/Material Interfaces

2.8.1 Introduction

In a typical complex impedance plot of ceramic materials, we often see either a semicircle or a spike (tail) in the low frequency region that is due to the electrode/material interface, which is also called the electrode effect. The electrode effect is dependent not only on the properties of bulk materials, but also on what type of electrode is used. The response from the electrode/material interface often provides extra information about the electrical properties of the bulk materials and even gives indications of the surface state of the bulk materials. In terms of different conducting charge carriers in bulk materials, we have electrode/semiconductor interfaces and electrode/ionic conductor interfaces, while the electrode is normally always made from metallic materials.

2.8.2 Electrode/Semiconductor Interfaces

The electrode /semiconductor interfaces can give either Ohmic or non-Ohmic contact. In the case of an Ohmic contact, the electrode effect is hardly identifiable in the impedance spectra, while a semicircle at low frequency can been seen for the case of non-Ohmic contact. Strictly speaking, there is always a Schottky barrier present at the electrode/semiconductor interface; that is even an Ohmic contact involves a thin depletion layer. The capacitance of the Schottky barrier in some respects resembles a parallel-plate capacitor, and the capactive effect of an Ohmic contact does not emerge in impedance spectra because the depletion layer is so thin that the carriers can readily tunnel through it (Rhoderick, 1978). Consequently, electrode /semiconductor interfaces are comprised of both capacitive and resistive elements (Maiti and Basu, 1986) and can be analysed using a parallel RC circuit, with the Ohmic contact being a special case with an extremely low resistance of the barrier.

The resistance of the Schottky barrier is dependent not only on the oxidation potential of the electrode metal, but also on the metal-metal interaction at the interface. For example, the InGa/$BaTiO_3$ interface is found to be an Ohmic contact, while the Pt/ $BaTiO_3$ interface yields a large barrier resistance (Cann and Randall, 1996).

It is important to note that an Ohmic contact is a distinctively unique characteristic of electrode/electronic conductor interfaces. The absence of a semicircular arc in the impedance spectra due to the electrode/sample interface indicates that the conduction process in the sample is electronic (Chiang *et al.* 1997). It is impossible for an ionically conducting sample to have an Ohmic contact with a metal electrode.

2.8.3 Electrode/Solid Electrolyte Interfaces

From an electrochemical point-of-view, the electrode/solid electrolyte interface can be either a blocking or a non-blocking one. An interface is blocking when the charge carrying species cannot cross the interface or exchange charge with the electrode, and there is no immediate equilibration of charged species. The interface across which the charged species tend to equilibrate once contact has been made is called a non-blocking interface (Armstrong and Todd, 1995). A non-blocking interface often behaves like a resistance and a capacitance in parallel, which leads to a semicircle in the impedance plane. This is quite like the case of non-Ohmic electrode/semiconductor contact. But an idealised blocking interface, where there is no charge transfer, should behave like a parallel plate capacitor, which should lead to a straight line perpendicular to the real axis in the complex plane.

In a real electrode/solid electrolytic interface system, a non-blocking electrode may behave like a blocking interface if an exchange current at the interface is very low. In other cases, a blocking electrode may have charge transfer across the interface if an extremely high potential is applied (Armstrong and Todd, 1995). But in impedance measurements with low applied voltages, the latter case rarely occurs.

Another important fact is that almost all the electrode/solid electrolyte interfaces exhibit CPE behaviour to some extent. It is believed that even an ideally polarisable electrode could exhibit CPE behaviour because in the double layer region energy can be dissipated in various ways other than by charge transfer (Lang and Heusler, 1998). Due to the distributed nature of response, a non-blocking interface always shows a depressed semicircle in the impedance spectra, which can be simulated by a CPE in parallel with a resistance, while a blocking interface causes a straight line inclined to the real axis at an angle smaller than 90°, which can often be simulated using a single CPE.

2.8.4 Effect Of Heterogeneities Of Interfaces On IS

The effect of heterogeneities of interfaces on IS is of particular interest and significance, because the heterogeneities of the interfaces are closely associated with the bulk properties. Hence the special features of an electrode effect in IS may provide information not only about the interface itself, but also of bulk properties.

The CPE for describing an electrode/electrolyte interface should be defined as Eqn. 2-23, whereas an alternative definition:

$$Y_{CPE}=(Aj\omega)^n \qquad (2\text{-}27)$$

which sometimes appears in the literature should be abandoned, since it does not scale linearly with electrode area (Zoltowski, 1998).

Although the CPE is an empirical assumption, where constant 'A' and exponent 'n' have no well-defined physical meanings, many studies revealed that the value of the exponent 'n' is associated with heterogeneities, particularly the electrode roughness, the porosity of a porous electrode, or a number of different charge accumulation modes such as deep traps, inhomogenous doping etc. Many attempts have been made to seek quantitative correlation between the exponent 'n' obtained from the macroscopic response of the IS and the microstructural features of the interface, e.g. the roughness of the electrode (Liu, 1985) or the pore size distribution of the porous electrode (Song *et al.* 1999). Therefore the value of 'n' is a very important parameter in the characterisation of materials.

As mentioned earlier, a blocking interface would show a straight line inclined to real axis at an angle α, the value of 'n' is related to the angle α:

$$\alpha = (1-n)\frac{\pi}{2} \qquad (2\text{-}28)$$

which is the same as the depression angle as defined in Eq.2-26.

Thus the slope of an inclined line (frequently observed as a tail or spike), or the depression of a semicircle, which are present in an impedance spectrum due to the electrode effects, could be an indication of the extent of heterogeneities at the interface.

The impedance of a CPE can be transformed into an equivalent circuit containing frequency-dependent resistor R_V in parallel with a frequency-dependent capacitor C_V (McCann and Badwal, 1982):

$$Y = \frac{1}{R_V} + j\omega C_V \qquad (2\text{-}29)$$

By comparing Eq.2-29 with the following:

$$Y = Q^1(j\omega)^n = Q\omega^n[\cos(\frac{n\pi}{2}) + j\sin(\frac{n\pi}{2})] \qquad (2\text{-}30)$$

we have:

$$R_V = Q^{-1}\omega^{-n}\cos^{-1}(\frac{n\pi}{2}) \qquad (2\text{-}31)$$

$$C_V = Q\omega^{n-1}\sin(\frac{n\pi}{2}) \qquad (2\text{-}32)$$

In other words, the CPE describes the extent to which both the resistive and capacitive effects are frequency-dependent. The frequency dispersion of the interface is due to various heterogeneities, such as roughness, pore size distribution, and even an anisotropic surface structure (Motheo *et al.* 1997) and a surface disorder of the polycrystalline of electrode (Kerner and Paijkossy, 1998). There is a large amount of literature covering this field. However only the roughness effect and porous electrodes will be considered here, because these are more relevant to the issue of non-destructive characterisation of materials. The knowledge of these two aspects will certainly be helpful for a better understanding and interpretation of the IS of ceramic materials.

2.8.4.1 Effect Of Porous Electrodes

The frequency dispersion of porous electrodes was first modelled by De Levie (1967). De Levie's model shows that a cylindrical pore can be represented by a transmission line as in Fig. 2-12.

With the transmission line, the following equations can be derived:

$$de + iRdx = 0 \qquad (2\text{-}33)$$

$$di + \frac{e}{Z} = 0 \qquad (2\text{-}34)$$

where e stands for the potential, i stands for the electrical current, x is the length, R is the electrolyte resistance per unit length of the pore and Z is the Faradaic resistance per unit length of the pore. On combining Eqs. 2-33 and 2-34, we obtain

$$\frac{d^2e}{dx^2} - \frac{R}{Z}e = 0 \qquad (2\text{-}35)$$

$$\frac{d^2i}{dx^2} - \frac{R}{Z}i = 0 \qquad (2\text{-}36)$$

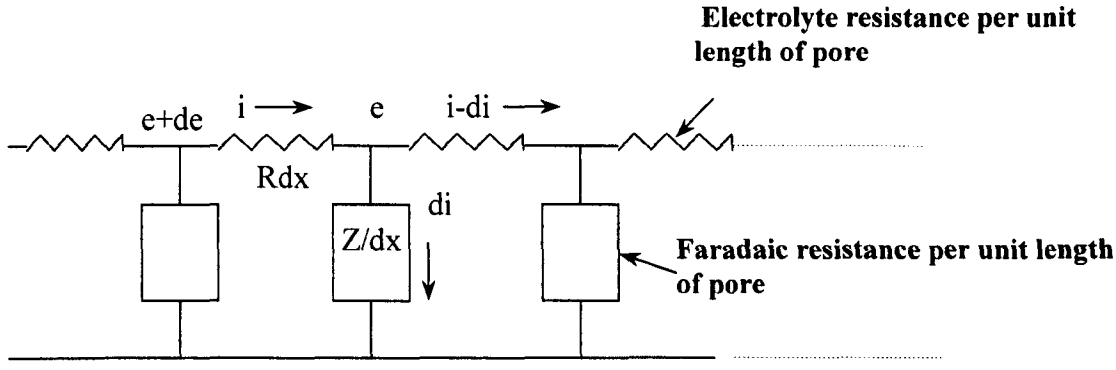

Figure 2-12 Equivalent circuit of a pore.

The boundary conditions are:

$$x = 0 \qquad e = e_o$$

$$x = l \qquad de/dx = 0$$

The solution of Eqs. 2-35 and 2-36 can be expressed (De Levie, 1967):

$$e = e_o \frac{\cosh(\rho x - \rho l)}{\cosh \rho l} \qquad (2\text{-}37)$$

$$i_o = \frac{\rho e_o}{R} \tanh \rho l \qquad (2\text{-}38)$$

where

$$\rho = (R/Z)^{1/2}$$

and therefore

$$Z_o = \frac{i_o}{e_o} = (RZ)^{1/2} \text{ cotanh } \rho l \qquad (2\text{-}39)$$

If the electrode/electrolyte interface is a blocking interface, then the impedance of the double layer charging:

$$Z = -j/\omega C \qquad (2\text{-}40)$$

For a semi-infinite pore, the cotanh term in Eqn.2-39 can be dropped, thus, by combining Eqs.2-39 and 2-40, a Warburg-like impedance can be obtained:

$$Z_o = (1-j)\sqrt{\frac{R}{2\omega C}} = \sqrt{\frac{jR}{\omega C}} \qquad (2\text{-}41)$$

where R is the electrolyte resistance per unit pore length and C is the double layer capacitance at the interface between electrolyte and electrode. This can explain why a porous electrode in the absence of Faradaic reactions follows a linear line with a phase angle of –45°.

However many experimental data of impedance show that the phase angle is not exactly -45° at high frequency or -90° at low frequency. It is believed that the impedance frequency dispersion of the porous electrode can be affected by the shape of the pore, and more importantly, by the pore size distribution of a porous electrode (Song *et al.* 1999).

According to the model of Song *et al.* (1999), the impedance of a blocking porous electrode is determined by two representative parameters: penetrability and the standard deviation of the pore size distribution. The penetrability α_u is the penetration depth λ divided by the length of pores and the penetration length λ is a function of electrolyte conductivity σ, frequency ω and double layer capacitance C_d:

$$\lambda \propto \sqrt{\frac{\sigma}{\omega C_d}} \qquad (2\text{-}42)$$

At high penetrability, i.e., when the penetration depth is larger than the length of the pores, the impedance behaves like that of a planar electrode, the phase angle approaching -90°. At low penetrability, the penetration depth is shallower than or similar to the depth of the pore, the impedance behaves like a porous electrode. Meanwhile a wider pore size distribution leads to a more porous characteristic of impedance, i.e., a smaller phase angle at low frequency range (Song *et al.* 1999).

2.8.4.2 Roughness Effect

The roughness effect can be understood better according to a theory of lateral charge spreading in a diffusion double layer (Scheider, 1975). A schematic of a rough surface is shown in Fig. 2-13 (after Scheider), here an ideally polarised electrode is assumed.

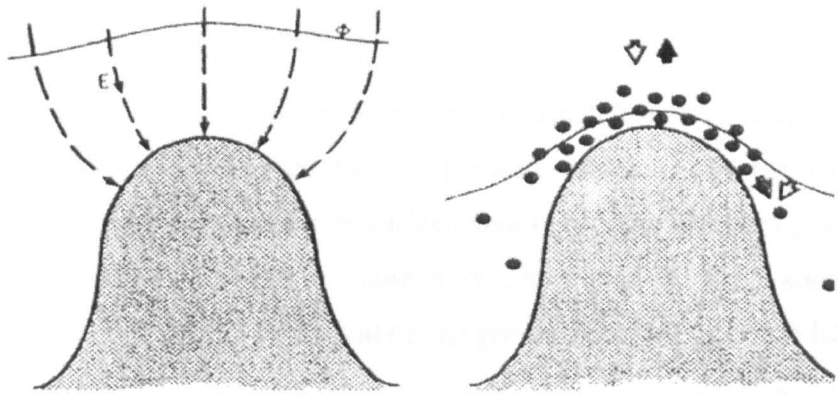

Figure 2-13 Schematic of a "mound" type of surface irregularity; after Scheider (Scheider, 1975).

At the very first moment when an electrical field is applied, no concentration gradients are present, and ionic flow follows the lines of electric force (Fig.2-13 a) to the peak of the mound. As charge accumulates in the double layer at the peak, the folding down of the equipotential lines combines with lateral concentration gradients to cause tangential spreading of ions to the remoter portions of the surface (Fig.2-13b). As more surface becomes accessible to charge with the elapse of time, the effective capacitance increases (Scheider, 1975). This gives a clear picture of how capacitance is dependent on frequency.

A rough electrode can be modelled by equivalent circuits composed of various RC networks, among which the simplest one is the same as that is used in the modelling of a semi-infinite pore shown in Fig.2-12. As the frequency decreases, more signal travels through the resistive part of the network before being shunted across the interfacial capacitance (Liu, 1985). This explains why the resistive effect of a rough interface also increases with decreasing frequency.

The transmission line as shown in Fig.2-12 results in a Warburg impedance:

$$Z \propto (\omega^{-0.5} + j\omega^{-0.5}) \qquad (2\text{-}43)$$

which can be considered to be a CPE with n=0.5.The transmission line also describes the behaviour of a semi-infinite diffusion process (Raistrick,1987). For this reason, the electrical response of a rough blocking interface sometimes is similar to that of a smooth, non-blocking interface having the slow diffusion of a reactant species to the interface (Armstrong and Todd, 1995)

However, for a real rough interface, a simple RC ladder network as shown in Fig. 2-12 is still too simple to describe the complicated situation, and branched ladder networks should be used to model the surface topology. The frequency dependence of these branched ladder networks is completely determined by the branching type (Scheider, 1975), which in turn is dependent on the geometric topology of the interface.

A fractal model for CPE at rough interfaces was proposed by Liu (1985). A quantitative relation between the exponent 'n' and the geometry of the rough interface was established as: n=1-d, where d is the fractal dimension of the rough surface that can be determined by measurement of its area using different scales.

Meanwhile, according to its physical model (in Fig.2-13), the lateral charge spreading takes place within the bulk electrolyte adjacent to interface. Then it is not difficult to understand that the resistive elements in the transmission line are actually bulk electrolyte elements, and the conductivity varies directly with the bulk conductivity. Thus an increase in the bulk conductivity is expected to have an effect on the CPE of the interface by increasing the constant A. Therefore the impedance of a rough interface is not only related to the roughness of the interface (via changing exponent 'n'), but also associated with bulk conductivity (via changing the constant A).

Similarly to the concept of penetration depth, a propagation wavelength λ_{rc} along the transmission line was introduced by Scheider (1975):

$$\lambda_{rc} \propto \sqrt{\frac{\sigma}{\varepsilon\omega}} \qquad (2\text{-}44)$$

where σ is the electrolyte conductivity, ε is the dielectric constant and ω is the angular frequency. It is not difficult to see that Eqs. 2-44, 2-42 are exactly the same.

The concept of propagation wavelength (or penetration depth) is very important. It means that a long propagation wavelength has a low 'sensitivity' to the presence of the roughness. According to Eqn. 2-44, the wavelength increases as the bulk conductivity is increased, therefore the impedance of an interface is expected to behave less 'roughly' if the conductivity of the bulk is increased in some way.

It is important to note that all of the above mentioned results were based on the electrode/liquid electrolyte systems, where the contact between the two phases are always very intimate because of the fluidity of the liquid electrolyte. Very few studies have been made on the electrode/solid electrolyte systems where the contact between the two phases is not as intimate as in the electrode/liquid electrolyte systems. Obviously the situation of the electrode/solid electrolyte system is much more complicated. Nevertheless many basic principles of liquid electrolyte systems are applicable to solid electrolyte systems.

2.9 Characterisation Of Structural Defects By IS

2.9.1 Introduction

Although IS has long been found to be a powerful tool for studying electroceramic and solid electrolytic materials since Bauerle's pioneering work (Bauerle, 1969), it is only recently that a number of studies have implied that IS could also be a promising nondestructive tool for detecting structural defects in structural ceramics. So far it appears that the majority of studies in this respect have been focused on zirconia-based and cementitious materials, because it is of great commercial significance to apply the simple and economic IS method for the nondestructive characterisation of these materials.

2.9.2 Zircoinia-Based Ceramics

Zirconia-based ceramics have many important applications in industry. The characterisation of the structural defects in zirconia-based materials using IS is desirable, because zirconia-based ceramics, especially the partially stabilised zirconia materials (PSZ), are often employed as structural materials

In zirconia-based materials, the ion conduction can be blocked by various microstructural defects, such as cracks, pores and second phase inclusions, as well as by grain boundaries (Dessemond *et al.* 1993). Ion-blocking can be quantitatively characterised by the blocking factor, which in turn can be calculated by comparing the diameters of grain and grain boundary semicircles in impedance spectra (Kleitz *et al.* 1995).

The formation and evolution of cracks in structural ceramics are always a crucial issue. Dessemond and Kleitz (1992) employed IS to characterise the cracks that were locally induced by Vickers indentation in zirconia ceramics by applying a pin-shaped electrode near an indentation fracture pattern. It was found that the intragrain resistance and intragrain capacitance remain nearly unaffected by the indentation pattern, while the intergrain resistance and intergrain capacitance vary with the indentation patterns and with the load. Khalili and Kromp (1993), based on SEM observations and by referring to the investigation of Dessemond and Kleitz (1992), further suggested that IS parameters, such as intergrain resistance and capacitance, blocking factor etc. could be regarded directly as parameters characterising the development of microcracks in zirconia materials (Khalili and Kromp, 1993). A similar conclusion was reached in the report of Tiefenbach and Hoffmann (2000): the crack has its effect on impedance in the low frequency range, and the magnitude of the impedance increases with increasing crack length. In an attempt to characterise microcracks in alumina/zirconia ceramic composites, Smith *et al.* (1994) pointed out that the presence of microcracks decreases the effective current carrying cross-section, and as a consequence the resistance is increased.

Based on the theoretical modelling, it is expected that, in addition to the relaxation processes of grain and grain boundary, one or two separate relaxation processes should appear in the impedance spectra after cracking in zirconia-based materials. But in real cases, the responses from cracks and grain boundary tend to overlap and hence the

impedance spectra are characterised by only two relaxation processes before and after cracking (Tiefenbach and Hoffmann, 2000).

Zirconia exists in three different phases: cubic, tetragonal and monoclinic. Phase transformations may take place under various circumstances, for example, during high temperature heat treatment, in a water vapour at low temperatures or by thermal shock. In the partially stabilised zirconia, high temperature annealing resulted in the formation of monoclinic grains. In this case the impedance diagrams show the characteristic grain and grain boundary semicircles, as well as an extra arc at intermediate frequencies corresponding to monoclinic grains (Muccillo and Kleitz, 1996). Similarly, for a nano-sized 2Y-TZP, isothermal ageing in a water atmosphere resulted in an increase of monoclinic phase which in turn led to a change of the impedance spectrum shape (Djurado *et al.* 2000). In addition, Muccillo *et al.* (1998) observed that an increase in cubic/tetragonal phases as a consequence of thermal shock produced a better resolution of initially overlapping intergrain and intragrain semicircles All of these observations imply that the phase transformations in zirconia can be detected and characterised by IS.

It is known that zirconia-based electrolytes acting as oxygen sensors are easily corroded when in direct contact with glass melts. The inner corrosion of YSZ by glass melts was investigated using IS by Rodrigues *et al.* (1997&1998). The electrical response of the YSZ/glass composite materials was found to be strongly influenced by the presence of a YSZ-glass interface, which can be easily identified because of its typical relaxation frequency. A large shift in the relaxation frequency of the intermediate frequency impedance arc can be used to monitor the progress of glass through the zirconia-based electrolytes (Rodrigues *et al.* 1998).

The porous effect of the YSZ samples with a fairly narrow pore size distribution can be clearly identified in the impedance spectra. The diameter of the grain boundary semicircle increases with the porosity present in the samples. It is documented that the porosity of porous material can be characterised by a blocking factor (α_R), a capacitance ratio (α_C) and a frequency ratio (α_f). The product of $\alpha_f\alpha_R$ was found proportional to porosity (Steil *et al.* 1997).

2.9.3 Cementitious Materials

Cement paste is a heterogeneous mixture of solid, liquid, and gaseous components. The solids are precipitated hydration products and un-reacted cement grains. The liquid is a pore fluid which permeates the matrix through the pore structure and the gas is entrapped air in empty or partially fluid-filled pores (Macphee *et al.* 1997). The hydration product of cement paste is mainly an amorphous, hydrous gel, designated C-S-H. This phase is the principal binder in Portland cement pastes and is characterised by a high surface area, a variable composition and a variable structure (Glasser *et al.* 1987). For this reason, porosity and ionic conductivity are the main physicochemical parameters defining the mechanical properties and lifetime of concrete structures (Andrade *et al.* 1999). McCarter *et al.* (1988) were among the first who found that the hydration (hardening) process of the cement paste could be monitored by IS. Since then there has been a large amount of research devoted to the characterisation of cementitious materials using IS.

In the impedance spectra of cement paste there appears a depressed semicircular arc at high frequencies that is due to a bulk effect and a low frequency tail due to the electrode effect. As the hydration proceeds, the structure and composition of the hydration products keep changing. It was found that in impedance spectra, the bulk resistance and depression angle increases while the relaxation frequency bulk arc decreases with the prolonged hydration time (McCarter *et al.* 1988).

Several IS parameters can be directly related to the microstructure of cementitious materials, for example the bulk resistance can be related to the connectivity of the pore structure and the arc depression factor appears to be a measure of the inhomogeneity of the underlying microstructure (Christensen *et al.* 1994). Use of the frequency at the top of the bulk arc makes it possible to estimate the relative dielectric constant of the material, which is in turn governed by the ratio of an average pore size to a blocking layer thickness for the microstructure (Christensen *et al.* 1994). A linear dependence has been recently found between the high frequency dielectric constant and the cement paste porosity (Andrade *et al.* 1999).

IS has also found application in the investigation of crack growth mechanisms in cementitious materials. This is based on the fact that the high frequency arc (HFA)

diameter is dependent on the microstructural characteristics of the specimen. When cracks are formed and saturated with liquid phase, small values of bulk resistance are obtained. Consequently during compressive loading, the HFA diameter decreases with increasing loading, due to the formation and propagation of cracks. The rate of decrease of the HFA diameter reflects the rate of crack formation and propagation (Gu *et al.* 1993).

2.9.4 Debonding And Pullout Of Fibres In Composites

Two bulk arcs could appear in impedance spectra when chopped conductive fibres (steel and carbon) are added to cementitious materials (Ford *et al.* 1998), which can be explained by a 'frequency switchable fibre coating' model (Torrents *et al.* 2000). The high frequency arc represents the bulk between wire tips and the electrodes, while the low frequency bulk arc is the response from the ion spreading in the vicinity of the wire tips (Torrents *et al.* 2001).

In a pullout test, a single steel fibre was being pulled out from a cement sample while impedance measurements were made between the two electrodes. It was found the resistance of the high frequency semicircle is sensitive to the debonding and pullout of the embedded fibre. The high frequency bulk resistance increases progressively as the fibre is pulled out and the extent of pullout can be related quantitatively to the increase in the resistance. A significant increase in this resistance also occurs during the debonding phase of the crack opening displacement (Torrents *et al.* 2001). Therefore IS can be applied to detect and monitor both debonding and pullout of the embedded fibres in fibre-reinforced cementitious materials.

2.10 Summary

According to this literature review, we know that IS is a cheap, quick and convenient non-destructive technique for characterising electrical properties of solid electrolytes and electroceramics. However, it has also been seen that the interpretation of IS needs a sound understanding of electrical conduction mechanisms in materials, the establishment of an appropriate physical model and proper representations of IS.

The electrical conduction in the majority of polycrystalline ceramic materials is either semi-conductive or ionic, while silicate glasses exhibit mainly alkali ion conduction. For porous oxide ceramics the electrical conduction along free surfaces is an important factor that has to be considered.

There are dozens of ways of representing IS. Different IS representations highlight different features; for example electrical modulus spectra emphasise the capactive effect, while impedance spectra demonstrate more clearly the resistive effects of different phases. Therefore to render a set of impedance data to be more informative, many different representations should be tested before final representations are decided.

All realistic materials show non-ideal behaviour, which can be fitted by using constant phase elements (CPEs). The depression angle of a semicircle in complex impedance spectra is an indication of the extent of the frequency dispersion of a material.

There are two kinds of electrode/material interface in terms of the charge carriers in the material: electrode/semiconductor interface and electrode/electrolyte interface. The heterogeneities at the interface, such as electrode porosity and roughness can be related to a few IS parameters. The electrode effect is also reflective of the properties of bulk materials. Therefore in analysing the impedance data, attention should be paid not only to the bulk semicircles, but also to the electrode tail in the impedance spectra.

The interest in using IS to characterise structural defects in materials is increasing. Previous studies have demonstrated that structural defects such as cracks/microcracks, porosity, phase changes and other second phase inclusions etc, can be characterised by IS parameters. However, so far only zirconia-based materials and cementitious materials have been investigated in this respect. The present study is an attempt to extend IS as a NDC technique to a wider range of structural ceramics both in-process and in-service applications.

3 Experimental Procedures

3.1 Sample Preparation

A number of different ceramic materials have been used in this project, some of which were provided by other research groups or industrial companies that will be separately specified later on at appropriate occasions and others, unless otherwise denoted, were prepared by the following processing procedure:

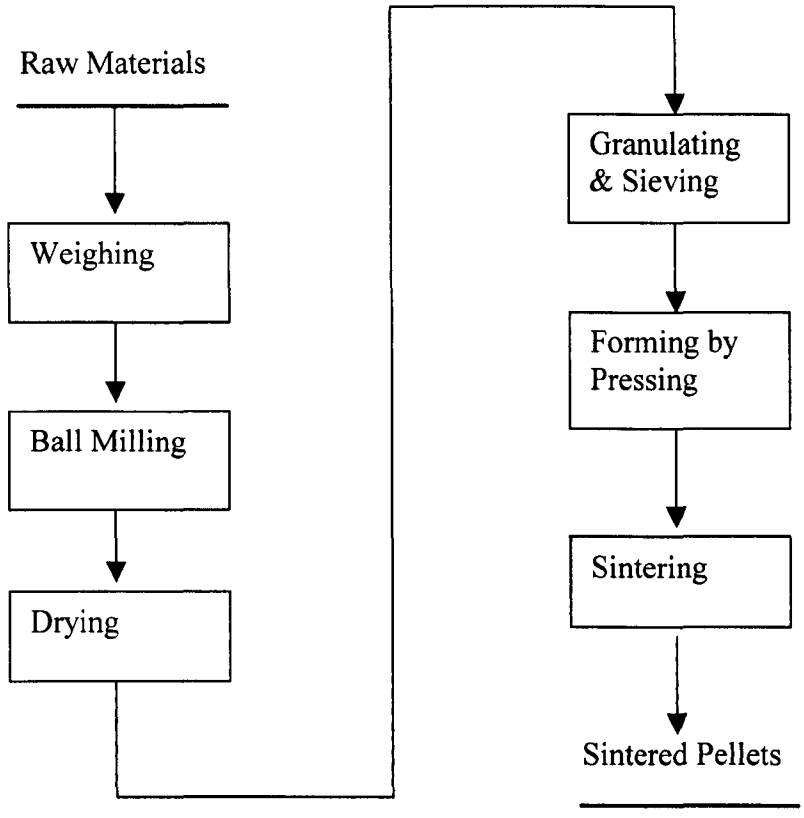

Figure 3-1 Flow chart for preparing sintered ceramic pellets.

The green form pellets were 13 mm in diameter and 3~4 mm in thickness, formed by uni-axial pressing using a pressure of 120 MPa. The pellets were sintered in a tubular furnace (Lenton, with SiC heating elements), using a heating rate of 3 K•minute^{-1} and a cooling

rate of 5 K•minute^{-1}. The dwell time depended on different circumstances that will be given in particular situations in the following chapters.

3.2 Measuring Cell Preparation

3.2.1 Electrode Preparation

An electrode can be applied either by pressing a metal foil directly to a surface of the solid material under investigation, or by applying a thin conductive paint to the surface. Since it is extremely difficult to make an absolutely flat surface for solid materials, the contact between the electrode and the material using the former method is usually very poor. To ensure a good contact, painted electrodes were normally used.

To apply a painted platinum electrode, the sample was painted firstly with a thin layer of platinum conductive ink (Engelharh Clal, UK) over a defined area on the sample surface, followed by baking at 1100°C for 45 min.

Likewise, a painted silver electrode was applied by painting a thin layer of silver conductive ink (E8100, Johnson Matthew Electronics, UK) on the sample surface, and this was followed by baking at 450°C for 15 min.

3.2.2 Measuring Cell Containing A Dense Ceramic Sample

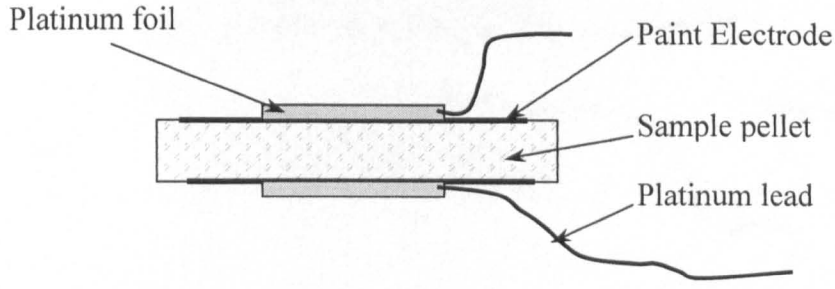

Figure 3-2 A typical measuring cell with a sintered ceramic pellet.

A typical measuring cell for impedance measurements is shown in Fig. 3-2. Here the cell is composed of a pellet specimen sandwiched by two platinum foils. The cell is

symmetric, with two identical electrodes. The electrodes are either painted platinum or painted silver electrodes.

Two platinum foils were applied to the painted electrodes to ensure a good contact between the painted electrode and the lead.

The procedure for preparation of the measuring cell is as follows:

(a) a sample pellet was ground using SiC papers of P180 and P800 grit;

(b) the sample pellet was polished using a polishing disc with 6μm and 1μm diamond pastes;

(c) the sample pellet was cleaned using acetone and then dried in air;

(d) the sample pellet was painted with platinum or silver pastes.

3.2.3 Measuring Cell For Measurements Of Green Form Ceramics

A measuring cell for green form ceramics is shown in Fig.3-3. Because the green form is porous and fragile, it is difficult to apply the painted electrodes. Therefore, two platinum foils were used here as electrodes.

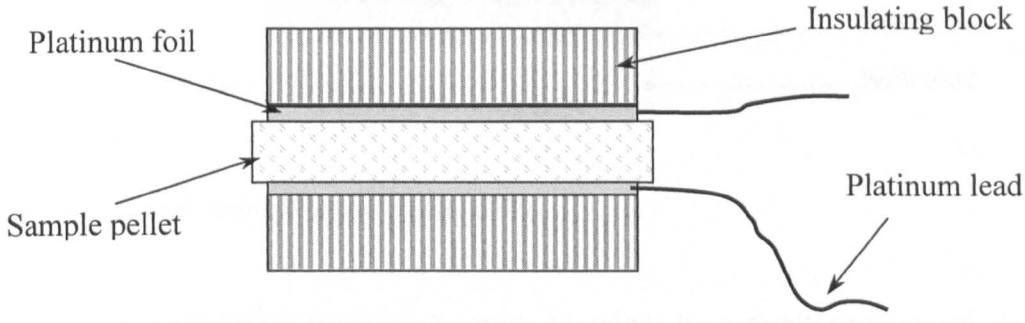

Figure 3-3 A measuring cell with a green powder compact.

In order to make as a good contact between the sample and the electrodes as possible, the contacting surfaces of both the green compact pellet and electrodes need to be as flat as possible. For this reason the green compact was carefully polished with fine SiC paper

(P1200 grit) to ensure both surfaces were flat and smooth enough. Meanwhile, the platinum foils were bonded to insulating blocks by the following procedure:

(a) two Al_2O_3 blocks were polished using 6μm and 1μm diamond pastes;

(b) the Al_2O_3 blocks were painted with a thin layer of platinum ink;

(c) the platinum foils (200μm in thickness) were attached to the painted area on the Al_2O_3 blocks before the drying of the platinum ink;

(d) the Al_2O_3/foil joint were formed after sintering at 1250°C under a pressure of 5N for 60 minutes.

3.2.4 Measuring Cell For Impedance Measurements Of TBCs

The cell for impedance measurements of TBCs was asymmetric (Fig.3-4). In this cell a silver electrode was painted at the top surface of the YSZ coating, while another one was the bond-coat beneath the YSZ top layer in TBCs (see Fig.3-4).

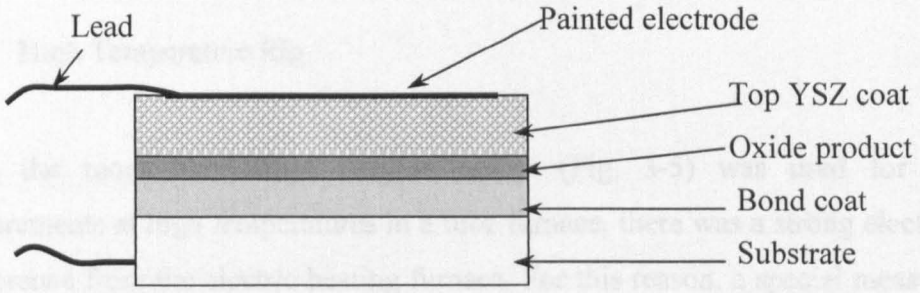

Figure 3-4 A measuring cell with TBCs.

In the preparation stage, care must be taken to prevent mechanical damage to the coatings, especially during the cutting of the samples. To avoid damaging the top coat (YSZ), the top surface was not polished before applying electrodes, but the samples were cleaned using acetone before the application of the painted silver electrode.

3.3 Sample Holders

3.3.1 The Sample Holder For The Room Temperature Measurements

For the room temperature measurements, a simple sample holder as shown in Fig. 3-5 was used, where an adjusting bolt was used to ensure an intimate contact between specimen and the platinum electrodes.

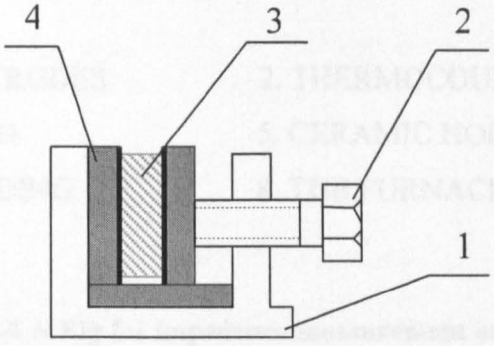

1. STEEL FRAME
2. ADJUSTING BOLT
3. MEASUREMENT CELL
4. INSULATING BLOCK

Figure 3-5 Sample holder for room temperature measurements.

3.3.2 High Temperature Rig

When the room temperature sample holder (Fig. 3-5) was used for impedance measurements at high temperatures in a tube furnace, there was a strong electromagnetic interference from the electric heating furnace. For this reason, a special measurement rig was designed, as shown in Fig. 3-6. Here a Fecralloy tube that was connected to ground was used as an electromagnetic shield to prevent the interference from the furnace winding. A wire spring was used to apply a constant pressure of about 5 N to the specimen to ensure an intimate contact between electrodes and the specimen. The electrodes were two platinum foils bonded to Al_2O_3 plates and connected to the impedance analyser. A thermocouple (Type R, Carbolite, with a digital 2132 indicator) was placed next to the specimen in order to measure accurately the temperature of the specimen.

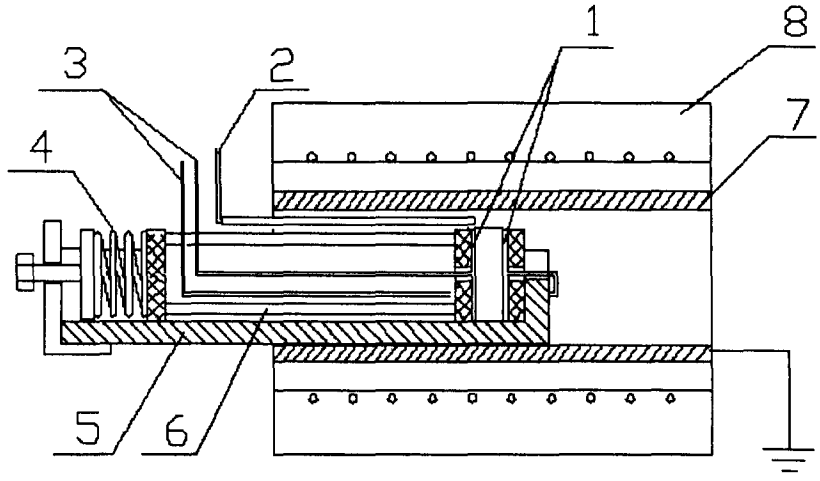

1. ELECTRODES 2. THERMOCOUPLE 3. LEADS
4. SPRING 5. CERAMIC HOLDER 6. SILICA TUBE
7. SHIELDING 8. TUB FURNACE

Figure 3-6 A Rig for impedance measurement at high temperatures.

Since both the Fecralloy tube and ceramic holder used in this rig are capable of withstanding a high temperature environment (higher than 1250°C), this rig can be used for impedance measurements up to 1200°C.

3.4 Impedance Measurements

3.4.1 Impedance Spectroscopy

The set up for impedance spectroscopy is shown in Fig. 3-7, in which a Solartron 1296 dielectric interface was used in conjunction with a Solartron Frequency Response Analyser (FRA) 1255. The 1296 interface/1255 FRA unit was controlled by a personal computer.

The basic function of the 1296 hardware is to extend the current measurement range of the FRA, thus enabling the measurement of very high impedances (Solartron, 1999). This is essential when we conduct a measurement on a dielectric material with a high resistivity.

The main features of the 1296 interface/1255 FRA combination are:

Frequency range: 10μHz to 10MHz

Signal amplitude: 0 to 3V rms

Current measurement: 1fA to 100mA

Tan δ range: $<10^{-4}$ to 10^{3}

Impedance range: 100 Ω to 100TΩ (10^{14}Ω)

Capacitance range: 1pF to >0.1F

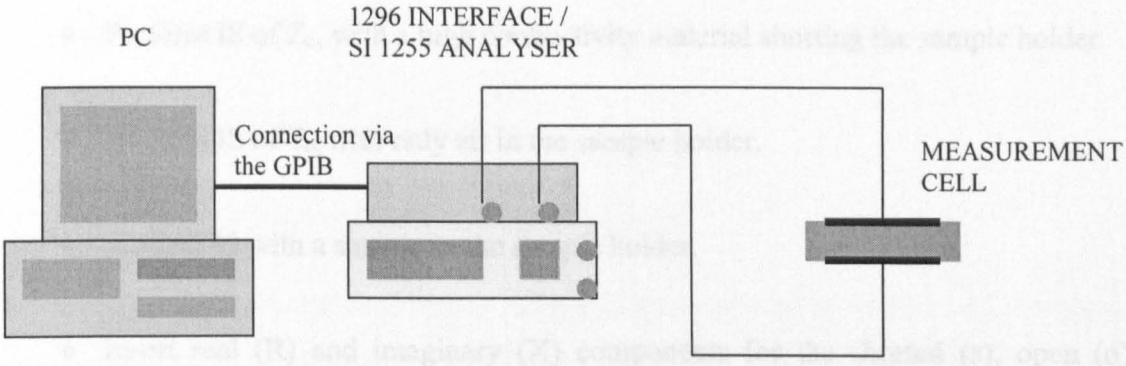

Figure 3-7 Schematic of the set up of impedance spectroscopy

3.4.2 Correction Of Impedance Data At High Frequencies

At high frequencies, especially when the frequency is greater than 1MHz, an abnormal feature was always present in the impedance spectra. This is because at high frequencies impedance data can be seriously affected by stray or residual capacitance and inductance effects due to the cabling and sample holder. For a real measurement system, the measured impedance Z_m can be considered to be a mixed contribution of the impedance of the sample Z_s, the impedance of the short circuit Z_c, and the impedance of open circuit Z_o, as schemed as in Fig. 3-8 (Christensen *et al.* 1994).

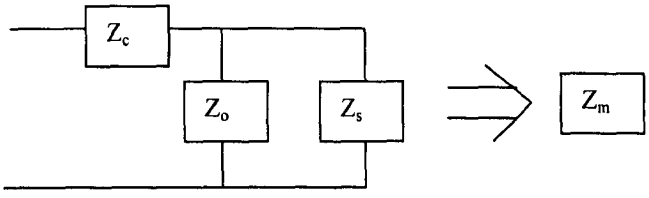

Figure 3-8 Schematic representation of the elements contributing to a typical impedance measurement.

In an ideal case, Z_o should be infinite and Z_c should be zero. However, Z_c increases and Z_o decreases with increasing frequencies. So, at high frequency, errors resulting from the effects of stray capacitance and inductance can be very large, which have to be corrected by a proper procedure. One of the most efficient ways is by the following procedure (Christensen *et al.* 1994).

- Perform IS of Z_c, with a high conductivity material shorting the sample holder.
- Perform IS of Z_o, with only air in the sample holder.
- Collect IS with a sample in the sample holder.
- Insert real (R) and imaginary (X) components for the shorted (s), open (o), and measured (m) responses into the following equations at each frequency:

$$R_1 = R_m(R_o^2 + X_o^2) - R_o(R_m^2 + X_m^2) \quad (3\text{-}1)$$

$$R_2 = R_c(R_o^2 + X_o^2) + R_o(R_c^2 + X_c^2) \quad (3\text{-}2)$$

$$R_3 = 2R_cR_oR_m + 2R_oX_cX_m \quad (3\text{-}3)$$

$$X_1 = X_m(R_o^2 + X_o^2) - X_o(R_m^2 + X_m^2) \quad (3\text{-}4)$$

$$X_2 = X_c(R_o^2 + X_o^2) + X_o(R_c^2 + X_c^2) \quad (3\text{-}5)$$

$$X_3 = 2R_cX_oR_m + 2X_cX_oX_m \quad (3\text{-}6)$$

$$D = (R_m - R_c - R_o)^2 + (X_m - X_c - X_o)^2 \quad (3\text{-}7)$$

$$Z_s^{real} = (R_1 - R_2 + R_3)/D \quad (3\text{-}8)$$

$$Z_s^{imag} = (X_1 - X_2 + X_3)/D \qquad (3\text{-}9)$$

where R_1, R_2, R_3, X_1, X_2, X_3 and D are intermediate functions, Z_s^{real} is the real part and Z_s^{imag} the imaginary part of the impedance of the sample under measurement. This procedure has been used for eliminating the high frequency abnormality in some cases in this project. Meanwhile there is also a correction procedure provided in the Solartron 'Operating Manual', which is called 'normalising a measurement' (Solartron, 1999). This Solartron approach is much less time-consuming, but according to my personal experience, it seemed less effective in eliminating the errors.

Nevertheless it is important to note that the impedance data at the frequencies under 1MHz were reliable even without undergoing a correction procedure. This had been proven by, in several cases, our comparing the raw experimental data with the corrected data obtained following the correction procedures.

3.5 Other Analytical Techniques

3.5.1 Density Measurements

The density measurements were conducted by measuring the weight and the geometrical dimensions of the samples. The samples were in a circular disk shape. The faces of the disk were carefully polished using P800 grit SiC paper, then the diameter and the thickness of the disk were measured using a micrometer. The disks were dried at 200°C for 24h before being weighed using a digital balance. The density was calculated by:

$$D = \frac{4W}{\pi D^2 \delta} \qquad (3\text{-}10)$$

where W is the weight (g), D (cm) the diameter and δ (cm) the thickness of the sample disk.

3.5.2 Thermogravimetric Analyses

Thermogravimetric analyses (TGA) were carried out in a thermogravimetric analyser (FGS-2, Perkin-Elmer) to examine the weight loss of a ceramic compact during heating.

The thermogravimetry instrument consists mainly of a precision balance, a furnace controlled by a temperature programmer and a data acquisition system as shown schematically in Fig.3-9. TGA allows monitoring and precisely measuring the thermal weight change of the sample at varying temperatures up to 1100°C.

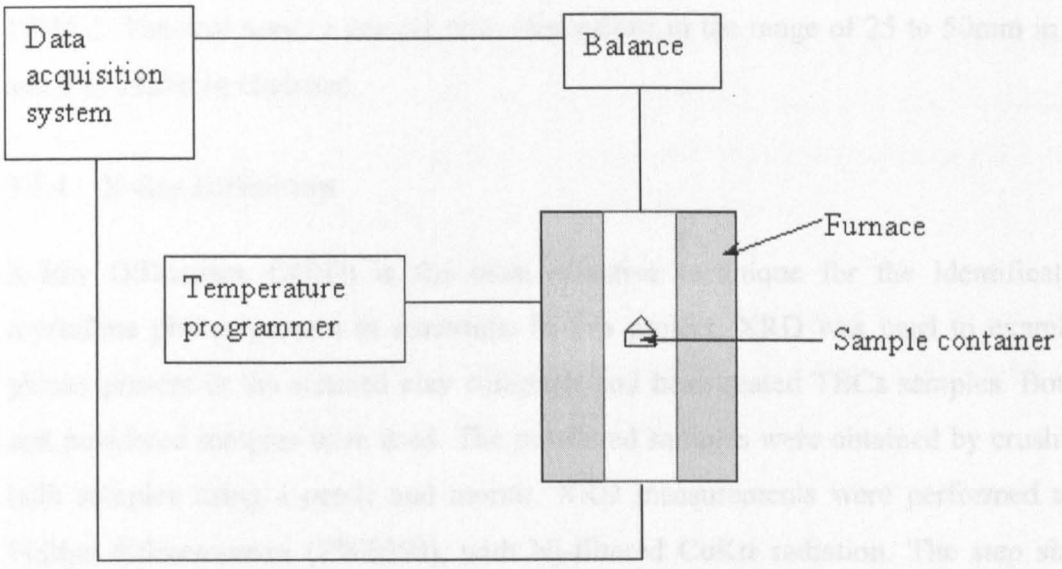

Figure 3-9 Schematic of a thermogravimetry instrument.

3.5.3 Dilatometry

The shrinkage behaviour of a green powder compact as a function of temperature was measured using a dilatometer (402E, Netzsch-Geratebau GmbH).

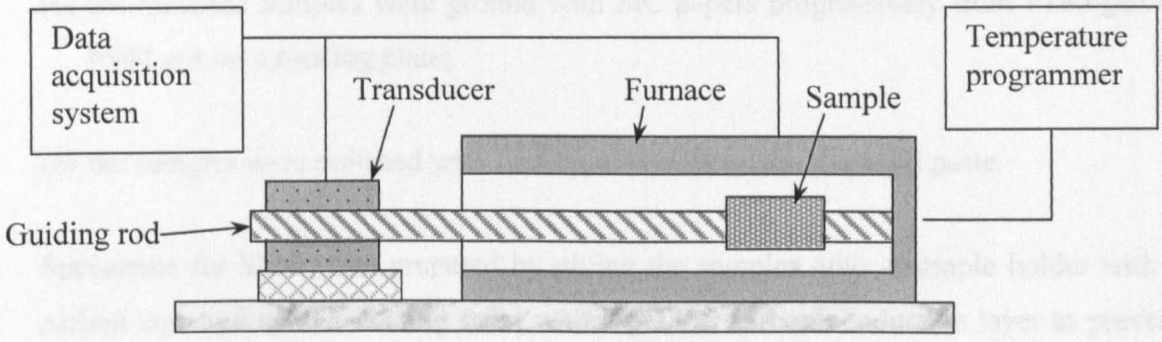

Figure 3-10 Schematic of a dilatometer instrument

The dilatometer consists of an electronic transducer, a furnace controlled by a temperature programmer and a data acquisition system as shown schematically in Fig.3-10. This instrument allows the continuous measurement and observation of the thermal change in length of a specimen at temperatures ranging from room temperature to 1700°C. This test needs a sample with dimensions in the range of 25 to 50mm in length and 3 to 14mm in diameter.

3.5.4 X-Ray Diffraction

X-Ray Diffraction (XRD) is the most effective technique for the identification of crystalline phases present in materials. In this project, XRD was used to examine the phases present in the sintered clay compacts and heat-treated TBCs samples. Both bulk and powdered samples were used. The powdered samples were obtained by crushing the bulk samples using a pestle and mortar. XRD measurements were performed using a Philips diffractometer (PW1050), with Ni-filtered CuKα radiation. The step size was 0.01° and angular scan speed was 0.8°/minute. The angular scan range was 15 ~ 90°.

3.5.5 Optical And Scanning Electron Microscopy

Optical microscopy and Scanning Electron Microscopy (SEM) were used to study the microstructures of the materials. The samples for the optical microscopy and SEM observations were prepared by the following procedure:

(a) samples were mounted in resin and cured at room temperature for 24h;

(b) the mounted samples were ground with SiC papers progressively from P180 grit to P800 grit on a rotating plate;

(c) the samples were polished with first 6μm, and then 1μm diamond paste.

Specimens for SEM were prepared by gluing the samples onto a sample holder with a carbon tape and sputter-coating them with a gold or carbon conductive layer to prevent electron charging effects.

SEM observations were carried out with a JEOL, JXA-840A instrument.

3.5.6 Energy Dispersive Spectroscopy

Energy dispersive spectroscopy (EDS) is an electron probe microanalysis technique. In this technique, an electron beam is focused on the surface of a specimen. X-rays are emitted as a consequence of interactions between the electron beam and materials. The X-ray spectrum consists of characteristic peaks at different energy levels. Qualitative and quantitative analyses of the component elements can be made by measuring the energies and intensities of these characteristic lines in the spectrum.

In this project, the microanalysis was made with an energy-dispersive X-ray analyser (AN10000, Oxford Instrument) coupled to a scanning electronic microscopy (JEOL JXA-840A). All the microanalysis was conducted qualitatively.

4 Impedance Data Analysis

4.1 Introduction

Once we have obtained a set of experimental impedance data, we can conduct equivalent circuit modelling by using computer software to get the values of elements in the equivalent circuit. In this project we have used 'Zview for Windows' (Scribner Associates, Inc) in simulation. Obviously equivalent circuit modelling is only useful when an appropriate model is selected. Software cannot select a model for you, although it can determine the values which best fit your data based on a model you design (Scribner, 1998).

To select an appropriate equivalent circuit, we need to rely on our own knowledge of the physical processes in the measured system. Also, and almost of equal importance, is that we need to make many trials to see what features of the spectrum will change if we adjust certain value(s) of elements in the equivalent circuit. In this way we can examine whether or not the equivalent circuit model on trial is 'reasonable'. If not, elements need to be either added, or cancelled, or rearranged based on the changes in spectrum features when values of elements are changed.

The analytical approach to IS analysis to be presented in the following section is not only necessary for a better understanding of IS, but also very useful for the fitting of impedance data and the proper representations of IS.

4.2 Analytical Approach

In reference to a brick layer model, we assume that grain, grain boundary and electrode/material interface are ideally represented by R_1C_1, R_2C_2, R_3C_3 elements respectively, which are connected in series as in Fig. 4-1.

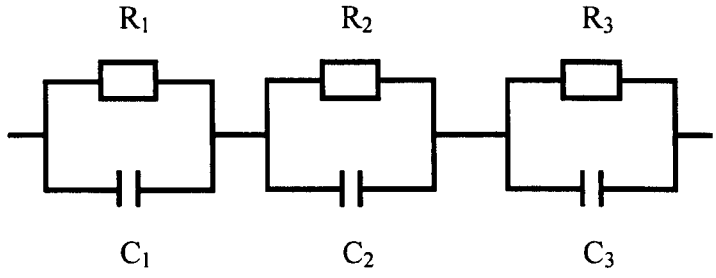

Figure 4-1 Equivalent circuit for an idealised brick layer model.

The impedance of this electrical circuit can be expressed as:

$$Z = \frac{1}{\frac{1}{R_1} + j\omega C_1} + \frac{1}{\frac{1}{R_2} + j\omega C_2} + \frac{1}{\frac{1}{R_3} + j\omega C_3} = Z' - jZ'' \qquad (4\text{-}1)$$

where ω is the angular frequency, ω=2πf. From this equation, we have:

$$Z' = \frac{R_1}{1+(\omega R_1 C_1)^2} + \frac{R_2}{1+(\omega R_2 C_2)^2} + \frac{R_3}{1+(\omega R_3 C_3)^2} \qquad (4\text{-}2)$$

and

$$Z'' = \frac{\omega R^2{}_1 C_1}{1+(\omega R_1 C_1)^2} + \frac{\omega R^2{}_2 C_2}{1+(\omega R_2 C_2)^2} + \frac{\omega R^2{}_3 C_3}{1+(\omega R_3 C_3)^2} \qquad (4\text{-}3)$$

The relaxation frequency of an RC element is determined by its resistance and capacitance:

$$\omega_i = \frac{1}{R_i C_i} \qquad (4\text{-}4)$$

then we have

$$Z' = \frac{R_1}{1+(\frac{\omega}{\omega_1})^2} + \frac{R_2}{1+(\frac{\omega}{\omega_2})^2} + \frac{R_3}{1+(\frac{\omega}{\omega_3})^2} \qquad (4\text{-}5)$$

$$Z'' = \frac{R_1\frac{\omega}{\omega_1}}{1+(\frac{\omega}{\omega_1})^2} + \frac{R_2\frac{\omega}{\omega_2}}{1+(\frac{\omega}{\omega_2})^2} + \frac{R_3\frac{\omega}{\omega_3}}{1+(\frac{\omega}{\omega_3})^2} \qquad (4\text{-}6)$$

These expressions are in the same form as those given by Abrantes *et al.* (2000b).

Based on Eq.2-6 ($M^*=j\omega C_0 Z^*$), it is not difficult for us to get similar equations for modulus components:

$$M' = \frac{\frac{C_o}{C_1}*(\frac{\omega}{\omega_1})^2}{1+(\frac{\omega}{\omega_1})^2} + \frac{\frac{C_o}{C_2}*(\frac{\omega}{\omega_2})^2}{1+(\frac{\omega}{\omega_2})^2} + \frac{\frac{C_o}{C_3}*(\frac{\omega}{\omega_3})^2}{1+(\frac{\omega}{\omega_3})^2} \qquad (4\text{-}7)$$

$$M'' = \frac{\frac{C_o}{C_1}*\frac{\omega}{\omega_1}}{1+(\frac{\omega}{\omega_1})^2} + \frac{\frac{C_o}{C_2}*\frac{\omega}{\omega_2}}{1+(\frac{\omega}{\omega_2})^2} + \frac{\frac{C_o}{C_3}*\frac{\omega}{\omega_3}}{1+(\frac{\omega}{\omega_3})^2} \qquad (4\text{-}8)$$

Now a demonstration will be given, mathematically, that there can be three separate semicircles in complex impedance and modulus plots, if the relaxation frequencies of different RC elements are orders of magnitude different to one another.

Assuming $\omega_1 >> \omega_2 >> \omega_3$, in high frequency range, we have: $\omega/\omega_2 >> 1$ and $\omega/\omega_3 >> 1$. R_2 and R_3 usually have finite values. If R_2 is assumed to be much smaller than ω/ω_2 and R_3 is assumed to be much smaller than ω/ω_3, then we can have two approximations:

$$\frac{R_2}{1+\frac{\omega}{\omega_2}} \Rightarrow 0 \quad (4\text{-}9a) \qquad \text{and} \qquad \frac{R_3}{1+\frac{\omega}{\omega_3}} \Rightarrow 0 \quad (4\text{-}9b)$$

Based on these two approximation, then according to Eqs. 4-5 and 4-6, we have

$$Z' = \frac{R_1}{1+(\frac{\omega}{\omega_1})^2} \qquad (4\text{-}10)$$

$$Z'' = \frac{R_1 \frac{\omega}{\omega_1}}{1+(\frac{\omega}{\omega_1})^2} \qquad (4\text{-}11)$$

Upon combining Eqs. 4-10 and 4-11, we have

$$(Z'')^2 + (Z' - \frac{R_1}{2})^2 = (\frac{R_1}{2})^2 \qquad (4\text{-}12)$$

This means in the high frequency range, the contributions from the R_2C_2 and R_3C_3 is negligible and the impedance of the R_1C_1 element follows a circular equation, with a diameter R_1 and the center on the x-axis ($R_1/2$, 0).

In the medium frequency range, $\omega/\omega_1 << 1$, $\omega/\omega_3 >> 1$ and by assuming $R_3 << \omega/\omega_3$, then

$$\frac{R_1}{1+\frac{\omega}{\omega_1}} \Rightarrow R_1 \qquad \text{and} \qquad \frac{R_3}{1+\frac{\omega}{\omega_3}} \Rightarrow 0$$

Eqs. 4-5 and 4-6 can be approximated by

$$Z' = R_1 + \frac{R_2}{1+(\frac{\omega}{\omega_2})^2} \qquad (4\text{-}13)$$

$$Z'' = \frac{R_2 \frac{\omega}{\omega_2}}{1+(\frac{\omega}{\omega_2})^2} \qquad (4\text{-}14)$$

By combining Eqs.4-13 and 4-14, we can obtain another circular equation:

$$(Z'')^2 + [Z' - (R_1 + \frac{R_2}{2})]^2 = (\frac{R_2}{2})^2 \qquad (4\text{-}15)$$

In this frequency range, the impedance of the R_2C_2 element also follows a circular equation, with a diameter R_2 and the center on the x-axis $[R_1+(R_2/2), 0]$.

Likewise at low frequency, $\omega/\omega_1 \ll 1$ and $\omega/\omega_2 \ll 1$,

The impedance of R_3C_3 element follows a circular equation, with a diameter of R_3 and the center at $[R_1+R_2+(R_3/2), 0]$:

$$(Z'')^2 + [Z' - (R_1 + R_2 + \frac{R_3}{2})]^2 = (\frac{R_3}{2})^2 \qquad (4\text{-}16)$$

By following similar deduction procedures, the circular equations for modulus spectra in different frequency ranges can be obtained:

$$(M'')^2 + (M' - \frac{C_o}{2C_1})^2 = (\frac{C_o}{2C_1})^2 \qquad (4\text{-}17) \quad \text{at low frequencies}$$

$$(M'')^2 + [M' - (\frac{C_o}{C_1} + \frac{C_o}{2C_2})]^2 = (\frac{C_o}{2C_2})^2 \qquad (4\text{-}18) \quad \text{at medium frequencies}$$

$$(M'')^2 + [M' - (\frac{C_o}{C_1} + \frac{C_o}{C_2} + \frac{C_o}{2C_3})]^2 = (\frac{C_o}{2C_3})^2 \qquad (4\text{-}19) \quad \text{at high frequencies}$$

4.3 Numerical Analysis

According to the above mathematical analyses, the electrical responses from different phases in a specimen can be distinguished in impedance and modulus spectra as resolved semicircles, if the relaxation frequencies of different phases are 'sufficiently' different. But how different should the relaxation frequencies be to get a well-resolved spectrum? Meanwhile in the light of Eqn. 4-4, we know the relaxation frequency is associated with both the resistance and capacitance. The relaxation frequency can differ as a consequence of the difference in either resistance or capacitance, or both. These different factors may have different effects on the resolution and other features of the spectra. To answer these questions, numerical analysis is necessary.

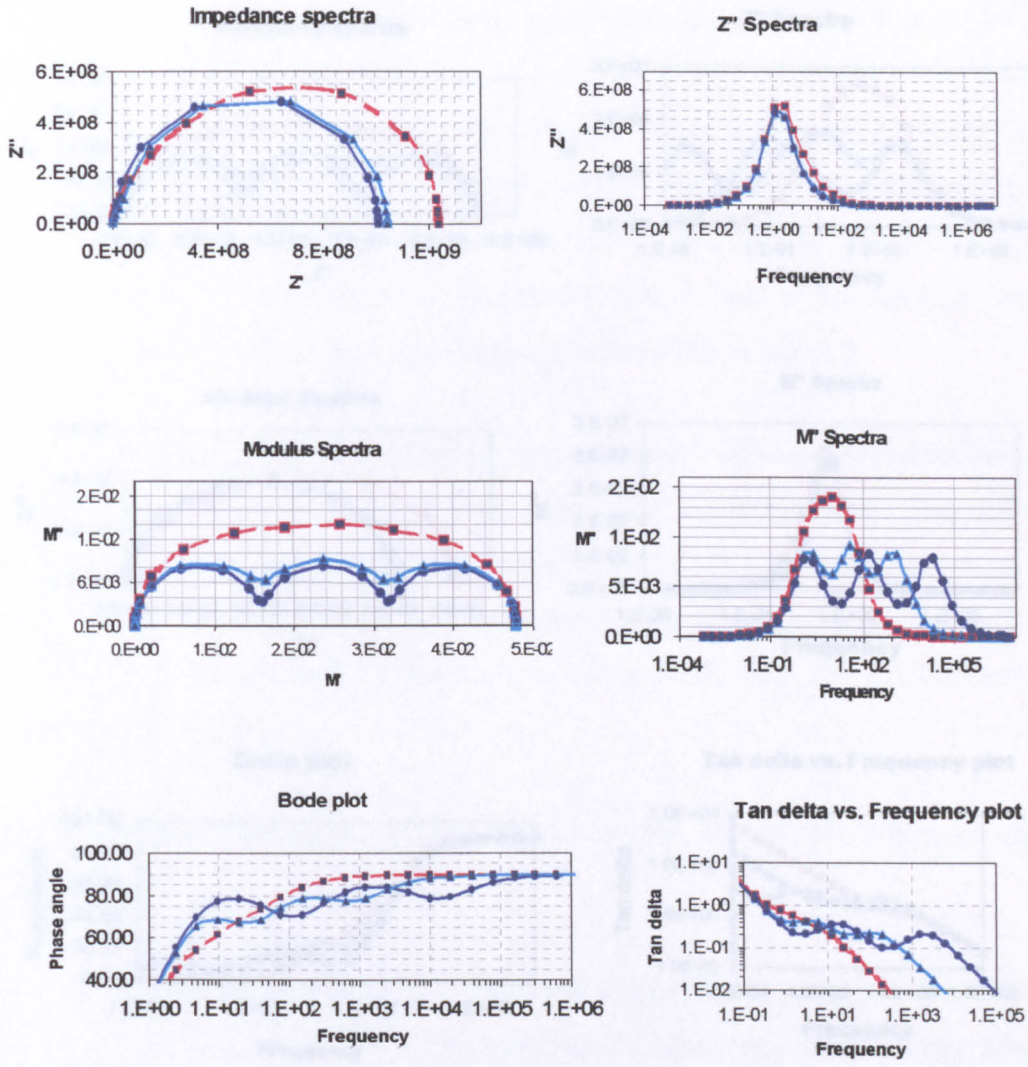

Fig. 4-2 Various representations of IS corresponding to equivalent circuit model as shown in Fig. 4-1, with ····■···· representing $R_3/R_2=R_2/R_1=5$, —▲— representing $R_3/R_2=R_2/R_1=25$, —●— representing $R_3/R_2=R_2/R_1=100$. The values of elements employed in this simulation are listed in Table 4-1.

Table 4-1 Values of the elements in the equivalent circuit model (Fig. 4-1) used for numerical analysis.

R_1	R_2	R_3	C_1	C_2	C_3	Co^*	$R_3/R_2=R_2/R_1$
$3x10^8$	$1x10^7$	$1x10^9$	$1x10^{-10}$	$1x10^{-10}$	$1x10^{-10}$	$1x10^{-11}$	100
$3x10^8$	$4x10^7$	$1x10^9$	$1x10^{-10}$	$1x10^{-10}$	$1x10^{-10}$	$1x10^{-11}$	25
$3x10^8$	$2x10^8$	$1x10^9$	$1x10^{-10}$	$1x10^{-10}$	$1x10^{-10}$	$1x10^{-11}$	5

*** Empty capacitance of the measuring cell.**

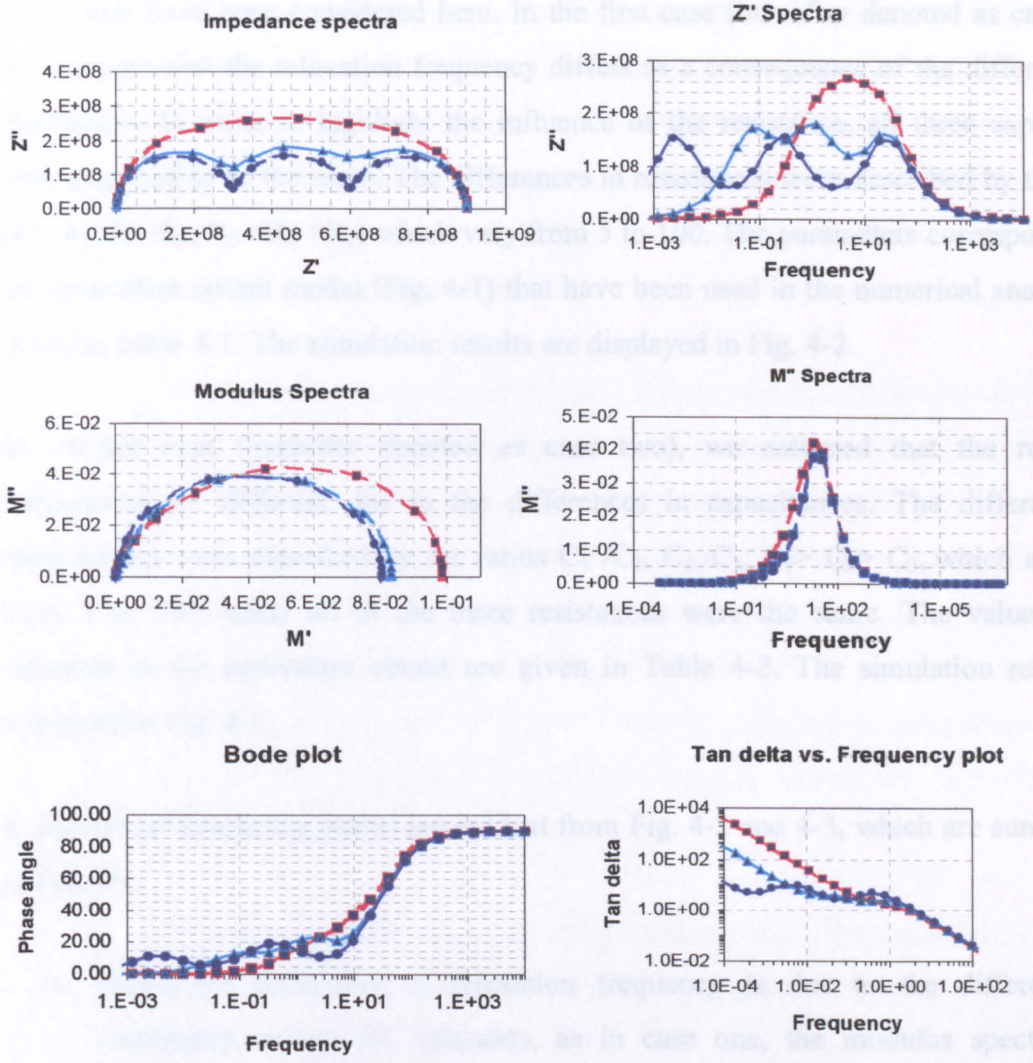

Fig. 4-3 Various representations of IS corresponding to equivalent circuit model as shown in Fig. 4-1, with ····■···· representing $C_1/C_2=C_2/C_3=5$, —▲— representing $C_1/C_2=C_2/C_3=25$, —●— representing $C_1/C_2=C_2/C_3=100$. The values of elements employed in this simulation are listed in Table 4-2.

Table 4-2 Values of the elements in the equivalent circuit model (Fig. 4-1) used for numerical analysis

R_1	R_2	R_3	C_1	C_2	C_3	Co^*	$C_1/C_2=C_2/C_3$
$3x10^8$	$3x10^8$	$3x10^8$	$2x10^{-11}$	$2x10^{-9}$	$2x10^{-7}$	$1x10^{-11}$	100
$3x10^8$	$3x10^8$	$3x10^8$	$2x10^{-11}$	$5x10^{-10}$	$7.5x10^{-9}$	$1x10^{-11}$	25
$3x10^8$	$3x10^8$	$3x10^8$	$2x10^{-11}$	$1x10^{-10}$	$5x10^{-10}$	$1x10^{-11}$	5

*** Empty capacitance of the measuring cell.**

Two cases have been considered here. In the first case (hereafter denoted as case one), we assumed that the relaxation frequency differs as a consequence of the differences in resistances. In order to highlight the influence of the resistance, all three capactances were assumed to be the same. The differences in resistances were described by the ratios (R_3/ R_2, R_2 /R_1, $R_3 > R_2 > R_1$) which vary from 5 to 100. The parameters corresponding to the equivalent circuit model (Fig. 4-1) that have been used in the numerical analysis are given in Table 4-1. The simulation results are displayed in Fig. 4-2.

In another case (hereafter denoted as case two), we assumed that the relaxation frequencies are different due to the differences in capacitances. The differences of capacitances were described by the ratios C_1 /C_2, C_2 /C_3, $C_1 > C_2 > C_3$, which also vary from 5 to 100, while all of the three resistances were the same. The values of the elements in the equivalent circuit are given in Table 4-2. The simulation results are displayed in Fig. 4-3.

A number of interesting points are evident from Fig. 4-2 and 4-3, which are summarised as follows:

a. When the difference in relaxation frequency is due to the differences in resistances among RC elements, as in case one, the modulus spectra (both complex modulus plot and M'' spectroscopic diagram) show well-resolved semicircles corresponding to different elements in the equivalent circuit, while semicircles in the impedance spectra (both complex impedance plot and Z'' spectroscopic diagram) entirely overlap. By contrast, in case two where the capacitances of the RC elements are different, the semicircles in the impedance spectra are resolved but modulus spectra are not resolved. This means that the difference in resistance leads to resolution in the modulus spectra, while the difference in capacitance leads to the resolution in the impedance spectra.

b. In both cases, we can see peaks and valleys in the phase angle (Bode) plot and tan (δ) vs. lg(f) diagram. This means that the phase angle (Bode) plot and tan (δ) vs. lg(f) diagram are sensitive to the differences both in resistances and capacitances.

c. In both cases, spectral resolution depends on the degree of difference in resistances or capacitances. When the ratio between resistances or capacitances is larger than 25, semicircles can be distinguished. However, when the ratio between resistances or capacitances is smaller than 5, the semicircles overlap to such an extent that only one depressed semicircular arc can be seen in the complex impedance or modulus spectra.

d. When semicircles are well resolved (i.e., if the relaxation frequency difference is larger than 25-times), the resistances can be worked out straightaway from the complex impedance plot, as the resistances are equal to the diameters of the semicircle. However in practice the semicircles are not perfect due to the overlap, the resistances need be worked out with reference to the cusp, i.e. the lowest point where two semicircular arcs meet. The real component at the first cusp from the left is the resistance of the RC element with the highest relaxation frequency, the length in the real components between the first cusp and second cusp corresponds to the second RC element and so forth.

e. The resistances can also be easily obtained using the Z'' spectroscopic diagram. According to Eqn. 4-6, the peaks in the Z'' spectroscopic diagram are $R_1/2$, $R_2/2$ and $R_3/2$ respectively.

f. In a similar way, the capacitance can be obtained by using the complex modulus plots. According to Eqs.4-17 ~ 4-19, the diameters of the semicircles are C_o/C_1, C_o/C_2, C_o/C_3, respectively, where C_o is the capacitance of the empty space. Here again the diameters of arcs should be determined by reference to the cusps of the spectrum.

Also the capacitances can be obtained by examining the M'' spectroscopic diagram. According to Eqn. 2-8, the peaks in the M'' spectroscopic diagram are $C_o/(2C_1)$, $C_o/(2C_2)$, $C_o/(2C_3)$, respectively.

4.4 Summary And Conclusions

The representations of IS need to be made in as many formalisms as possible. To represent IS only in one formalism, for example only in the impedance or modulus formalism, may miss valuable information that could have been available in impedance data.

When the relaxation frequencies of different RC elements are close (the difference is below 5 times), semicircles will overlap to form one single semicircular arc similar to a depressed semicircle. This will seriously complicate the impedance analysis. Care must be taken when we attempt to draw any conclusions in this situation.

The Bode (phase angle) plot and tangent loss plot are sensitive to the differences both in resistances and capactances. They are useful in determining the presence of relaxation processes. However a data analysis which combines the modulus and impedance spectra is more effective. The advantage of this method is that not only qualitative information, such as how many relaxation processes are present and how well resolved is the spectra, but also quantitative information, such as the values of resistances, capacitances and relaxation frequencies can be obtained from both complex plane and spectroscopic plots of impedance and modulus.

5 Nondestructive Characterisation of Alumina/Silicon Carbide Nanocomposites Using IS

5.1 Introduction

Non-destructive characterisation (NDC) of ceramic matrix composites is essential for developing reliable ceramics for industrial applications. The brittleness, catastrophic failure behaviour and therefore, the low reliability of ceramics have been the main obstacles for the application of ceramics. Without NDC, a slight improvement in the reliability of ceramics would require a much higher cost of manufacture, because expensive processing techniques have to be used to ensure the high performance of products, which quite often is unnecessary. A high performance does not necessarily provide a high reliability, whereas an effective NDC technique will certainly help improve the applicability of ceramic materials. Extensive studies have been carried out to investigate the processing and properties of advanced structural ceramics, which have resulted in significant improvements in the performance of ceramics. However, very few studies have been done on NDC of structural ceramics, which is critical in controlling the quality of ceramics (Van de Voorde, 1998). This largely is due to the lack of availability of an efficient and comprehensive nondestructive technique that could be applied to evaluating ceramics.

In this study, in order to investigate the feasibility of using impedance spectroscopy as a NDC technique for characterising structural ceramic materials, Al_2O_3/SiC nanocomposites were selected as model materials for the following reasons:

(a) SiC particles and whiskers are important reinforcing components to strengthen and toughen ceramics and glasses, but reports about the electrical properties of the materials of this category are limited (Wang *et al.* 2000; Zhang *et al.* 1992). Under certain circumstances, the electrical properties may be of concern in the application of these composites, therefore an investigation into the electrical properties of these materials is necessary.

(b) Al_2O_3/SiC nano-composites represent a series of insulator/electronic conductor composites, for which particular examples are the SiC or Carbon-fibre-reinforced ceramics and glasses. A success in applying IS as a NDC technique for Al_2O_3/SiC nanocomposites means that IS could be extended to the whole series of insulator/electronic conductor composites.

(c) Al_2O_3/SiC nanocomposites have been attracting growing interest because significant improvements in strength and toughness have been achieved by the addition of SiC nanoparticles (Niihara, 1991; Ohji *et al.* 1996). They are amongst the most promising structural materials that could be applied at high temperatures up to 1000°C.

In addition, it was revealed that the oxidation rates of Al_2O_3/SiC nanocomposites were several orders of magnitude higher than that of monolithic SiC (Luthra and Park, 1990; Sciti and Bellosi 1998). Oxidation at elevated temperature could be a crucial factor in controlling the degradation of Al_2O_3/SiC nanocomposites at high temperatures. Therefore it is highly desirable to develop a nondestructive evaluation technique for studying the oxidation of the Al_2O_3/SiC nanocomposites at high temperature.

The purpose of this work is to study the electrical properties of Al_2O_3/SiC nanocomposites and their dependence on the microstructure, and thereby to characterise the microstructural features of composites and microstructural changes when subjected to high temperature heat treatment. It has been found that IS can be used to (i) examine the conducting mechanisms of ceramic materials; (ii) determine the content and orientation of conductive phase in insulating materials; (iii) determine the thickness of oxide scales formed at the surface of ceramic composites.

5.2 Experimental

5.2.1 Materials

Al_2O_3/SiC nanocomposites containing 5 vol %, 10 vol %, 20 vol % SiC (denoted hereafter as 5SA, 10SA and 20SA, respectively), and a monolithic alumina (hereafter denoted as MA) were obtained by hot-pressing at 1600~1700°C, of which the detailed

fabrication procedures had been documented in the literature by Sternitzke *et al.* (1998) and Wu *et al.* (1998). All the Al_2O_3/SiC nanocomposites used in this investigation were provided by the solid mechanics group of the Department of Materials, Oxford University. Samples in plate form of about 10mm×6mm×2mm in size were cut from the as-hot-pressed discs.

5.2.2 Microstructure of Materials

The microstructure of the Al_2O_3/SiC nanocomposites consists of Al_2O_3 grains and superfine SiC particles (Fig-5-1). The Al_2O_3 grain size is 2- 4 μm, while the SiC particle size is 100- 300 nm. The SiC particles are uniformly dispersed in alumina grains or at the alumina grain boundaries.

Figure 5-1 TEM picture of 5SA, where the dark grey speckles are SiC particles (courtesy of Houzheng. Wu, Department of Materials Science at Oxford University)

5.2.3 Oxidation Treatments

Before oxidation treatments all the Al_2O_3/SiC nanocomposite samples were polished using 6μm diamond paste and then cleaned with acetone. Oxidation treatments were conducted in a chamber furnace (Carbolite) at different temperatures from 800°C to 1400 °C, for a period ranging from 1h to 100h. The heating and cooling rates were 3 K•minute^{-1} and 15 K•minute^{-1} respectively.

5.2.4 Impedance Measurements

The measuring cells were about 10mm by 6mm by 2mm in size, with silver or platinum paste on the two parallel surfaces of the plate specimen as electrodes. For impedance measurements at temperatures above 400°C, platinum was used as electrodes. For impedance measurements of oxidised samples, platinum foils were applied directly to the surfaces of the specimens as the electrodes.

Impedance measurements were made over a range from room temperature (R.T) to 800°C. Data were recorded over frequency ranges of 10^6 down to 10^{-4} ~10^{-1} Hz with 4 data readings per decade, using an 0.1 Vrms signal. A special rig as shown in Fig. 3-6 was used for impedance measurements at high temperatures.

5.3 Results

5.3.1 Impedance Spectra Of the Monolithic Alumina (MA)

Pure alumina is a very good insulator. At low temperatures, say below 400°C, the resistivity of alumina was so high that the electrical current through a thin plate sample was too low to be measured using IS. As a consequence, at low temperatures MA behaved like a pure capacitor: as shown in Fig.5-2a, a straight line is almost vertical to the x-axis, indicating the electrical response is almost purely capacitive.

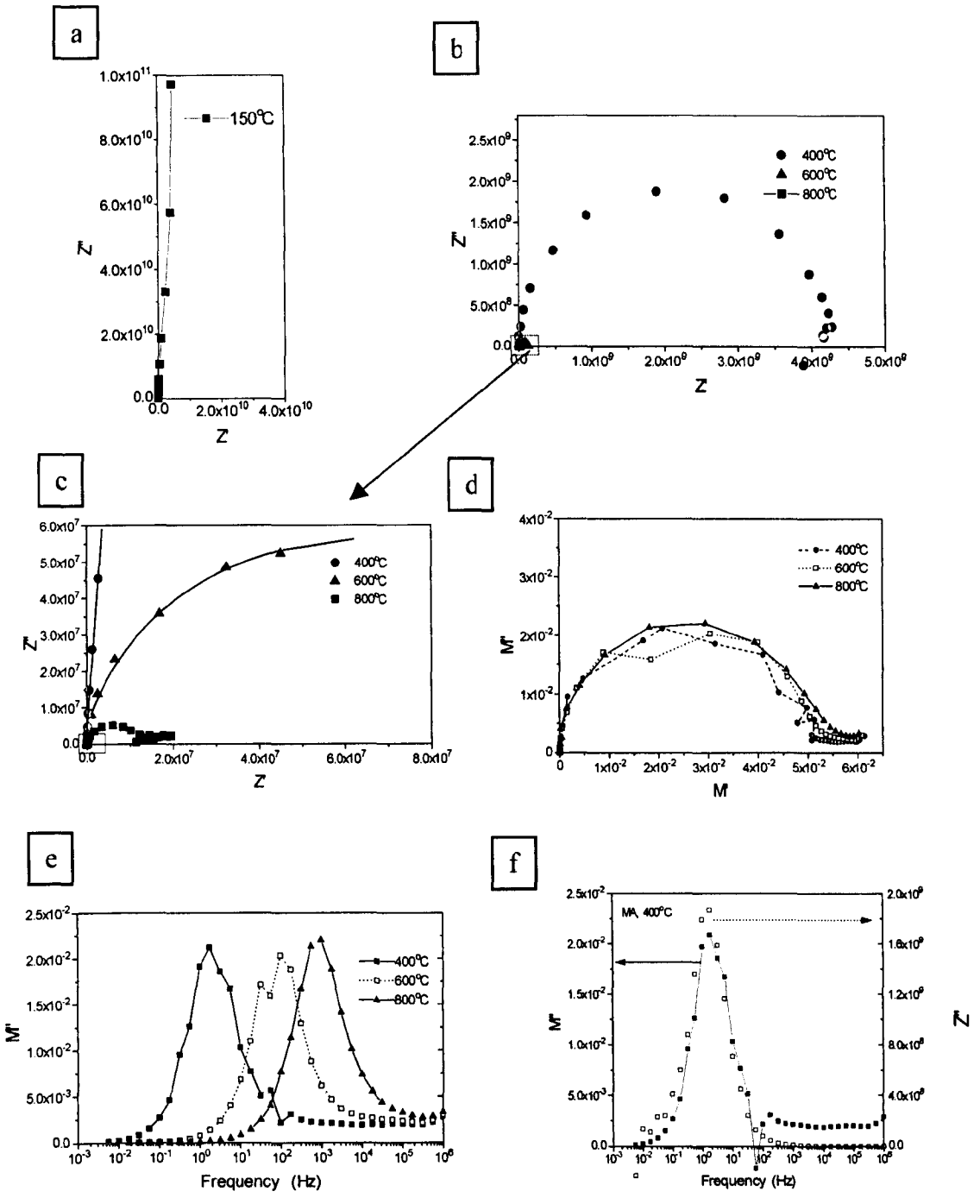

Figure 5-2 Impedance spectra of monolithic alumina: (a) complex impedance plot at 150°C; (b) and (c) complex impedance plots at various measurement temperatures, note (c) is a zoomed view of (b); (d) complex modulus plane plots; (e) modulus spectroscopic plots; (f) comparison of modulus and impedance spectroscopic plots, where the hollow square symbols represent the impedance data while the solid square symbols represent the modulus data.

At temperatures above 400°C, the resistances were still very large, but were measurable. The complex impedance plots at different temperatures are given in Figs.5-2b-c. Obviously there is only one semicircle at all measuring temperatures. The resistance decreased drastically with increasing temperature. For this reason, the impedance spectra at different temperatures need be displayed in different scales. By contrast, the diameters in complex modulus plots, or the height of the M'' peaks in the modulus spectroscopic plots (Fig.5-2d-e) at different temperatures, are similar. By reference to Fig. 5-2e, the relaxation frequencies corresponding to the M'' peaks at 400°C, 600°C, 800°C were 2Hz, 70Hz, and 1000Hz respectively. The capacitive effect remained almost unchanged as the temperature was increased. Because $\omega=1/RC$, the variation in relaxation frequency (ω) is entirely attributed to the changes of resistance. The product of frequency and resistance (ωR) was calculated to be about $6x10^{10}$ for MA at all the measurement temperatures.

The full-width at the half-maximum (FWHM) in the Z'' and M'' spectroscopic plots is about 1.2~1.25 decades, which is very close to the ideal Debye peak that is 1.14 decades (Morrison *et al.* 2001). In addition, the semicircles present in the complex plane are nearly perfect, with only a slight depression. The M'' peak and Z'' peak coincide at the same frequency as shown in Fig5-2f. All of these features indicate that the response of MA is nearly ideal.

5.3.2 Impedance Spectra Of Al_2O_3/SiC Nanocomposites

5.3.2.1 Impedance Spectra Of 5SA

Al_2O_3/SiC nanocomposite with 5vol% SiC (5SA) exhibited very poor conductivity at temperatures below 400°C. At low temperatures, the impedance spectra were similar to that of MA. At the temperatures above 400°C, the impedance spectra of 5SA are given in Fig. 5-3. The spectra of 5SA are similar to those of MA in a few aspects: only one relaxation process can be seen in all forms of representations; the resistance decreased drastically with increasing temperature; modulus spectra at different temperatures were similar.

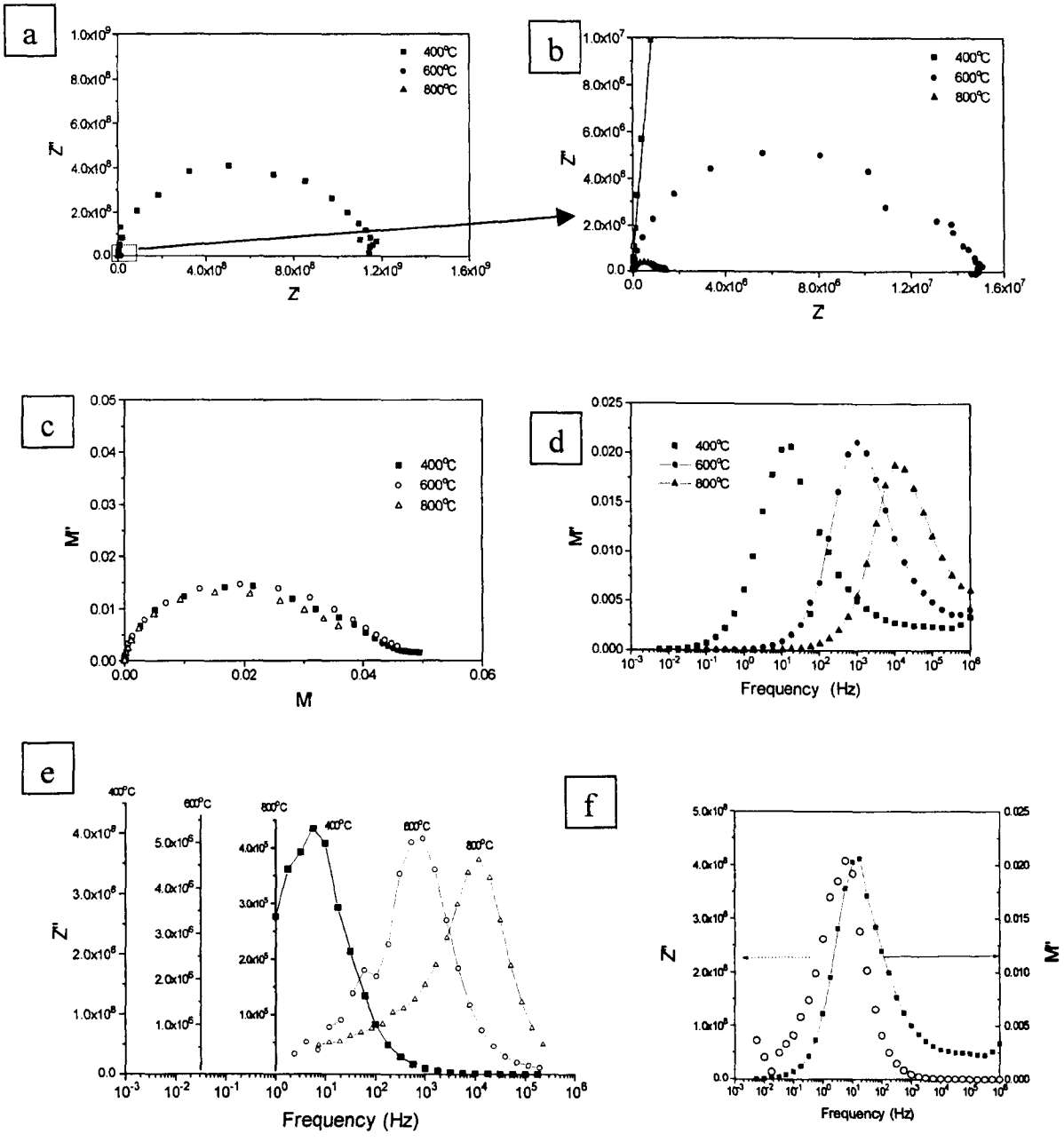

Figure 5-3 Impedance spectra of 5SA: (a) and (b) complex impedance plane plot, please note the different scales used; (c) complex modulus plane plots; (d) modulus spectroscopic plots; (e) impedance spectroscopic plots, note the different scales of y-axis; (f) comparison of modulus and impedance spectroscopic plots, where small squares represent modulus data, while the hollow circles represent the impedance data.

However, with regard to the spectral features, 5SA is different from MA in the following aspects: the semicircles in the spectra are more depressed; Z'' and M'' peaks are broader; and Z'' and M'' peaks no longer coincide at the same frequencies. For example, FWHM in the Z'' and M'' spectroscopic plots were measured as 1.9~2.0 decades, which are much broader than those of MA. The frequencies corresponding to the Z'' peak in impedance spectroscopic plots were 7Hz, 400Hz, and 5000Hz, while the frequencies at the M'' peak were 20Hz, 900Hz, 10000 Hz, at 400°C, 600°C and 800°C respectively. The average mismatch between the Z'' peak and M'' peak was about 0.2 decade. All these features indicate that the response from 5SA was more distributed, or in other words, more frequency-dependent, than MA.

The impedance spectra of 10SA were similar to those of 5SA, except that the resistance was lower and the depression angles of impedance semicircles were noticeably larger than that of 5MA. To save space, the results of the measurements on 10SA (please refer to **Appendix II** for the impedance spectra of 10SA) are not to be presented in detail here.

5.3.2.2 Impedance Spectra Of 20SA

Al_2O_3/SiC nanocomposites with 20 vol% SiC (20SA) had a distinctive behaviour compared to those with lower SiC content. Firstly this material was 'measurable' even at R.T, because the resistance of the measuring cells was lower than 10^9 Ω. However, at low temperatures (e.g., below 300°C), the reproducibility of the impedance data was poor, this could be a consequence of either a contact problem between electrode and material, or the surface conductivity of moisture, or both.

Secondly, the electrical response was strongly dependent on the electrodes used. When painted silver or painted platinum electrodes were used, there were, consistently, two fairly well-resolved semicircles in the complex impedance plots. But when platinum foils were used as electrodes, there was only one depressed semicircle, as illustrated in Fig. 5-4a.

Thirdly the response from 20MA was the most frequency-dispersed among all the composites investigated. At 400°C, FWHMs in the impedance and modulus spectroscopic plots were about 2.0 decades, and the frequency at the Z'' peak was

900Hz, while the frequency at the M'' peak was 4500 Hz. The mismatch between them was 0.6 decade, compared to 0.2 decade for the case of 5SA.

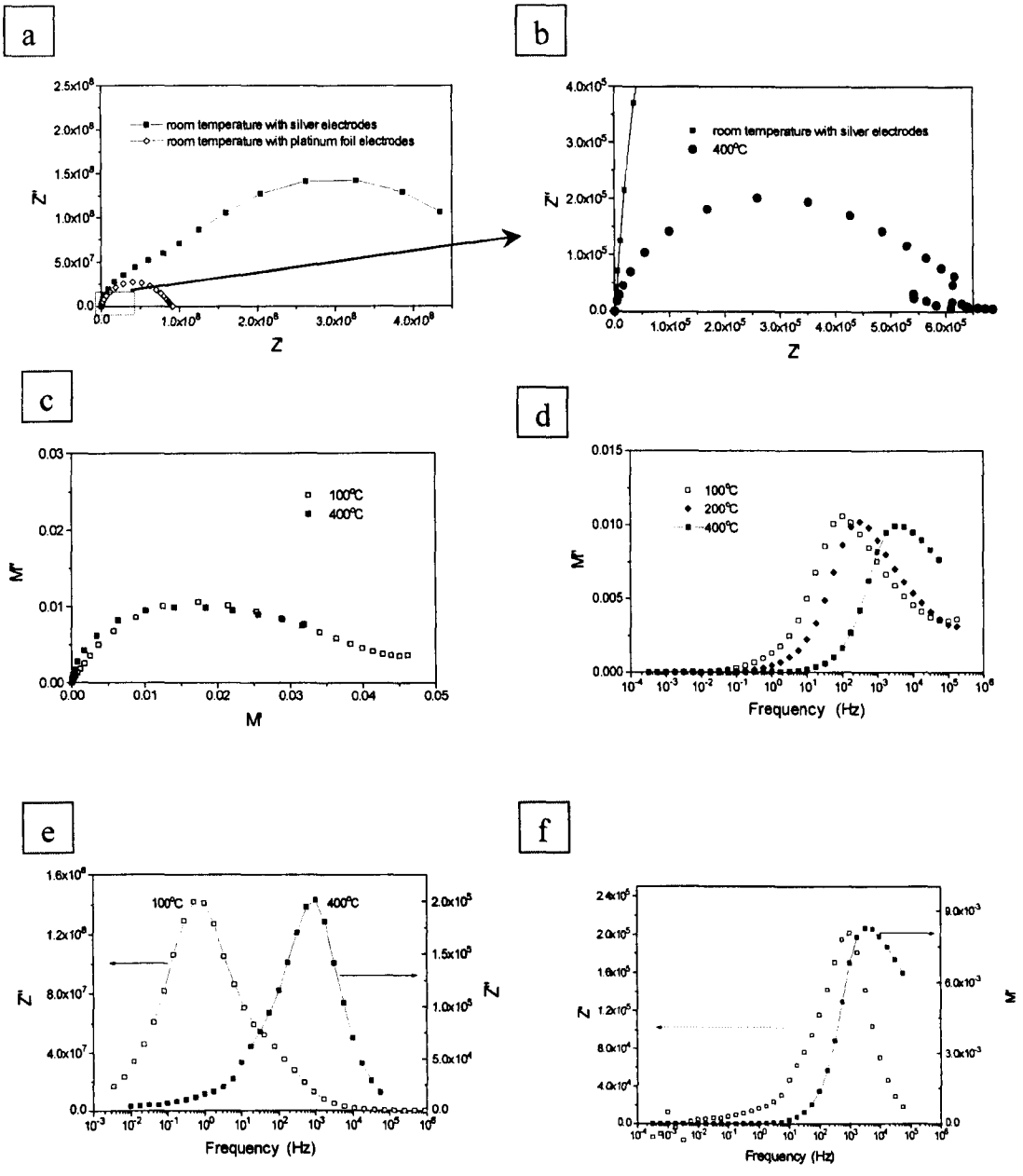

Figure 5-4 Impedance spectra of 20SA: (a) complex impedance plane plot; (b) a partly zoomed view of (a); (c) complex modulus plane plots; (d) modulus spectroscopic plots; (e) impedance spectroscopic plots, note the different scales of y-axis; (f) comparison of modulus and impedance spectroscopic plots

5.3.3 Impedance Spectra Of Oxidised Samples

5.3.3.1 Impedance Measurements At Room Temperature

Al_2O_3/SiC nanocomposites can be oxidised at elevated temperature in air. During oxidation, SiC is oxidised into silica and carbon dioxide.

$$SiC + 2O_2 = SiO_2 + CO_2 \uparrow \qquad (5\text{-}1)$$

Silica stays where it is produced by oxidation, or further reacts with alumina to form mullite (Luthra and Park, 1990), whereas carbon dioxide evaporates. Since SiC is a conductor, while SiO_2 and mullite are insulators, the electrical properties of the oxide layer are expected to be different from those of the bulk materials.

For the case of 20SA, there was a drastic increase of impedance after oxidation. As can be seen from Fig. 5-5a, at R.T, the Z'' peak of the sample that had been oxidised at 1100 °C for 1h was more than four orders of magnitude higher than that of the same sample without oxidation. In the meantime it has been noticed there are two fairly resolved arcs in the modulus spectra of the oxidised samples, as shown in Fig 5-5b&c.

It is also very interesting to note that not only the resolving of the arcs, but also the diameter of the low frequency arc depended on oxidation temperature and duration, as is shown in Fig. 5-5c.

Based on the above observation, we can confidently attribute the LF circular arc to the oxide layer formed after oxidation, while a HF semicircle is attributed to the bulk effect. The diameters were determined according to the criteria described in section 4.3.

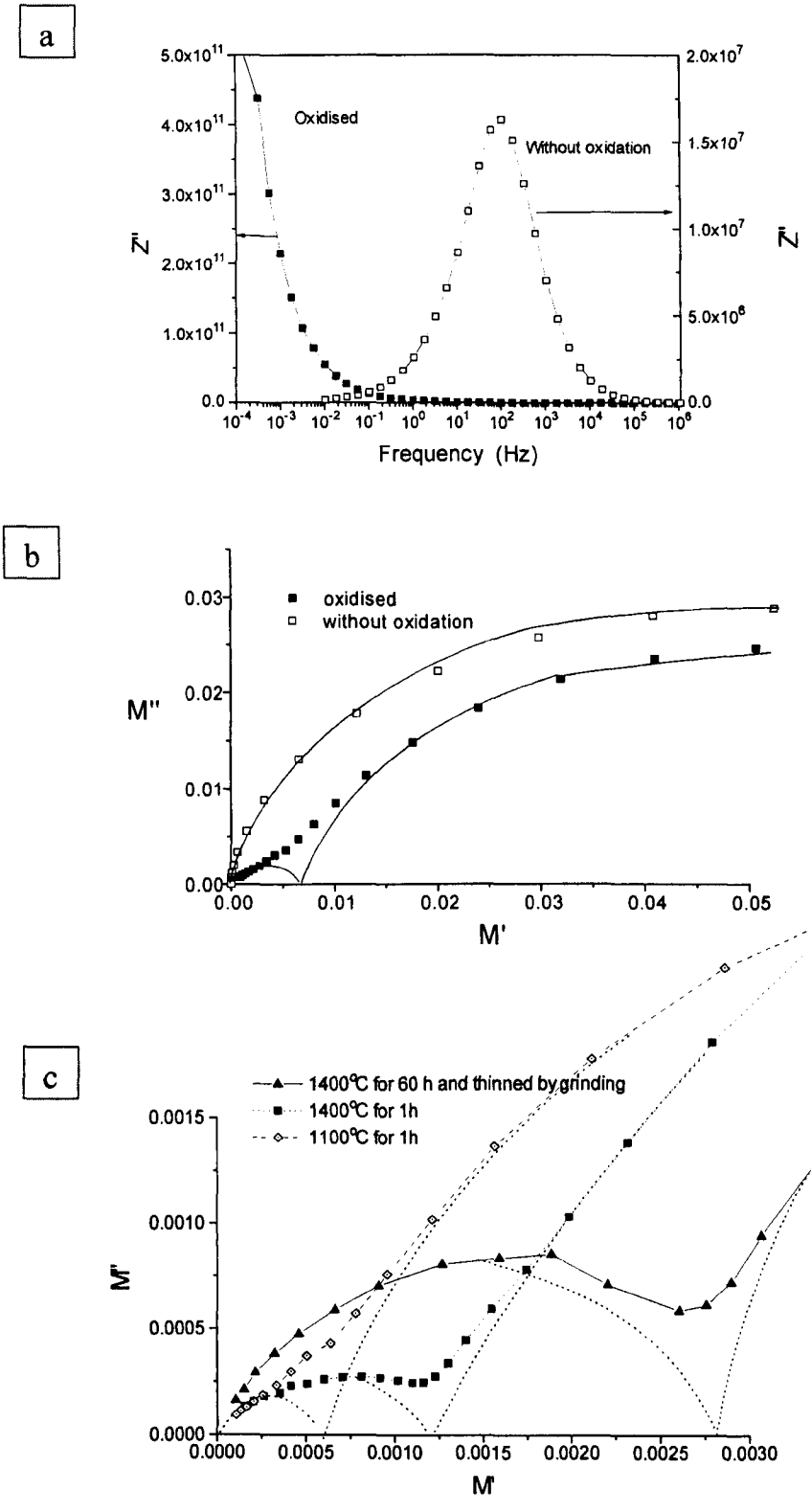

Figure 5-5 (a) Impedance spectroscopic plots for the samples with and without an oxidation treatment, please note the different scales used in y-axes; (b) modulus complex plane plots for the same samples; (c) the low frequency arcs for the samples oxidised under different conditions.

Table 5-1 gives a summary of semicircle diameters of both LF and HF for specimens oxidised at various temperatures. The diameter of the LF arc increases with an increase of oxidation temperature, whereas the diameter of the high frequency semicircle is nearly constant. This indicates that little change occurred in the bulk specimens, in contrast there was clearly a monotonic change of the oxide layer formed at the surface as a function of oxidation temperature.

Table 5-1 Semicircle diameters for 20SA oxidised for 1h at various temperatures.

Oxidation condition	LF semicircle diameter (D_{LF})	HF semicircle diameter (D_{HF})	D_{LF}/D_{HF}
800°C 1h	$2.5x10^{-5}$	$3.7x10^{-2}$	$6.8x10^{-4}$
950°C 1h	$1.0x10^{-4}$	$3.7x10^{-2}$	$2.7 x10^{-3}$
1100°C 1h	$3.0x10^{-4}$	$3.7x10^{-2}$	$8.2x10^{-3}$
1250°C 1h	$6.0x10^{-4}$	$3.6x10^{-2}$	$1.7x10^{-2}$
1325°C 1h	$1.2x10^{-3}$	$3.6x10^{-2}$	$3.4x10^{-2}$
1400°C 1h	$2.2x10^{-3}$	$3.5x10^{-2}$	$6.3x10^{-2}$

5.3.3.2 Impedance Measurements At High Temperatures

The impedance spectra of the oxidised 20SA at high temperatures are displayed in Fig. 5-6. The sample had been oxidised at 1100°C for 1h. It is important to note that the spectral resolution, i.e., the separation of semicircles in the complex impedance plots increased, while the spectral resolution in the complex modulus plots decreased as the measuring temperature was raised. At 200°C, the spectral resolution in the complex impedance plot (Fig. 5-6a) was very poor, but that in the complex modulus plots was better as shown in Figs. 5-6e-f. When the temperature increased to 400°C, there appeared two clearly resolved semicircles in the complex impedance plots in Fig. 5-6b, while the separation of semicircles in the complex modulus plots disappeared in Fig.5-6 e-f. At 600°C the spectral resolution was obviously better than that at 400°C, by comparing Fig5-6b with Fig. 5-6c. Meanwhile, the FWHM in modulus spectroscopic plots decreased with temperature.

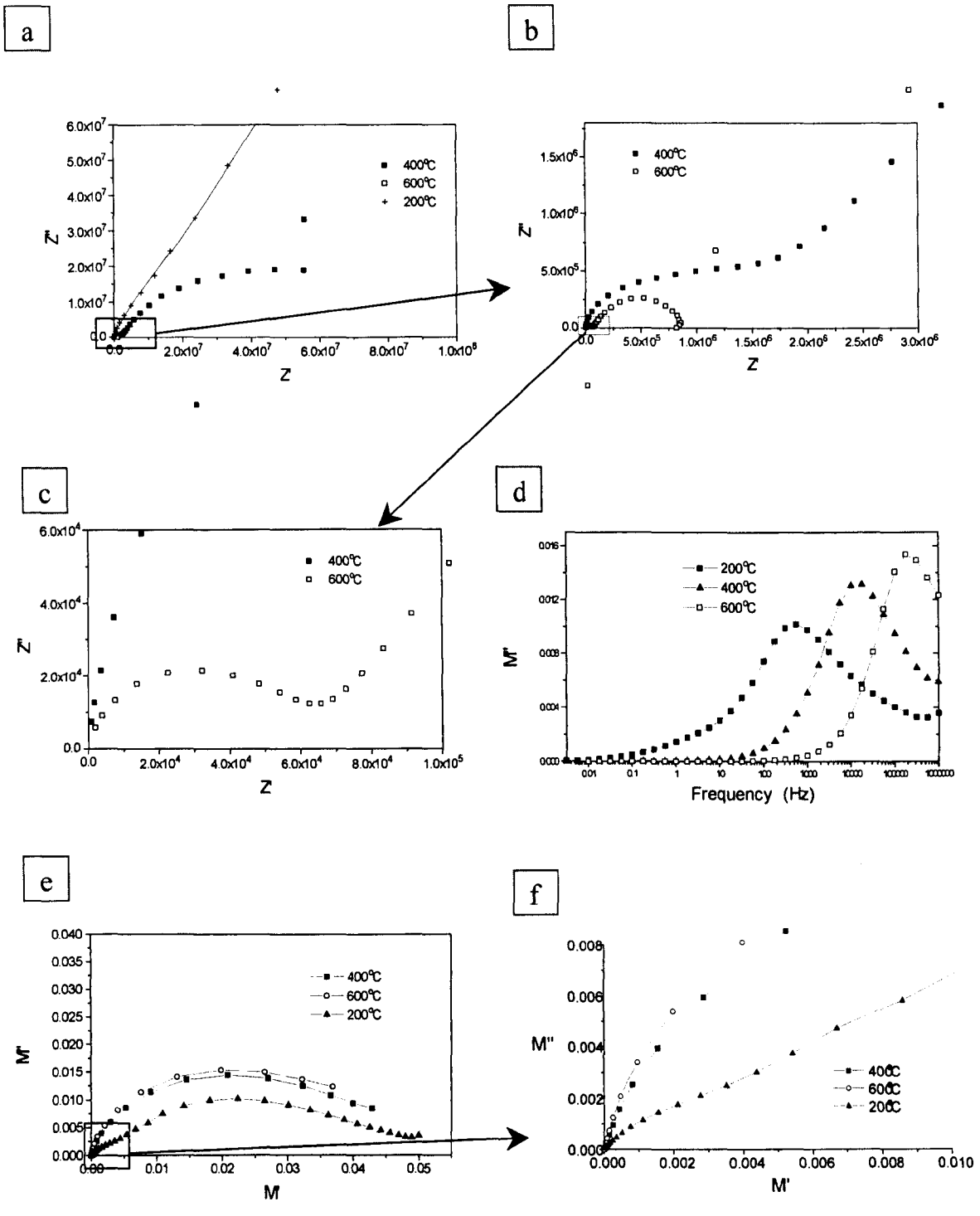

Figure 5-6 Impedance spectra of oxidised 20SA: (a), (b) and (c) complex impedance plots, note that (b) is a zoomed view of (a) and (c) is a zoomed view of (b); d) modulus spectroscopic plots; e) and f) complex modulus plane plots, (f) is a zoomed view of (e). The measuring temperatures are indicated in each figure.

5.3.4 Dielectric Properties At Room Temperature

As mentioned previously, it is difficult to measure the impedance of 5SA and 10SA materials at R.T, because of the extremely high resistance of these materials. In order to obtain a stable current from materials with an extremely high resistance to determine the dielectric properties of the 5SA and 10SA materials, impedance measurements were taken by connecting a 1GΩ resistor in parallel with the specimens as shown in Fig.5-7a. The capacitance of the resistor (3×10^{-12} F) is less than 10% of that of the 5SA and 10SA specimens (5×10^{-11} F) to be measured, while the resistance of the resistor (1GΩ) is much lower than that of the 5SA and 10SA specimens. The capacitive effect of this circuit is mainly contributed by the specimen, while conduction mainly occurs across the resistor in parallel with specimens. The modulus spectra of this circuit (Fig.5-7b) show that all semicircles have a depressed part at high frequency. The conduction of the circuit (the imaginary part of the electrical modulus) arises from the conduction of the resistor at lower frequency and conduction from the specimen at high frequency. Measurements of 10SA specimens without being connected to the resistor-generated spectra at high frequency as indicated in the amplified diagram in Fig.5-7b (denoted a). No spectra could be obtained at low frequency since the impedance at low frequency is too high to be detected. The increasing conductivity of specimens results in more depressed semicircles in the modulus spectra.

Fig. 5-7c shows the dielectric constants obtained from measurements shown in Fig.5-7b as a function of the content of SiC in the Al_2O_3 matrix. The small error bars indicate that the data are quite consistent with repeat measurements. The dielectric constant increases with increasing content of SiC in Al_2O_3. According to Fig.5-7c, the dielectric constant is 11.8 for pure Al_2O_3, which is a little higher than the value of 6-10.2 that can be found in the literature (Buchanan, 1991), which might be due to the edge effect.

a

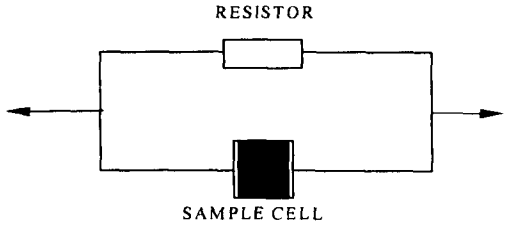

b

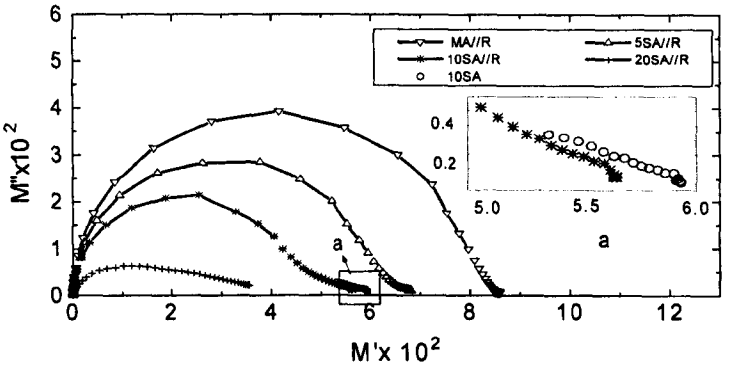

c

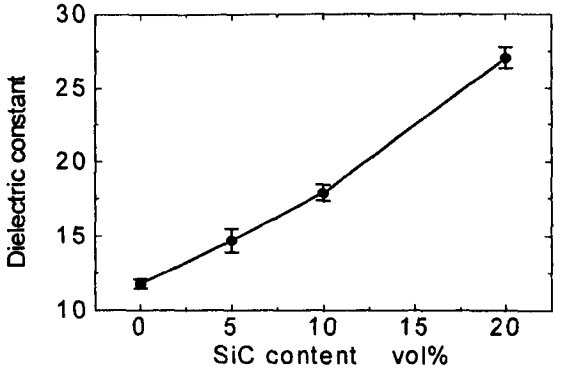

Figure 5-7 (a) A circuit with a resistor connected in parallel to the measured sample; the resistance of the resistor (R) is $1x10^9$ Ω, while its capacitance is about $2\sim4x10^{-13}$ F; (b) modulus spectra obtained at room temperature from measurements of the circuit shown in (a) with specimens containing different amounts of SiC; (c) dielectric constant as a function of SiC content, where the standard deviation is based on six sets of impedance measurements for each sample.

5.4 Discussion

5.4.1 Equivalent Circuit Models And IS Parameters

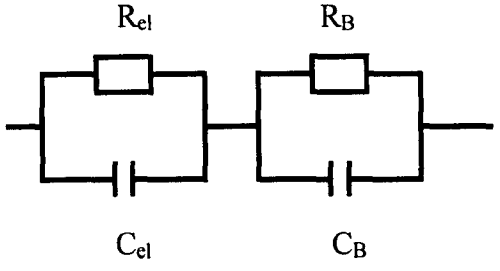

Figure 5-8 Equivalent circuit for monolithic alumina. Indices: el= electrode effect, B=bulk.

Our experimental results demonstrated that monolithic alumina (MA) gave a nearly ideal Debye response and there was only one semicircle attributed to the bulk effect (Fig.5-2). At high temperatures (say 800°C), a tail appears at low frequency in the complex impedance plane (Fig.5-2c). This is most likely due to the Schottky barrier in the material at the electrode / material interface. From this observation, the equivalent circuit of MA is supposed to be like the one given in Fig. 5-8. No grain boundary effect was seen in the impedance spectra, this might be either due to very thin grain boundaries in hot pressed MA materials, or because of the similar electrical properties of the grain boundary and grain. Therefore from the viewpoint of electrical properties, the MA is monolithic with little inhomogeneity. This also explains why MA exhibits a nearly ideal behaviour during impedance measurements.

Based on the microstructure of Al_2O_3/SiC nanocomposites(see Fig. 5-1), the equivalent circuit should be like that in Fig.5-9. Based on this model we may expect two semicircles, but the experimental results showed that all the Al_2O_3/SiC nanocomposites without an oxidation treatment had only one relaxation process in impedance spectra. The relaxation frequencies of 5SA and MA at various temperatures are listed in Table 5-2. The relaxation frequency does not change greatly when a small amount of SiC is incorporated. Therefore it can be assumed that the impedance spectra of 5SA and 10SA mainly reflect a response from alumina. No separate spectrum corresponds to the SiC,

because SiC is conductive and it is supposed to behave like an electrical connector. This situation can also be ascribed to the relaxation frequency of SiC which is much higher than the upper frequency limit of the impedance analyser (10^7 in this case).

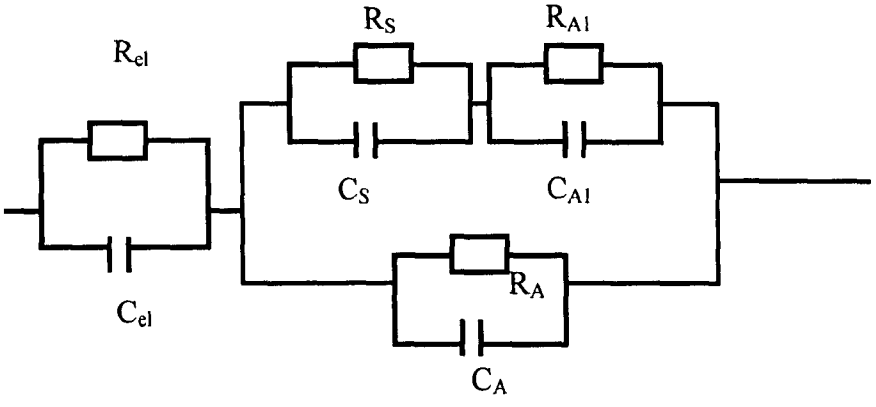

Figure 5-9 Equivalent circuit for alumina/silicon carbide nanocomposites. Indices: el= electrode effect, S=silicon carbide, A=alumina between electrodes, A1= alumina between SiC particles.

Table 5-2 Comparison of relaxation frequencies for MA and 5SA

Temperature (°C)	Relaxation frequency* of MA (Hz)	Relaxation frequency of 5SA (Hz)
400	2	7
600	60	400
800	500	5000

*** All the relaxation frequencies here are the frequencies corresponding to the Z'' peaks in impedance spectroscopic plots.**

The conductivity relaxation frequency (f) of a material can be calculated from:

$$f = \frac{1}{2\pi RC} = \frac{\sigma}{2\pi\varepsilon\varepsilon_o} \qquad (5\text{-}2)$$

where σ is the conductivity, ε is the dielectric constant of the material and $\varepsilon_0 = 8.85\times10^{-14}$ F/cm. The conductivity of SiC is about 10^{-4}~10^{-3} $(\Omega cm)^{-1}$ (Kingery *et al.* 1976c), while the dielectric constant of ceramics are normally about 5-20. Thus the relaxation

frequency of SiC can be calculated to be 1×10^{8}~ 2×10^{9} Hz. For this reason the relaxation of SiC cannot be detected in the frequency range for IS measurements, which is normally 10^{6}~10^{-4} Hz.

However for the case of 20SA, the relaxation frequencies were much higher than those of MA, 5SA and 10SA. For example at 400°C, the relaxation frequency of 20SA was 900 Hz, more than two orders of magnitude higher than those of MA and 5SA at the same temperature. This implies the conduction mechanism in this material might be different from other materials.

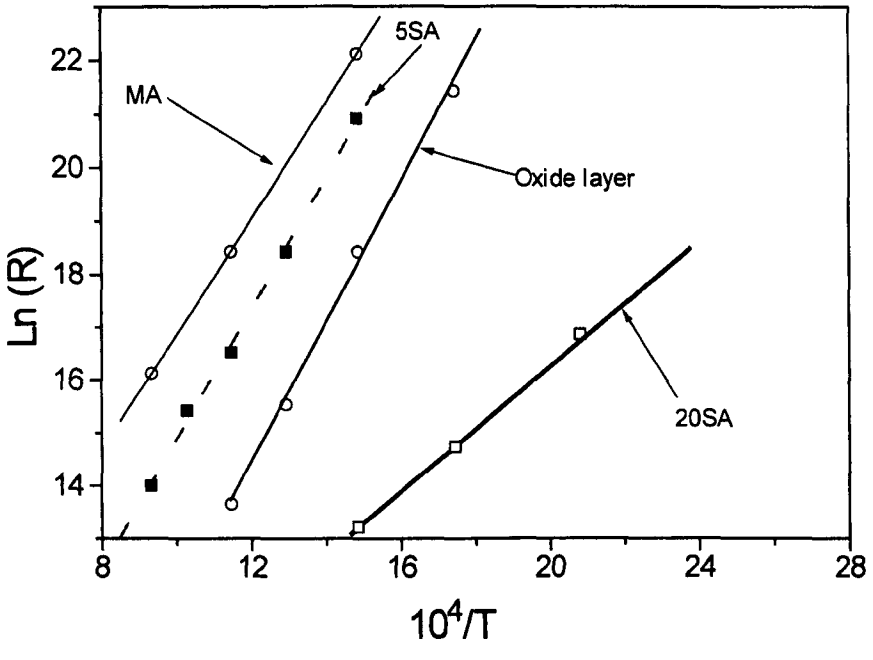

Figure 5-10 Arrhenius plot of resistances for different materials

Fig.5-10 shows the Arrhenius plots of the resistances of 20SA, 5SA and MA as well as the oxide layer formed at the surface of 20SA, where we can see that the linear slopes are similar for all the cases except for bulk 20SA. According to the linear slopes in the Arrhenius plots, the activation energies of electrical conduction can be calculated as shown in Table 5-3, where we can see the activation energy for the 20SA specimen is only about half of those for other materials.

Table 5-3 Activation energies for different materials

Materials	MA	5SA	Oxide layer	Bulk of 20 SA
Activation energy (eV)	0.93	1.05	1.12	0.49

The low activation energy and high relaxation frequency may be due to the percolating network of SiC formed in the alumina matrix when the SiC content is 20 vol%.

When a composite is composed of insulator as a matrix and conductor as a filler, the overall electrical behaviour of the composite is governed by percolation behaviour through the formation of a continuous network of conductive particles in the insulating matrix. It has been observed that there exists a threshold filler volume fraction, f*, above which the conductive filler forms a continuous network. When the fraction of the filler is close to f*, the resistivity changes drastically. The threshold volume fraction strongly depends on the particle sizes and particle distribution (Kim *et al.* 1998).

In the Al_2O_3/SiC nanocomposites, the grain size of alumina (R_A) is about 3μm, while the grain size of SiC particles (R_S) is about 200 nm (refer to Fig.5-1). So the ratio of R_A/Rs is about 15. If all of the SiC particles are located at grain boundaries, the threshold volume percentage can be estimated to be about 10 vol% according to Kim *et al.* (1998). In the present Al_2O_3/SiC nanocomposites, not all of the SiC particles are segregated at the grain boundaries. It may be reasonable to assume that the threshold volume percentage is between 10 vol% to 20 vol%.

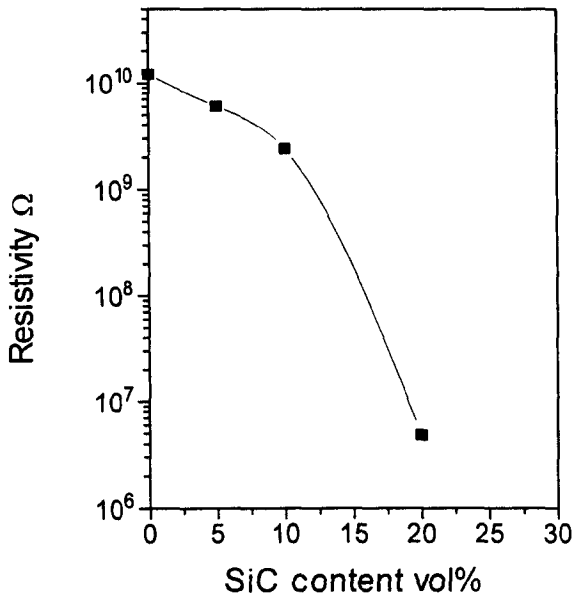

Fig.5-11 Resistivity at 400 °C of the alumina/silicon carbide nanocomposites as a function of SiC content.

Fig.5-11 shows the resistivity of the Al_2O_3/SiC nanocomposites at 400 °C as a function of SiC content. The composite shows a more significant change in resistivity when the SiC content is increased from 10 vol% to 20 vol%. At the same time, the mapping of the silicon element in Al_2O_3/ SiC nanocomposites illustrated that SiC particles were clustered in the alumina matrix and these clusters are more densely populated in 20SA (Fig.5-12b) as compared to 5SA (Fig.5-12a). This may imply that the threshold volume percentage for the Al_2O_3/SiC nanocomposites with a microstructure as in Fig. 5-1 is between 10vol% to 20 vol%. The formation of the percolation of SiC particles can explain why 20SA is distinctive in conductivity and relaxation frequency as compared with the composites with lower SiC content.

a

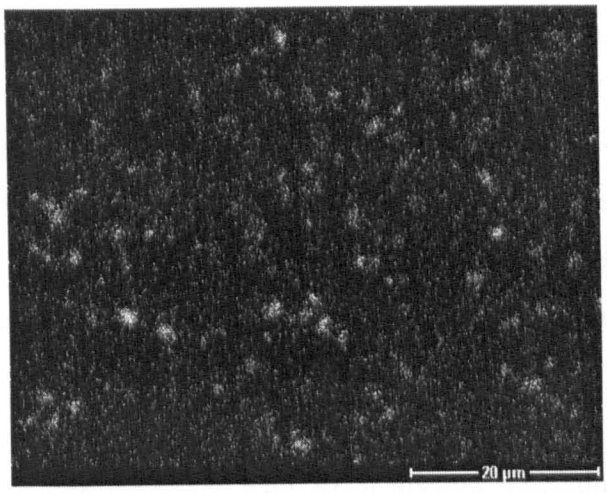

b

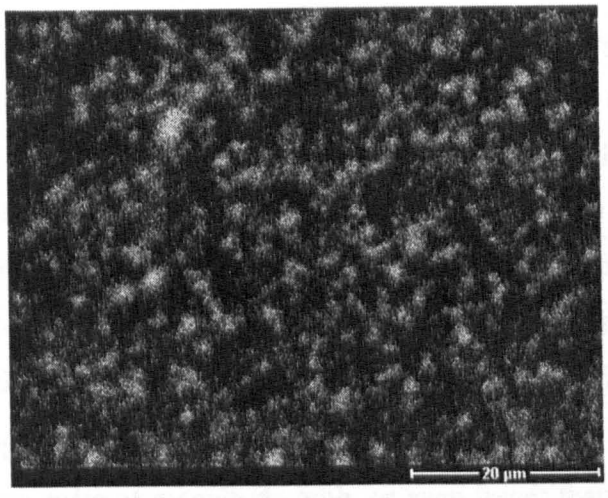

Figure 5-12 Silicon element mapping of SiC phase in a) 5SA and b) 20SA, where white pixels represents the silicon content in the alumina matrix.

5.4.2 Spectral Resolution

Spectral resolution is an important factor when different physical processes need to be de-convoluted. As discussed in chapter 4, the spectral resolution in the modulus spectra depends on the difference in resistances. Based on Figs. 5-6 a-c, the ratio of the resistance of the oxide layer (R_{ox}) to that of the bulk (R_{Bu}) was calculated to be 50 and 12 respectively at 400°C and 600°C. According to these data, the ratio of R_{ox} /R_{Bu} was calculated to be 900 at 200 °C, by assuming the activation energies of the oxide layer and the bulk are constant in the range of 200~400°C. Therefore it can be understood that the better resolution in the modulus spectra at lower temperatures was a consequence of larger difference in resistances. For an ideal case, as has been discussed in chapter 4, when the resistance ratio is larger than 25, a distinct resolution should appear in the modulus spectra. However, current experimental results indicate that for a non-ideal case such as 20SA, the resistance difference needs be greater than 50 to get a resolved spectrum.

On the other hand, the spectral resolution in the impedance spectra not only depends on the difference between capacitances as has been pointed out in chapter 4, but also is associated with the conductivities of different microstructural components in the material. The higher the conductivities, the better resolved are the spectra. According to the analysis presented in chapter 4, whether or not the responses from different microstructural factors can be resolved in impedance spectrum depends on how well the conditions specified in Eqs 4-9 a-b, i.e., $R_i/(1+\omega/\omega_i)\Rightarrow 0$, are fulfilled. Eqs. 4-9 a-b are obviously better approximated when R_i is smaller, given ω_i to be constant. If R_i is very large and in the same order of magnitude with, or even larger than the ω/ω_i in value, we can see that Eqs.4-9 a&b will never be fulfilled, and therefore the spectrum will never be resolved. As we can see from Figs. 5-6 a-c, the impedance spectra were shown to be better resolved at higher temperatures, because the conductivities of both the bulk and oxide layer increase with temperature. This is a reason why IS is more powerful in characterising a material that has a reasonable conductivity. It is impossible for IS to distinguish the electrical responses from different microstructural factors if the material is totally insulating.

5.4.3 Dispersion Of Electrical Responses

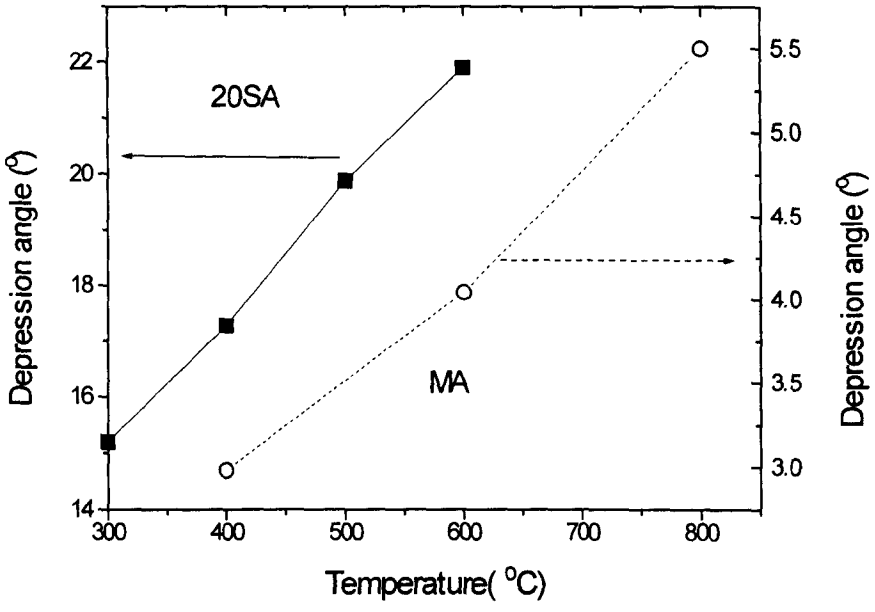

Figure 5-13 Dependence of depression angle of MA and 20SA on the temperature.

As discussed in the literature review (Chapter 2), the non-ideality of a response from a real material, i.e., the distribution of relaxation times, or a dispersion of electrical response, depends on either chemical, or physical or geometrical inhomogeneities in the material. The extent of departure from an ideal response can be expressed by a depression angle (α) of the semicircle in the complex impedance plot or the exponential index (n) in a CPE. The larger the depressed angle (i.e., the smaller the n value), the greater the dispersion. The departure from ideality also results in the broadening of the Z'' and M'' peaks in spectroscopic plots and the displacement of M'' peaks from corresponding Z'' peaks.

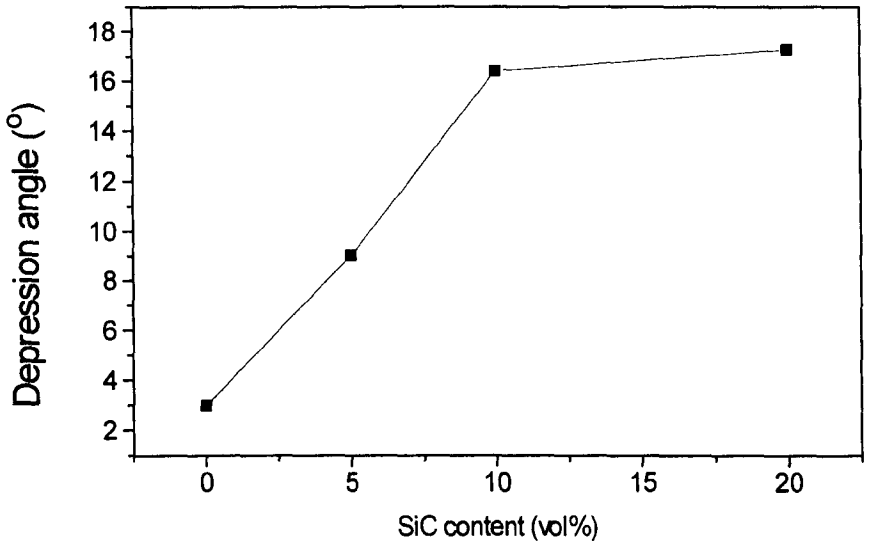

Figure 5-14 Depression angle at 400°C of Al_2O_3/SiC nanocomposites as a function of the SiC content.

Based on the understanding detailed in section 2.7, the depression angle α is related to exponential index n by the equation: $\alpha=(1-n)\ \pi/2$, whereas the exponential index, n, can be obtained by simulation using 'Zview' software. Here the depression angle of the Al_2O_3/SiC nanocomposites depends not only on the temperature, but the SiC loading as well. Fig. 5-13 demonstrates a strong dependence of the depression angle on the measuring temperature. The dispersion increases with increasing temperature, this is probably because at high temperatures more heterogeneities are activated which make the conductivity relaxation times more distributed. The variation of depression angle as a function of the SiC content is shown in Fig.5-14. The depression angle increases as the SiC content increases. The increase in the dispersion of composites probably mainly results from the incorporation of impurities, i.e., the increase in chemical inhomogeneity. The impurity substance that is most likely introduced is SiO_2. It is well established that there is always a thin layer of SiO_2 formed at the surface of SiC particles, thus SiO_2 can

be introduced as a kind of impurity as a consequence of an addition of SiC particles into the alumina matrix. The higher the SiC loading in composites, the more the SiO_2 is introduced, then the more dispersed the materials will become. As mentioned earlier, the SiC phase behaves like a conductive connector, so it is not expected to change the distribution of the relaxation times of the materials.

5.4.4 Dependence Of Dielectric Response On SiC Content

Experimental results showed there was a strong correlation between modulus spectra and the content of SiC in the Al_2O_3 matrix as shown in Fig.5-7, indicating that modulus spectroscopy can be used to determine the content of the conducting phase in an insulating matrix nondestructively.

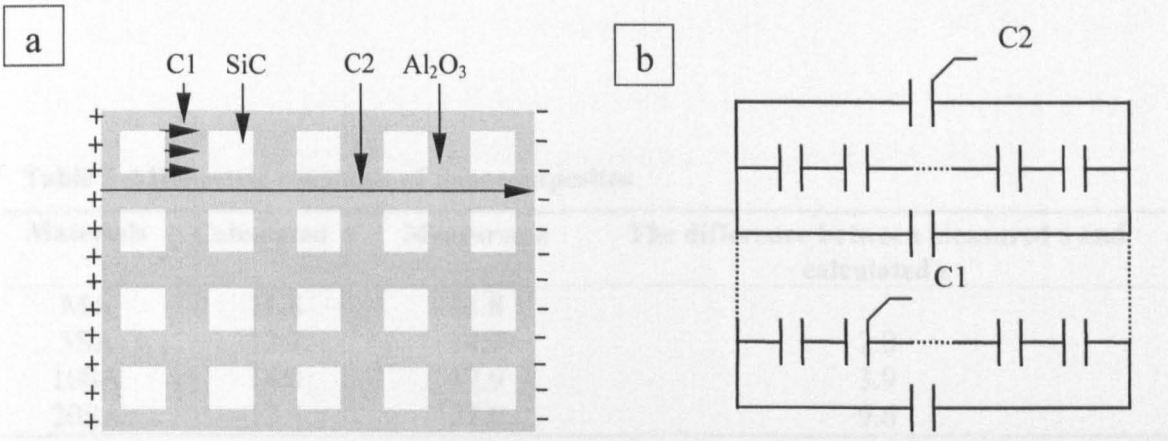

Figure 5-15 a) The idealized microstructure of the SiC/Al_2O_3 composites and b) its equivalent circuit model.

To simulate the dielectric property of the composites containing both conductive and insulating materials, the microstructure of the Al_2O_3/SiC nanocomposites is simplified as cubic units packed as shown in Fig.5-15a where SiC cubes are packed inside Al_2O_3 uniformly. The conductive SiC cubes behave as connection lines between capacitors with Al_2O_3 as the dielectric material. Where there is no SiC present along the electrical field direction, Al_2O_3 behaves as a capacitor with small area but large thickness. There is no edge effect being considered in this case. SiC cubes are assumed to be of uniform size inside the Al_2O_3. Assume the particle size of the SiC (i.e. each edge of the SiC cubes) is

l, the volume percentage of the SiC particles in the alumina matrix is V_{pct}. Based on the model in Fig. 5-15, the dielectric constant of the composite, ε, i.e. the capacitance of a cubic configuration of 1cm by 1cm by 1cm is derived as:

$$\varepsilon = \varepsilon_o(1 + \frac{\sqrt[3]{V_{pct}^2}}{1-\sqrt[3]{V_{pct}}} - \sqrt{V_{pct}^2}) \quad 5\text{-}3$$

where we can see the dielectric constant of the composites is independent of the SiC particle size, because the edge effect is neglected here.

As the dielectric constant of the matrix (Al_2O_3), ε_o was determined to be 11.8 in Fig.5-7c, the dielectric constants (ε) of the composites containing different volume percentage of the SiC particles can be calculated according to Eqn. 5-3 and these values are shown in Table 5-4.

Table 5-4 Dielectric constants of nanocomposites

Materials	Calculated ε	Measured ε	The difference between measured ε and calculated ε
MA	11.8	11.8	-
5SA	12.7	14.7	2.0
10SA	14.0	17.9	3.9
20SA	17.4	27.0	9.6

Apparently the predicted data are lower than the experimental data because this model is too simplified to give an accurate prediction of the capacitance of the composites. Factors such as the irregular shape, non-uniform distribution of SiC particles and edge effects have not been taken account in this model, so further work is needed to predict the capacitance of the Al_2O_3/SiC composites accurately.

5.4.5 Nondestructive Detection Of Oxide Layer In Al_2O_3/SiC Nanocomposites

Previous research on the oxidation of SiC/Al_2O_3 composites was carried out at temperatures above 1300°C because it is difficult to use weight gain measurements or

electron microscopy for characterising the oxide scales formed at lower temperatures (Luthra and Park, 1990; Sciti and Bellosi 1998). In the present study modulus spectroscopy was used to examine oxide scales formed at temperatures from 800 to 1400°C. The thickness of oxide scales can be predicted from the measurements of modulus spectra. For a sample of thickness t with an oxide layer of thickness δ at its surface (Fig5-16a), the equivalent circuit is like a series layer model (Fig.5-16b).

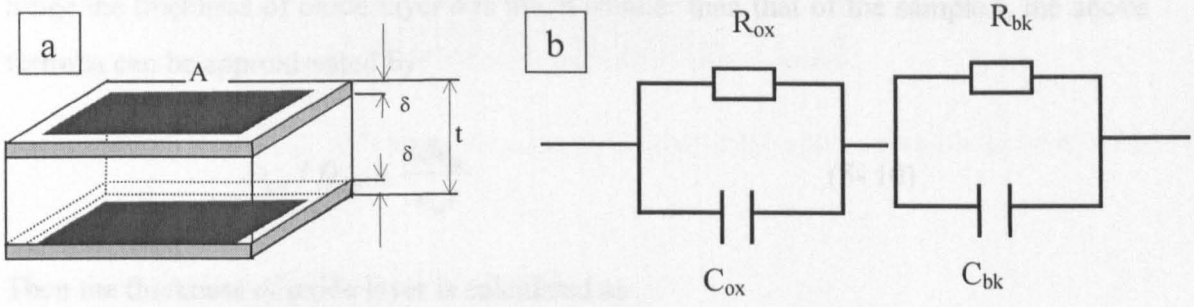

Fig. 5-16 SiC-Al_2O_3 composite of thickness t with an oxidation layer of thickness δ, 'A' representing the electrode area. Indices: ox=oxidation layer, bk=bulk of 20SA.

Here, we can have:

$$C_{ox} = \frac{\varepsilon_{ox}\varepsilon_o A}{2\delta} \qquad (5\text{-}4)$$

$$C_{bk} = \frac{\varepsilon_{bk}\varepsilon_o A}{t - 2\delta} \qquad (5\text{-}5)$$

$$C_o = \frac{\varepsilon_o A}{t} \qquad (5\text{-}6)$$

where C_{ox}: capacitance of the oxide scale; C_{bk}: capacitance of the bulk specimen without the oxide scale; C_o: capacitance of empty space occupied by the specimen.

The low frequency (LF) semicircle diameter is given by

$$D_{LF} = C_e / C_{ox} = \frac{2\delta}{\varepsilon_{ox} t} \qquad (5\text{-}7)$$

The high frequency (HF) semicircle diameter is given by

$$D_{HF} = C_e / C_{bk} = \frac{t - 2\delta}{\varepsilon_{bk} t} \qquad (5\text{-}8)$$

The ratio of the LF semicircle diameter to HF semicircle diameter is given by:

$$D_{LF} / D_{HF} = \frac{2\delta\varepsilon_{bk}}{\varepsilon_{ox}(t - 2\delta)} \qquad (5\text{-}9)$$

Since the thickness of oxide layer δ is much smaller than that of the sample t, the above formula can be approximated by:

$$D_{LF} / D_{HF} = \frac{2\delta\varepsilon_{bk}}{\varepsilon_{ox} t} \qquad (5\text{-}10)$$

Then the thickness of oxide layer is calculated as

$$2\delta = \frac{\varepsilon_{ox} t}{\varepsilon_{bk}} (D_{LF} / D_{HF}) \qquad (5\text{-}11)$$

where t ,ε_{ox} and ε_{bk} can be assumed to be unchanged during oxidation. The values of D_{LF}/D_{HF} are listed in Table 5-1.

The dielectric constant of the 20SA sample was determined as 27.0 (Table5-4). According to Eqn. 5-11, ε_{ox} can be obtained if the thickness of the oxide scale is known. Fig. 5-17 shows an optical micrograph of the cross-section of oxide scales formed at the surface of the 20SA sample, which had been oxidised at 1400°C for 64h. The bright phase layer is the mullite/alumina composite and the dark phase layer is mainly alumina (Luthra and Park, 1990; Sciti and Bellosi, 1998)). Alumina and mullite have similar dielectric constants (6.2~6.8 for mullite and 6~10.2 for alumina) (Buchanan, 1991). SEM observations showed a large amount of porosity in the surface layer.

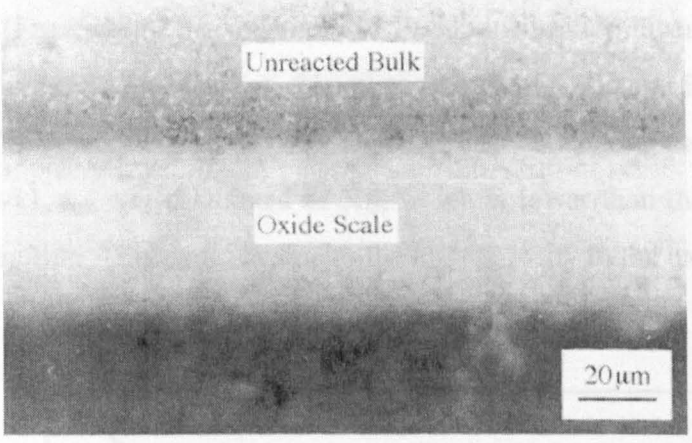

Fig. 5-17 Optical micrograph of cross-section of sample 20SA after oxidation at 1400°C for 64h.

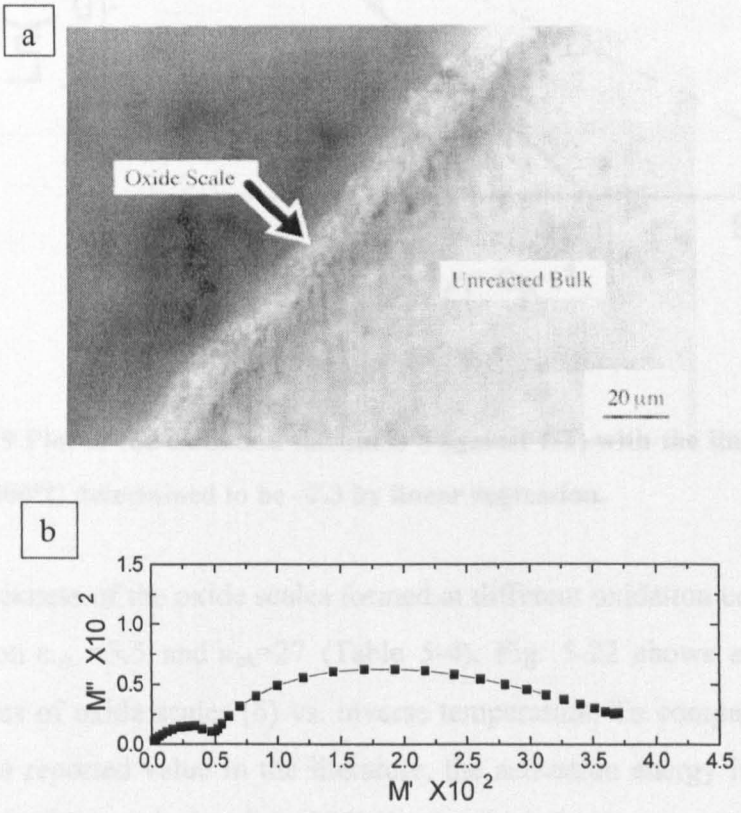

Fig. 5-18 (a) optical micrograph (b) modulus spectrum of the 20SA sample after oxidation at 1400°C for 64h. The oxide scale thickness was reduced to ~20μm by polishing.

The oxide layer on one of the faces of this sample was totally removed, meanwhile the oxide scale on another face was thinned by polishing. According to the optical micrograph (Fig. 5-18a), the thickness of the thinned oxide layer was determined to be 20μm. The overall thickness of this plate sample is 1.1mm. Based on the modulus spectrum of this sample (Fig. 5-18b), D_{LF}/D_{HF} was obtained approximately as 0.15. By using Eqn.5-11, ε_{ox} was calculated as 3.5, which is lower than the dielectric constant of alumina or mullite. This could be due to the high porosity in the oxide scale.

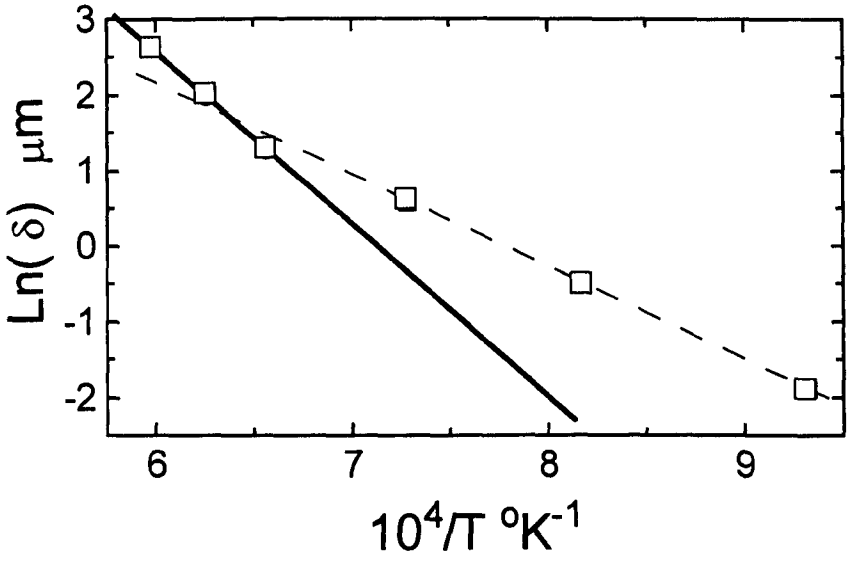

Fig. 5-19 Plot of the oxidation thickness δ against 1/T, with the linear slope in the range of 1250-1400°C determined to be –2.3 by linear regression.

The thickness of the oxide scales formed at different oxidation conditions was calculated based on ε_{ox} =3.5 and ε_{bk}=27 (Table 5-4). Fig. 5-22 shows a plot of the calculated thickness of oxide scales (δ) vs. inverse temperature. To compare the activation energy with the reported value in the literature, the activation energy in the temperature range 1250-1400°C is calculated as 378kJ/mol, which is close to the reported value of 450 kJ/mol (Luthra and Park, 1990). The thickness of the oxide scales is very difficult to measure using SEM due to the low contrast in the image between the oxide scale and the substrate. Meanwhile it is also very difficult to measure the thin oxide scale using optical microscopy, whereas IS is sensitive to a very thin oxide scale that is formed at as low

temperature as 800°C. Therefore, IS is a powerful tool for determining oxide growth due to oxidation of ceramics.

5.4.6 The Effect Of Particle Orientation On IS

In composite materials, the preferential orientation of the dispersed particles is unavoidable during the manufacture, if they are non-equiaxed, e.g., in plate or fibre form. The orientation of fibres or plates in composites is an important issue, because it leads to anisotropy in both mechanical and electrical properties of the materials. IS has been found to be sensitive to the content of conductive SiC particles. Likewise IS may be also sensitive to the orientation of particles.

Since SiC particle in Al_2O_3/SiC nanocomposites are equiaxed, to investigate the dependence of IS on the orientation of the dispersed conductive phase in an insulator matrix, the clay/graphite composites containing different amount of flaky graphite were fabricated for impedance measurements. As shown in **Appendix III,** the experimental results clearly show that in the direction parallel to the orientation of the particles, the resistance was lower and dielectric constant was higher.

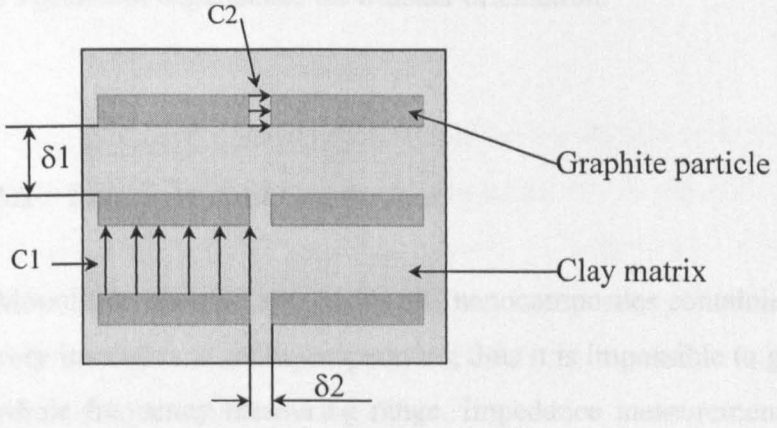

Fig.5-20 An idealised model for clay/graphite composites.

To explain this phenomenon, an idealised model is given in Fig. 5-20 for the clay/graphite composites. The graphite particles are assumed to be in the form of a

square plate. The average distance between conductive particles is shorter in the lateral direction than in normal direction ($\delta 1 > \delta 2$), then the probability of forming a continuous path along the lateral direction is higher than in the normal direction, thus the conductivity is higher in the lateral direction.

The explanation for the higher dielectric constant in the lateral direction is not so straightforward. Based on the idealised model, the dielectric constant should be the same along both directions. However, as mentioned in the previous section, factors such as the irregular shape, non-uniform particle distribution and edge effects will also have effects on the dielectric constant. The difference between measured ε and calculated ε can be considered to be an extra contribution from these factors which cannot be explained by the idealised model. As can be seen in Table 5-4, the extra contribution increases with SiC loading, i.e., it increases as the distance between particles is decreased. This can be used to explain the observation of higher dielectric constant in the lateral direction.

Form the viewpoint of NDC, the significance of this finding is that we can use the IS technique to detect non-destructively the orientation of conductive particles in composite materials. Recently a study (Wang *et al.* 2000) has been published on the effect of whisker orientation on the electrical properties of Si_3N_4/SiC whiskers composites. Similarly to the results presented here, it was found that the impedance spectra exhibited a significant dependence on whisker orientation.

5.5 Summary And Conclusions

Monolithic alumina and Al_2O_3/SiC nanocomposites containing small amounts of SiC are very insulative at room temperature, thus it is impossible to get measurable signals in the whole frequency measuring range. Impedance measurements have to be made at high temperatures to obtain a full spectrum in the whole frequency range.

Al_2O_3/SiC nanocomposites exhibit only one relaxation process. The conductive SiC phase dispersed in the alumina matrix does not have a corresponding semicircle in the

impedance spectra because it has a very high relaxation frequency (outside the measuring range of the instrumentation used here).

The response of monolithic alumina is very close to an ideal Debye response, while Al_2O_3/SiC nanocomposites exhibit considerable frequency-distribution. The depression angle in the complex impedance plane shows a clear increasing trend as the SiC content is increased. As the electrical response becomes more distributed, Z'' and M'' peaks in the spectroscopic plot become broader, and the M'' peak is separated further from the Z'' peak.

20SA has distinctive electrical properties as compared to those with lower SiC loading, which is attributed to a percolating network of SiC particles formed in the material. The activation energy of 20SA is much lower than that of MA, 5SA, and the oxide layer, indicating that 20SA has a distinctively different conduction mechanism from the other materials.

There were two relaxation processes in the impedance response after 20SA is oxidised, one of which corresponds to the bulk effect, the other is from the oxide layer. The resolution of the modulus spectra at low temperature is better, due to a larger difference in resistance between the bulk and oxide layer at low temperatures. By contrast, the impedance spectra are better resolved at high temperatures because of the higher conductivity.

The effect of the SiC in composites on the dielectric properties of the composite was examined by room temperature measurements. A microstructural model was developed to calculate the dielectric properties of composites with insulating matrices and conductive inclusions. Impedance spectra strongly depend on the orientation of conductive particles, a similar microstructural model was used to explain the effect of the orientation of conductive particles.

Oxidation kinetics of 20SA was examined by room temperature measurements. The activation energy was determined to be 378kJ/mol, which is close to the reported value using other methods. The oxide growth was predicted based on models developed for calculating capacitance of multi-layer structures.

This study demonstrates that IS is a useful technique for non-destructive evaluation of ceramic composites with insulating matrices and conductive inclusions.

6 Nondestructive Characterisation Of Thermal Barrier Coatings Using IS

6.1 Introduction

Thermal barrier coatings (TBCs) have been extensively applied to engine components to allow engines to operate at higher temperatures; hence achieving higher thrusts and greater thermodynamic efficiency of the engine (Lee *et al.* 1996). Due to its low thermal conductivity and comparatively high thermal expansion coefficient, together with its chemical and thermal stability, yttria stabilised zirconia (YSZ) has been widely used as a thermal insulating material (Bartlett and Maschio, 1995; Sergo and Clarke, 1998; Wolfe and Singh, 1998).

A TBC normally consists of a top coat of YSZ and a bond coat typically of the formula MCrAlY where M represents either Co, Ni or Fe. As an oxygen ion conductor at high temperature, the YSZ top coat does not block the oxidation of the underlying bond coat. A protective alumina layer forms at the interface between the bond-coat and the YSZ due to oxidation of the bond coat at high temperature (Tawancy *et al.* 1998). Therefore, the bond coat between YSZ and the substrate superalloy is designed not only to promote adhesion of the YSZ to the substrates, but also to provide oxidation resistance (Meier and Gupta, 1994).

The oxidation of the bond coat is a dominant factor leading to the failure of TBCs (Demasi-Marcin *et al.* 1990; Wu *et al.* 1989). As the oxidation proceeds, more and more aluminium element diffuses outward to the bond coat/YSZ interface to form an alumina layer. When the aluminium in bond coat is being depleted, other elements, such as chromium and nickel, can be oxidised at the same time, and then form mixed spinel phases. The spallation of YSZ was found to be associated with the phase conversion of the initially-formed α-alumina to a mixed spinel phase (Wu *et al.* 1989; Schillington and Clarke, 1999), one of the reasons is that the interfacial fracture resistance of the TBC/spinel interface is lower than that of the TBC/α-Al_2O_3 interface (Schillington and Clarke, 1999).

As the alumina layer grows to a certain thickness, usually about 10μm, the TBC fails, either at the bond coat /YSZ interface or in the YSZ close to the interface due to thermal mismatch between the alumina layer and the bond coat. Failure of TBCs will expose the underlying metallic components to hostile environments, which might result in a catastrophic failure of the component. For application of TBCs on engine components, it is vital to predict the coating lifetime which is controlled by this oxide growth at the bond coat/YSZ interface. Finding a method of measuring and monitoring the thickness of the oxide layer non-destructively will provide a way of predicting the lifetime of TBCs; hence avoiding unexpected failure of TBCs and prevent any disastrous consequence.

By making impedance measurements at 469K, Ogawa *et al.* (1999) found that impedance spectra were sensitive to the thickness of different layers in TBCs. In the present work, impedance measurements were made at room temperature and 350°C in order to monitor the oxide growth in TBCs due to oxidation at 1100°C for a period up to 1500hr. At a measuring temperature of 350°C, YSZ is a moderate ionic conductor whereas the alumina layer is a good insulator. The large difference in electrical properties of the alumina and YSZ lead to a distinction of the electrical response of the alumina layer from that of YSZ in the impedance spectra of TBCs. In order to examine the detailed microstructure of TBCs after oxidation, different equivalent circuit models representing different microstructures of TBCs were established to simulate impedance spectra of TBCs after oxidation for different periods.

6.2 Experimental Procedure

6.2.1 Specifications Of Materials

Table 1 The Composition of Haynes 230 Alloy (wt%)

Ni	Cr	W	Mo	Fe	Co	Mn	Si	Al	C	La	B
57**	22	14	2	3*	5*	0.5	0.4	0.3	0.10	0.02	0.015*

*maximum, ** as balance.

The Haynes 230 alloy (for composition see table 1) with a thickness of 2mm was sprayed with a HVOF MCrAlY bond coat (38.5 wt%Co-32 wt%Ni-21 wt%Cr-8 wt%Al-0.5

wt%Y) and a Metco 204 NS TBC top coat (8 wt% yttria stabilised zirconia) at Sermatech, Lincoln, UK.

6.2.2 Oxidation Treatment

The plates with thermal barrier coatings were cut into 10 mm × 10 mm squares with a precision diamond cutting saw at low speed to avoid any mechanical damage to the coating layers. The samples were placed in a chamber furnace at 1100°C for periods ranging from 2 h to 1500 h. The heating and cooling rates were 3 K•minute^{-1} and 15 K•minute^{-1} respectively. Four samples for each oxidation time were prepared, of which one sample was examined by SEM coupled with energy dispersive x-ray spectroscopy (EDS) and the remaining three samples were used for impedance measurements.

6.2.3 Impedance Measurements

The measurement cells were about 10mm x 10mm x 2mm in size, which were obtained by painting silver electrodes on the top coat (YSZ). The painted area was 9mm x 9mm and was 1mm away from the edge to avoid possible current leakage. The substrate (Haynes 230 alloy) acted as the other electrode. Impedance measurements were made at room temperature and 350°C in air. Data were recorded over frequency ranges of 10^6 down to 10^{-3} Hz with 5 readings per decade, using a 1 Vrms signal. To ensure the steady state of the specimen, impedance measurements were made after the samples had been placed in a furnace at 350°C for 30 minutes. ZView Impedance Analysis software (Scribner Associates, Inc.) was used to simulate the impedance spectra based on equivalent circuit models.

6.3 Results

6.3.1 Microstructure Of TBCs

There were two coating layers in the as-received TBCs samples: the top coat and bond coat, as shown in Fig. 6-1a. The top coat was about 300 μm in thickness, while the bond coat was about 100 μm thick. The typical as-sprayed top coat exhibited about 10-15

vol% porosity (Haynes *et al.* 1996) and the t'-phase zirconia in the top coat has a micro-cracked structure (Miller *et al.* 1981 & 1983). For this reason we observed there were a lot of pores and small cracks in the top coat. By contrast, the bond coat was fully dense. After oxidation at 1100°C, an oxide layer was formed at the interface between the top coat and bond coat, as shown in Fig. 6-1b.

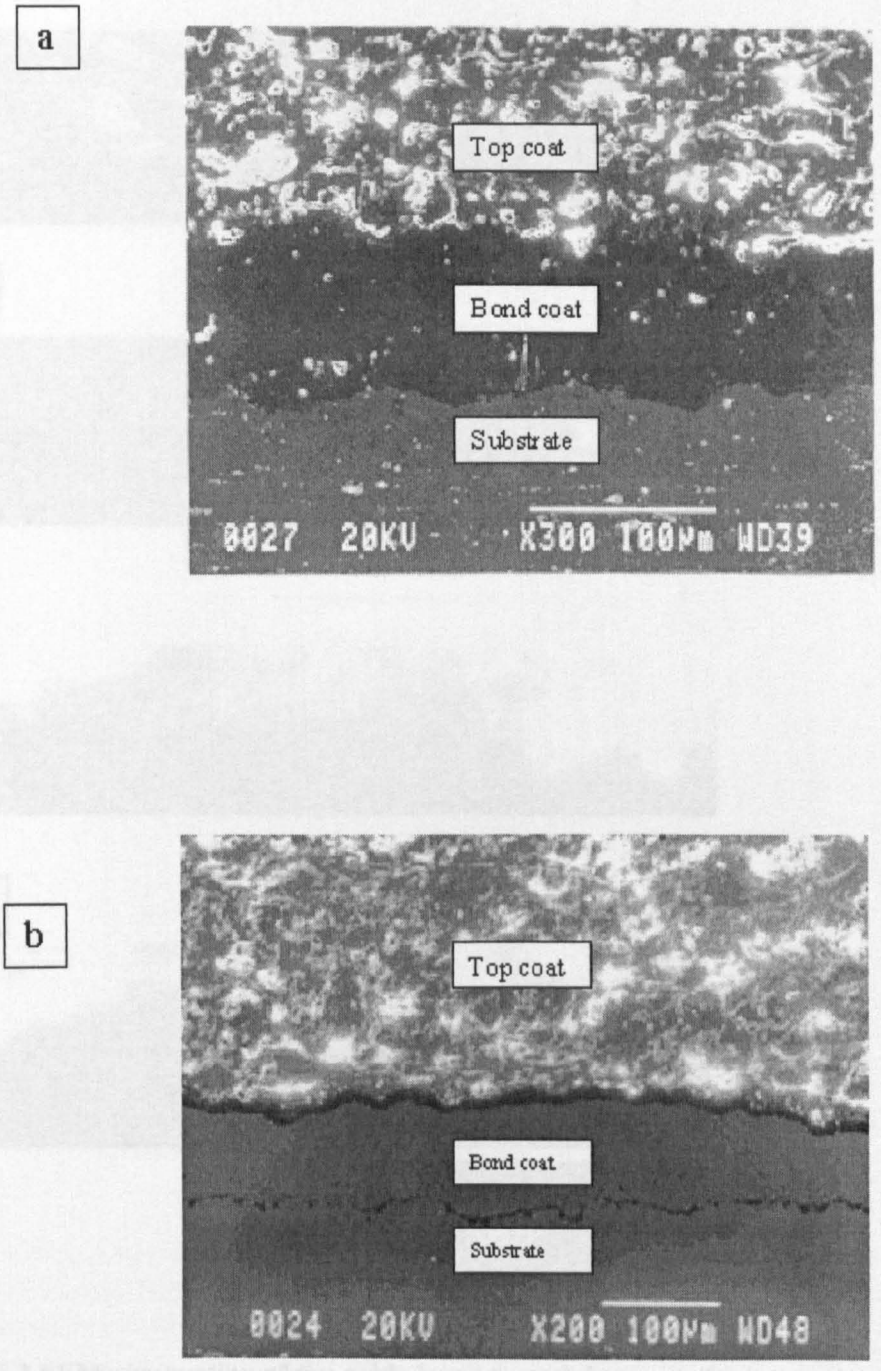

Figure 6-1 SEM images for (a) cross section of an as-received sample; (b) cross section of a sample oxidised for 1500h at 1100°C.

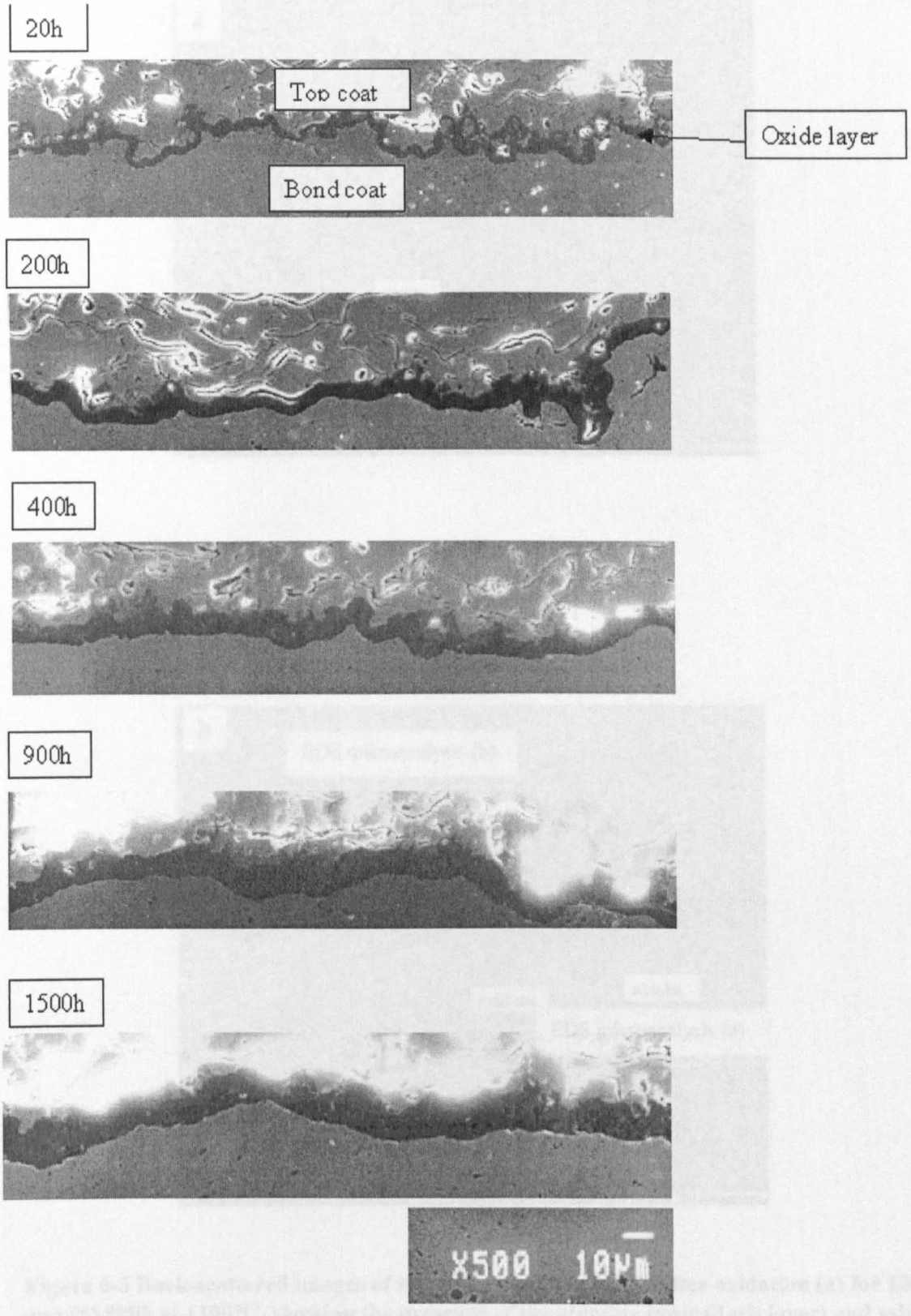

Figure 6-2 SEM observation of the oxide layer growth between the top coat and bond coat. Please note that all the images were taken at the same magnification.

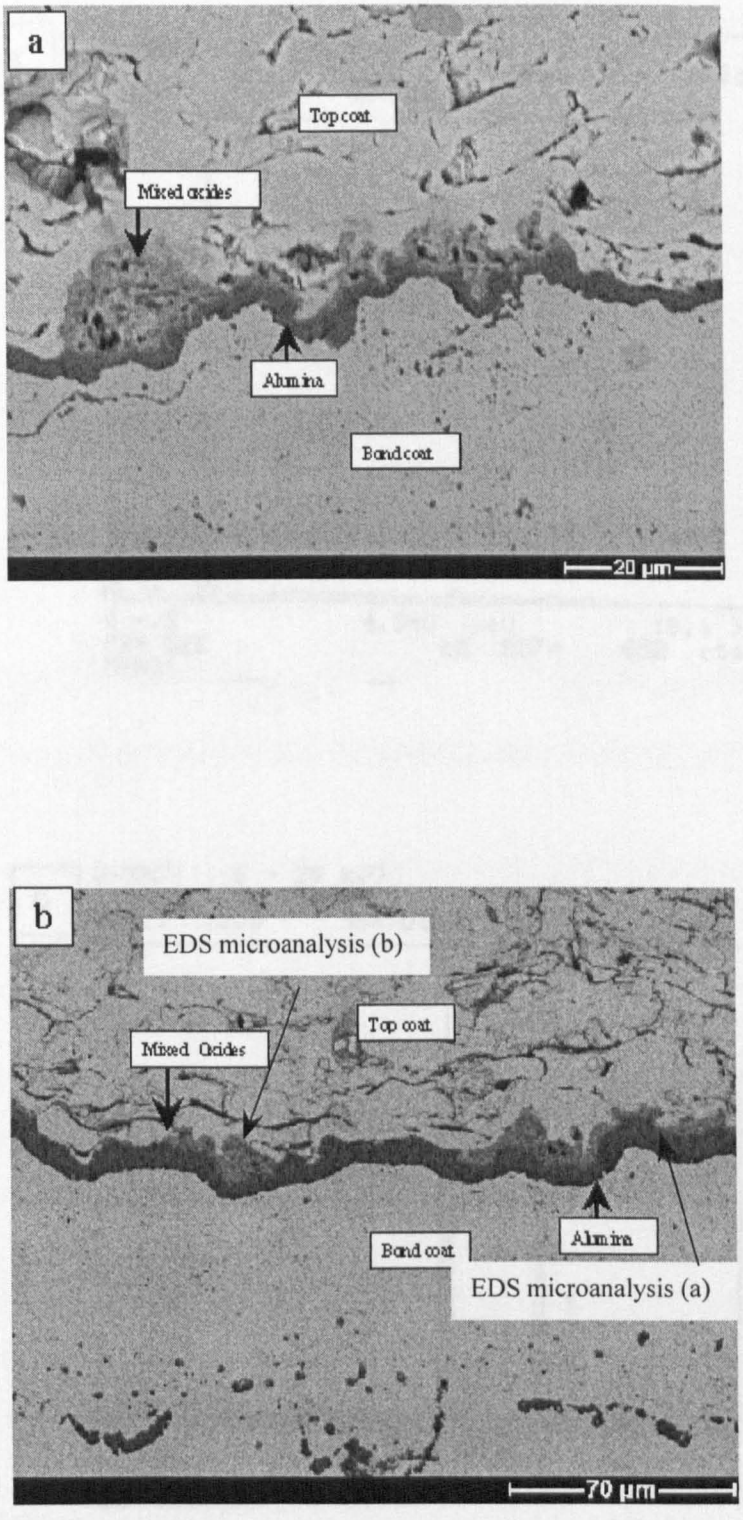

Figure 6-3 Back-scattered images of the cross section of TBCs after oxidation (a) for 100h and (b) 800h at 1100°C, showing the presence of the alumina layer (dark layer) and mixed oxide (grey), the magnification being different between a and b.

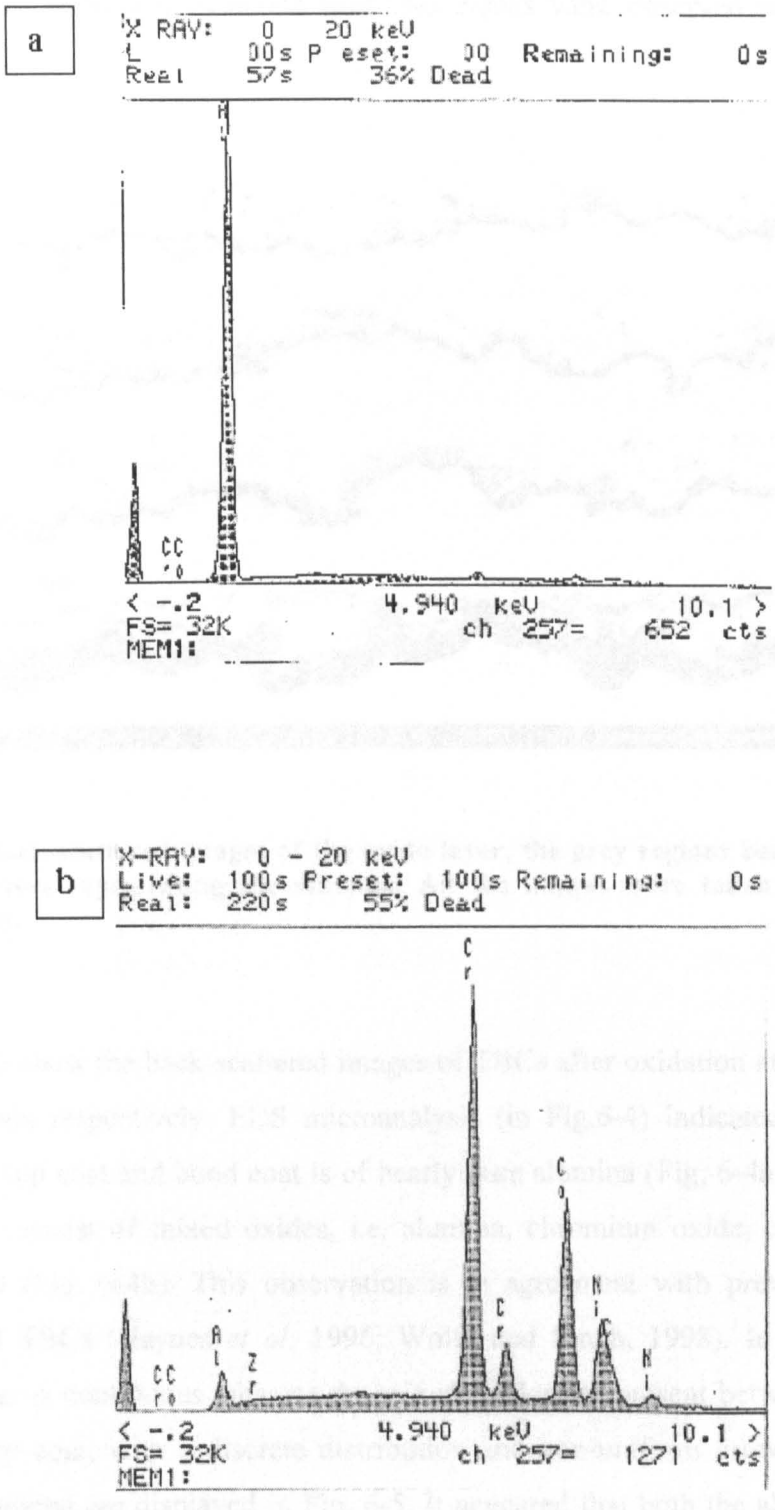

Figure 6-4 Energy dispersive mirco-ananlysis of (a) a selected point in the dark layer and (b) a selected point in the grey region as shown on Fig. 6-3b.

The oxide layer grew along the rough interface between the top coat and the bond coat. As can be seen in Fig. 6-2, the oxide layer appeared to be continuous and became

thickened with prolonged oxidation time. No cracks were observed within the oxide layer.

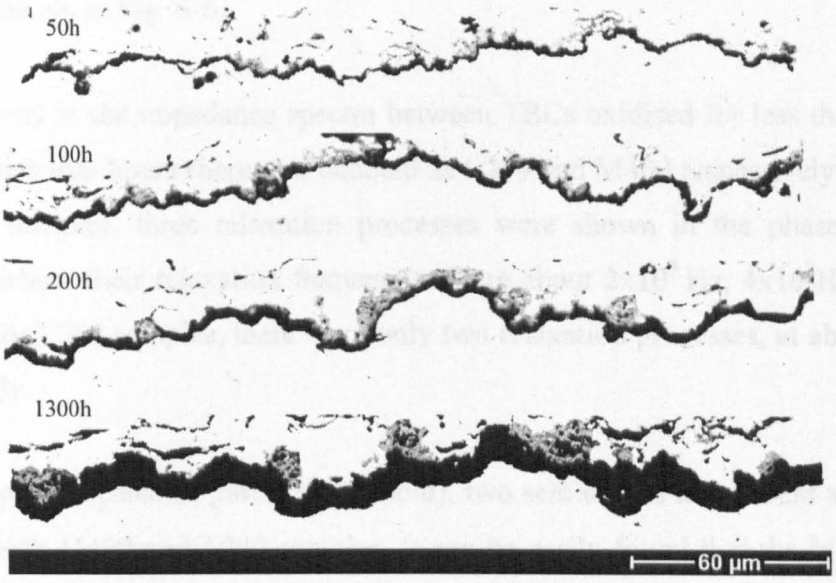

Figure 6-5 Back-scattered images of the oxide layer, the grey regions being mixed oxides and dark layers representing the alumina. All the images were taken using the same magnification.

Figs.6-3 a&b show the back-scattered images of TBCs after oxidation at 1100°C for 100 and 800 hours respectively. EDS microanalysis (in Fig.6-4) indicated the dark layer between the top coat and bond coat is of nearly pure alumina (Fig, 6-4a), while the dark grey region consist of mixed oxides, i.e. alumina, chromium oxide, cobalt oxide and nickel oxide (Fig. 6-4b). This observation is in agreement with previous studies on oxidation of TBCs (Haynes *et al.* 1996; Wolfe and Singh, 1998). In most areas, the alumina layer is continuous whereas the mixed oxides are present between the alumina layer and top coat, with a discrete distribution and non-uniform growth. Images with enhanced contrast are displayed in Fig. 6-5. It appeared that both the alumina layer and the mixed oxides grew with increase in oxidation time. In the samples that have been oxidised for less than 200 h, the alumina layer is not uniform or continuous; in some parts the mixed oxides were formed between the top coat and the bond coat. For the samples that have been oxidised for more than 400h, the alumina layer is continuous and relatively uniform.

6.3.2 Impedance Spectra At 350°C

The impedance spectra obtained from impedance measurements of various samples at 350°C are shown in Fig. 6-6.

The difference in the impedance spectra between TBCs oxidised for less than 200 hours and more than 400 hours (hereafter denoted as L200 and M400 respectively) is apparent. For M400 samples, three relaxation processes were shown in the phase angle plots (Fig.6-6a) where their relaxation frequencies were about $2x10^5$ Hz, $4x10^2$Hz and 10 Hz. However, for L200 samples, there were only two relaxation processes, at about $2x10^5$ Hz and $4x10^2$Hz.

In the complex impedance plots (Figs.6-6c-d), two semicircles are present and a tail-like curve for both M400 and L200 samples. It can be easily found that the high frequency arcs for all samples were similar in diameter, the resistances were consistently in the range of $5\sim9x10^3$ Ω. However the low frequency semicircles increased gradually with oxidation time from 0 to 200h, and then jumped abruptly from $5x10^4$ Ω at 200h oxidation time (Fig6-6c) to greater than $1x10^7$ Ω at 400h oxidation time (Fig. 6-6 d).

For L200 samples, two relaxation processes can be identified in both complex impedance and phase angle plots. However, for M400 samples, the complex impedance plot shows only two semicircles, while the phase angle plot shows three relaxation processes. The relaxation frequencies for M400 samples are estimated as $4x10^5$Hz and 6Hz for the high frequency semicircle and low frequency semicircle in the complex impedance plot, which match the $2x10^5$ Hz and 10Hz relaxation processes shown in the phase angle plot. The relaxation process at $4x10^2$ Hz shown in the phase angle plot does not appear in the complex impedance plot.

In the complex modulus plots (Fig. 6-6e-f), again we can see the distinction between L200 and M400 samples: there are two well-resolved semicircles for M400 samples, but only one semicircle for L200 samples. The peak frequencies are about $6x10^5$ Hz and 5Hz (see Figs. 6-6 b, e) respectively for high frequency semicircle and low frequency semicircle.

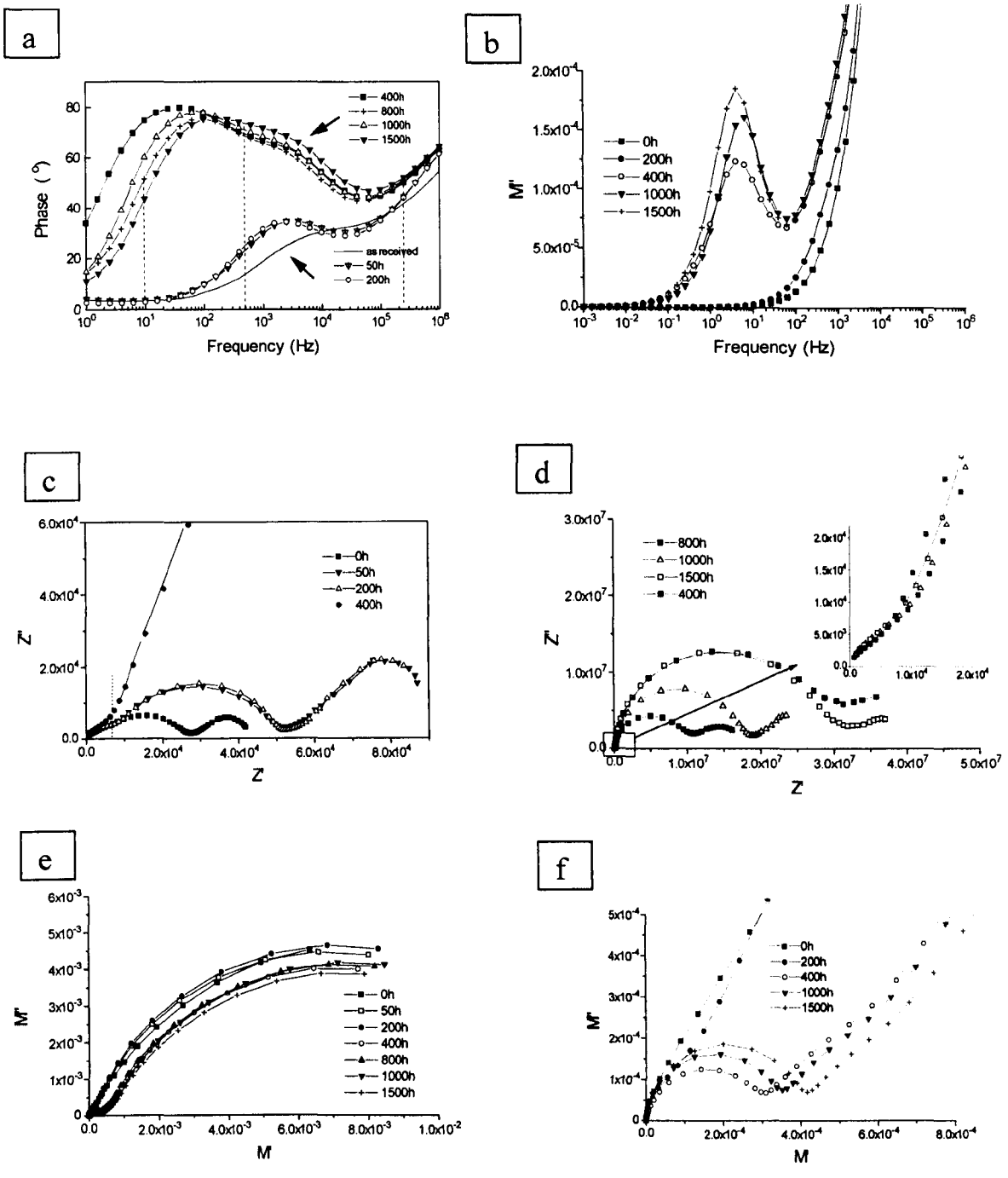

Figure 6-6 impedance spectra at 350°C: (a) phase angle plots; (b) modulus spectroscopic plots; (c) complex impedance plots for L200 samples; (d) complex impedance plots for M400 samples, with an enlarged presentation for high frequency arcs; (e) complex modulus plane plots and (f) enlarged presentation for low frequency semicircles

It is important to note that the diameter of the low frequency semicircle in the complex modulus plot increases monotonically with oxidation time, while the high frequency semicircle does not appear to vary with oxidation time. Similarly the low frequency peak

height in the modulus spectroscopic plot also increases with oxidation time, indicating that the capacitive effect of the low frequency process decreases with the oxidation time.

With the evidence presented in Fig. 6-6, and in combination of our SEM observations presented in 6.3.1, we can quite confidently ascribe the low frequency process to the oxide layer and the high frequency process to the top coat (YSZ). What is responsible for the intermediate frequency process (i.e. at ~$4x10^2$ Hz) will be dealt with in detail later in this chapter.

6.3.3 Impedance Spectra At Room Temperature

At room temperature (R.T), the reproducibility of impedance data was found to be much poorer than that at 350°C. This is due to the low conductivities of the samples at R.T. Materials with a conductivity of lower than 10^{-5} $(\Omega \bullet cm)^{-1}$ are thought to be susceptible to the influences of other unpredictable factors (Kingery *et al.* 1976c), such as moisture in the atmosphere and impurities that were probably brought in by the painted electrodes. Typical impedance spectra obtained by R.T measurements are shown in Fig. 6-7.

At R.T, quite different from the impedance spectra at 350°C, the as-received (i.e., denoted as 0h) sample showed only one relaxation process in the phase angle plot (Fig. 6-7a), one semicircle and one low frequency tail in the complex impedance plot (Fig.6-7b). All the oxidised samples exhibited two relaxation processes, one at a frequency in the range of 5-100Hz and the other at a frequency in the range of 0.004-1Hz. The scattered relaxation frequencies were probably a consequence of the poor reproducibility of the impedance data. Nevertheless, similarly to the case of the measurements at 350°C, it was consistently found that the high frequency semicircular arc in the complex impedance plot was similar in diameter, while the low frequency semicircular arc was very different. For instance, the low frequency semicircular arc for L200 samples were at least two orders of magnitude smaller than those for M400 samples.

Similarly to the case of 350°C spectra, the complex modulus plots at R.T had two semicircles for M400 samples, but only one semicircle for L200 samples (Figs. 6-7c-d). The high frequency semicircle in the complex modulus plot became more depressed (Fig.6-7c), and the high frequency peak became broader (Fig.6-7e) when the oxidation

time was extended above 800h, indicating the top coat microstructure might change as well during heat treatment.

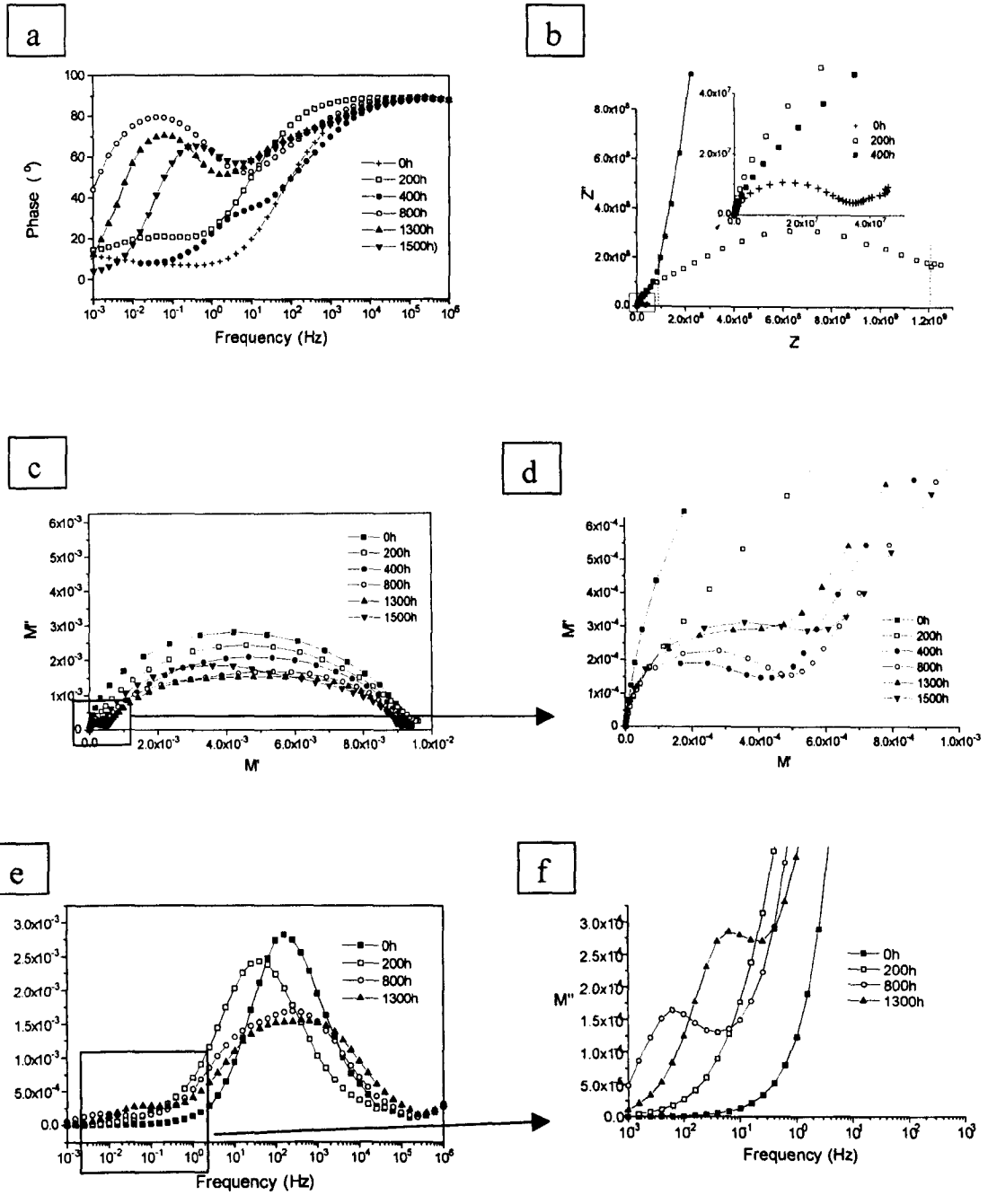

Figure 6-7 Impedance spectra at R.T: (a) phase angle plots; (b) complex impedance plots, with an enlarged presentation for high frequency arcs; (c) complex modulus plots and (d) enlarged presentation for low frequency semicircles of modulus spectra; (e) modulus spectroscopic plots for the whole frequency range; (f) modulus spectroscopic plots focused on high frequency processes.

6.4 Discussion

6.4.1 Oxidation Kinetics

Based on the analysis of SEM images as shown in Fig. 6-2, the oxide layer thickness was found to be a function of oxidation time (Fig.6-8a). By plotting oxidation layer thickness against the square root of time, we can obtain two linear regions in the plot (Fig.6-8b): one is below an oxidation time of 25h, the other above 50h. Thus the oxidation kinetics of the bond coat can be assumed to follow a parabolic law:

$$\delta = \sqrt{kt} \qquad (6\text{-}1)$$

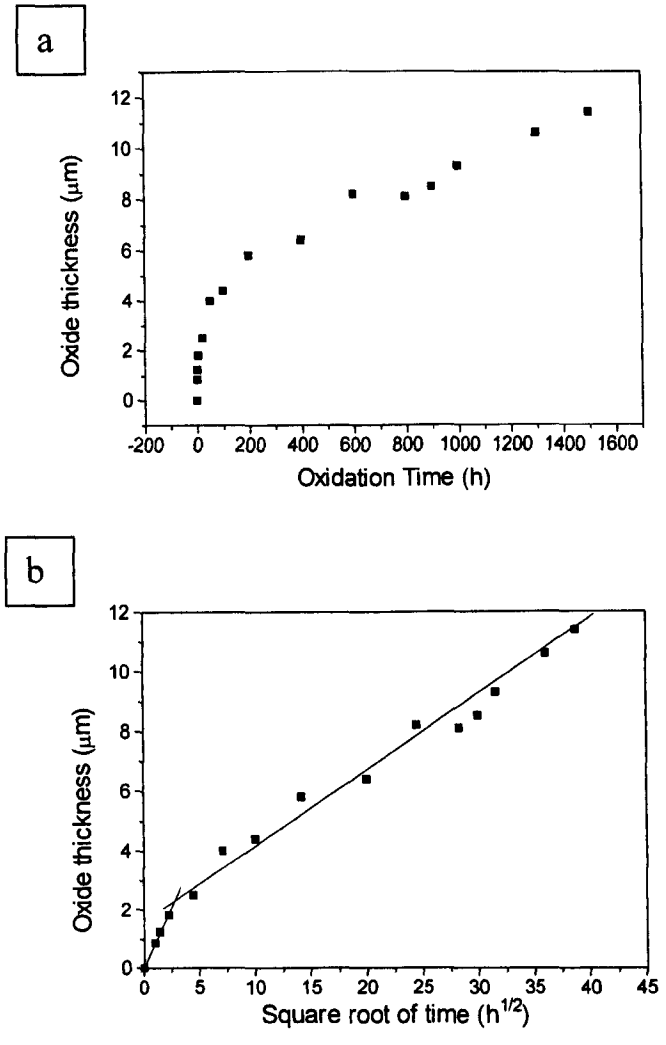

Figure 6-8 Oxide thickness determined by image analysis plotted vs. (a) time and (b) square root of time.

According to Fig.6-8b, the parabolic rate constant is calculated to be $1.8x10^{-12}$ cm^2s^{-1} for the initial 25h and $0.3x10^{-12}$ cm^2s^{-1} for the later oxidation. The faster initial oxidation rate is commonly known as a transparent effect in oxidation where Ni or Cr-rich oxide may form before a steady-state alumina film is established. This is in agreement with our SEM observation. Our SEM observation revealed that mixed oxides (grey areas in Fig.6-5) were formed in the initial stage. In the initial oxidation, the alumina layer was not continuous, other elements such as Ni, Cr, etc., in the bond coat were oxidised to form a mixed oxide along the interface. In the later stages the alumina layer was literally continuous, which is supposed to prohibit the diffusion of other elements, except around defected areas, such as cracks, pores or other forms of defects, which could allow other elements to pass across the alumina layer. For this reason mixed oxides grew like mushrooms in the case of long oxidation period (in Fig. 6-5).

6.4.2 Equivalent Circuit Models

Based on microstructural observations, the electrical conduction paths in TBCs are illustrated schematically in Fig. 6-9, where the alumina layer is continuous for M400 samples, but discontinuous for L200 samples. Electrical conduction first passes the electrode/top coat interface and then the top coat itself. The top coat is composed of polycrystalline YSZ, where grains and grain boundaries would respond differently to electrical signals in different frequency domains (Steil, *et al.* 1997; Badwal, 1995), therefore two R-CPE elements should be used for grain and grain boundary, respectively in the top coat. Then the electrical conduction is divided into two paths: path one and path two. For M400 samples, path one and path two meet again in the alumina layer because it is continuous, whereas, for L200 samples, path one and path two will not come together until they reach the bond coat. In the light of the analysis of conduction paths, the comprehensive equivalent circuits corresponding to the two cases are illustrated in Fig. 6-10.

Obviously we could not use these equivalent circuits directly to fit the impedance data in order to get meaningful IS parameters. Normally it is hoped that there is a separate relaxation process corresponding to each R-C (or R-CPE) element in an equivalent circuit. Since only two or three relaxation processes appeared in the impedance spectra for TBCs, this means that electrical responses from some microstructural factors may

overlap, or do not give significant contributions to the impedance in the measuring frequency range. To understand better the impedance spectra and generate meaningful IS parameters by fitting impedance spectra, the equivalent circuits shown in Fig. 6-10 need be simplified.

Firstly, equivalent circuits can be simplified by putting aside the electrical responses from all the interfaces, e.g., the YSZ/electrode, alumina/YSZ and alumina/bond coat. This is because, in most cases, the responses from the interfaces either occur at low frequencies that will be clearly separated from the bulk effect, or make only minor contributions to the impedance. Secondly, when there are parallel conduction paths, the electrical conduction always finds the easiest path. Thus the equivalent circuit can be further simplified to the easiest path.

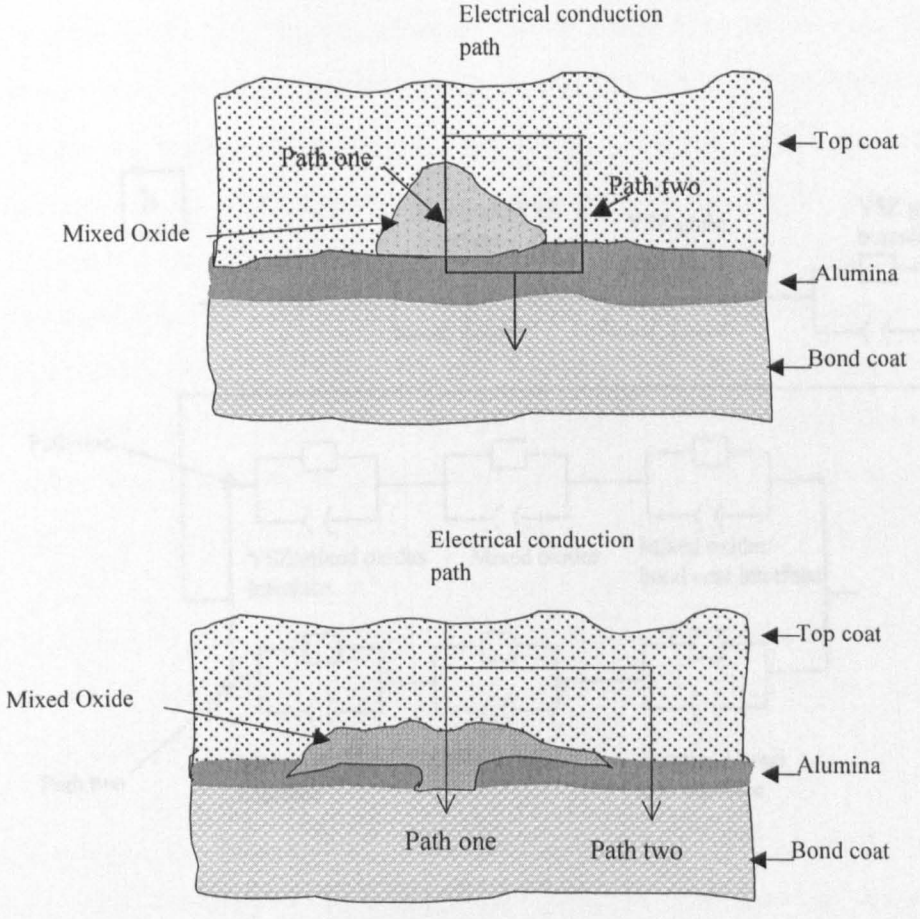

Figure 6-9 Schematic of electrical conduction paths for (a) M400 samples and (b) L200 samples.

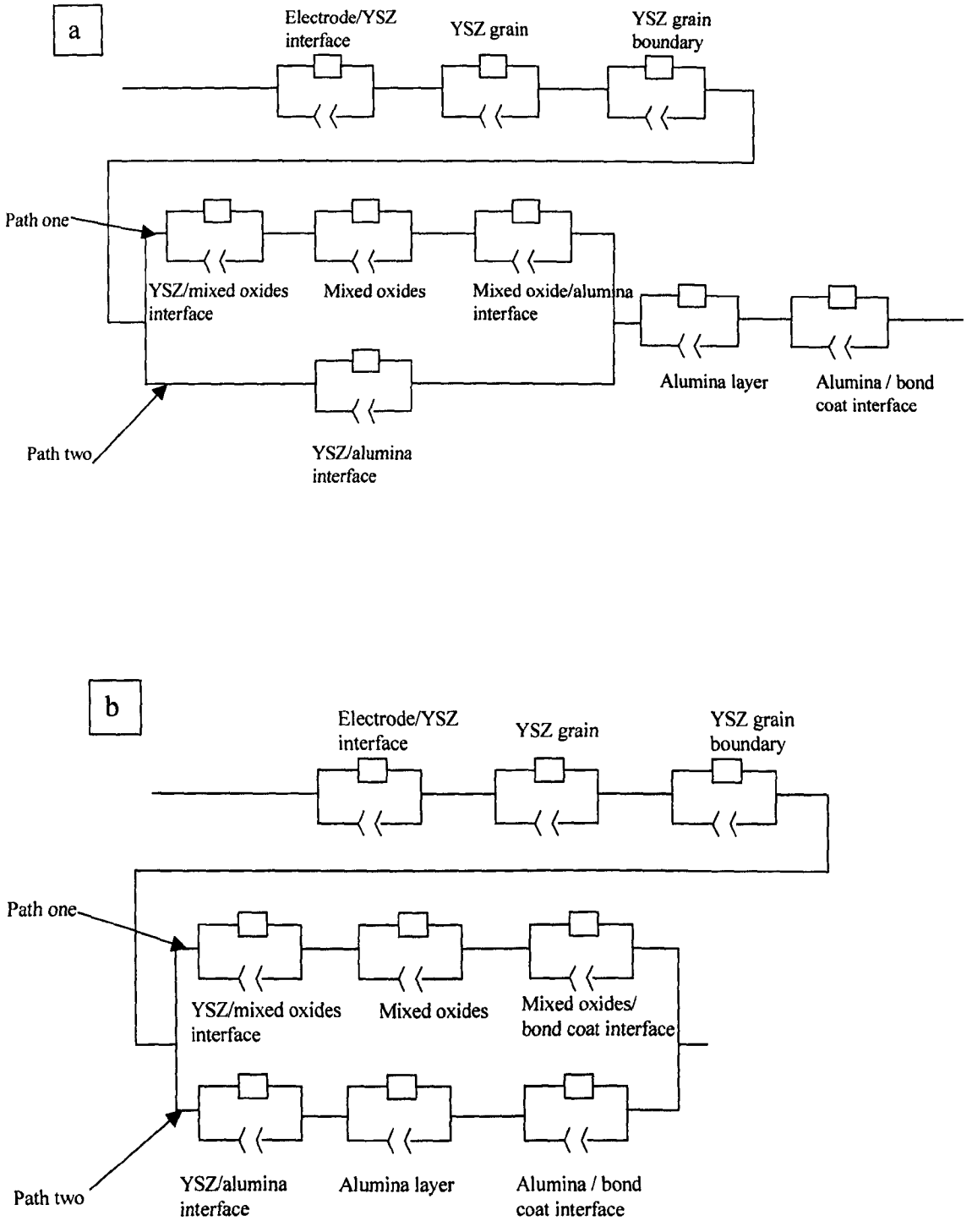

Figure 6-10 Equivalent circuits for (a) M400 samples and (b) L200 samples

By neglecting all the interfaces in the equivalent circuits, there are only four components left for consideration: YSZ grains and grain boundaries in YSZ, the mixed oxide and the alumina layer. For the M400 samples, the alumina layer is in series connection with the mixed oxide, while for L200 samples, the alumina layer is connected in parallel to the mixed oxide. As mentioned earlier on, three relaxation processes appeared in the impedance spectra of M400 samples at 350°C, of which the high frequency and low frequency relaxation processes corresponded to the top coat and the alumina layer respectively. As a consequence of this, the intermediate frequency process can only be attributed to a mixed response from the grain boundaries in YSZ and the mixed oxide, which will be discussed in detail later on in this chapter. Therefore the equivalent circuit shown in Fig. 6-10a can be simplified to that shown in Fig. 6-11a.

For the L200 samples, as shown in Fig. 6-9b, the mixed oxide and alumina layer are parallel connected. The mixed oxide can be assumed to be semi-conductive, and would show much higher conductivity than alumina at high temperatures. Therefore the conduction through the mixed oxide in L200 samples at 350°C (path one in Fig. 6-10a) is an easy path and the response from alumina is shielded. The low frequency process in the impedance spectra of L200 samples measured at 350°C has the same relaxation frequency as the intermediate frequency process of M400 samples, indicating they represent a similar physicochemical process. For these reasons, the high frequency relaxation can be attributed to the top coat and low frequency relaxation process to the mixed response from the grain boundaries in the YSZ and the mixed oxide layer. The equivalent circuit shown in Fig. 6-10b can be simplified that shown in Fig. 6-11b

At R.T, both the mixed oxide and alumina are assumed to be very insulating and the electrical responses from the mixed oxide and alumina can overlap. In this case the equivalent circuit can be simplified to that shown in Fig. 6-11c.

In practice, the impedance spectra usually cannot be fitted simply by employing ideal RC elements, because of the distributed nature of the electrical response from realistic materials. In terms of the various representations of impedance data as shown in Fig. 6-6 and Fig. 6-7, it is not difficult to see that the impedance and modulus spectra are rather depressed, so it is necessary to use constant phase elements (CPEs), rather than ideal capacitances, in the equivalent circuits.

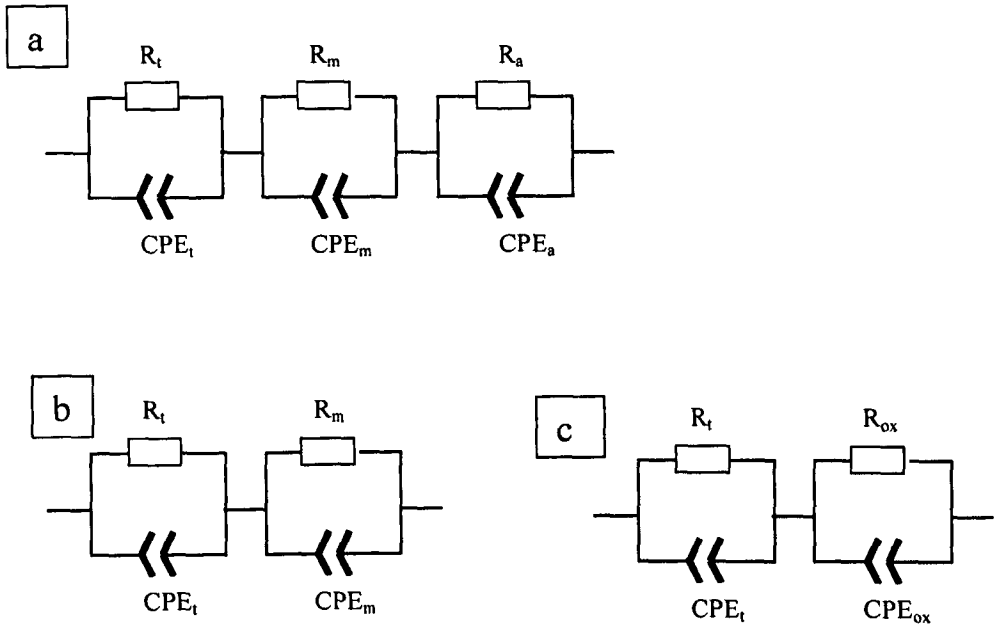

Figure 6-11. Equivalent circuits of (a) M400 samples at 350°C; (b) L200 samples at 350°C and (c) all samples at R.T, t=top coat, m=mixed oxides, a=alumina and ox=oxide layer.

6.4.3 Fitting Of Impedance Spectra

The equivalent circuit models shown in Fig. 6-11 were used to fit the impedance data. These models fit very well the experimental data as shown in Figs. 6-12a-c. The IS parameters that can be obtained by fitting are R, A and n. R represents the resistance, while A and n are the parameters in CPE ($Y=A(j\omega)^n$). Since the fitted results obtained from three sets of experimental data are different, error bars are used to indicate the standard deviation of the three sets of fitted data.

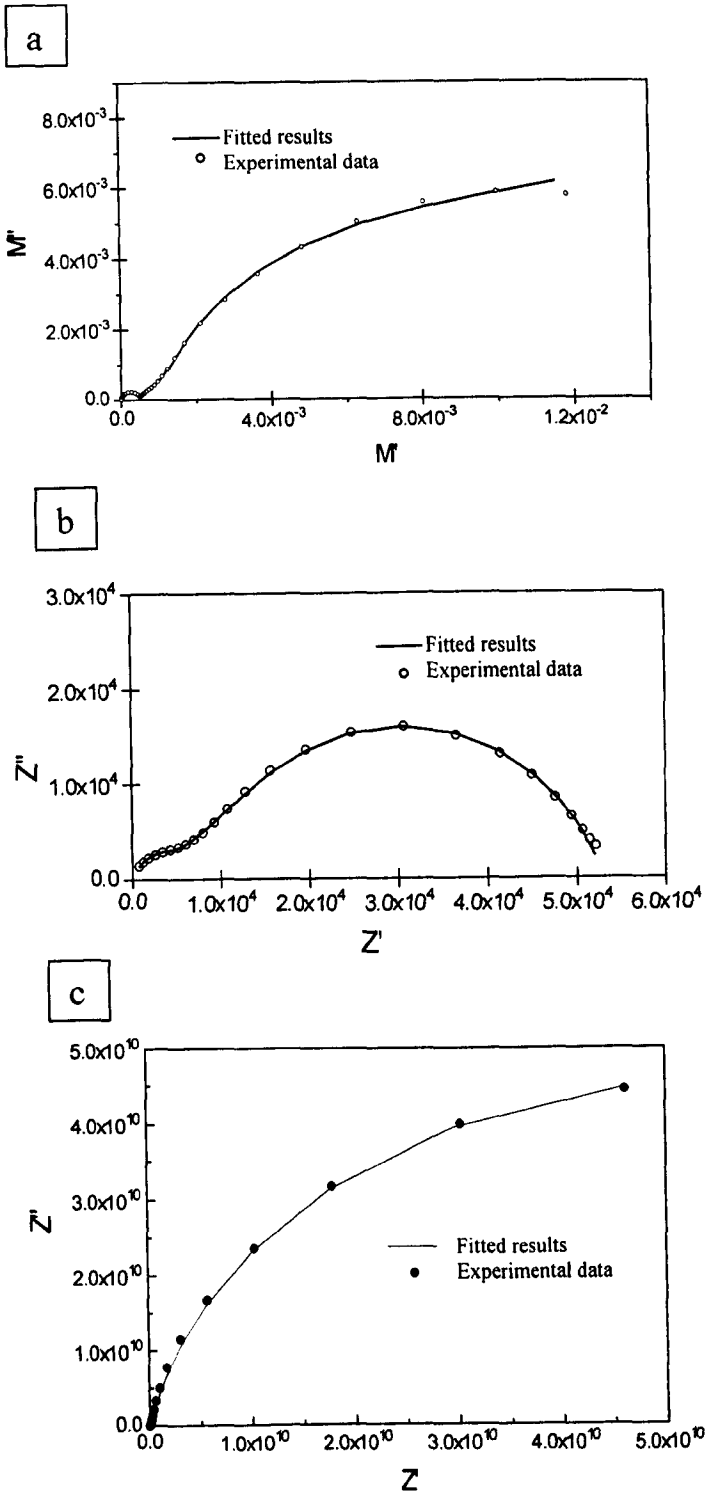

Figure 6-12 Fitted experimental data of (a) 1000h oxidised sample measured at 350°C, (b) 200h oxidised sample measured at 350°C (c) 1000h oxidised sample at R.T.

The IS parameters obtained from the fitting of impedance data measured at 350°C are shown in Fig. 6-13. Although the standard deviation for the resistance data is very large, the resistance of the top coat appears to have a fixed pattern: it increases drastically for the first 10 hours, and then appears to gradually increases with oxidation time. In contrast, the resistances for the oxide layer (alumina) and mixed responses do not appear to show a clear trend.

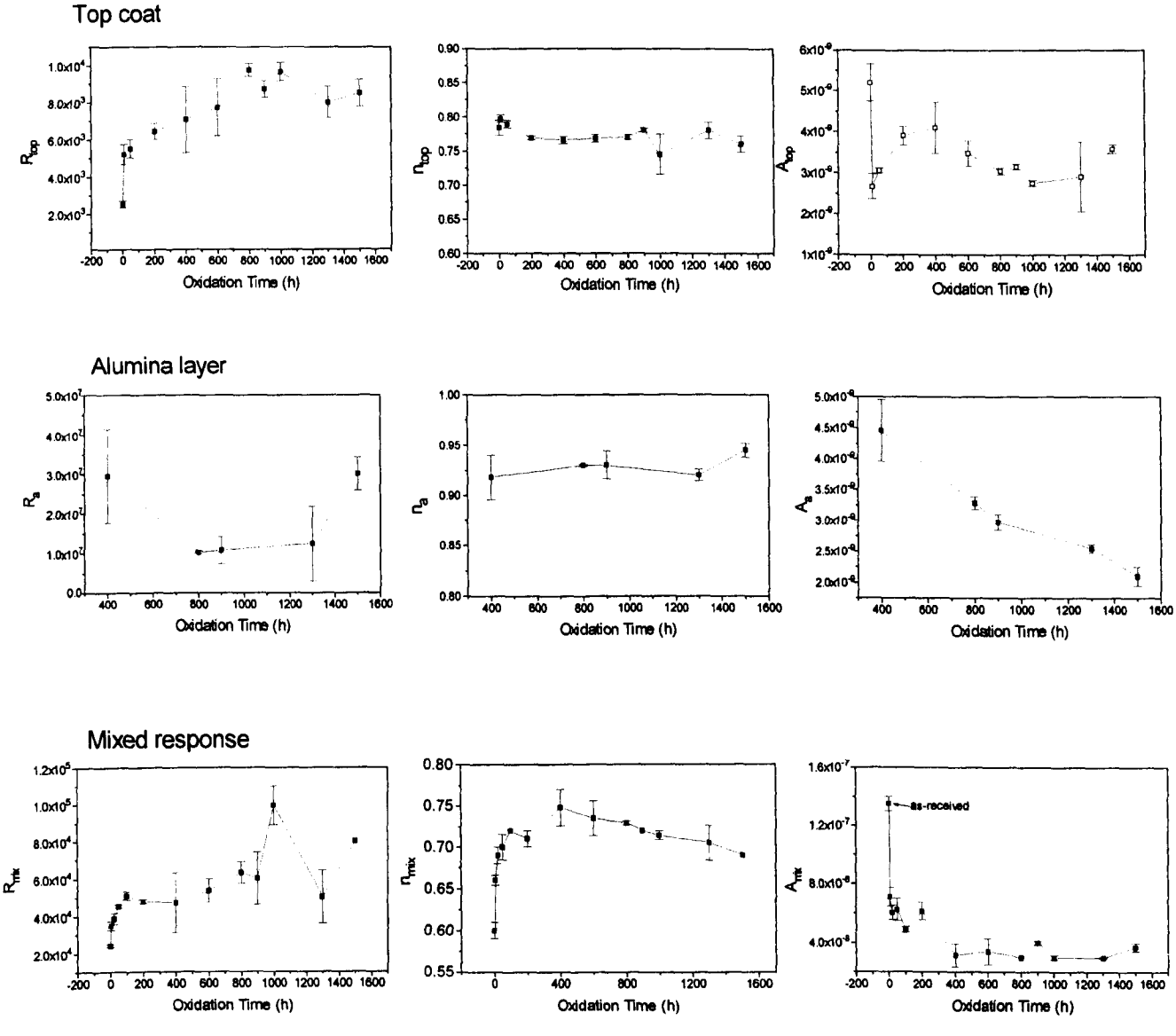

Figure 6-13 IS parameters obtained from the fitting of impedance spectra measured at 350°C by using equivalent circuits as shown in Figs. 6-11a & b.

The n values for the top coat and oxidation layer do not appear to vary with oxidation time, while the n value of the mixed response show a steep increase in the initial oxidation, then it decreases gradually with oxidation time

The parameter A of the top coat shows a drastic decrease in the first 10h of oxidation, followed by a less significant and unsteady change. The parameter A of the mixed response shows a sharp drop within the first 200h oxidation, then stays constant during heat treatment, while an apparent decreasing trend is shown for the parameter A of the alumina layer.

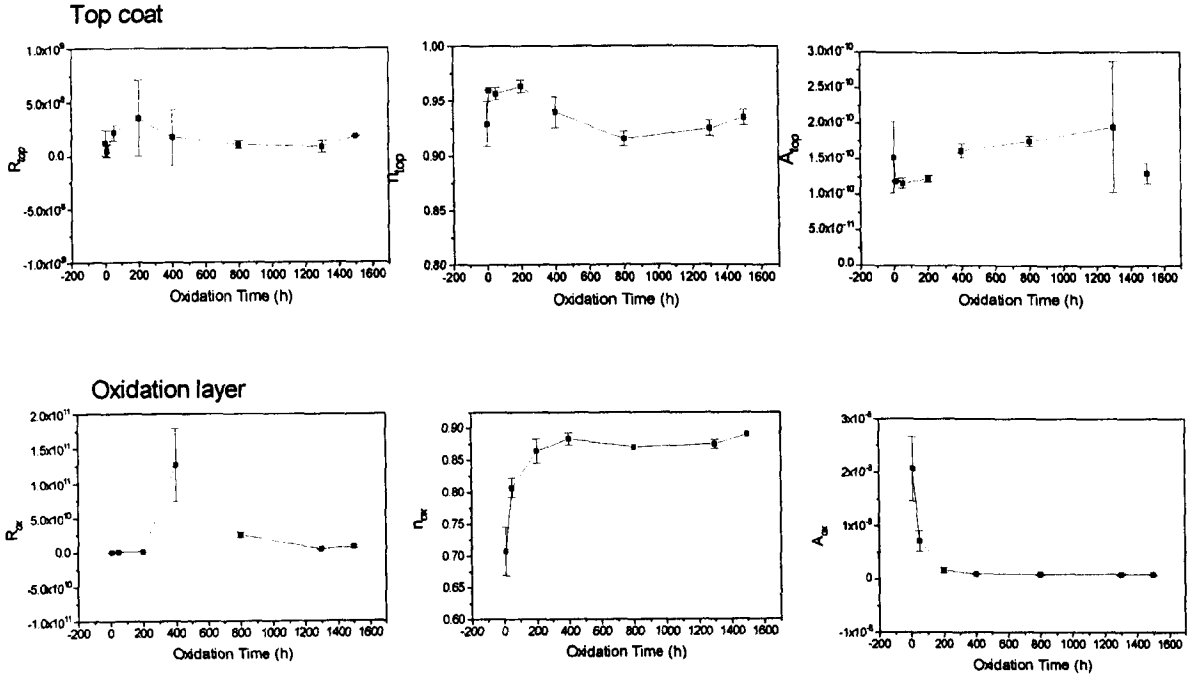

Figure 6-14 IS parameters obtained by fitting the impedance spectra measured at R.T by using the equivalent circuit as shown in Fig. 6-11c.

The IS parameters resulting from fitting the impedance data measured at R.T are shown in Fig. 6-14. Here, of particular interest is that the n value of the oxide layer demonstrates a rapid increase within the first 400h of oxidation and then stays unchanged afterwards, while the parameter A of the oxide layer decreases abruptly in the first 200h of oxidation time and shows little change afterwards. Other IS parameters do not seem to show a clear trend.

It is important to note that the parameter A does not have a defined physical meaning. By contrast, capacitance represents the capability of accumulating electric charge, which is related to the geometric aspects of a given microstructural factor. The capacitance of an ideal capacitor is frequency-independent and can be defined by:

$$C = \varepsilon_o \varepsilon \frac{A_o}{l} \qquad (6\text{-}2)$$

where ε_0 is the vacuum permitivity:8.85×10^{-14}, ε is the dielectric constant, A_o is the area and l is the thickness of the microstructural factor of concern. Therefore capacitance is more meaningful than the parameter A. However for a real material with a non-ideal behaviour, the capacitance is frequency-dependent, i.e., the lower the frequency, the larger the capacitance. In order to make the capacitance of a non-ideal system comparable with that of an ideal system, the capacitance corresponding to the frequency at the top of the arc is regarded as the equivalent capacitance. According to Jacobsen *et al.* (1996), the equivalent capacitance for a R-CPE circuit can be calculated by:

$$C = (R^{1-n} A)^{1/n} \qquad (6\text{-}3)$$

where R is the resistance, n and A are parameters for the CPE.

Based on the fitting results shown in Fig. 6-13 and Fig. 6-14, the capacitances of the top coat and oxide layer at R.T and 350°C were calculated employing Eqn. 6-3. The results are presented in Fig. 6-15. The capacitance of the top coat measured at both RT and 350°C (Fig. 6-15a) shows a sudden drop in the first 10h of oxidation. Afterwards the capacitance does not seem to change much with oxidation time. The mixed response (Fig. 6-15b) shows a steep rise in capacitance for the first 50h oxidation, then decreases gradually with oxidation time. The capacitance of the alumina layer measured at 350°C decreases with oxidation time (Fig. 6-15c). The capacitance of the oxide layer at R.T (Fig. 6-15d) drops quickly in the initial stage and then decreases gradually.

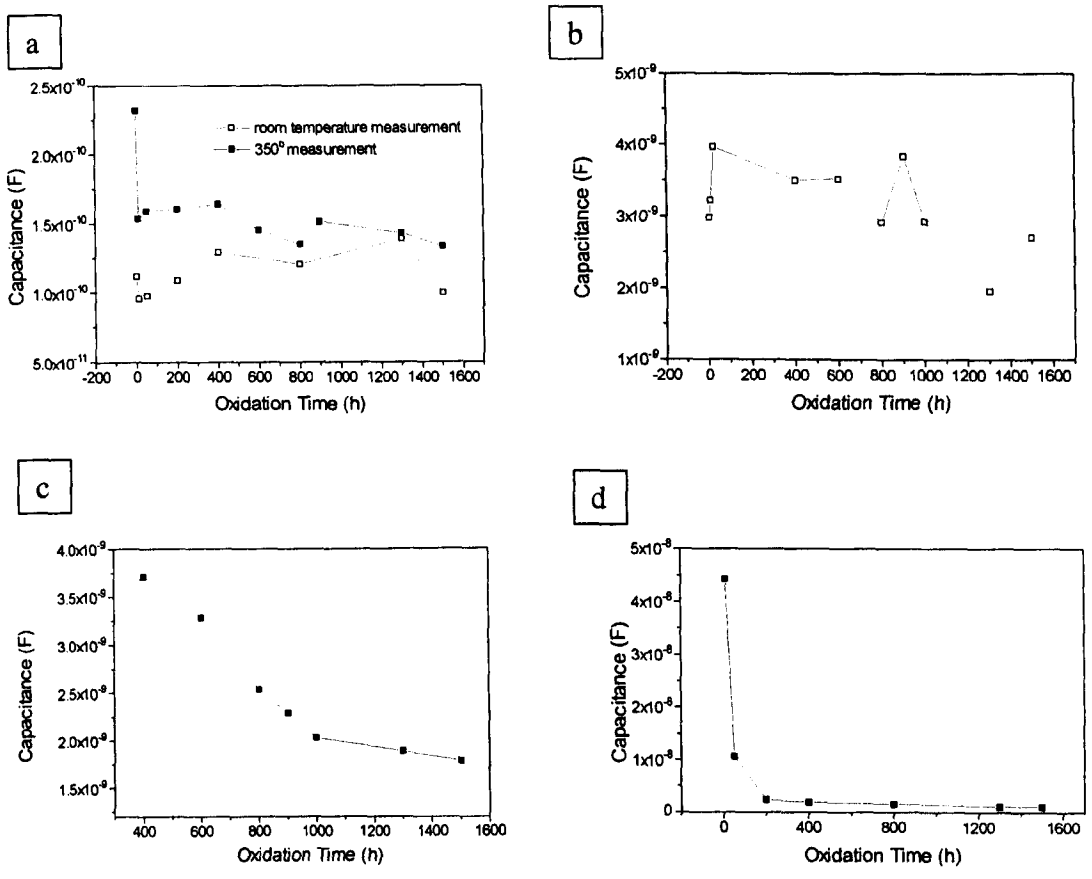

Figure 6-15 Equivalent capacitances of (a) top coat derived from both R.T and 350°C impedance data; (b) mixed response at 350°C (c) alumina layer at 350°C; (d) oxide layer at RT.

6.4.4 Interpretation Of The Impedance Spectra And Fitting Results

6.4.4.1 HF Relaxation Process – Response Of Top Coat

There are three pieces of evidence supporting the attribution of the high frequency relaxation process to the top coat (YSZ bulk). Firstly, the high frequency relaxation process of TBCs is similar to that of a free-standing top coat, for which the impedance spectrum will be presented later on (in Fig 6-17). Secondly, the relaxation frequency reflected in the impedance spectra is in agreement with the calculation based on the data of conductivity and dielectric constant. The relaxation frequency can be calculated as:

$$f_n = \frac{1}{2\pi RC} = \frac{\sigma}{2\pi\varepsilon_o\varepsilon} \qquad (6\text{-}4)$$

where σ is the conductivity and other symbols have the normal meanings. The conductivity of a free-standing top coat was measured to be $6x10^{-6}$ S•cm, $\varepsilon_0=8.85x10^{-14}$F/cm, the dielectric constant (ε) for YSZ can be assumed as 30 (Bonanos *et al.* 1987), then the relaxation frequency is calculated as $3x10^5$ Hz, which is good agreement with the value of $2x10^5$ Hz that is observed in the impedance spectra.

Thirdly, the capacitance deduced from IS parameters is in accordance with the calculated value using Equ.6-2. The electrode area of the measuring cell is 0.9 cm^2, the thickness of top coat is about 300 μm, ε=30. Thus the capacitance of top coat is calculated to be $8.85x10^{-11}$, which is lower, but fairly close to the value of $1\sim1.2x10^{-10}$ derived from IS parameters for R.T impedance spectra, as shown in Fig. 6-15a. This further justifies the ascription of the high frequency relaxation process to the top coat.

In the as-received TBCs, the top coat (YSZ) is mainly composed of the t' phase (Miller *et al.* 1981&1983). According to the ZrO_2-Y_2O_3 phase diagram (Scott, 1975), for the YSZ containing 8 wt % (4.5 mol %) of Y_2O_3, the equilibrium phases should be in tetragonal (t) phase plus cubic (c) phase region. However, on the rapid cooling of the molten droplets of YSZ during plasma spraying, the diffusional process, which leads to the formation of the equilibrium phases: a low-Y_2O_3 -content t-phase and a high-Y_2O_3-content c-phase, is prohibited. Therefore the c-phase in the cubic single-phase field at high temperature undergoes a displacive transition to a non-equilibrium phase that is crystallographically identical to the tetragonal phase, but with higher Y_2O_3 content. This phase is commonly referred as t'-phase (Scott, 1975).

The t' phase has a higher electrical conductivity than the cubic and tetragonal phase (Drennan and Auchterlonie, 2000). The t' phase is a metastable, distorted fluorite–type phase (Badwal, 1998). When thermally aged, it rapidly dissociates into c-phase and t-phase (Miller *et al.* 1981 &1983). Thus the dissociation of the t' phase is expected to be accompanied by an increase in electrical resistance. The oxidation temperature used in this research is 1100°C. According to the phase diagram (Scott, 1975), the equilibrium phase at this temperature for 8 wt% PSZ is c-phase plus t-phase. So it is possible that the t' phase transformed into the equilibrium phases when heat-treated at this high temperature. Therefore it can be speculated that the drastic increase of top coat resistance in the initial heat treatment (refer to Fig.6-13) might be due to the dissociation of the t'

phase. This also can explain the drop of capacitance of the top coat (Fig. 6-15a) during initial 10h oxidation. According to the discussion in chapter 5, the dielectric constant increases with the content of conductive phase. When the t' phase is transformed into c-phase and t-phase, the conductive phase is reduced and then the dielectric constant is expected to become smaller.

The X-ray diffraction analysis of the top coat after heat treatment revealed that prolonged oxidation led to an increase in monoclinic (m) phase as shown in Fig. 6-16. Since m-phase is less conductive than the tetragonal and cubic phases (Muccillo and Kleitz, 1996), the increase in the m-phase may explain the gradual increase in resistance of the

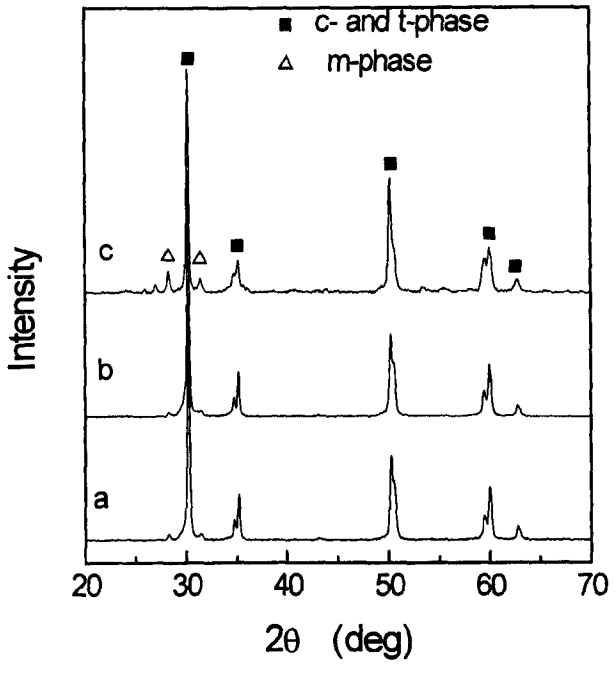

top coat as the oxidation is prolonged.

Figure 6-16 X-ray diffraction analysis of top coat after heat treatment using various heat treatment schemes (a) at 1100°C for 2h;(b) at 1100°C for 100h and (c) 1150°C for 2000h.

The response of the top coat corresponds to a small semicircle in the complex impedance plot and a large semicircle in the complex modulus plot, because the top coat has a high

conductivity and low capacitance as compared with the oxide layer. At R.T, the modulus spectra (Figs. 6-7 c-e) demonstrate that a prolonged oxidation time results in a more frequency-dispersed response of the top coat. When the oxidation time exceeds 800h, the peak corresponding to the top coat becomes abnormally broadened. It is quite likely that it consists of two overlapping peaks (Fig. 6-7 e), because we can see the semicircle of the top coat in complex modulus plot appears to separate into two semicircles. This might be due to the presence of a considerable amount of monoclinic phase when the oxidation time is prolonged. Because the electrical response from monoclinic zirconia is expected to be different from those from tetragonal and cubic zirconia, even an additional semicircle is possible (Muccillo and Kleitz, 1996).

The degradation of the top coat (YSZ) is strongly related to the polymorphisms of zirconia. For example it is well established that the t' phase is the major reason for the superior TBC performance of YSZ (Miller, 1987). The phase transitions: t' phase $\rightarrow$ t-phase + c-phase, and t-phase $\rightarrow$ m-phase, have promotion effects on the degradation of the top coat. The results presented here indicate that impedance measurements can be used to monitor the phase changes in the top coat. Therefore IS should be informative regarding the degradation of the top coat. Further detailed work, however, is needed to establish an explicit correlation between IS parameters and the degradation status of the top coat.

6.4.4.2 Low Frequency Process- Response Of Oxide Layer

The electrical response from the oxide layer is at low frequencies. At 350°C, the relaxation frequency of the oxide layer is about 10 Hz. However the relaxation frequency at room temperature is much lower and varies from one measurement to another. In order to verify the assignment of the low frequency relaxation process to the oxide layer, the capacitance of the oxide layer is estimated based on microstructural observations. For the case of the 1500h oxidised samples, the observed average thickness of oxide layer is 11.4μm, the dielectric constant of oxides can be assumed to be about 10. Using Eqn. 6-3, the capacitance can be calculated to be 7×10^{-10} F, which is close to the equivalent capacitance of 1.06×10^{-9} derived from the IS parameters for the R.T impedance spectra (see Fig. 6-15c).

At 350 °C, the response from the oxide layer is split into two responses, one from the mixed oxide and the other one from the alumina layer, because the differences of relaxation frequency between the mixed oxide and the alumina layer are expected to be very large. At 350°C, the relaxation frequency of the mixed oxide, which will be discussed in detail later on, should be at a very high frequency, therefore the mixed oxides may not contribute to the low frequency relaxation process.

Table 6-2 shows the equivalent capacitance of the low frequency relaxation process of TBCs at 350 °C and R.T respectively. On average, the capacitance of the alumina layer at 350°C is about twice that of the oxide layer at R.T. The dielectric constant of the oxide layer could not be doubled from RT to 350°C, so the increase in the capacitance of the low frequency relaxation process must be due to the decrease in thickness. This justifies the speculation that the low frequency relaxation process in the R.T measurement corresponds to the overall oxide layer, including both alumina and mixed oxide, while the low frequency relaxation process at 350°C 'senses' only the alumina layer. The capacitance of low frequency process at 350°C is mainly from the continuous alumina layer. The effective thickness will be smaller than the overall oxide thickness and the capacitance is expected to be higher than that at R.T. This is in accordance with the capacitance values derived from the IS parameters as shown in Table 6-2. This also suggests that the thickness of both alumina and mixed oxides can be detected by IS measurements at different temperatures.

Table 6-2 Equivalent capacitance of low frequency process at R. T. and 350°C

Oxidation time (h)	Equivalent capacitance (F) of low frequency process at R.T.	Equivalent capacitance (F) of low frequency process at 350°C
400	$1.8x10^{-9}$	$3.7x10^{-9}$
800	$1.5x10^{-9}$	$2.5x10^{-9}$
1300	$1.1x10^{-9}$	$1.9x10^{-9}$
1500	$1.0x10^{-9}$	$1.8x10^{-9}$

6.4.4.3 Intermediate Frequency Process – A Mixed Response

In the impedance spectra measured at 350°C, an intermediate frequency relaxation process can be observed at about 400Hz. As mentioned earlier on, when the alumina layer is not continuous, the response from the alumina layer is suppressed by the short-circuiting of the mixed oxide. There are only two relaxation processes for the L200 samples at 350°C, of which the low frequency process is at about 400Hz which corresponds to the IF process in the impedance spectra for the M400 samples. The intermediate frequency process was ascribed to the mixed oxide by Ogawa *et al.* (1999), as it was observed there was a mixed oxide layer present between the top coat and bond coat in the microstructure of TBCs. However this ascription is questionable.

In order to make clear whether or not the mixed oxide is mainly responsible for the intermediate frequency relaxation process, a free-standing top coat (YSZ), in which the presence of mixed oxide can be ruled out, was measured using two identical silver electrodes. The free-standing top coat was as-sprayed and provided by the same company as our TBCs. The impedance spectra of the free-standing top coat (Fig. 6-17) was very much the same as that of 0h TBCs sample, except the electrode effect which was absent with silver electrodes. This is understandable because a silver electrode has been found to show less polarisation resistance. The high solubility of oxygen in silver induces the spreading of the electrode reaction zone over the whole electrolyte interface, thus reducing the blocking of oxygen ions at the interface (Drevet *et al.* 2000). This also indicates that the low frequency tail in the impedance spectra for L200 samples should be due to the response of the top coat/mixed oxides interface. The electrode effect curve becomes larger as oxidation time is prolonged. This implies the YSZ/mixed oxides interface is changing with oxidation time. It is possible that more meaningful information can be extracted by analysing systematically the change of the electrode effect. This, however, is beyond the scope of the present study.

The free-standing YSZ has a relaxation process at about 800 Hz, which is very close to that of the YSZ as top coat in TBCs after oxidation. In the meantime, the capacitance associated with this relaxation process of the free-standing YSZ is also similar to that of the intermediate frequency relaxation of TBCs after oxidation. This indicates that the intermediate frequency relaxation process may not be associated with mixed oxide.

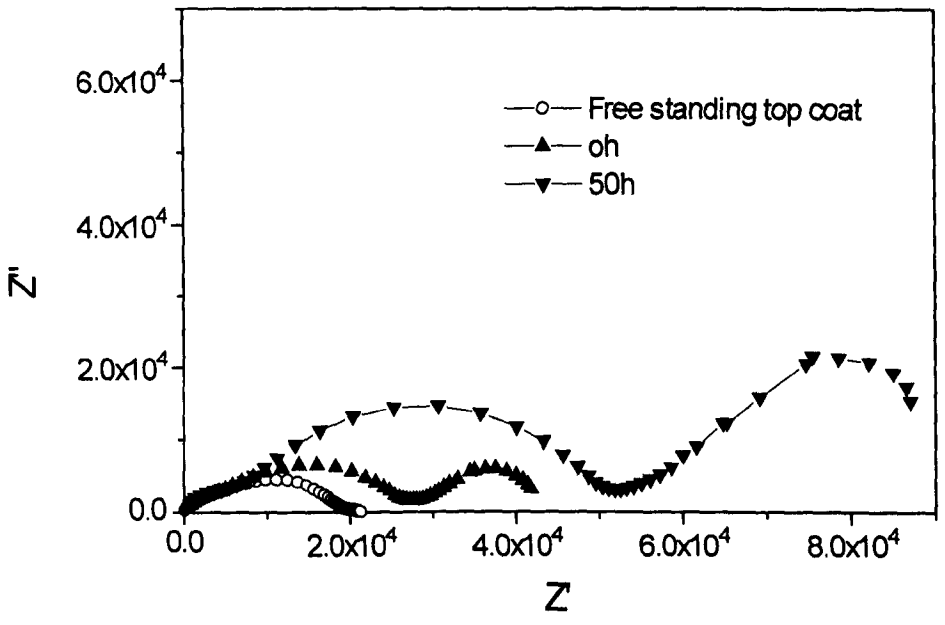

Figure 6-17 Comparison of the IS of a free-standing top coat with those of oxidised samples.

The capacitance of the intermediate frequency relaxation process (i.e., the mixed response) does not seem to decrease monotonically with the oxidation time (Fig. 6-15b), although our SEM observations clearly revealed that the amount of mixed oxide increased with the oxidation time. This suggests the mixed oxides should not be the main contributor to the intermediate frequency process. In addition, our impedance measurements on Ni_2O_3 and Cr_2O_3 revealed that Ni_2O_3 and Cr_2O_3 exhibit quite high conductivity and the relaxation for these materials are well above 10^6 Hz at 350°C. Assuming the mixed oxide have similar electrical properties to nickel oxide and chromium oxide, since both of which are the main constituents of the mixed oxide according to EDS micranalysis, the relaxation frequency of the mixed oxide should be much higher than the intermediate relaxation frequency. Therefore it seems more reasonable that the intermediate frequency relaxation process can be ascribed to the blocking effect of microstructural defects in the top coat. It is well established that microstructural defects: including grain boundaries, pores, microcracks and impurity inclusions etc., normally have a combined contribution to the same relaxation process

that is called intergrain (or grain boundary) semicircle in the complex impedance plot (Steil *et al.* 1997; Tiefenbach and Hoffmann, 2000).

A typical YSZ microstructure is composed of grains a few microns in size and with grain boundaries a few nanos thick (Badwal, 1995). Thus the capacitive effect of grain boundaries should be at least 2~3 orders of magnitude higher than that of the bulk. The capacitive effect of the intermediate frequency process for the L200 sample is about one order of magnitude higher than that of top coat. This further supports the assumption that the intermediate frequency process is not only from grain boundaries, but from other microstructural defects as well.

According to the fitted results in Fig. 6-13, the n value of the mixed response shows a sharp increase during the initial 200h oxidation and the parameter A shows a sudden drop for the same oxidation period. After 400h, the n value decreases gradually with oxidation, while parameter A does not appear to change with oxidation. Meanwhile the resistance also exhibits an increase in the first 200h oxidation. It is difficult in this stage to find out what is exactly responsible for these variations of IS parameters. However, there are a few speculations that are worth mentioning. The first is that high temperature annealing leads to not only the disappearing of the t' phase, but also grain boundary degradation (Badwal *et al.* 1998). For example, segregation of yttrium along grain boundaries has frequently been observed (Whalen *et al.* 1987; Hughes and Badwal, 1991). This would increase the resistance of grain boundaries. The second is that Cr_2O_3 is gaseous at high temperature, due to a reaction of Cr_2O_3 with oxygen (Sterns *et al.* 1974). Gaseous Cr_2O_3 could reach, through the porous top coat, to the inside surfaces of cracks and pores, as well as at the grain boundaries. This would aggravate the degradation of grain boundaries and increase the inhomogeneities, and therefore result in the decrease of n value with prolonged periods of time. The third is that the tetragonal to monoclinic phase transformation is rapid and accompanied by 5~7 % of volume expansion (Lange, 1982a & b), which could result in an increase of microcracks in the top coat because of the volume mismatch between monoclinic zirconia and tetragonal/cubic zirconia. The increase of microcracks in the top coat is expected to increase the resistance and decrease the capacitive effect of the intermediate frequency process, which seems to agree with the variations of IS parameters of the top coat with oxidation time as shown in Figs. 6-13 and Fig. 6-15b. However, the steep increase of the n value and abrupt drop of the

parameter A for the initial 100h oxidation still cannot be explained based on current knowledge. Obviously, further detailed work is needed to elucidate the relation between the impedance and the degradation of the top coat.

6.4.5 Determining The Thickness Of The Oxide Layer

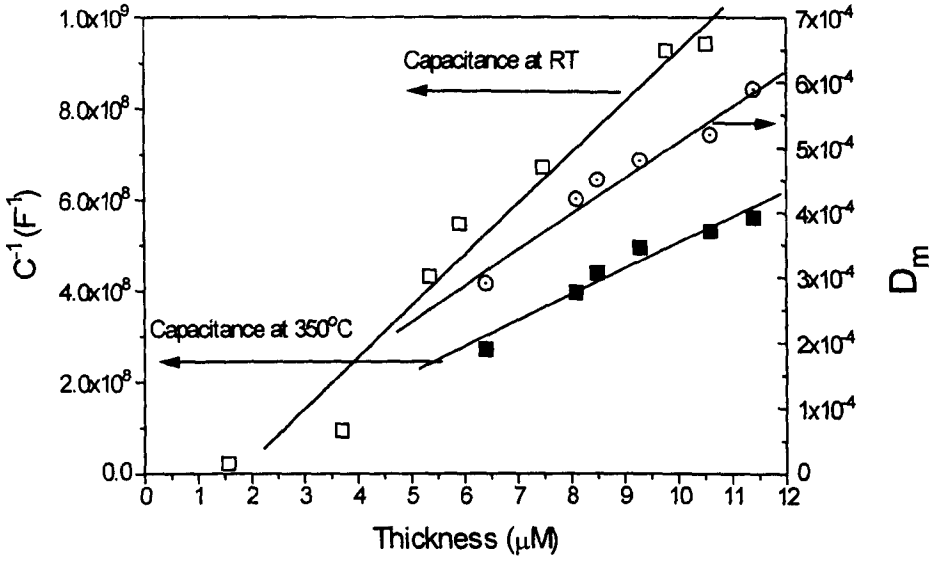

Figure 6-18 Linear relationships of the reciprocal capacitance vs thickness and diameter in modulus spectra (D_m) vs thickness, where $D_m=C_o/C_{ox}$, a dimensionless parameter.

One of the main objectives of this work was to detect nondestructively the thickness of the oxide layer. As discussed in section 6.4.3, the thickness of the oxide layer is quantitatively related to the capacitance by Eqn.6-3. To examine the linear relationship between the thickness and the reciprocal capacitance as indicated by Eqn.6-3, the capacitance derived from the IS parameters is plotted in Fig. 6-18 as a function of the thickness that was determined based on the SEM observations. A linear relationship is well established for both cases at R.T and 350°C, indicating that it is feasible to determine the thickness using capacitance. However, to work out the equivalent capacitance of the oxide layer is not that straightforward. To obtain the IS parameters, tedious fitting procedures are needed. By contrast, the method using the complex modulus plot to determine the thickness of the

oxide layer is simple and effective, and has been successfully applied in the detection of the oxide layer in Al_2O_3/SiC nanocomposites as described in chapter 5.

Figs. 6-6e,f give the complex modulus plane plots at 350°C of the as-received and oxidised samples, where the low frequency process is at the left hand and the high frequency process is at the right hand; corresponding to the oxide layer and the top coat respectively. The diameter of the right semicircle is similar for all the samples, while the diameter of the left semicircle increases with the oxidation time, indicating the thickness of the oxide layer increased with the oxidation time.

By referring to the discussion in section 4.3, the diameter (D_m) for the left semicircle is equal to C_o/C_{ox}, where C_o is the capacitance of the empty cell, C_{ox} is the capacitance of oxide layer. In the light of Eqn. 6-3, the diameter D_m is related to the thickness of the oxide layer by the following equation:

$$D_m = \frac{C_o \bullet \delta}{\varepsilon \bullet \varepsilon_o \bullet A_e} \qquad (6\text{-}5)$$

where the electrode area (A_e) was the same for all the impedance measurements, C_o was assumed to be constant when the electrical modulus data were calculated by using the equation: $M^*=-2\pi f C_o Z^*$. Therefore, the diameter in the modulus spectrum (D_m) should be linearly related to the thickness (δ) of the oxide layer in TBCs:

$$D_m = C_c \delta$$

with the constant:

$$C_c = \frac{C_o}{\varepsilon \varepsilon_o A_e}$$

As shown in Fig. 6-18, D_m is in a good linear relationship with the thickness; by linear regression fitting, the slope, i.e., $C_c=5.5\times10^{-5}$ μm^{-1}.

6.5 Summary And Conclusions

The bond coat in TBCs exhibited a fast oxidation in the initial stages when heat-treated at 1100°C in air. The oxide grew steadily after 20h oxidation. The kinetics of oxidation followed a parabolic law. SEM observations and EDS analyses revealed the oxide layer formed in the initial stages was composed of both mixed oxides and alumina and a continuous alumina layer was not formed until after 400h oxidation.

Impedance measurements at R.T demonstrated that there were two relaxation processes for oxidised samples, one corresponding to the top coat and the other to the oxide layer. The impedance measurements at 350°C showed that there were three relaxation processes in the samples oxidised for more than 400h, while only two relaxation processes for the samples oxidised for less than 200h. The high frequency process corresponds to the top coat and the low frequency process to the oxide layer. It is postulated that the third relaxation process at about 400Hz was a response mainly from grain boundaries, pores and cracks in the top coat, rather than from the mixed oxide.

Comprehensive equivalent circuits were proposed and these can be significantly simplified based on the analysis of the microstructure of TBCs. The simplified equivalent circuits fit experimental data very well, indicating the IS parameters obtained by fitting are reliable. Based on the analysis of impedance spectra and IS parameters, it has been found that not only the characteristics of the oxide layer, but also the degradation of the top coat, can be monitored non-destructively by impedance measurements. However, further work is needed to clarify the relation between the IS parameters and the top coat degradation.

The capacitance derived from impedance measurements at both RT and 350°C shows a monotonic dependence on the oxidation time. The reciprocal capacitance and the semicircle diameter in the complex modulus plane have a linear relation with the thickness of the oxide layer. Modulus spectra have been proven to be a very useful non-destructive approach to examine the growth of the oxide layer in TBCs. Therefore it is highly feasible to determine the degradation of TBCs using IS.

7 Characterisation Of Clay Sintering Process Using IS

7.1 Introduction

In-situ monitoring of sintering processes is extremely important for understanding the sintering mechanisms and improving the efficiency of ceramic manufacturing processes. Clay is the principal raw material for producing conventional ceramics, such as whiteware and porcelain, so the majority of conventional ceramics are clay-based ceramics. Clay-based ceramics have a wide range of applications and they are the most complex ceramic materials. Whiteware, i.e., floor and wall tile, artware and pottery, dinnerware and fine china, sanitaryware and food-serviceware etc., embraces an important industry, which accounts for about 7% of the entire ceramic market worldwide (Carty and Senapati, 1998). Because the complicated reactions occurring in clay based ceramics are kinetically governed, rather than thermodynamically equilibrated processes, the measurement of temperature alone often does not provide sufficient information for monitoring and thereby controlling the sintering processes (Carty and Senapati, 1998). Traditionally pyrometric cones were developed to follow the firing progress. Pyrometric cones are three-sided pyramids made from mixtures of kaolin, feldspar, quartz and other raw materials resembling the body composition that function as true indicators of reaction kinetics in porcelain bodies (Fairchild and Peters, 1926; McCaughey and Neff, 1944). Modern commercial firing processes are still often checked with pyrometric cones for verification of the heat work accomplished. For this reason, it is desirable to develop an effective approach for the *in-situ* characterisation of the sintering of clay-based ceramics.

The purpose of this work is to use IS as a non-destructive approach for characterising the real-time sintering process of clay-based ceramics. Liquid phase sintering is the dominant mechanism in the sintering of clay-based ceramics (Kingery *et al.* 1976b). The formation of the liquid phase is a crucial step in the process in which the fluidity of liquid initiates compact shrinkage. The quantity and the viscosity of the liquid phase are the two important factors that determine the kinetics of sintering (Anseau *et al.* 1981). The liquid phase formed in the ceramic compact at high temperatures is an ionic conductor and thus

acts as an electrolyte (Morgan and Koutsoutis, 1986). Microstructural parameters, such as the quantity of liquid phase, the porosity content and the distribution of different phases as well as the chemical composition of the liquid phase would affect sintering process and these parameters would also keep changing as sintering proceeds. Monitoring the sintering of clay-based ceramics using IS will provide important information on sintering phenomena in clay-based ceramics.

In this study, impedance measurements were made *in-situ* while a clay compact was being fired at different temperatures. The impedance spectra of clay compacts under firing consist of a high frequency semicircle and a low frequency tail, which have been proven to correspond to bulk specimen and electrode effect respectively. The high frequency semicircle is informative regarding the electrical properties of the bulk specimen. The variation of bulk conductivity with sintering time, which can be deduced from isothermal impedance spectra, was found to be in agreement with the shrinkage curve. An equation relating the electrical conductivity to the density of the specimen has been established. The electrode effect curve has a strong temperature dependence, which is directly related to the capacitive effect of the electrode /specimen interface. This capacitive effect has been proven to correspond to the blocking anode where a double layer charging is built up by the accumulation of the non-bridging oxygen ions nearby anode. The low frequency tail can be an indicator of local temperature. In addition, variations of the IS parameters with sintering temperature were found to be sensitive to the formation of liquid phase.

7.2 Experimental Procedure

7.2.1 Sample Preparation

Ball clay (Dorset, HYMOD PRE) was ball-milled in the dry mode for 5 h to produce a powder of uniform particle size. The chemical composition and particle size distribution specified by the powder supplier are given in Table 7-1 & 7-2 respectively. Pellets 13 mm in diameter and 3~4 mm in thickness were prepared by uni-axial pressing using a pressure of 120 MPa. Before sintering the green clay compacts were carefully polished with SiC paper to ensure every sample was in a regular geometric shape.

Table 7-1 Chemical composition of ball clay (wt %)

SiO_2	Al_2O_3	Fe_2O_3	TiO_2	CaO	MgO	K_2O	Na_2O	L.O.I*	C
54	30	1.4	1.3	0.3	0.4	3.1	0.5	8.8	0.3

- Loss of ignition

Table 7-2 Particle size distribution of ball clay (wt %)

< 5μm	< 2μm	< 1μm	< 0.5μm
96	88	79	67

7.2.2 Impedance Measurements

The rig shown in Fig. 3-6 was used for impedance measurements at high temperature. Since the resistance of the leads connecting the electrodes to the impedance analyser was much smaller than that of the tested samples, the influence of the leads on the impedance measurements was negligible. Data acquisition was undertaken using a PC computer in real time when the clay compact was being fired at different temperatures. Measurements were taken over a frequency range of 10^6 to 0.1 Hz using a 1 Vrms applied voltage with 3~6 readings per decade of frequency. Our preliminary experiments revealed that measurements with voltages lower than 0.2 Vrms resulted in an unstable signal, while measurements with voltages 0.2~3 Vrms gave stable signals and reproducible results. Therefore, the voltage of 1 Vrms was chosen for all the impedance measurements.

7.3 Results

7.3.1 Impedance Spectra During Heating

Impedance measurements need to be made using a set of frequencies, usually scanning from high frequency down to low frequency with a few data readings for each decade. For this reason, a single cycle of measurement will take a few minutes, sometimes even a few days, depending on the chosen frequency range and the number of data readings for

each decade. Therefore the sample under investigation needs to be kept in a steady state during the impedance measurements so that it does not change with time and many measurements can be averaged (Macdonald and Johnson, 1987). For this reason, the measurement needs to be made isothermally, and the measuring temperature needs to be controlled to be as steady as possible.

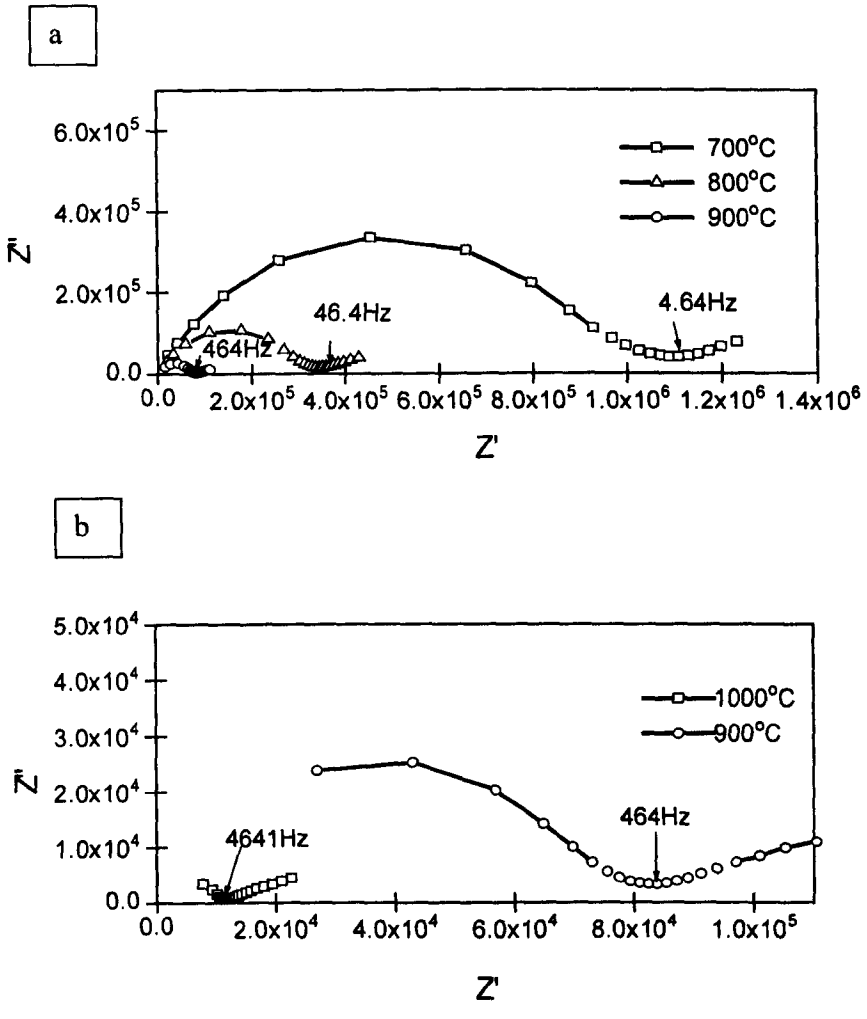

Figure 7-1 Complex impedance plots of the clay compact at (a) 700°C, 800°C, 900°C; (b) 900°C, 1000°C.

In this work, isothermal impedance measurements were made at various temperatures in the range of R.T~1200°C during heating. It was found that the impedance spectra

measured at temperatures above 500°C are reproducible, but at temperatures below 500°C, the reproducibility was poor. Several factors could affect the reproducibility of impedance measurements, e.g. incomplete contact between sample and electrode, short circuit through a less resistive path in the clay (for example, because of the presence of moisture in clay), as well as possible physicochemical reactions occurring in the compact, which will be dealt with later on.

Typical complex impedance plots are shown in Fig. 7-1 where the spectra at 700°C, 800°C, 900°C and 1000° are given. There is a high frequency semicircular arc and a low frequency tail in each of the complex impedance plots. Both the high frequency arc and the low frequency tail become smaller with increasing temperature and the cut-off frequency between the high frequency arc and low frequency tail increases from 4.6 Hz at 700°C to 4600 Hz at 1000°C. The cut-off frequency represents the transition from one relaxation process to another. Measurements made by using samples with different thicknesses showed that the thickness of the sample only affected the high frequency arc radii, but had little effect on the low frequency tail. Therefore the high frequency arc may be attributed to bulk effect and the low frequency tail to the effect of electrode.

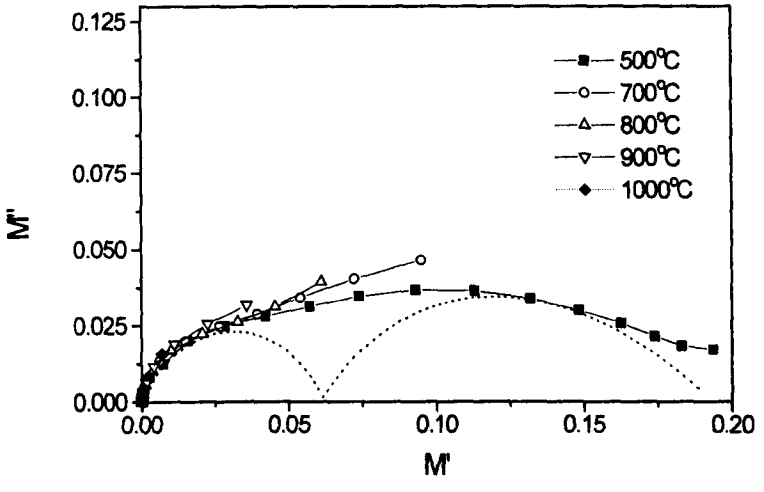

Figure 7-2 Complex modulus plots at different temperatures of green clay form during heating.

Fig.7-2 shows the complex modulus plots at different temperatures. The modulus spectrum at 500°C seems to consist of two overlapped arcs, and the high frequency arc

(right hand) gradually disappeared when the temperature increased. When the temperature reached 1000°C, even the low frequency arc became smaller. The disappearance of the bulk arc in the modulus spectra indicates that the clay compact becomes more conductive with increasing temperatures.

In order to examine the time dependence of the impedance spectra, the impedance measurements were made repeatedly every 5 minutes at a given temperature. As mentioned earlier on, a single cycle of impedance measurements needs at least a few minutes to finish. Here the frequency range of 10^6 –10^3 Hz was selected with 6 data acquisitions per decade, which would take 2.62 minutes for a single cycle to finish. Therefore the total time elapsed between two cycles was 7.62 minutes.

Fig.7-3a shows the multi-cycle impedance measurements at 800°C, where the impedance spectra for different cycles entirely overlap. This suggests that there could not be significant physicochemical change occurring in the clay compact at this temperature. On the other hand, the impedance spectra measured at temperatures above 950°C (Figs. 7-3b-c) show a gradual shift towards the left. As shown in Figs.7-3b-c, the spectra shift is faster at the initial stages of sintering than at the later stages of sintering. In addition, the spectra shift is faster at the higher sintering temperature. The trend of spectrum shifting is consistent with the sintering behaviour of ceramics where the densification rate is higher at higher temperature and it slows down when the shrinkage curve approaches an asymptote.

As will be discussed in detail later in this chapter, the shrinkage curve measured by dilatometry shows the clay compact starts to shrink at a temperature of about 950°C, the shifting of the spectrum can be a consequence of the densification of the compact under firing. During sintering, the density increases with the sintering time. The increase in density means the effective conduction area in the bulk is increased, which gives rise to a decrease in resistance.

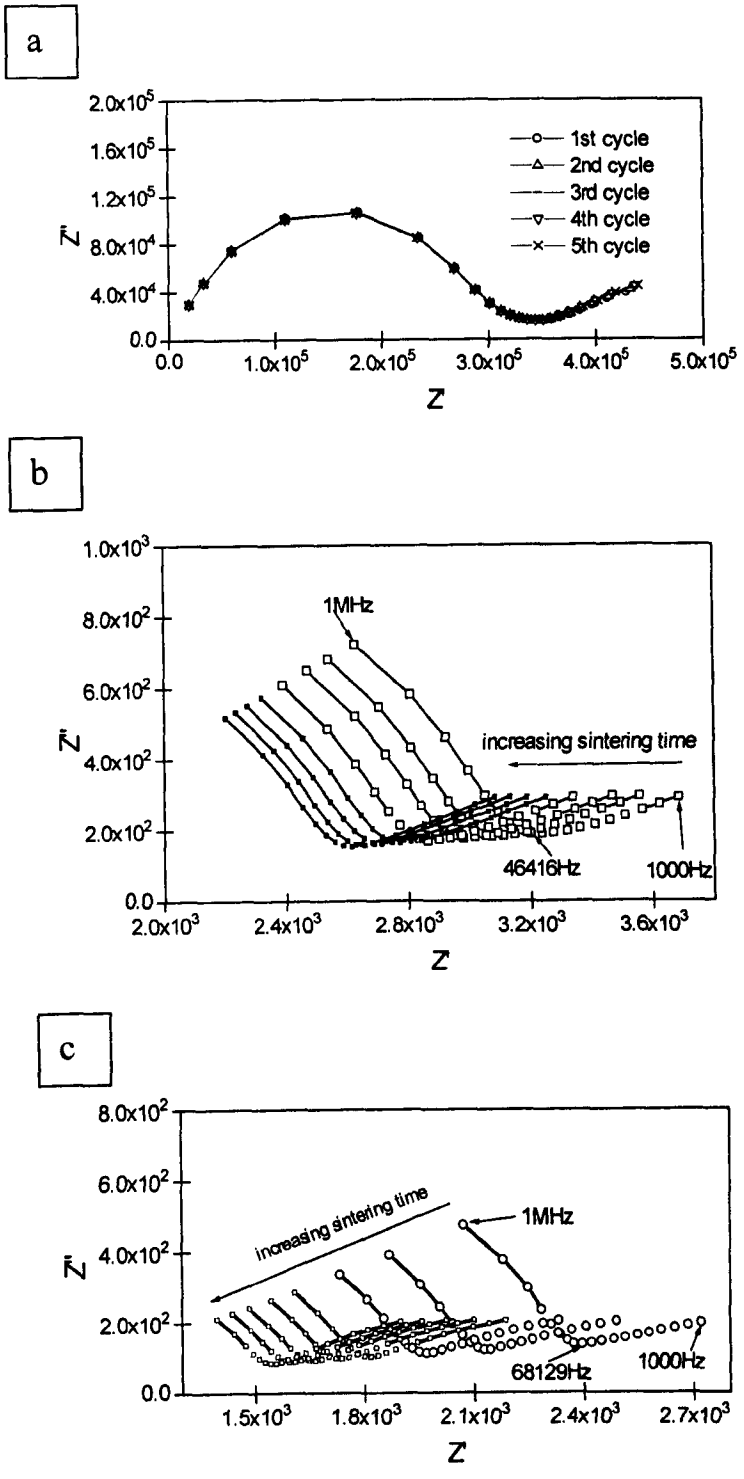

Figure 7-3 Multiple impedance measurements at time intervals of 5 min, each measurement taking 2.62 minutes at (a) 800°C; (b) 1050°C; (c) 1100°C.

It is worthwhile noting that during isothermal sintering, some spectrum features, e.g., the dielectric loss, the cut-off frequency and the height of the low frequency tail, etc., hardly changed as the sintering time was increased. This might indicate that there was not much change in the physical and chemical properties during isothermal sintering, except the change in the size of the specimen.

It is also important to point out that the height of the low frequency tail appeared to be an indicator of temperature. As in Fig. 7-4, the height of the low frequency tail is referred to as the imaginary component of the impedance at 0.1Hz, the lowest frequency used in these measurements. For all the cases, the tail height changed little during isothermal sintering, but changed significantly with the temperature. Table 7-3 gives the tail height at different temperatures.

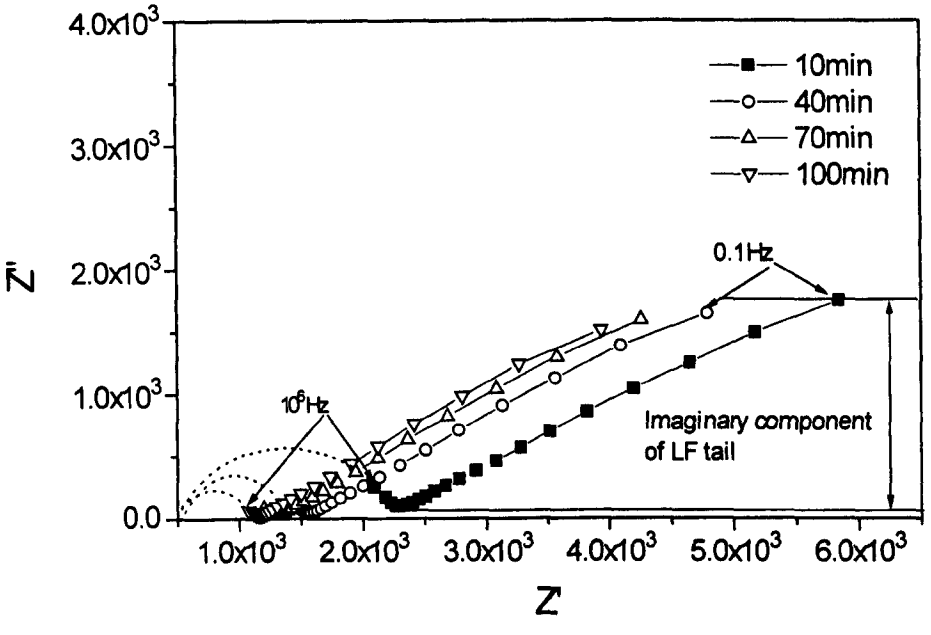

Figure 7-4 Complex impedance plots for clay compact under firing at 1100°C, at different sintering times, frequency range used being 10^6 ~10^{-1} Hz.

Strictly speaking, it is impossible to obtain a set of impedance data corresponding to a steady state of the material under sintering, because the material is undergoing a

continuing change at a given temperature, so the electrical properties under this circumstance should change continuously. However we found that the main features of the impedance spectrum obtained during sintering remained more or less the same. In impedance measurements, the high frequency data takes less time than low frequency data to acquire. For example in this study, data acquiring for the bulk semicircle (in the high frequency range) took less than 0.5 minute. The measurements for the bulk effect were very quick, so the impedance spectra thus obtained can be regarded as representing an average state of the specimen over a single cycle of measurement, which was 2.62 minutes in the case shown in Fig. 7-3.

Table 7-3 Tail height at different temperatures

Temperature (°C)	**700**	**800**	**900**	**1000**	**1100**
Tail height (Ω)*	$1x10^5$	$4x10^4$	$1.5x10^4$	$4.2x10^3$	$1.8x10^3$

*** The electrode area was the same for all the measurements: equal to 0.64cm^2.**

7.3.2 Impedance Spectra During Cooling

After having been sintered at 1200°C for 4h, the sintered body was cooled to R.T. To observe the variation of the impedance spectra with the change in temperature, similarly to the case of the green compact during heating, isothermal impedance measurements were made at every interval of 100°C from 1200 °C to R.T, during the cooling of the sintered body.

Figs.7-5a-c show the impedance spectra at different temperatures. The spectra of the sintered specimen consisted of a high frequency semicircle and a low frequency tail, as in the spectra of the green compact. The semicircle diameter increased with the decrease in temperature. As expected, there was no change in the spectra during the isothermal measurements.

As a whole, the features of the impedance spectra are very similar to those of the green compact, except that the bulk semicircle of the sintered body is much smaller, and the bulk and electrode effects are better resolved. The complex modulus plots of the sintered

body shown in Fig. 7-6 are also similar to those of the green compact: as measurement temperature decreased, the bulk arc became more complete.

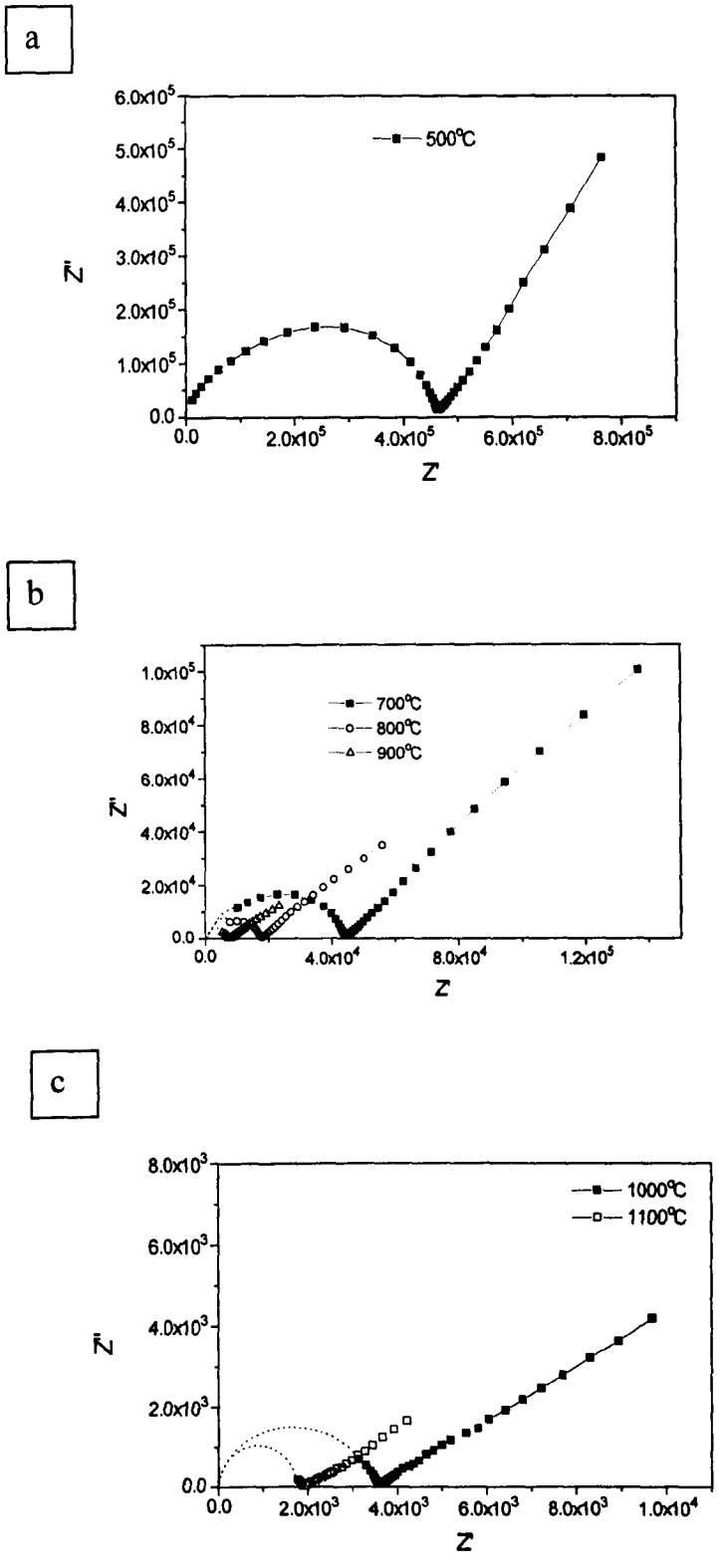

Figure 7-5 Complex impedance plots for sintered bodies measured isothermally at different temperatures.

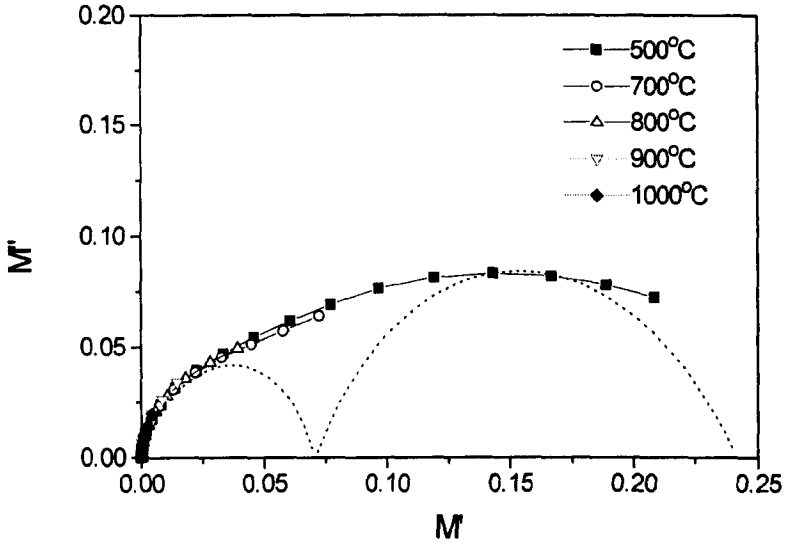

Figure 7-6 Complex modulus plots for sintered bodies at various temperatures during cooling.

7.3.3 Characterisation Of Clay Compacts Using Conventional Characterisation Techniques

In order to examine what physicochemical processes occurred in clay compacts during heating and sintering, and relate these to the impedance spectra, some conventional characterisation techniques, i.e., TGA, XRD, dilatometer measurements and SEM were used to examine the clay compact.

Fig. 7-7 gives the TGA result from the clay powder, where we can see two steep drops, one in the temperature range of 50-150°C, the other one between 420 and 550°C. Kaolinite is the main constituent of clay mineral. The crystal structure of kaolinite contains hydroxyl groups and the dehydroxylation of these groups to form metakaolin occurs at about 550°C (Brindley and Nakahira, 1959a&b):

$$Al_2O_3 \cdot 2SiO_2 \cdot 2H_2O \rightarrow Al_2O_3 \cdot 2SiO_2 + 2H_2O\uparrow \qquad (7\text{-}1)$$

Therefore the weight loss occurring in the range 420-550°C can be attributed to the dehydroxylation of kaolinite. The weight loss in the range 50-150°C is probably due to

the loss of moisture that is physisorbed at the particle surfaces. Since both physisorbed and chemisorbed moisture can significantly affect the electrical properties of the powder compact (Traversa, 1995), the poor reproducibility of impedance data we observed at temperatures below 500°C was largely due to the presence of moisture in the clay compact.

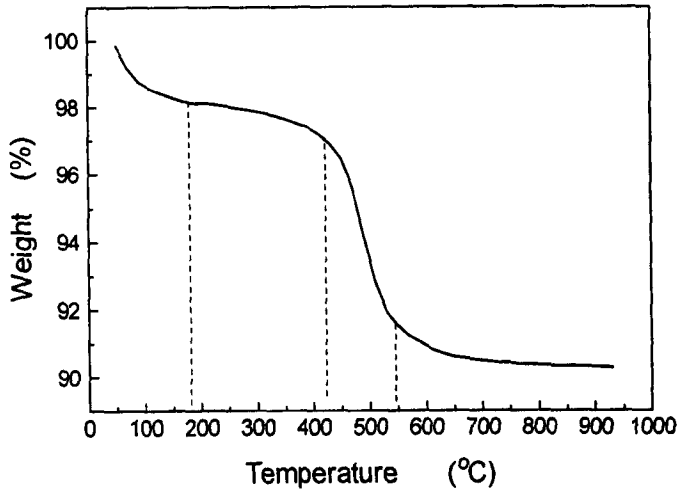

Figure 7-7 Thermogravimetric analysis of clay powder from R.T to 950°C

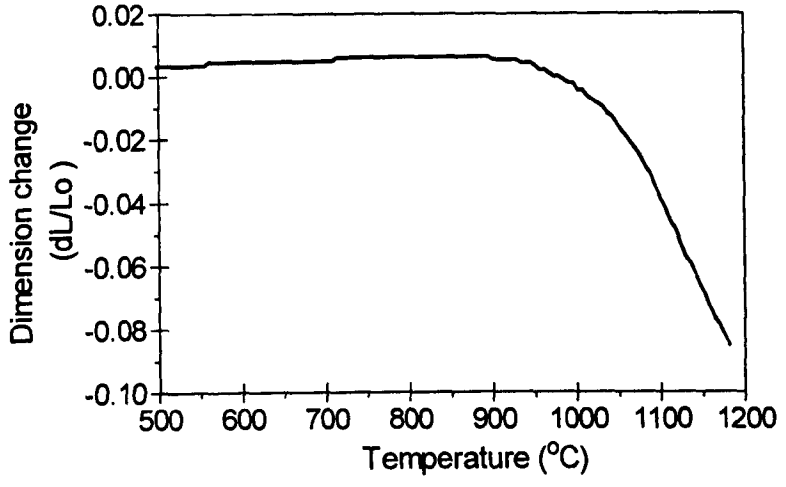

Figure 7-8 Shrinkage curve of clay compact obtained from dilatometer measurements.

The shrinkage curve of the clay compact measured by dilatometer is shown in Fig.7-8, where we can see noticeable shrinkage starts at about 950°C and the shrinkage rate increases as the temperature is then raised.

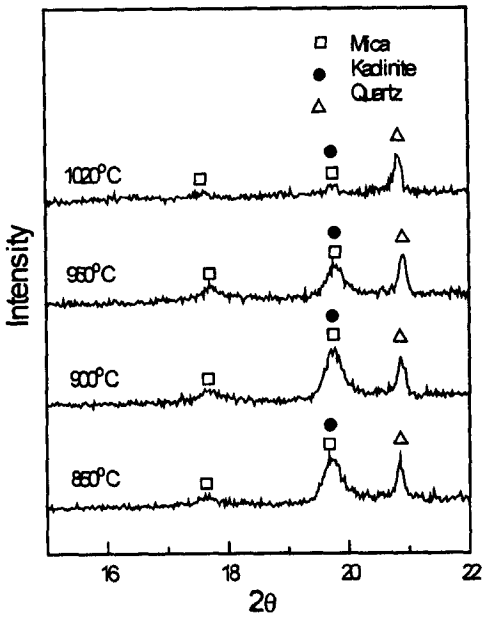

Figure 7-9 X-ray diffraction patterns of the clay compacts after 15minutes sintering at different temperatures.

The XRD analyses (Fig. 7-9) after heat treatment at 850°C and 900°C shows that no apparent phase transformations occurred in the clay compacts, whereas after heat treatment at 950°C the amount of kaolinite and mica appeared to decrease. The heat treatment at 1020°C led to almost complete disappearance of kaolinite and mica. Meanwhile the phase transformation in the clay also involved the disappearance and formation of glassy phases. It is believed that the diminishing mica and kaolinite contents in the clay compacts are related to the formation of a liquid phase (Shuller, 1964; Sonuparlak *et al.* 1987;Okada *et al.* 1986). Therefore the XRD analyses suggest the presence of the liquid phase in clay at temperatures between 900 and 950°C.

The dominant mechanism in the sintering of clay-based ceramics is vitrification where significant shrinkage cannot occur unless a certain amount of liquid phase is present (Anseau *et al.* 1981). In this sense, the XRD analyses in Fig. 7-9 are in agreement with the shrinkage measurement shown in Fig.7-8, both suggesting that the liquid phase occurs at about 950°C. This is further confirmed by the SEM observations (Fig. 7-10).

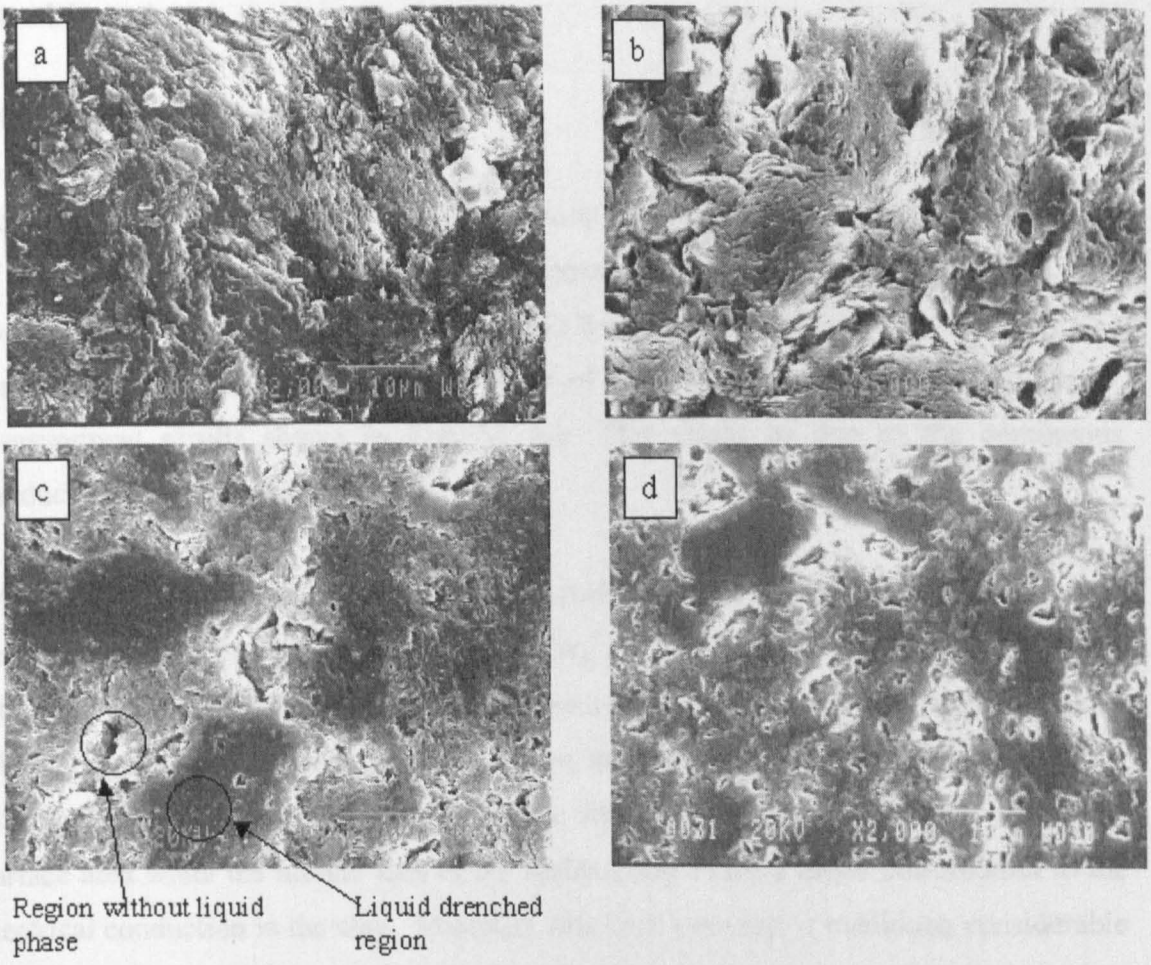

Figure 7-10 SEM micrographs of polished surfaces of the sintered or semi-sintered clay compacts after being fired for 15minutes at (a) 850°C; (b) 900°C; (c) 960°C; (d) 1020°C.

Clay mineral has a platy habit, because the main constituent of clay–kaolinite is composed of $[Si_2O_5]^{2-}$ layers and $Al_2[(OH)_4]^{2-}$ layers (Kingery *et al.* 1976a). At temperatures below 950°C (Fig.7-10a, b) when there is no liquid phase in the clay compact, the polished surface shows a rough morphology and the platy nature of the clay mineral can be identified. At 960°C (Fig.7-10c), most of the surface area is covered by smooth morphology, which is a consequence of liquid drenching, but some regions still have not been touched by the liquid phase. When the temperature goes up to 1020°C (Fig.7-10d), liquid phase seems to have reached everywhere except pores, and therefore the clay compact is composed of a continuous network of glass drenched-regions and many small pores.

7.4 Discussion

7.4.1 Equivalent Circuit Models

According to a brick layer model as discussed in Chapter 2, the complex impedance plot of a polycrystalline ceramic material is expected to have two semicircular arcs, one corresponding to grains and the other to grain boundaries. However, there was only one semicircle corresponding to the bulk effect of the clay, according to the impedance measurement results shown in Figs.7-1 a-b. This might be due to the continuous conduction path in the clay compact.

At relatively low temperature before the liquid phase was formed, the conduction is through the surfaces of the clay particles. Clay minerals consist of hydrated aluminum silicates that are fine-grained and usually have a platy habit where positive ions, such as alkali ions and alkali earth ions, can fit on the surface of the particles or between different layers (Kingery *et al.* 1976a). The fine microstructure leads to a large free surface area while the mobile ions at the surface may make a major contribution to the electrical conduction in the clay. Materials with high porosity, if exhibiting considerable particle surface conduction, normally do not show resolved grain and grain boundary effects in their impedance spectra, because the conduction path along particle surfaces is an 'easy path'. This is similar to the case of ionic-type humidity sensors. In these sensors, the proton hopping between neighbouring water molecules on particle surfaces is the dominant conduction mechanism (Traversa, 1995). Because of the 'easy path' at the surface, there is usually only one semicircle corresponding to these sensors, which have been witnessed in the works of Hwang *et al.* (1995) and Gusmano *et al.* (1996).

At temperatures above 950°C when a continuous network of glass phase is present in the clay, the charge carriers, e.g., the alkali ions, can transport along the network without experiencing a significant blocking effect. Therefore there is usually only one semicircle in the complex impedance plot for glass samples. Such behaviour has already been observed by other researchers with the glass containing crystallised particles and pores (Murugan and Varma, 2001; Abrahams and Hadzifejzovic, 2000). Therefore the continuous conductive path model as mentioned in Section 2.5 is applicable to the clay compact during sintering.

A tail (sometimes called a 'spike') is always present in the complex impedance plot at low frequencies, which is an electrode effect. The electrode effect is frequently seen in the impedance measurements of cement paste (McCarter *et al.* 1988; Christensen *et al.* 1992), humidity sensors (Hwang *et al.* 1995; Gusmano *et al.* 1996), and other ionically conducting materials (Steil *et al.* 1997). According to the equivalent circuit fitting, a high capacitive effect is associated with the low frequency tail. The electrode effect is a response from the electrode/material interface which is very thin in thickness and the electrode effect normally has a very high capacitive effect.

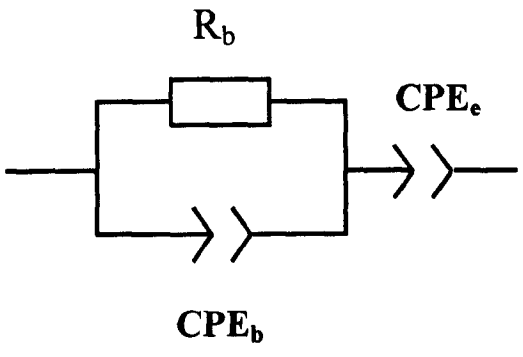

Figure 7-11 Equivalent circuit model for clay compact.

The equivalent circuit for the clay compact can be given as in Fig. 7-11, where a parallel R-CPE element represents the bulk clay compact, and a CPE represents the electrode effect. Here a single CPE, rather than a parallel R-CPE, is used to represent the electrode effect. This is because the platinum/clay interface is believed to be a blocking interface, i.e., the resistance can be regarded as infinitely large. The electrode effect should have been purely capacitive and represented by a straight line vertical to the x-axis. Here a tail-like line, rather than a straight line normal to the x-axis, is obtained in the complex impedance plane. This is because the electrode/material interface is very rough and the electrode/material contact is far from ideal.

7.4.2 Fitted Results

Table 7-4 Fitted results for clay compact during heating

Temperature (°C)	R_b (ohm)	A_b ($ohm^{1-n} \bullet F^{-n}$)	n_b	A_e ($ohm^{1-n} \bullet F^{-n}$)	n_e
700	$1.0x10^6$	$2.0x10^{-10}$	0.73	$2.6x10^{-6}$	0.17
800	$3.2x10^5$	$2.7x10^{-10}$	0.73	$7.0x10^{-6}$	0.16
900	$7.6x10^4$	$3.6x10^{-10}$	0.74	$2.6x10^{-5}$	0.16
1000	$7.8x10^3$	$4.5x10^{-10}$	0.75	$7.8x10^{-5}$	0.25
1100	$2.2x10^3$	--------	-------	$1.0x10^{-4}$	0.27

The fitted results for the green clay compact during heating are given in table 7-4. The resistance of the specimens decreases with increasing temperature while the parameters for CPEs increase with increasing temperature. The parameter A_e (for the electrode effect) is about five orders of magnitude larger than A_b (for the specimen). The exponential index for the bulk, n_b, is much closer to 1 than that for the electrode effect, n_e. This indicates that the CPE_e in Fig. 7-11 assigned for the electrode effect is far from being an ideal capacitor. For a perfect flat blocking electrode, the electrode effect is expected to be purely capacitive (Armstrong and Todd, 1995; Raistrick, 1987). But under the experimental conditions, the contact between the clay compact and platinum electrode was poor and the electrode/clay interface was rough. It is well established that the porosity of specimen or roughness of the electrode surface leads to a frequency dispersion of the interfacial impedance and produces a constant phase angle (Armstrong and Todd, 1995; Raistrick, 1987). The n_e obtained here is only 0.157~0.274, which implies that the electrode/clay interface is very rough.

Table 7-5 IS parammeters of the sintered specimen

Temperature (°C)	R_b (ohm)	A_b ($ohm^{1-n} \bullet F^{-n}$)	n_b	A_e ($ohm^{1-n} \bullet F^{-n}$)	n_e
500	$3.6x10^5$	$1.9x10^{-10}$	0.76	$2.2x10^{-6}$	0.62
700	$4.5x10^4$	$2.0x10^{-10}$	0.80	$1.1x10^{-5}$	0.52
800	$1.9x10^4$	$8.5x10^{-11}$	0.86	$2.2x10^{-5}$	0.47
900	$5.1x10^3$	$1.9x10^{-10}$	0.80	$6.3x10^{-5}$	0.38
1000	$3.5x10^3$	$1.2x10^{-10}$	0.85	$1.5x10^{-5}$	0.36
1100	$2.1x10^3$	-------	---------	$1.0x10^{-4}$	0.27

Table 7-5 shows the IS parameters obtained from fitting the impedance spectra of sintered specimens at different temperatures. The bulk resistance increased with a decrease in temperature. Temperature had little effect on A_b, however A_e decreased considerably with a decrease in temperature. It is interesting to note that n_e shows an increasing trend as the temperature is decreased, which cannot be interpreted at the present stage. However, by comparing Table 7-4 and Table 7-5, it is obvious that the n_e value for the sintered body is higher than that for the green clay compact. This is reasonable, because the sintered specimen has a smoother contact with the electrodes, while the green clay compact had a poor contact with electrode due to the rough compact surface. Therefore the steepness of the low frequency tail seems to be able to represent the condition of the electrode/compact interface.

The dielectric constant of the bulk specimen can be obtained by employing an equation developed by Christensen *et al.*(1994):

$$\varepsilon=(2\pi f_{top})^{(2\theta/\pi-1)} \bullet l/RA_s\varepsilon_o \qquad (7-2)$$

where f_{top} is the frequency at the top of the impedance arc corresponding to the specimen, θ is the depression angle, R is the resistance, $1-2\theta/\pi$ is equal to the n value in Eqn. 7-2

and l/A_s represents the geometrical factor of sample. According to Eqn. 7-2, the dielectric constants of the clay compact at 700~900°C were calculated as 400~500. At temperatures above 900°C, the frequency at the top point of the bulk arc is out of the measurement range. Therefore the dielectric constant cannot be calculated. The dielectric constant of 400~500 is unusually high, which can only be explained by an underlying "dielectric amplification factor" (DAF) mechanism (Christensen *et al.* 1994). DAF usually results from a microstructural arrangement where isolated conductive domains are imbedded in a continuous insulating matrix. This factor is responsible for the large effective dielectric constants of a barrier layer capacitor, where conductive grains are surrounded by the insulating grain boundary. DAF was also found to exist in cements where a conductive pore solution is separated by an insulating product C-S-H layer (McCarter *et al.* 1988; Christensen *et al.* 1992) and as mentioned in chapter 6, in Al_2O_3/SiC nano-composite where conductive SiC particles imbedded in Al_2O_3 matrix result in larger capacitance. However, further work is needed to clarify what is responsible for DAF in clay compact at high temperatures.

7.4.3 Sensitivity Of IS To The Formation Of Liquid Phases

Fig. 7-1b shows an incomplete bulk semicircle where the high frequency part is incomplete when the measurements were made at 900°C and 1000°C. The relaxation frequency of the clay at 1000°C was well above 1MHz. This suggests that the clay is very conductive at 1000°C, which is due to the formation of a continuous conductive liquid phase in the clay compact.

Based on the data in Table 7-4, the bulk conductivity can be calculated by: $G_o=1/R_b$. The logarithmic of the conductivity against the reciprocal temperature is plotted in Fig. 7-12. The data in the range of 600-900°C shows a linear relationship, indicating a consistent conductivity mechanism in this temperature range. The data at temperatures above 900°C apparently do not fit the same linear relation, which implies a new physicochemical process may occur between 900-1000°C. Meanwhile, based on impedance spectra, the dielectric loss factor (at 1MHz) in the clay compact (Fig.7-13) also shows a steep increase at temperatures above 900°C. All of this suggests that IS is sensitive to the formation of liquid phase in clay compacts.

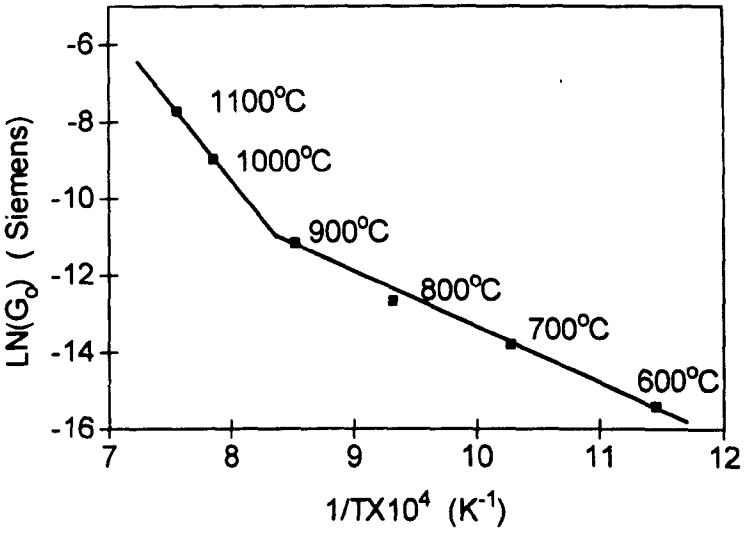

Figure 7-12 Plot of logarithmic conductivity vs. reciprocal temperature.

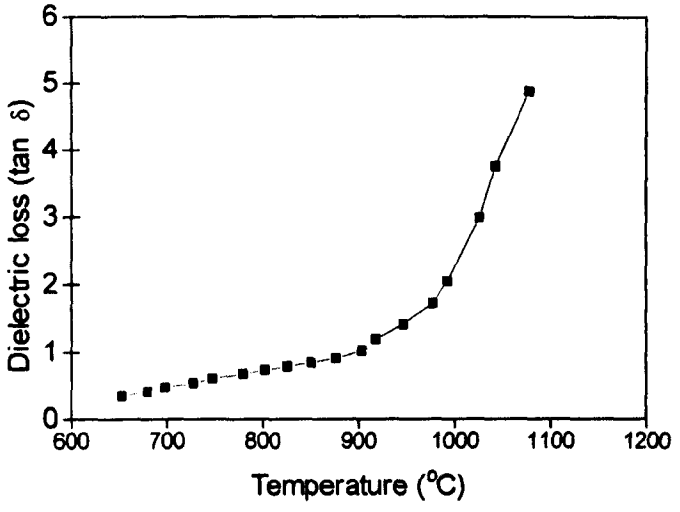

Figure 7-13 Loss tangent (at1MHz) obtained from impedance measurements as a function of temperature.

D.C. electrical conductivity measurements have already been used to detect the presence of liquid phase in the Al_2O_3-1 mol% TiO_2-0.5 mol% $NaO_{1/2}$ system (Morgan and Koutsoutis, 1986). D.C. electrical measurements were found to be sensitive to the presence of a small amount of liquid phase that may influence or control the sintering of

many ceramic compositions. IS is a much more sophisticated technique than the D.C. conductivity measurement technique. More information, e.g. capacitive effects, dielectric loss and electrode polarisation, etc., can be obtained from impedance spectra. Also the electrode effect can be excluded to examine the electrical properties of the specimen only. In this work, the formation of liquid phase during firing was not only detected by the change in the activation energy for electrical conduction, but also determined by a steep increase in the dielectric loss (Fig. 7-13) and spectrum shifting (Fig.7-3).

7.4.4 Electrode Effects

The electrode effect corresponds to a low frequency tail in the complex impedance plane plot. It has been observed that the height of the low frequency tail remains unchanged during sintering at a constant temperature as shown in Fig.7-4. The height appeared to have a strong temperature-dependence. This is of interest from the viewpoint of *in-situ* monitoring of sintering, because this seems to provide the extra information regarding local temperature, i.e., the temperature at the contact between electrode and specimen. This means the low frequency tail could become an effective indicator of temperature, which used to be checked by pyrometric cones. For this reason, it is necessary to elucidate what is responsible for the presence of the low frequency tail and what kind of information can be sought based on the features and parameters of the low frequency tail.

The so-called electrode effect here is a response from the platinum electrode/clay compact interface. At high temperatures when clay is vitrified, the glass phase is the predominant phase in the clay compact. In alkali oxides-silica glasses, some Si-O-Si bonds are broken and non-bridging oxygen ions are generated. The ionic species, such as alkali ions and non-bridging oxygen are distributed among the strongly covalent network or chain structure of Si-O-Si. Those ionic species are the charge carriers for conduction (Doi, 1987). Since alkali ions have much greater mobility than the non-bridging oxygen ions, alkali ions will first conduct to the cathode and generate the alkali-depleted region (ADR) near the anode as shown in Fig.7-14 (Carlson *et al.* 1974; Doi, 1987). In the ADR, the non-bridging oxygen ions are not charge-compensated, and tend to move to the anode due to electrostatic attraction. Thus oxygen ions accumulate underneath the blocking anode, and a double layer is formed at the anode. In the meantime, alkali ions gather near the cathode, so a double layer can be built up at the cathode. The double layer

at either anode or cathode could be responsible for the low frequency tail in impedance plot. The platinum electrode is supposed to be blocking to both oxygen and alkali ions at a small voltage signal and a pure capacitive effect from electrode is expected. However, as mentioned previously, the non-ideal situations arising from effects, such as roughness and porosity of the electrode, the poor contact between electrode and the material etc., could lead to a constant phase angle (CPA) behaviour and produce a 'tail' at low frequencies.

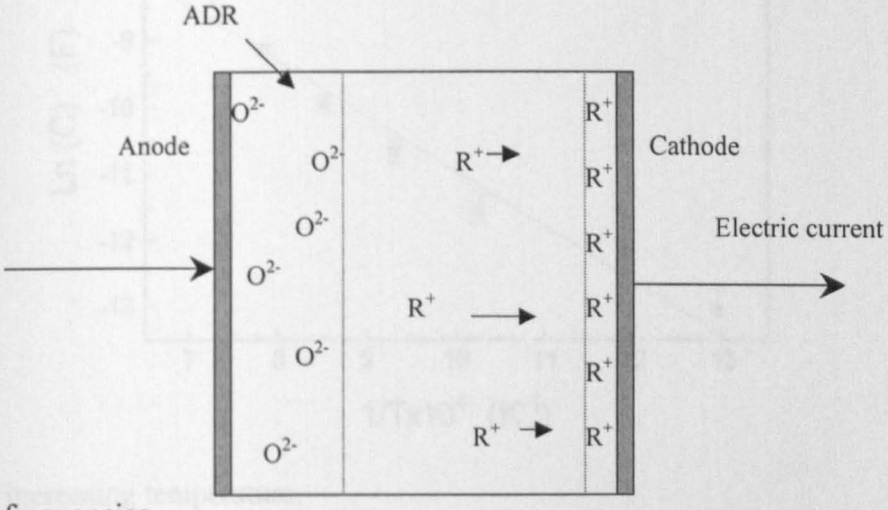

Figure 7-14 An alkaline depleted region (ADR) underneath anode, R^+ representing alkali ions.

The constant angle behaviour means the capacitance is dependent on frequency. The capacitance of a blocking electrode can be calculated by employing Eqn.2-31:

$$C=A\omega^{n-1}\sin(n\pi/2).$$

Based on the fitted results as shown in Table 7-5, the capacitance at a given frequency can be obtained. In order to investigate the temperature-dependence of capacitance of the electrode effect in detail, we take the capacitance at 0.1Hz as representative of the behaviour throughout the frequency range. This is reasonable because: (i) the capacitance at 0.1Hz is reliable in representing the electrode effect, as at such a low frequency the influence of the bulk effect on the low frequency tail can be ruled out; (ii) the capacitances of electrode effect at different temperatures thus obtained are

comparable, since the influence of frequency on capacitance is excluded. The logarithmic capacitance of the electrode effect is plotted against the reciprocal temperature in Fig. 7-15. Obviously, the capacitance is thermally activated, i.e., the capacitance increases with

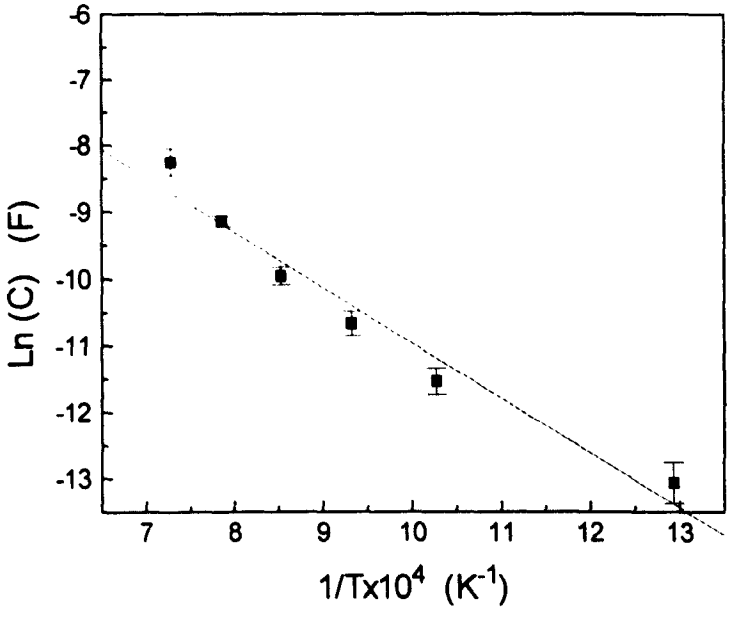

increasing temperature.

Figure 7-15 Arrhenius plot of capacitive effect of electrode / sintered body interface.

A thermally activated capacitance is most likely due to some transport processes. Jonscher and Reau (1978) proposed an interpretation for this phenomenon: capacitance arises from a near-equilibrium situation near an incompletely replenishing electrode, where the interfacial field is screened within a Debye length λ^* and the resulting capacitance per unit area is given by the expression (Jonscher and Reau, 1978):

$$C_b = \varepsilon_v / \lambda = [e^2 \varepsilon_v N / kT]^{1/2} \qquad (7\text{-}3)$$

* There is balance between two factors that affect the distribution of the mobile ions near electrode: the electrostatic attraction that causes the mobile ions to be as near to the interface as possible, and thermal motion that causes a spread into the bulk. The Debye length is an important parameter describing the spreading of the mobile ions into the bulk: $\lambda=(\varepsilon kT/e^2N)^{1/2}$ (Armstrong and Todd, 1995). The larger the Debye length, the more spread are the mobile ions.

where e is the magnitude of the electronic charge and N is the density of the mobile ions, ε_v is dielectric constant and other symbols have normal meanings. The density N is clearly thermally activated and the activation energy for density N should be similar to the conductivity activation energy (Jonscher and Reau, 1978). Therefore, according to Eqn. 7-3, the capacitance is expected to have an activation energy that is half of the conductivity activation energy†. Based on Fig.7-15, the slope of the linear relation: Ln(C) vs. $1/Tx10^4$ is –0.846. The activation energy of capacitance (E_c=R*slope) is calculated as

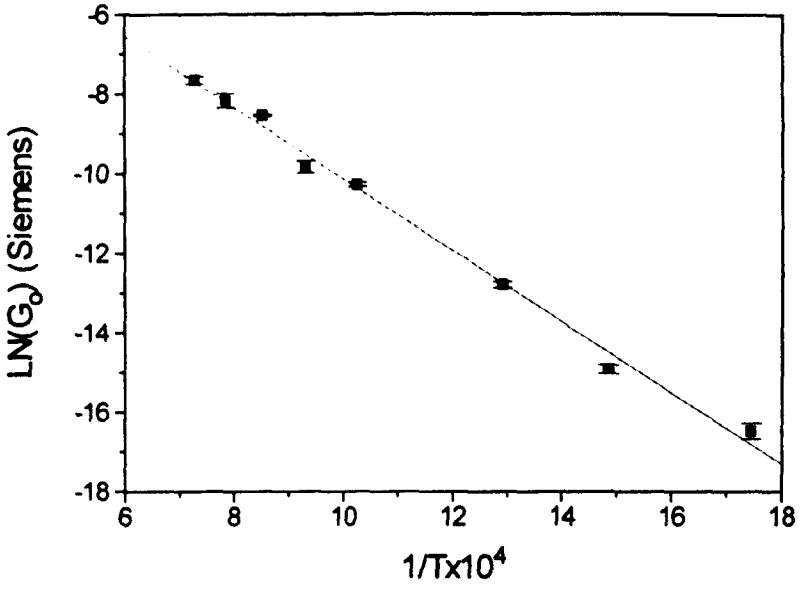

16.8 kcal/mol, from which the activation energy of ion density N is calculated as 33.6 kcal/mol (1.46 eV).

Figure 7-16 Arrhenius plot of bulk conductivity for sintered clay body.

Based on the fitted results as shown in Table 7-5, the conductivity of the sintered specimen is plotted against the reciprocal temperature in Fig. 7-16. The slope of the linear relationship: Ln(G) vs. $1/Tx10^4$ is 0.89, so the activation energy for the bulk conductivity is calculated as 17.7kcal/mol (0.77eV). This is in good agreement with the results reported in the literature. The activation energy of bulk conductivity for commercial soda lime glass was reported as 18.2kcal/mol (i.e., 0.79eV) (Doi, 1987) and

† N is thermally activated: $N=N_o\exp(E_a/kT)$, where E_a is the activation energy. On combining this equation with Eqn. 7-3, we have $C_b=(e_2\varepsilon_v N_o/kT)^{1/2}\exp(Ea/2kT)$. Therefore the activation energy for capacitance is $E_a/2$.

that of a normal glass was reported as about 17.0kcal/mol (i.e., 0.74eV)(Carlson *et al.* 1974).

The activation energy of the movement of non-bridging oxygen ions in the ADR was reported to be 41.4 kcal/mol (i.e., 1.8eV) (Carlson *et al.* 1974). The activation energy of the moving ions obtained based on Fig. 7-15 is very close to the reported activation energy of the movement of non-bridging oxygen ions, but much higher than that of the bulk conductivity. This indicates that the electrode effect is mainly from the blocking anode‡ where non-compensated oxygen ions in the ADR are mobile, but have a much higher energy barrier than the alkali ions in the bulk.

The assignment of the low frequency tail to the blocking anode is also reasonable on physical grounds. The cathode is expected to have a much higher capacitance than anode, because alkali ions are much more mobile than the non-compensated oxygen ions in the ADR (Carlson *et al.* 1974). Sufficient alkali ions can approach that cathode as near as they can once an electrical field is established near the electrode. By contrast, the oxygen ions in the ADR are less mobile and tend to spread in the bulk near the interface, therefore the capacitive effect is smaller. The anode and cathode are connected in series, hence the impedance response from the cathode double layer that has a much greater capacitive effect is negligible.

If the electrode area and the contact between electrode and material remain constant, the capacitive effect of the anode double layer is only dependent on the temperature according to Eqn.7-3. This is the reason why the height of the tail can be an indicator of local temperature of the electrode/specimen contact area.

7.4.5 Monitoring Densification Process

Our experimental results showed that when temperature is increased to above 950°C, the clay compact started to shrink. Meanwhile the impedance spectrum began to show a gradual shift towards the left, as shown in Figs.7-3b-d. This indicated that the densification occurring at temperatures above 950°C can be monitored using IS.

‡ During impedance measurements, the anode and cathode keep switching sides, due to the alternating current used. However at any particular moment, there is always an electrode acting as the blocking anode, while the other one acting as the cathode.

As is well established, the diameter of a semicircle in the complex impedance plot is representative of the resistance. The semicircle corresponding to the bulk specimen is well resolved from the spectra corresponding to the electrode effect. The diameter of the semicircle can be taken as the real part at the cut-off frequency. By neglecting the resistance of leads that is less than 0.1% of the resistance of bulk clay, the diameter of the semicircle can be taken as the bulk resistance. The electrical resistance can be described as:

$$R= \delta/\sigma \bullet A_e \qquad (7-4)$$

where σ is the conductivity, δ is the distance between electrodes and A_e is the area of electrodes. During impedance measurements, the parameter A_e can be considered as a constant, but both σ and δ changed due to densification of the clay compact. Therefore both increasing electrical conductivity and decreasing distance between electrodes contribute to the decreasing resistance of the specimen.

According to SEM observation and XRD analyses, the sintered clay compact mainly contains a continuous glass phase and isolated pores where the quartz and mullite particles are imbedded in the glass phase. To analyse the electrical conductivity of the clay, we can treat this material as a two-phase composite. The continuous glass phase containing crystal particles is treated as one single conducting phase while the isolated pores can be regarded as an insulating phase. The structure of the clay is very similar to the 3-0 connectivity pattern shown in a piezoelectric-pyroelectric composites studied previously (Newnham *et al.* 1978). The conductivity of the insulating phase, e.g. pores, can be assumed to be zero, the electrical conductivity of the composite can be estimated using the equation (Mclachlan *et al.* 1990):

$$\sigma_m=\sigma_h(1-f)^m \qquad (7-5)$$

where σ_m is the electrical conductivity of the composite, σ_h is the electrical conductivity of the continuous conductive network in the composite, f is the fraction of the insulating phase and m here is an exponent which is associated with the particle shape and distribution (Mclachlan *et al.* 1990).

Another approach for calculating the transport properties of porous materials has been developed as (Fan *et al.* 1992; Fan, 1996):

$$\Phi^c/\Phi_m=f_{\alpha c} \qquad (7-6)$$

where Φ^c refers to the transport properties of a porous material, Φ_m refers to the transport properties of the matrix without porosity and $f_{\alpha c}$ is a topological parameter. The topological parameter $f_{\alpha c}$ depends not only on the volume fraction of the matrix phase, but also on the microstructure parameters, such as pore size, pore shape and pore distribution. In general, it can be assumed to follow a power law (Fan *et al.* 1992; Fan, 1996):

$$f_{\alpha c}=f_\alpha^{\ m} \qquad (7-7)$$

where f_α is the volume fraction of matrix, the m here is a parameter which is dependent on several microstructural parameters as mentioned above. Combining Eqs.7-6 and 7-7, we have:

$$\Phi^c=\Phi_m f_\alpha^{\ m} \qquad (7-8)$$

It is obvious that Eqn. 7-8 is the same as Eqn.7-5.

In Eqn.7-8, f_α is equal to the ratio (D_b/D_t) of the actual bulk density (D_b) to the theoretical density (D_t) of the sample. Therefore, by combining Eqs. 7-4 &7-8, we express the electrical conductance (G) in terms of the density, D_b and the thickness of the specimen, δ:

$$G=1/R=C\bullet D_b^{\ m}/\delta \qquad (7-9)$$

where $C=A_e\bullet\sigma_m/D_t^{\ m}$, which can be assumed to be constant during sintering at a given temperature.

Based on the impedance spectra measured at 1100°C (Fig. 7-3c), the conductance G of the bulk sample under firing was obtained as a function of sintering time (Fig. 7-17a.)

For comparison, the density and dimensional change of the clay compacts that have been sintered at 1100°C for various periods were measured. The isothermal densification curve and isothermal shrinkage curve are shown in Figs. 7-17b and c, respectively. Obviously, the three plots show the same trend.

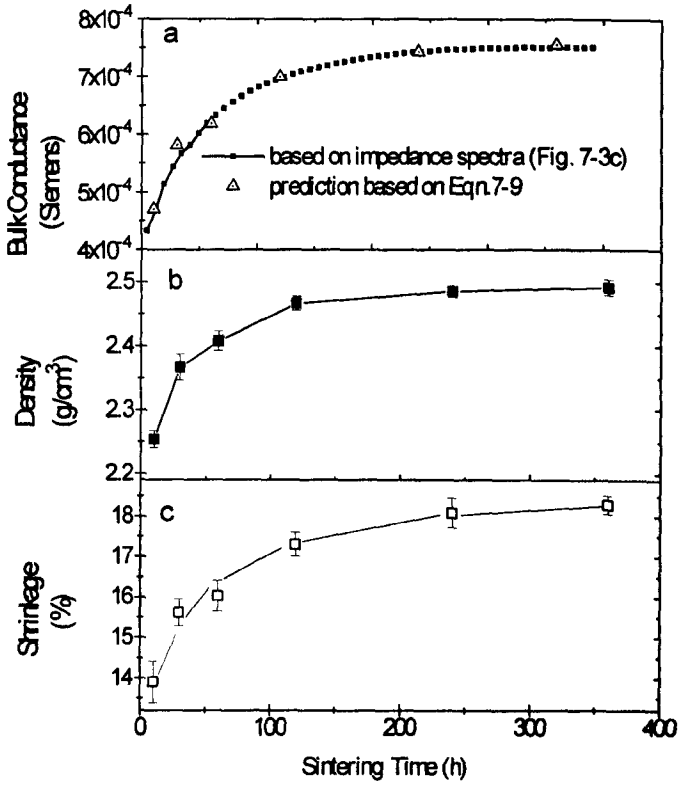

Figure 7-17 (a) the dependence of bulk conductivity on sintering time; (b) and (c) the density and dimensional variations as a function of sintering time, each value being obtained by averaging five samples.

By using the data of D_b and δ shown in Figs 7-17b,c and assuming m=2, the conductance of the sample was calculated according to Eqn.7-9. The change of conductance is displayed in Fig.7-17a, showing the calculated data of the conductance fits the measured curve from the impedance measurements very well. It is interesting to note that the assumption of m as a constant of 2 gives a very good fit to the experimental results, while m is dependent on the microstructural parameters, e.g. pore shape and pore distribution.

The value of m often has been found to be in the range of 1.65 to 2.0 (Mclachlan *et al.* 1990), so m=2 in this work is reasonable. When m=3~5, this implies extreme geometries or complex structures for the dispersing phase (Balberg, 1987). In the clay during sintering where the continuous phase is a glass phase and the material is quite pliable, pores are more likely to have regular shapes and be homogeneously distributed, which can be observed in Fig. 7-10 d. This might be the reason why m remains constant during the densification process.

7.5 Summary And Conclusions

Impedance measurements for both green clay compacts during heating and sintered bodies during cooling were conducted *in-situ* isothermally at high temperatures. In both cases, the effect of the bulk specimen is well distinguished from the electrode effect. Instead of two semicircles, there is only one semicircle present in the complex impedance plot corresponding to the bulk effect. This is because continuous conductive paths are present in both cases. In the green clay compact, the continuous conductive path is due to the surface conduction of mobile ions adsorbed on the surface of clay particles. In the sintered body the continuous glassy phase forms a continuous conductive path.

By employing the continuous conductive path model to simulate the impedance spectra, IS parameters for both the bulk and electrode effects were obtained. Based on these IS parameters, a lot of useful information can be generated, for example, the conductivity, dielectric constant and dielectric loss of a bulk specimen, the capacitive effect and inhomogeneity of electrode / specimen interface etc. A discontinuity in the Arrhenius plot of the bulk conductivity and a drastic increase in the dielectric curve coincide with the formation of liquid phase in clay compacts which occurs at ~950°C. This was confirmed by all the conventional analytical techniques used, i.e., XRD, dilatometer measurement and SEM. Therefore IS is sensitive to the formation of a phase transition during heating. An unusually large dielectric constant was found to be associated with the bulk effect which needs further detailed study.

The electrode effect was found to have a strong temperature dependence. The activation energies for the bulk conductivity and mobile ions associated with electrode effect were calculated. Based on IS parameters, it has been found that the activation energy of the

latter is very close to the reported activation energy for non-bridging oxygen ions in an alkali-depleted region (ADR). Therefore it can be assumed that the electrode effect is reflective of the double layer charging in the ADR. The mobility of the non-bridging oxygen ions in the ADR is thermally stimulated. Therefore the height of the low frequency tail in the complex impedance plot is indicative of the local temperature.

A shifting of impedance spectrum was observed for clay compacts under firing at >950°C, which is a direct consequence of a densification occurring in the clay compact. The variation of the bulk conductivity with the sintering time, which can be deduced from isothermal impedance spectra, was found to be in agreement with the shrinkage curve. An equation relating the electrical conductivity to the density of the specimen has been established.

In conclusion, IS can be used to detect the formation of a liquid phase, sense the local temperature around the electrode, and monitor the densification of the specimen. Therefore impedance spectroscopy is a promising tool for investigating the sintering process of clay-based ceramics.

8 Conclusions And Suggestions For Future work

8.1 General Summary And Conclusions

The development of a simple non-destructive technique for characterisation of structural ceramics is desirable. Although it has already been recognised by some scientists that IS has an important area of application in the study of structural ceramics, most of the previous studies have been restricted to zirconia-based and cementitious materials. So far no attempt seems to have appeared in the literature to characterise a wide range of structural ceramics using IS. This project was designed to contribute to this new research field, and to explore the potentiality of the IS technique in an attempt to extend its application to the majority of structural ceramics. For this purpose, materials studied represent a wide range of structural ceramics. The microstructure, phase distribution and composition of these structural materials have been characterised.

To set up an equivalent circuit model for a specific system is essential for the correct interpretation of its impedance spectra, which in turn strongly relies on a clear understanding of electrical conduction mechanisms. Knowledge of the microstructure-electrical conduction relationship is essential. For structural ceramics, the electrical properties are not the major concern for their application, but provide the basis which can be used to extract microstructural information from the corresponding impedance spectra. Various conduction mechanisms and physical models have been reviewed in chapter 2. The fundamentals of IS, such as the non-ideality of response and electrode effects have been discussed in detail.

The real power of the IS technique lies in its capability of distinguishing the electrical responses from different microstructural origins. An analytical approach and numerical analyses have been conducted to illustrate why impedance spectra become resolved and how different parameters corresponding to an equivalent circuit affect the spectral resolution. It has been revealed that different representations highlight different features, therefore representations in various formalisms are useful in order to obtain more information of the measured system.

With regard to the electrical properties of a material, whether or not the electrical responses from the different microstructural origins can be distinguished depends on the extent of the difference in their electrical properties, as different electrical properties result in different relaxation frequencies. For example, IS does not discriminate the grains and grain boundaries in Al_2O_3/SiC nanocomposites, presumably due to the similarity of conductivities of grains and grain boundaries. Whereas for thermal barrier coatings, there are three separated relaxation processes which correspond to the YSZ bulk, the blocking effect from various defects in the top coat and oxide layer respectively, due to their distinct relaxation frequencies (time constants).

The existence of continuous conduction paths masks the responses from grains and grain boundaries in ceramics. For example, in the case of clay powder compacts, surface ionic conduction is assumed to be a dominant conduction mechanism before the formation of liquid phase, while after the appearance of liquid phase, the liquid phase tends to form a continuous network which can transport the charge carriers without experiencing the blocking effect of other phase(s). For this reason there are no grain and grain boundary effects shown in the impedance spectra of clay compacts.

The existence of a conductive phase could not lead to a separate curve in the impedance spectrum, as its relaxation frequency is too high to be measured. For example, the dispersed SiC particles in Al_2O_3/SiC nanocomposites and mixed oxide in TBCs at 350°C are quite conductive; in both cases it is believed that their relaxation processes should be outside of the measurable frequency range. However, the presence of the conductive phase leads to a change of the capacitive effect. In this sense IS still is sensitive to the existence of the conductive suspended phases. This has been shown in the experimental observations that the dielectric constant of Al_2O_3/SiC nanocomposites depended on the SiC content and, more interestingly, the orientation of suspended conductive particles in composites had an influence on bulk capacitance as well. This observation offered a base on which a qualitative or even quantitative characterisation of a given microstructural factor can be conducted. A quantitative establishment was attempted to explain the dependence of dielectric constant on SiC content as presented in chapter 5.

Microstructural changes are supposed to be related to the variations of corresponding IS parameters, so the core issue in characterising structural ceramics using IS is the establishment of the relationship between microstructure and IS parameters.

The exponential index n for CPE is often related to heterogeneities in materials. It has been found that pure, monolithic Al_2O_3 material gives a nearly ideal Debye response, while the incorporation of SiC particles apparently introduces frequency dispersion to the electrical response of Al_2O_3/SiC nanocomposites. The depression angle increased as the SiC content is increased. Meanwhile it was also found that the n values corresponding to both the top coat and oxidation layer in TBCs varied with oxidation time. This gives extra information concerning the degradation of materials, although the exact underlying mechanism has yet been established.

The capacitive effect has been found to be closely related to the geometric dimensions of a given microstructure. This is useful especially for the characterisation of the multi-layer structure. The inverse capacitance of the oxide layer in TBCs has been illustrated to have a linear relationship with the layer thickness. Modulus spectra can be used to highlight the capacitive effects of different layers having different conductivities. The diameter of a semicircle in a complex modulus plot is proven theoretically to be proportional to the thickness. Meanwhile in practice examination of modulus spectra have been found to be a very useful approach for non-destructive examination of the growth of the oxide layer in both TBCs and Al_2O_3/SiC nanocomposites.

The change in resistivity (or conductivity) may reflect the change in phase composition of a material. In TBCs, the top coat was found to show a decrease in its conductivity with the heat treatment time. This was speculated to be associated with the phase changes: t'-phase $\rightarrow$ t-phase + c-phase, and t-phase$\rightarrow$m-phase, which in turn could be an effective indicator of the degradation of the top coat. In an impedance study of clay sintering, the conductivity increase was also related to the formation of liquid phase in the clay. During isothermal sintering, clay compacts show an increase in conductivity with sintering time, which represents the densification progress of clay compacts. A quantitative relationship has been established to relate the variation of bulk conductivity to the bulk density.

The electrode effect is an electrical response from the electrode/material interface. Although complications may be involved in the analysis of the electrode effect, the electrode effect does provide extra information regarding the microstructure and electrical properties of the bulk material itself. For the case of clay compacts under firing, the equivalent capacitance of the electrode effect (platinum/clay interface) was found to be closely related to the temperature at the electrode/material interface, which means it may be used to give indication of the local temperature.

A lot of valuable information concerning microstructural changes in ceramics that occur in service or in manufacturing processes can be generated non-destructively using IS. Based on the research results presented in this thesis, the following conclusions can be drawn:

1) The content and orientation of the conductive phase in insulator/electronic conductor composites, are closely related to the IS parameters deduced from impedance spectra. This proves that IS is capable of identifying the concentration, orientation and distribution of the suspended conductive phase(s).

2) A dramatic change in the electrical properties of insulator/electronic conductor composites occurs when a percolating network of the conductive phase(s) is formed. The oxidation scale formed at the surface of the composites with a percolating network of the suspended conductive phase(s) can be determined non-destructively using IS, which is a difficult task for other test techniques, such as, SEM, weight gain measurements, optical microscopic observations etc. to accomplish.

3) In TBCs, the electrical response from the oxide layer of the bond coat is well separated from those from other phases. Well-defined semicircles in a complex modulus plot were obtained. The oxide layer consists of two main components: mixed oxide and alumina. The impedance spectrum obtained by room temperature measurement detects the whole oxide layer, while at 350°C the impedance spectrum measures the alumina layer.

4) There are two relaxation processes corresponding to the top coat in TBCs measured at 350°C; one corresponds to the bulk effect, the other to the blocking factors, such as grain boundaries, cracks, pores and impurities etc. Both of them show a clear trend of variation with heat treatment time, which can be used to indicate the extent of degradation of the top coat.

5) During the sintering of clay-based ceramics, the formation of liquid phase and the shrinkage rate of the ceramic body can be monitored by *in-situ* impedance measurements. The electrode effect in impedance spectra is representative of the local temperature, which can be an effective indicator of heat work for the firing of clay-based ceramics.

8.2 Suggestions For Future Work

It is a new area of research to employ IS to characterise structural ceramics. The research presented in this thesis has indicated that this is a promising research field of scientific interest, which may also bring great benefit to the manufacturing and applications of structural ceramics. However this work represents only a first step into this area, there is a lot of space left for future research. With regards to the issues concerned in this thesis, the following aspects are suggested for future work.

1) In the fibre or particulate reinforced ceramic composite materials, it has been recognised that the distribution of the dispersed phase, such as SiC whiskers, SiC particles and carbon fibres, etc., is an important concern in the fabrication of these materials. As mentioned earlier on, IS is sensitive to the distribution and orientation of the dispersed particles. Further work should focus on the relationship between IS and the anisotropic mechanical properties resulting from different distribution modes (such as homogenous and clustered, oriented and isotropic etc.) of the dispersed conductive particles.

2) For the top coat in TBCs, the change in phase composition is an important factor leading to the degradation of the top coat, which then may contribute to the failure of TBCs. In the research presented in chapter 6, it has been demonstrated that both the conductance and capacitive effect of the top coat varied with the heat treatment duration. This was postulated to be due to the phase transformation of zirconia: t'-phase → t-phase + c-phase and t-phase→m-phase. However, more detailed work on phase identification and quantitative determination of phase composition is required to substantiate this proposition.

3) In the impedance spectra of TBCs, the mixed response was believed to be a combined contribution from all of the blocking factors contained in the top coat (YSZ) in TBCs, such as grain boundaries, cracks, pores and impurities etc. Our research results showed clearly that all the three IS parameters: R, n and A corresponding to this response had clear trends of variation as a function of heat treatment time. However, an unambiguous explanation for these variation patterns is not yet available. Further work is necessary to differentiate the influences from different blocking factors in order to find a satisfactory interpretation for this phenomenon, which may also lead to more in-depth knowledge about the degradation of the top coat in TBCs.

4) As has been addressed in chapter 6, there was always a tail-like curve in the low frequency range in the impedance spectrum of TBCs. The author attributed this tail-like curve to a response of the top coat/mixed oxide interface. This curve appeared to change with the heat treatment duration, which indicates the interface might keep changing during heat treatment. It has already been established that most of the TBCs failures occur at, or near, the top coat/bond coat interface. Further detailed study on the impedance of this electrode effect and its dependence on interface microstructure might be able to provide insight into the failure mechanism and possibly even a new approach to monitor the failure of TBCs.

5) A non-destructive technique of characterising the cracks and microcracks in ceramics is always desirable. Quartz is the most commonly used filler in clay-based ceramics. One of the issues in the production of whiteware and porcelain is the deterioration in mechanical properties as a result of the $\beta \rightarrow \alpha$ quartz inversion at 573°C during the cooling process, which results in a volume decrease of 2% and hence

produces sufficient strain to cause cracking of the glassy matrix and quartz particles (Carty and Senapati, 1998). This cracking should lead to a substantial change in electrical conductivity of ceramics. In the research presented in chapter 7, we have not found a change in conductivity of sintered clay bodies during the cooling process. This might be due to the lack of large quartz particles in the sintered body. Further work is needed to confirm whether or not IS is capable of detecting the presence of cracks and microcracks in traditional, clay-based ceramics.

References

Abrahams I. and Hadzifejzovic, E., (2000) Lithium ion conductivity and thermal behaviour of glasses and crystallised glasses in the system Li_2O-Al_2O_3-TiO_2-P_2O_5, *Solid State Ionics*, **134**, 249-257.

Abrantes, J. C. C., Labrincha J. A. and Frade, J. R., (2000a), An alternative representation of impedance spectra of ceramics, *Mater. Res. Bull.*, **35**, 727-740.

Abrantes, J. C. C., Labrincha J. A. and Frade, J. R., (2000b), Representations of impedance spectra of ceramics part I. simulated study cases, *Mater. Res. Bull.*, **35**, 955-964.

Abrantes, J. C. C., Labrincha J. A. and Frade, J. R., (2000c), Representations of impedance spectra of ceramics part II. Spectra of polycrystalline $SrTiO_3$, *Mater. Res. Bull.*, **35**, 965-976.

Ahn, H.- S., (1998), Detection of contact damage in ceramics by an ultrasonic method, *J. Mater. Res.*, **13**, 1899-1903.

Ambrus, J. H., Moynihan, C. T. and Macedo, P. B., (1972), Conductivity relaxation in a concentrated aqueous electrolyte solution, *J. Phys. Chem.*, **76**, 3287-3295.

Andrade, C., Blanco V. M., Collazo, A., Keddam, M., Novoa, X. R. and Takenouti, H., (1999), Cement paste hardening process studied by impedance spectroscopy, *Electrochimica. Acta.*, **44**, 4313-4318.

Anseau, M. R., Deletter, M. and Cambier, F., (1981), The separation of sintering mechanisms for clay-based ceramics, *Trans. J. Br. Ceram. Soc.*, **80**, 142-146.

Aoki, M., Chiang, Y. -M., Kosacki, I., Lee, I. J. R., Tuller, H. and Liu, Y. P., (1996), Solute segregation and grain boundary impedance in high-purity stabilised zirconia, *J. Am. Ceram. Soc.*, **79**, 1169-1180.

Armstrong, R. D., Dickinson, T. and Willis, P. M., (1974), The A.C. impedance of powdered and sintered solid ionic conductors, *J. Electroanal. Chem.*, **53**, 389-405.

Armstrong, R. D. and Todd, M., (1995), Interfacial electrochemistry, p. 265, in *Solid State Electrochemistry*, P. G. Bruce, (ed), Cambridge University Press, Cambridge.

Badwal, S. P. S., (1988), *Proceedings of the international seminar on solid state ionic devices*, World of Scientific Publishing, Singapore, p165.

Badwal, S. P. S., (1995), The grain boundary resistvity in zirconia-based materials: effect of sintering temperatures and impurities, *Solid State Ionics*, **76**, 67-80.

Badwal, S. P. S., Ciacchi, F. T., Rajendran, R. and Drennan, J., (1998) An investigation of conductivity, microstructure and stability of electrolyte compositions in the system 9 mol% (Sc_2O_3-Y_2O_3)-ZrO_2(Al_2O_3), *Solid State Ionics*, **109**, 167-186.

Balberg, I., (1987), Tunneling and nonuniversal conductivity in composites materials, *Phys. Rev. Lett.*, **59**, 1305-1308.

Bartlett, A. H. and Maschio, R. D., (1995), Failure mechanisms of a zirconia-8 wt% yttria thermal barrier coating, *J. Am. Ceram. Soc.*, **78**, 1018-24.

Bauerle, J. E., (1969), Study of solid electrolyte polarisation by a complex admittance method, *J. Phys. Chem. Solids*, **30**, 2657-2670.

Boccaccini D. N.and Boccaccini, A. R. (1997), Dependence of ultrasonic velocity on porosity and pore shape in sintered materials, *J. Nondes. Eva.*, **16**, 187.

Bockris, J. O'M, Kitchener, J. A., Igatowicz, S. and Tomlinson, J. W., (1952) Electric conductance in liquid silicates, *Trans. Faraday Soc.*, **48**, 75-91.

Bonanos, N., Steele, B. C. H. and Butler, E. P., (1987), Application of impedance spectroscopy, p191, in *Impedance Spectroscopy*, J. R. Macdonald, (ed.), John Wiley & Sons, New York.

Brindley, G. W. and Nakahira, M., (1959a), The kaolinite-mullite reaction series: I, a survey of outstanding problems, *J. Am. Ceram. Soc.*, **42**, 311-314.

Brindley, G. W. and Nakahira, M., (1959b), The kaolinite-mullite reaction series: II, a survey of outstanding problems, *J. Am. Ceram. Soc.*, **42**, 314-318.

Bruce P. G. and West, A. R. (1983), The A-C conductivity of polycrystalline LISICON, $Li_{2+2x}Zn_{1-x}GeO_4$ and a model for intergranular constriction resistance, *J. Electrochem. Soc.*, **130**, 662-669.

Buchanan, R. C., (1991), Properties of ceramic insulators, p1, in *Ceramic Materials for Electronics: Processing, Properties and Applications,* R. C. Buchanan, (ed), Marcel Dekker, Inc., New York.

Cann D. P. and Randall, C.A., (1996), Electrode effects in positive temperature coefficient and negative temperature coefficient devices measured by complex-plane impedance analysis, *J. Appl. Phys.*, **80**, 1628-1632

Carlson, D.E., Hang K. W. and Stockdale, G. F., (1972), Electrode 'polarisation' in alkali-containing glasses, *J. Am. Ceram. Soc.*, **55**, 337-34.

Carlson, D.E., Hang K. W. and Stockdale, G. F., (1974), Ion depletion of glass at a blocking anode II properties of ion depleted glasses, *J. Am. Ceram. Soc.*, **57**, 295-300.

Carty, W. M. and Senapati, U. (1998), Porcelain-raw materials, processing, phase evaluations, and mechanical behaviour, *J. Am. Ceram. Soc*, **81**, 3-20.

Challis, R., and Tebbutt, J., (1998), Ultrasonic wave interactions with colloidal mixtures, p23, in *Nondestructive Evaluation of Ceramics*, C. H. Schilling and J. N. Gray, (eds) (**Vol 89**, Ceramic Transaction), American Ceramic Society, Westerville, Ohio.

Chiang, Y.-M., Lavik E. B. and Blom, D. A., (1997), Defect thermodynamics and electrical properties of nanocrystalline oxides: pure and doped CeO_2, *NanoStructure Materials*, **9**, 633-642.

Choi G. M., and Tuller, H. L., (1988), Defect structure and electrical-properties of single-crystal $Ba_{0.03}Sr_{0.97}TiO_3$, *J. Am. Ceram. Soc.*, **71**, 201.

Christensen, B. J., Coverdale, R. T., Olson, R. A., Ford, S. J., Garboczi, E. J., Jennings, H. M. and Mason, T. O., (1994), Impedance spectroscopy of hydrating cement-based materials: measurement, interpretation and application, *J. Am. Ceram. Soc.*, **77**, 2789-2804.

Christensen, P. A. and Hamnett, A., (1994), Techniques giving mechanistic information, p154, in *Techniques and Mechanisms in Electrochemistry*, Blackie Academic & Professional, London.

Christensen, B. J., Mason, T. O. and Jennings, H. M., (1992), Influence of silica fume on the early hydration of portland cements using impedance spectroscopy, *J. Am. Ceram. Soc*, **75**, 939-945.

Cole, K. S. and Cole, R. H., (1941), Dispersion and adsorption in dielectrics I, alternating current characteristics, *J. Chem. Phys.*, **9**, 341-351.

Curtis, P. T., Gates, J. and Margerison, G. G., (1993), The selection of cyclic load frequency for the fatigue testing of fibre reinforced polymeric composites, *Rae Technical Report 93017* (Farnborough, Guildford, UK).

De Levie, R., (1967), Electrochemical response of porous and rough electrodes, p 329, in *Advances in Electrochemistry and Electrochemical Engineering*, vol. **VI**, Interscience, New York.

Demasi-Marcin, J. T., Sheffler, K. D. and Bose, S., (1990), Mechanisms of degradation and failure in a plasma-deposited thermal barrier coating, *J. Eng. Gas Turbines Power*, **Vol. 112**, 521-526

Dessemont L. and Kleitz, M., (1992), Effects of mechanical damage on the electrical properties of zirconia ceramics, *J. Euro. Ceram. Soc.*, **9**, 35-39.

Dessemond, L., Muccillo, R., Henault M. and Kleitz, M., (1993), Electric conduction-blocking effects of void and second phases in stabilised zirconia, *Appl. Phys.*, **A57**, 57-60.

Djurado, E., Dessemond, L. and Roux, C., (2000), Phase stability of nanostructured tetragonal zirconia polycrystals versus temperature and water vapour, *Solid State Ionics*, **136-137**, 1249-1254.

Doi, A., (1987), Ionic-conduction and conduction polarisation in oxide glass, *J. Mater. Sci.*, **22**, 761.

Drennan, J. and Auchterlonie, G., (2000) Microstructural aspects of oxygen ion conduction in solids, *Solid State Ionics*, **134**, 75-87.

Drevet, C., Henault, M. and Fouletier, J., (2000), Oxygen electrode reaction on stabilised zirconia under high oxygen pressure (up to 100bar), *Solid State Ionics*, **136-137**, 807-812.

Dunyak, T. J., Stiuchcomb, W. W. and Reifsnider, K. L. (1992), Examination of selected NDE techniques for ceramics composites damage detection, p3, in *Composite materials*, ASTM, STP 1128, J. E. Masters, (ed), American Society for Testing And Materials, Philadelphia.

Fairchild, C. O. and Peters, M. F. (1926), Characteristics of pyrometric cones, *J. Am. Ceram. Soc.*, **9**, 701-742

Fan, Z., (1996), A microstructural, approach to the effective transport properties of multiphase composites, *Philosophical Magazine A*, **73**, 1663-1684.

Fan, Z., Tsakiropoulos P. and Miodownik, A.P., (1992), Prediction of young's modulus of particulate two phase composites, *Mater. Sci. Technol.*, **8**, 922-929.

Fleig, J., (2000), The influence of non-ideal microstructures on the analysis of grain boundary impedance, *Solid State Ionics*, **131**, 117-127.

Fleig, J. and Maier, J., (1998), A finite element study on the grain boundary impedance of different microstructures, *J. Electrochem. Soc,* **145,** 2081-2089.

Fleig, J. and Maier, J., (1999a), The impedance of ceramics with highly resistive grain boundaries: validity and limits of the brick layer model, *J. Euro. Ceram. Soc,* **19**, 693-696.

Fleig, J. and Maier, J., (1999b), Finite element calculations on the impedance of electroceramics with highly resistive grain boundaries: I, laterally inhomogeneous grain boundaries, *J. Am. Ceram. Soc*, **82**, 3485-3493.

Fleming, W. J., (1981), A physical understanding of solid-state humidity sensors, *Proc. Int . Automotive Meet.*, SAE, Detroit, USA, paper no. **810432**, 51-62.

Ford, S. J., Shane J. D. and Mason, T. O., (1998), Assignment of features in impedance spectra of the cement paste/steel system, *Cem. Concr. Res.*, **28**, 1737-1751.

Gabrielli. C and Keddam. M., (1996) Contribution of electrochemical impedance spectroscopy to the investigation of the electrochemical kinetics, *Electrochemica Acta*, **41**, 957-965.

Glasser, F. P., Lachowski, E. E. and Macphee, D. E., (1987), Compositional model for calcium silicate hydrate (C-S-H) gels, their solubilities and free energies of formation, *J. Am. Ceram. Soc.*, **70**, 481-485.

Goller M. H. and Pye, L. D., (1998), Light scattering of particles in glasses, p327, in *Nondestructive Evaluation of Ceramics*, C. H. Schilling and J. N. Gray, (ed) (**Vol 89**, Ceramic Transaction), American Ceramic Society, Westerville, Ohio.

Gomes W. P. and Vanmaekelbergh, D., (1996), Impedance spectroscopy at semiconductor electrodes: review and recent development, *Electrochemica Acta*, **41**, 967-973.

Gu, P., Xu, Z., Xie P. and Beaudoin, J. J., (1993), An A.C. impedance spectroscopy study of micro-cracking in cement-based composites during compressive loading, *Cem. Concre. Res.*, **23**, 675-682.

Gusmano, G., Bianco, A., Montesperelli, G. and Traversa, E., (1996), An EIS study of the humidity-sensitive electrical conduction of alkali-doped TiO_2 films, *Electrochemica. Acta*, **41**, 1359-1368.

Haynes, J. A., Gigney, E. D., Ferber, M. K. and Porter, W. D., (1996), Oxidation and degradation of a plasma-sprayed thermal barrier coating system, *Surf. Coat. Tech.*, **86-87**, 102-108.

Hirose, N. and West, A. R., (1996), Impedance spectroscopy of undoped $BaTiO_3$ ceramics, *J. Am. Ceram. Soc.*, **79**, 1633-1641.

Hodge, I. M., Ingram M. D. and West, A. R., (1975), New method for analysing the A.C. behaviour of polycrystalline solid electrolytes, *J. Electroanal. Chem.*, **58**, 429-432.

Hodge, I. M., Ingram M. D. and West, A. R., (1976), Impedance and modulus spectroscopy of polycrystalline solid electrolytes, *J. Electroanal. Chem.*, **74**, 125-143.

Huggins, R. A., (1978), Crystal structure and fast ionic conduction, p27, in *Solid Electrolytes, General Principal, Characterisation, Materials, Applications*, P. Hagenmuller & W. Van Gool, (eds), Academic Press, London.

Hughes, A. E. and Badwal, S. P. S., (1991), Impurity and yttrium segregation in yttria-tetragonal zirconia, *Solid State Ionics*, **46**, 265-274.

Huss, S. P., Schilling, C. H., Gray, J. N., and Maranville, C. W., (1998), Recent advances in x-ray characterisation of composites and tape cast ceramics, p45, in *Nondestructive Evaluation of Ceramics*, C. H. Schilling and J. N. Gray, (eds), (**Vol 89**, Ceramic Transaction), American Ceramic Society, Westerville, Ohio.

Hwang, J.-H. Mason, T. O., Buehler, M. F., Darab, J. G., Matson, D. W. and Linehan, J. C., (1995), Characterisation of humidity-sensing NiO-$Ni(OH)_2$ nanocomposites by impedance spectroscopy, *Mater. Sci. Eng.*, **A204**, 252-257.

Ishida, A. and Miyayama, M., (1994), Prediction of fracture and detection of fatigue in ceramic composites from electrical resistivity measurements, *J. Am. Ceram. Soc.*, **77**, 1057-1061.

Jacobsen, T., Zachau-Christiansen, B., Bay, L., and Skaarup, S., (1996) SOFC cathode mechanisms, p29, *in Proceedings of the 17th Riso International Symposium on Materials Science*, F. W. Poulsen, N. Bonanos, S. Linderoth, M. Mogensen, and B. Zachau-Christiansen, (eds), Riso National Laboratory, Roskilde, Denmark.

Jiles, D., (1994), Electronic properties of semiconductors, p130, in *Introduction to the Electronic Properties of Materials*, by D. Jiles, Chapman & Hall, London.

Johnson, W. B. and Worrell, W. L., (1987), Solid state devices, p238, in *Impedance Spectroscopy*, J. R. Macdonald, (ed), John Willey & Sons, New York.

Jonscher, A. K., (1978), Analysis of the alternating current properties of ionic conductors, *J. Mater. Sci*, **13**, 553-562.

Jonscher A. K. and Reau, J.-M., (1978), Analysis of the complex impedance data for β-PdF_2, *J. Mater. Sci,* **13**, 563-570.

Kathrina, T. and Rawlings, R. D., (1996), Ultrasonic non-destructive evaluation of alumina powder during compaction, *Bri. Ceram. Trans.*, **95**, 233.

Kerner Z. and Paijkossy, T., (1998), Impedance of rough capacitive electrodes: the role of surface disorder, *J. Electroanal. Chem.*, **448**, 139.

Khalili A. and Kromp, K., (1993), On the correlation between mechanical damage and the electrical properties of zirconia ceramics, *J. Euro. Ceram. Soc.*, **11**, 455-461.

Kim, W. J., Taya, M., Yamada, K. and Kamiya, N., (1998), Percolation study on electrical resistivity of SiC/Si_3N_4 composites with segregated distribution, *J. Appl. Phys.*, **83**, 2593-2598.

Kingery, W .D., Bowen, H. K. and Uhlmann, D. R., (1976a), Structure of Crystals, p77, in *Introduction to Ceramics*, Second Edition, Burke, E., Chalmers, B., and Krumhansl, J. A., (eds), John Wiley & Sons, New York.

Kingery, W .D., Bowen and H. K. Uhlmann D. R., (1976b), Grain Growth, Sintering and Vitrification, p448, in *Introduction to Ceramics*, Second Edition, Burke, E., Chalmers, B., and Krumhansl, J. A., (eds), John Wiley &Sons, New York.

Kingery, W. D., Bowen, H. K. and Uhlamann, D. R., (1976c), Electrical conductivity, p851, in *Introduction to Ceramics*, Second Edition, Burke, E., Chalmers, B., and Krumhansl, J. A.,(eds) ,John Wiley & Sons, New York.

Kleitz, M., Dessemond, L. and Steil, M. C., (1995), Model for ion-blocking at internal interfaces in zirconias, *Solid State Ionics,* **75**, 107-115.

Knauth, P. and Tuller, H. L., (1999), Electrical and defect thermodynamic properties of nanocrystalline titanium dioxide, *Appl. Phys.* **85**, 897-902.

Komarenko, P., Messler, R. W. and Scarton, H. A., (1994) Ultrasonic *in-situ* monitoring of sintering in alumina, *Intl. J. Powd. Meta.*, **30**, 67-76.

Kubaschewski O. and Hopkins, B. E., (1962), Electrical properties of metal compounds-basic information, p25, in *Oxidation of Metals and Alloys*, Butterworth & Co. Limited, London.

Lanferdi, S. and Rodrigues, A. C. M., (1999), Impedance spectroscopy study of the electrical conductivity and dielectric constant of polycrystalline $LiNbO_3$, *J. Appl. Phys.*, **86**, 2215-2219.

Lang, G. and Heusler, K. E (1998), Remark on the energetics of interfaces exhibiting constant phase element behaviour, *J. Electroanal. Chem.*, **457**, 257-260.

Lange, F. F., (1982a), Transformation toughening 1: size effects associated with the thermodynamics of constrained transformation, *J. Mater. Sci.*, **17**, 225-234.

Lange, F. F., (1982b), Transformation toughening 2: contribution to fracture toughness, *J. Mater. Sci.*, **17**, 235-239.

Lee, J., Chung, T-J. and Kim, D-Y., (2000) Electrical and microstructural characterisation on nitrogen-stabilised zirconia, *Solid State Ionics*, **136-137**, 39-44.

Lee, W. Y., Stinton, D. P. and Berndt, C. C., Erdogon, F., Lee, Y. D. and Mutasim, Z., (1996), Concept of functionally graded materials for advanced thermal barrier coating applications, *J. Am. Ceram. Soc.*, **79**, 3003-12.

Liu, S. H., (1985), Fractal model for the AC response of a rough interface, *Phys. Rev. Lett.*, **55**, 529-532..

Luthra, K.L., Park, H.D., (1990), Oxidation of silicon carbide-reinforced oxide-matrix composites at 1375° to 1575°C, *J. Am. Ceram. Soc.*, **74**, 1014-1022.

Macdonald, J. R. and Franceschetti, D. R., (1987), Physical and electrochemical model, p84, in *Impedance Spectroscopy*, J. R. Macdonald, (ed), John Willey & Sons, New York.

Macdonald, J. R. and Johnson W. B., (1987), Fundamentals of impedance spectroscopy, p1, in *Impedance Spectroscopy*, J. R. Macdonald, (ed), John Willey & Sons, New York.

Macedo, P. B., Moynihan, C. T. and Bose, R., (1972), Role of ionic diffusion in polarisation in vitreous ionic conductors, *Phys Chem. Glass*, **13**, 171-176.

Macphee, D. E., Sinclair, D. C. and Cormack, S. L., (1997), Development of an equivalent circuit model for cement pastes from microstructural considerations, *J. Am. Ceram. Soc.*, **80**, 2876-2884.

Maiti H. S. and Basu, R. N., (1986), Complex-plane impedance analysis for semi-conducting barium titanate, *Mater. Res. Bull.*, **21**, 1107-1114.

McCafferty E. and Zettlemoyer, A. C.,(1971), Adsorption of water vapour on α–Fe_2O_3, *Discuss. Faraday Soc*,. **52**, 239-263.

McCann J. F. and Badwal, S. P. S., (1982), Equivalent circuit analysis of the impedance response of semiconductor/electrolyte/counterelectrode cells, *J. Electrochem. Soc.*,**129**, 551-559.

McCarter, W. J., Garvin S. and Bouzid, N., (1988), Impedance measurements on cement paste, *J. Mater. Sci. Lett.*, **7**, 1056-1057.

McCaughey, W. J. and Neff, J. M. (1944), Notes on constitution of pyrometric cones, *Am. Ceram. Soc. Bull.*, **23**, 373-375.

McGonnagle, W J., (1971), Preface, page vii, in *Nondestructive Testing*, Gordon and Breach Science Publishers, London.

Mclachlan, D. S., Blaszkiewicz, M. and Newnham, R. E., (1990), Electrical resistivity of composites, *J. Am. Ceram. Soc.*, **73**, 2187-2203.

Meier, S. M. and Gupta, D. K., (1994), The evolution of thermal barrier coating in gas turbine engine applications, *Transaction of the ASME*, **116**, 250-257.

Miller, R. A., (1987), Current status of thermal barrier coatings- an overview, *Surf. Coat. Technol.*, **30**, 1-11.

Miller, R. A., Garlick, R. G., and Smialek, J. L., (1983), Phase distributions in Plasma-sprayed zirconia-yttria, *Am. Ceram. Soc. Bull.*, **62**, 1355-1358.

Miller, R. A., Smialek, J. L., and Garlick, R. G., (1981), Phase stability in plasma-sprayed zirconia-yttria, partially stabilised zirconia-yttria, p241, in *Advances in*

Ceramics, **Vol 3**, Science and technology of zirconia, Heuer A. H. and Hobbs. L. W., (eds), American Ceramic Society, Columbus, Ohio.

Morgan, P. E. D., and Koutsoutis, M. S., (1986), Electrical conductivity measurements to detect suspected liquid phase in the Al_2O_3-1mol% TiO_2-0.5 mol% $NaO_{1/2}$ and other systems, *J. Am. Ceram. Soc.*, **67**, c254-c255.

Morrison, F. D. Sinclair D. C. and West, A. R., (2001), Characterisation of lanthanum-doped barium titanate ceramics using impedance spectroscopy, *J. Am. Ceram. Soc.*, **84**, 531-538.

Motheo, A. J., Sadkowski, A. and Neves, R. S., (1997), Electrochemical immittance spectroscopy applied to the study of the single crystal gold/aqueous perchloric acid interface *J. Electroanal. Chem.*, **430**, 253.

Muccillo, E. N. S. and Kleitz, M., (1996), Impedance spectroscopy of Mg-stabilised zirconia and cubic phase decomposition, *J. Euro. Ceram. Soc.*, **16**, 453-465.

Muccillo, R., Muccillo, E. N. S. and Saito, N. H., (1998), Thermal shock behaviour of ZrO_2: MgO solid electrolytes, *Mater. Lett.*, **34**, 128-132.

Murugan, G. S. and Varma, K. B. R., (2001), Characterisation of lithium borate-bismuth tungstate glasses and glass-ceramics by impedance spectroscopy, *Solid State Ionics*, **139**, 105-112.

Nevadunsky, J. J. and Lucas, J. J. (1975), Early fatigue damage detection in composite materials, *J. Composite Mater.*, **9**, 394-408.

Newnham, R. E. Skinner, D. P. and Cross, (1978), L. E., Connectivity and piezoelectric-pyroelectric composites, *Mater. Res. Bull.*, **13**, 525-36.

Niihara, K., (1991), New design concept of structure ceramic-ceramic nanocomposites, *J. Ceram. Soc. Jpn.*, **99**, 974-982.

Nowotny, J., Redecka, M., Rekas, M., Sugihara, S., Vance, E. R. and Weppner, W., (1998), Electronic and ionic conductivity of TiO2 single crystal within the n-p transition range, *Ceramics Int.*, **24**, 571-577.

Ogawa, K., Minkov, D., Shoji, T., Sato, M. and Hashimoto, H., (1999), NDE of degradation of thermal barrier coating by means of impedance spectroscopy, *NDT&E International*, **32**, 177-185.

Ohji, T., Hirano, T., Nakahira, N., and Niihara, K., (1996), Particle/matrix interface and its role in creep inhibition in alumina/silicon carbide nanocomposites., *J. Am. Ceram. Soc.*, **79**, 33-39.

Okada, K., Otsuka, N. and Ossaka, J., (1986), Characterisation of spinel phase formed in the kaolin-mullite thermal sequence, *J. Am. Ceram. Soc*, **69**, c251-c253.

Pape, D. A., (1998), Sonic detection of manufacturing flaws in ceramic components, p291, in. *Nondestructive Evaluation of Ceramics*, C. H. Schilling and J. N. Gray, (eds), (**Vol 89**, Ceramic Transaction), American Ceramic Society, Westerville, Ohio.

Provenzano, V. Boesch, L. P., Volterra, V., Moynihan, C. T. and Macedo, P. B., (1972), Electrical relaxation in $Na_2O \bullet 3SiO_2$ glass, *J. Am. Ceram. Soc.*, **55**, 492-496.

Raistrick, I. D., (1987), Electrical analogs of physical and chemical processes, p27, in *Impedance Spectroscopy*, J. R. Macdonald, (ed), John Willey & Sons, New York.

Ravaine D. and Souquet, J. L., (1978), Ionic conductive glasses, p277, in *Solid Electrolytes, General Principal, Characterisation, Materials, Applications*, P. Hagenmuller& W. Van Gool, (eds), Academic Press, London.

Rhoderick, G. H., (1978), Introduction and synopsis, page 1-17, in *Metal-Semiconductor Contacts*, Clarence Press, Oxford.

Rodrigues, C. M. S., Labrincha J. A. and Marques, F. M. B., (1997), Study of yttria-stabilised zirconia-glass composites by impedance spectroscopy, *J. Electrochem. Soc.*, **144**, 4303-4309.

Rodrigues, C. M. S., Labrincha J. A. and Marques, F. M. B., (1998), Monitoring of the corrosion of YSZ by impedance spectroscopy, *J. Euro. Ceram. Soc.*, **18**, 95-104

Ruud, C. O., (1984), Preface, page v, in *Nondestructive Methods for Material Property Determination*, C. O. Ruud and R. E. Green, Jr., (eds), Plenum Press, New York.

Scheider, W., (1975), Theory of the frequency dispersion of electrode polarisation: topology of networks with fractional power frequency dependence, *J. Phys. Chem.*, **79**, 127-136.

Schilling C.H. and Gray, J. N. (1998), Needs and opportunities for NDE in ceramic processing", p1, in *Nondestructive Evaluation of Ceramics*, C. H. Schilling and J. N. Gray, (eds) (**Vol 89**, Ceramic Transaction), American Ceramic Society, Westerville, Ohio.

Schillington, E. A. G., and Clarke, D. R., (1999), Spalling failure of a thermal barrier coating associated with aluminium depletion in the bond coat, *Acta. Meta.*, **Vol 47** No.4, 1297-1305.

Sciti, D., and Bellosi, A., (1998), Oxidation behaviour of alumina-silicon carbide nanocomposites. *J. Mat. Sci.*, **33**, 3823-3830.

Scott, H. G., (1975), Phase relationships in the zirconia-yttria system, *J. Mater. Sci.*, **10**, 1527-1535.

Scribner Associates, (1998), Impedance /gain phase graphing and analysis software-operating manual, **Version 2.1**, p5.1.

Sergo, V. and Clarke, D. R., (1998), Observation of subcritical spall propagation of a thermal barrier coating," *J. Am. Ceram. Soc.*, **81**, 3237-42.

Shuk, P., Wiemhofer, H. D., Guth, U., Gopel, W. and Greenblatt, M., (1996) Oxide ion conducting solid electrolytes based on Bi_2O_3, *Solid State Ionics*, **89**, 179-196.

Shuller, K. H., (1964), Reaction between mullite and glassy phase in porcelains, *Trans. Br. Ceram. Soc.*, **63**, 102-107.

Sidebottom, D. L., Green, P. F. and Brow, R. K., (1995), Comparison of KWW and power law analysis of an ion-conducting glass, *J. Non-Cryst. Solids*, **183**, 151-160.

Sinclair, D. C. and West, A. R., (1989), Impedance and modulus spectroscopy of semiconducting $BaTiO_3$ showing positive temperature coefficient of resistance, *J. Appl. Phys.*, **66**, 3850-3856.

Smith, D. S., Lavielle D. and Orange, G., (1994), Electrical response of microcracks in alumin/zirconia ceramic composites, *Silica. Indus.*, **5-6**, 165-167.

Solartron Group, (1999), 1296 Dielectric Interface Operating Manual, Solartron, Farnborough, UK.

Song, G. -L., (2000), Equivalent circuit model for AC electrochemical impedance spectroscopy of concrete, *Cem. Concr. Res.*, **30**, 1723-1730.

Song, H. -K., Jung, Y.-H., Lee K.-H. and Dao, L.-H., (1999), Electrochemical impedance spectroscopy of porous electrodes: the effect of pore size distribution, *Electrochimica. Acta.*, **44**, 3513-1519.

Sonuparlak, B., Sarikaya M. and Aksay, I. A., (1987), Spinel phase formation during 980°C exothermic reaction in the kaolin-mullite reaction series, *J. Am. Ceram. Soc.*, **70**, 837-842.

Souquet, J. L., (1995), Ionic transport in glassy electrolytes, p74, in *Solid State Electrochemistry*, P. G. Bruce, (ed), Cambridge University Press, Cambridge.

Steil, M. C., Thevenot F. and Kleitz, M., (1997), Densification of yttria-stabilised zirconia: impedance spectroscopy analysis, *J. Electrochem. Soc.*, **144**, 390-398.

Sternitzke, M., Derby, B. and Brook, R. J., (1998), Alumina/silicon carbide nanocomposites by hybrid polymer/powder processing: microstructures and mechanical properties, *J. Am. Ceram. Soc.*, **81**, 41-48.

Sterns, C.A., Kohl, F.J. and Fryburg, G. C., (1974), Oxidative vapour kinetics of Cr_2O_3 in oxygen from 1000 C to 1300C, *J. Electrochem. Soc.*, **121**, 953-959.

Tawancy, H. M., Sridhar, N., Abbas N. M. and Rickerby D., (1998), Failure mechanism of a thermal barrier coating system on a nickel-base superalloy, *J. Mater. Sci.*, **33**, 681-686.

Tiefenbach, A. and Hoffmann, B., (2000), Influence of a crack on the electrical impedance of polycrystalline ceramics, *J. Euro. Ceram. Soc.*, **20**, 2079-2094.

Torrents, J. M., Easley, T. C., Faber, K. T., Mason, T. O., and Shah, S. P., (2001), Evolution of impedance spectra during debonding and pullout of single steel fibres from cement, *J. Am .Ceram. Soc.*, **84**, 740-746.

Torrents, J. M., Mason T. O. and Garboczi, E. J., (2000), Impedance spectra of fibre reinforced cement based composites: a modelling approach, *Cem. Concr. Res.*, **30**, 585-592.

Traversa, E., (1995), Ceramic sensors for humidity detection: the state-of-the-art and future developments, *Sensors and Actuators*, **B23**, 135-156.

Tuller, H. L., (2000), Ionic conduction in nanocrystalline materials, *Solid State Ionics*, **131**, 143-157.

Turdogan, E. T., (1983), Chapter 2 Structural aspects, p57, in *Physicochemical Properties of Molten Slags and Glasses*, The Metals Society, London.

Van de Voorde, M. H. (1998), Non-destructive evaluation (NDE) of carbon-carbon (C-C) and ceramic composite material, *Bri. Ceram. Trans.*, **97**, 287-292.

Wadley, H. N. G., and Mehrabian, R., (1984), Acoustic emission for in-process monitoring and microstructure control, p207, in *Nondestructive Methods for Material Property Determination*, C. O. Ruud and R. E. Green, Jr., (eds), Plenum Press, London.

Wang, S. -K., Fu. X. -L. and Chung, D. D. L., (1998) Nondestructive evaluation of brittle-matrix composites during loading by electrical resistance measurement, p145, in *Nondestructive Evaluation of Ceramics*, C. H. Schilling and J. N. Gray, (eds) (**Vol 89**, Ceramic Transaction), American Ceramic Society, Westerville, Ohio.

Wang. C. -A., Huang, Y., Xie, Z. -P., Li, Y. and Zhang, Z. -T., (2000), Complex impedance analysis on the orientation effect of whiskers in oriented silicon carbide whisker/silicon nitride composites, *J. Am. Ceram. Soc.*, **83**, 2689-2692.

Waser R. and Hagenbeck, R., (2000), Grain Boundary in dielectric and mixed conducting ceramics, *Acta. Mater.*, **48**, 797-825.

West, A. R., (1995), Crystalline solid electrolytes I: general considerations and the major materials, p7, in *Solid state Electrochemistry*, P. G. Bruce, (ed), Cambridge University Press.

Whalen P. J., Reidinger, F., Correale, S. T. and Marti, J., (1987), Yttria migration in Y-TZP during high-temperature sintering, *J. Mat. Sci.*, **22**, 4465-4469.

Wolfe, D., and Singh, J., (1998), Functionally gradient ceramic/metallic coatings for gas turbine components by high-energy beams for high temperature applications, *J. Mater. Sci.*, **33** 3677-92.

Wu, B. C., Chang, E., and Chang, S., (1989), Degradation mechanisms of ZrO_2-8wt% Y_2O_3/Ni-22Cr-10Al-1Y thermal barrier coatings, *J. Am. Ceram. Soc.*,**72**, 212-218 .

Wu, H. Z., Lawrence, C. W., Roberts, S. G., and Derby, B., (1998), The strength of Al_2O_3/SiC nanocomposites after grinding and annealing, *Acta Mater.*, **11**, 3839-3848.

Zhang, J. -S., Huang, H., Cao, L.-H. and Xia, F., (1992), Semiconductive property and impedance spectra of alumina-silicon carbide whisker composites, *J. Am. Ceram. Soc.*, **75**, 2286-2288.

Zoltowski P, (1998), On the electrical capacitance of interfaces exhibiting constant phase element behaviour, *J. Electroanal. Chem.*, **443**, 149-154.

Appendix I

Representation Diagrams Of Impedance Spectroscopy:

For an equivalent circuit:

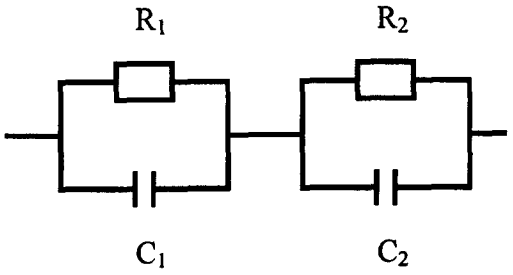

FigA1-1. An ideal equivalent circuit

$$Z' = \frac{R_1}{1+(\omega R_1 C_1)^2} + \frac{R_2}{1+(\omega R_2 C_2)^2} \qquad (A1-1)$$

$$Z'' = \frac{\omega R^2{}_1 C_1}{1+(\omega R_1 C_1)^2} + \frac{\omega R^2{}_2 C_2}{1+(\omega R_2 C_2)^2} \qquad (A1-2)$$

$$M^* = j\omega C_o Z^* = M' + jM'' \qquad (A1-3)$$

$$\varepsilon^* = (M^*)^{-1} \qquad (A1-4)$$

$$Y^* = (Z^*)^{-1} \qquad (A1-5)$$

$$Y^* = j\omega C_o \varepsilon^* \qquad (A1-6)$$

If assuming $R_1=1x10^7\ \Omega$, $C_1=1x10^{-11}$ F, $R_2=5x10^7\ \Omega$, $C_2=1x10^{-10}$ F, and based on above equations, various IS representation diagrams for this circuit can be illustrated as in Fig.A1-2a-i.

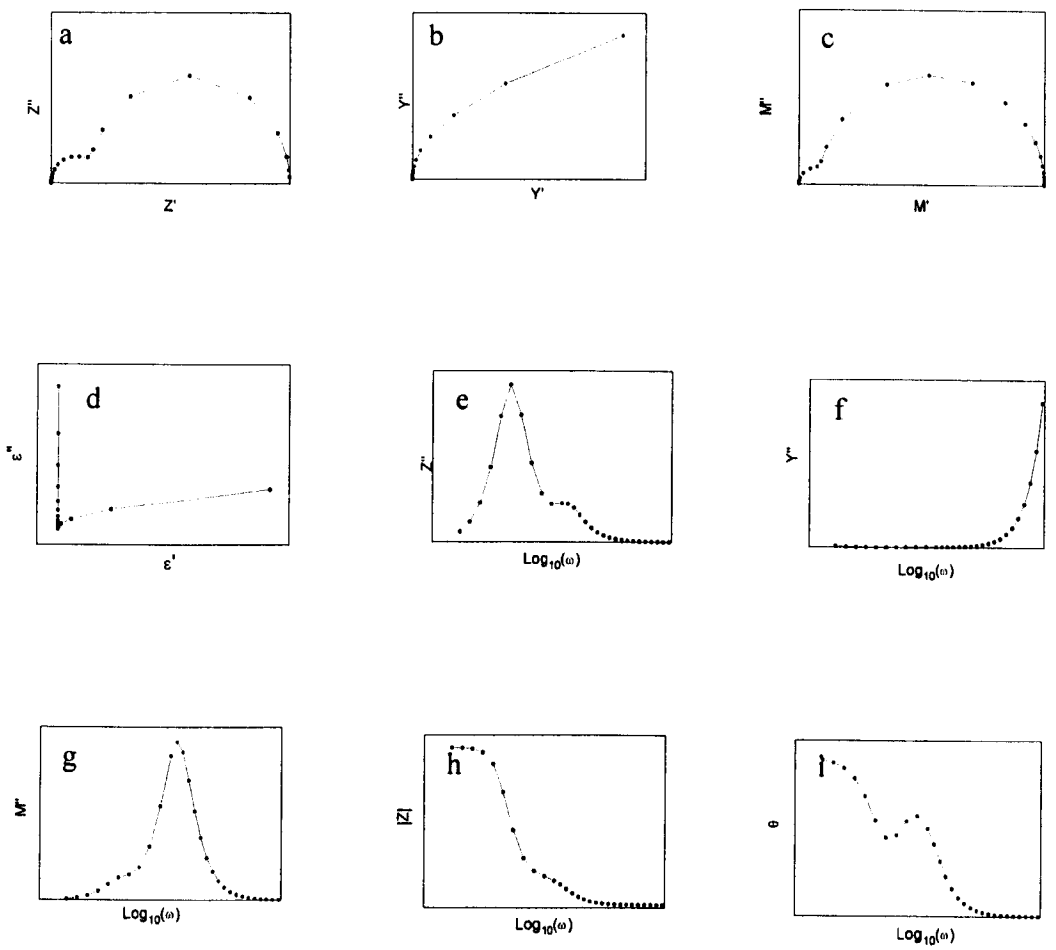

Fig. A1-2(a) complex impedance plot; (b) complex admittance plot; (c) complex modulus plots; (d) complex permittivity plot; (e) impedance spectroscopic plot; (f) admittance spectroscopic plot; (g) modulus spectroscopic plot; (h)Bode plot ($|Z|$ vs $\log_{10}(\omega)$); (i) Bode plot (θ vs $\log_{10}(\omega)$).

Appendix II

The Impedance Spectra Of 10SA Samples

The Impedance Spectra Of 10SA Samples see Fig.A2-1.

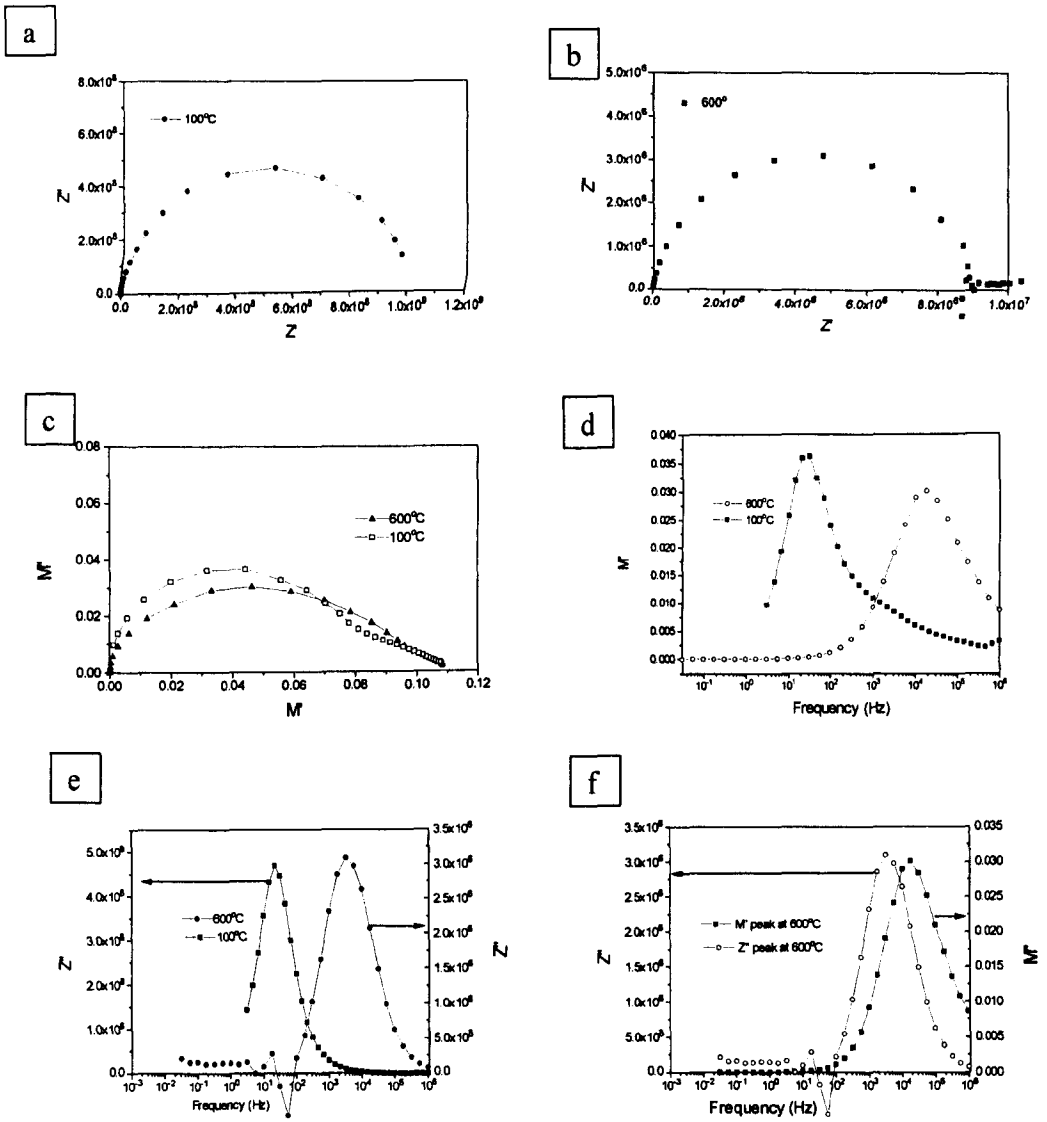

FigA2-1 (a) complex impedance plot at 100°C; (b) complex impedance plot at 100°C; (c) complex modulus plots; (d) modulus spectroscopic plots; (e) impedance spectroscopic plots, note the different scales of y-axis; (f) comparison of Z'' peak and M'' peak in modulus and impedance spectroscopic plots.

Appendix III

The Impedance Spectra Of Clay/Graphite Composites

In order to investigate the dependence of IS on the orientation of the dispersed conductive phase in an insulator matrix, clay/graphite composites containing 3 vol %, 6 vol% and 12 vol% flaky graphite were fabricated for impedance measurements. All the clay/graphite composites were sintered in argon to protect the graphite inclusions from oxidation. The sintering temperatures and dwell time were 1100°C~1250°C and 1~4h respectively.

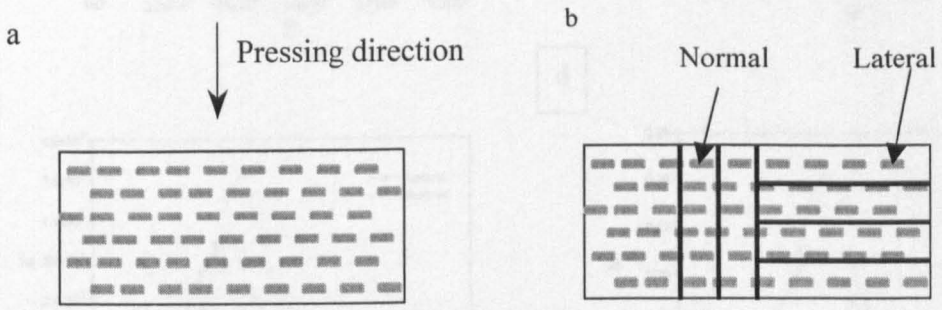

Figure A3-1 a) A schematic of the microstructure of the clay/graphite composites in cross section, with the flaky graphite particles oriented parallel to the top surface; b) definition of cutting direction.

Optical microscopy observations showed that the flaky graphite particles were oriented preferentially parallel to the top surface, i.e., perpendicular to the pressing direction as a consequence of uni-axial pressing, as shown in Fig. A3-1a. Samples were cut from the sintered thick pellets along two directions: parallel and normal to the top surface, as shown in Fig. 5-1b. All the samples were ground to the same dimension: 10mm (long) by 6mm (wide) by 2mm (thick).

The general IS features of clay/graphite composites were similar to those of Al_2O_3/SiC nanocomposites: only one relaxation process can be identified in the IS; the conductivity and dielectric constant increased with an increase in graphite particle loading. It was found the composite containing 5vol% graphite was insulative, but the composite became conductive when graphite content was 12 vol%, this indicates that the threshold

conductive volume fraction should be between 5 vol% and 12 vol%. Unlike SiC particles in Al_2O_3/SiC nanocomposites, the graphite particles are not equiaxed. The non-equiaxed nature of conductive particles could result in a lower threshold volume fraction. Therefore the threshold volume of clay/graphite composites should be lower than that of

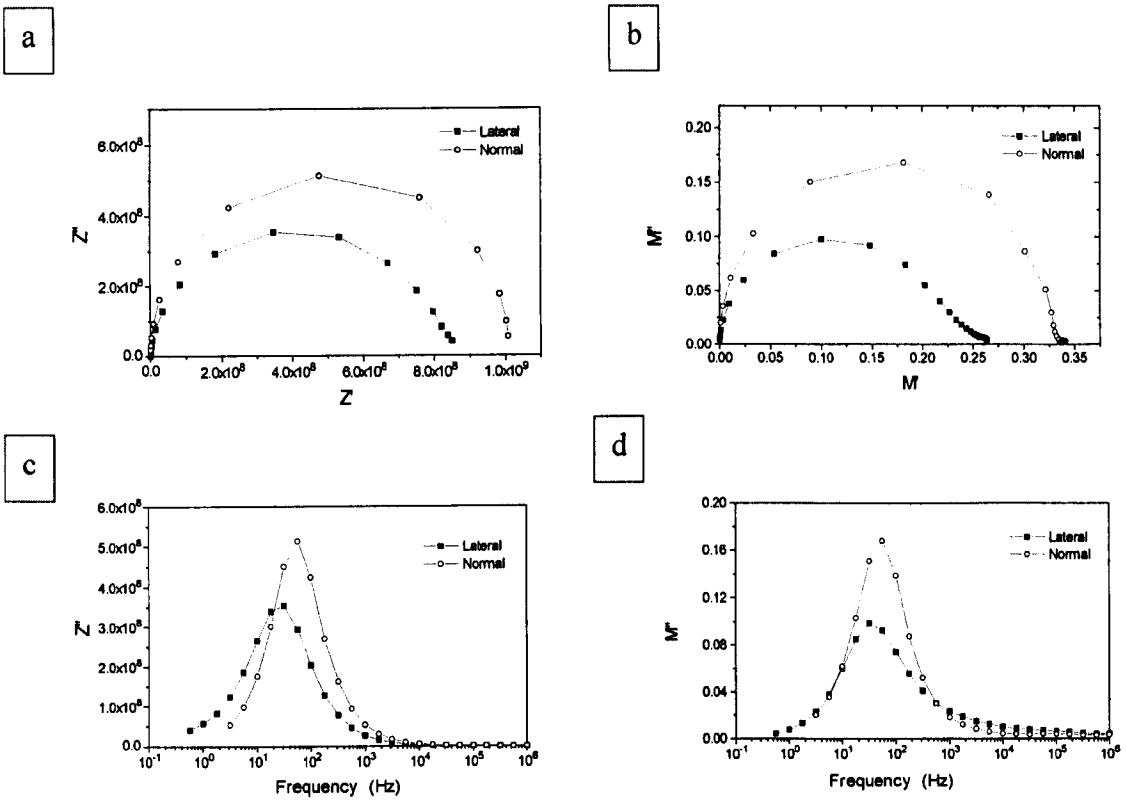

Al_2O_3/SiC nanocomposites.

Fig. A3-2 impedance spectra in different directions of a clay/graphite composite containing 3 wt% flaky graphite particles (a) impedance complex plane plot; (b) modulus complex plane plot; (c) impedance spectroscopic plot and (d) modulus spectroscopic plot. Please note that all of these quantities have been normalised in terms of the specimen's geometrical dimensions.

The impedance spectra of clay/graphite composite with 3 vol % graphite particles in two different directions are given in Fig.A3-2. We can see that in the direction parallel to the orientation of the particles, the resistance was lower and dielectric constant was higher. However there was not much difference in relaxation frequency in different directions.